The silicon photomultiplier telescope FAMOUS for the detection of fluorescence light

Von der Fakultät für Mathematik, Informatik und Naturwissenschaften der RWTH Aachen University zur Erlangung des akademischen Grades eines Doktors der Naturwissenschaften genehmigte Dissertation

vorgelegt von

Tim Niggemann, M.Sc. RWTH

aus Neuwied

Berichter: Universitätsprofessor Dr. rer. nat. Thomas Hebbeker
Privatdozent Dr. rer. nat. Oliver Pooth

Tag der mündlichen Prüfung: 31.10.2016

"The history of astronomy is a history of receding horizons"

(Edwin Powell Hubble, 1936)

Abstract

The faint fluorescence light of extensive air showers produced by cosmic rays is traditionally detected by means of optical telescopes equipped with photomultiplier tubes. Since these devices are fragile, the prototype telescope FAMOUS has been built to investigate the versatility of silicon photomultipliers whose photon detection efficiency surpasses the quantum efficiency of photomultiplier tubes. In this thesis, the 61 pixel telescope FAMOUS has been successfully commissioned and quantitative measurements of star trails have been performed. Furthermore, detailed simulations, especially for the silicon photomultipliers, have been developed and validated against measurements conducted in the laboratory.

Zusammenfassung

Das schwache Fluoreszenzlicht, emittiert von ausgedehnten Luftschauern, wird traditionell mit optischen Teleskopen ausgerüstet mit Photomultiplier-Röhren detektiert. Da diese Bauteile sehr empfindlich sind, wurde das Prototypteleskop FAMOUS entwickelt, um die Einsetzbarkeit von Silizium-Photomultipliern zu untersuchen, deren Photon-Nachweiswahrscheinlichkeit die der Röhren übertrifft. In dieser Arbeit wurde das 61 Pixel Teleskop FAMOUS erfolgreich in Betrieb genommen und eine quantitative Messung von Sternenspuren durchgeführt. Des Weiteren wurden detaillierte Simulationen, im speziellen für die Silizium Photomultiplier, entwickelt und mit Labormessungen verglichen.

Contents

Chapter 1

Introduction

Cosmic rays constantly hitting the atmosphere of the Earth have been of key interest to astroparticle physics research for several decades [1]. By means of carefully conducted measurements, conclusions on their sources and the genesis of the universe can be drawn. Since at the highest energies $E > 10^{18}\,\mathrm{eV}$ the flux is below several particles per square kilometer and year, indirect measurements of the extensive air showers induced by cosmic rays in the atmosphere are performed. Traditionally, mirror telescopes equipped with photomultiplier tubes sensitive in the ultraviolet regime are used to measure the faint, isotropically emitted fluorescence light of these showers [2, 3, 4, 5, 6, 7].

The prototype telescope FAMOUS has been developed to test the versatility of silicon photomultipliers for the use in fluorescence telescopes. FAMOUS is an apronym for "First Auger Multi-pixel photon counter camera for the Observation of Ultra-high-energy air Showers" (cf. figure 1.1).

Silicon photomultipliers (SiPMs) are arrays of silicon-based Geiger-mode avalanche photodiodes (GAPDs) whose photon detection efficiency can surpass the quantum efficiency of photomultiplier tubes [8]. Compared to the tubes, SiPMs are mechanically very robust and virtually indestructible by high intensity light which makes them ideal candidates for exposed applications such as in atmospheric telescopes. On the downside, SiPMs have a higher thermal and correlated noise resulting in a dark noise rate of $\mathbb{O}(100\,\mathrm{kHz})$ per square millimeter sensor area [9]. Nevertheless, due to the small timescale of the fluorescence light signal $\mathbb{O}(1\,\mu\mathrm{s})$ [6], the effect is small. Additionally, the signal is increased by coincident optical crosstalk which can be removed on a statistical basis. For less photon detection efficiency demanding applications, devices with crosstalk probabilities $< 1\,\%$ are available whereas otherwise typical values

Figure 1.1: The logo of the FAMOUS project. The apronym stands for "First Auger Multi-pixel photon counter camera for the Observation of Ultra-high-energy air Showers".

are $\mathbb{O}(10\,\%)$ [10]. The properties of SiPMs vary with the over-voltage, i.e. the voltage excess of the bias voltage ($< 100\,\mathrm{V}$) over the breakdown voltage which changes with temperature. By monitoring the ambient temperature, the bias voltage of the SiPMs can be adapted accordingly which results in a stable gain.

This thesis is structured as follows: firstly, the SiPM simulation package G4SiPM is presented. G4SiPM is a package for Geant4, a Monte Carlo framework for the simulation of the passage of particles through matter and widely used in particle physics [11]. G4SiPM implements a phenomenological model of SiPMs driven by quantities which can be easily obtained from datasheets of the manufacturers or by measurements in the laboratory [12]. Furthermore, each GAPD on the SiPM is simulated separately for a correct handling of the thermal and correlated noise and the dynamic range of these devices which is limited due to the limited amount of GAPDs on a device. The model is then validated against laboratory measurements.

Secondly, the mechanics and optics of the telescope FAMOUS are discussed. FAMOUS is a refractor whose main optical element is a 2.5 mm thin plastic Fresnel lens with a diameter of 502.1 mm [13]. The lens focuses the incoming light onto a focal plane of 61 pixels which each consist of a light funnel made from polished aluminum, a UV pass filter and the SiPM. The SiPMs are manufactured by Hamamatsu and have a sensitive area of $6\,\mathrm{mm} \times 6\,\mathrm{mm}$ each [14]. Furthermore, the imaging quality of the Fresnel lens is measured by recording the point spread function for different light incident angles and for varying lens to focal plane distances. The telescope is accompanied by several sensors continuously monitoring the ambient conditions and a CMOS camera which shoots images of the night sky. The visible stars in these images are identified to derive the viewing direction. For the focal plane, a dedicated power supply unit with 64 channels has been developed in-house [15]. It monitors the temperature of each SiPM and adjusts the bias voltage accordingly. Furthermore, the current flow through the SiPMs is recorded.

Thirdly, all optical components of the telescope are simulated by a Geant4 driven ray-tracing simulation. The results are compared to the measurements to reveal potential weaknesses of the simulation model. All components and G4SiPM in conjunction make up the detector simulation of FAMOUS which enables the simulation of signals of the fluorescence light of extensive air showers. The simulation process is sped up by the introduction of a telescope response parameterization which makes quasi instantaneous predictions of the SiPM signals possible.

Fourthly, the readout software and slow control of the telescope are introduced. The slow control consists of a web interface which allows the remote control and data display of all hardware components of the telescope and thus is essential to a successful operation. The main aspects of the slow control are stability and ease of use while preventing single point of failures.

Lastly, measurements of star trails performed with the successfully commissioned telescope operated during night are presented. By means of the current flow monitoring of the power supply unit of FAMOUS, the current rise of the SiPMs due to the transit of bright stars has been measured and compared to expected values. The expected photon rates of these stars are calculated from spectral irradiance measurements and models. Due to intrinsic absorption and aerosols the star light is attenuated depending on the path length through the atmosphere determined by the apparent height of the star above the horizon. Finally, the detector simulation of FAMOUS is used to consider the transmission efficiency of the optical system and the detection efficiency of the SiPMs in dependence on the photon wavelength.

CHAPTER 2

Cosmic rays

Cosmic rays have been discovered in 1912 as a result of an increase of radiation levels during high ascension balloon flights at an altitude of $> 5300\,\mathrm{m}$ above ground by the Austrian physicist Victor Hess who believed the increase is caused by gamma radiation originating from space. Later, in 1926, R. A. Milikan was the first to coin the expression of cosmic rays [16]. Not until 1939, mesons were correctly identified as possible byproducts of cosmic radiation [17] which indicated that the primary particles were likely charged hadrons such as protons. Apart from balloon flights, P. Auger and collaborators measured the coincidence rate of cosmic rays at ground with newly developed instruments allowing a timing resolution of $10\,\mu\mathrm{s}$ [18]. Unexpectedly, the rate of correlated arrivals of charged particles was much higher than expected for distances $> 300\,\mathrm{m}$, leading to the conclusion that energetic cosmic rays induce widely spread showers of secondary particles. P. Auger estimated that the primary particles of those cosmic rays were charged particles with an energy of $10^{15}\,\mathrm{eV}$ corresponding to a center of mass energy of $\sqrt{s} = \sqrt{2\,E\,m_p} = 1.4\,\mathrm{TeV}$. This discovery built the basis of modern astroparticle physics which tries to identify the sources and acceleration mechanisms of the radiation.

More detailed information can be found in the excellent overviews of this field of research in [1, 19, 20, 21].

2.1 Energy spectrum

Nowadays, the energy spectrum, i.e. the differential particle flux, of cosmic rays has been measured over 10 magnitudes of energy, by direct measurements such as airborne or satellite experiments in the lower energy regime $< 10^{15}\,\mathrm{eV}$ in which the flux is high, and by indirect measurements of extensive air showers (cf. figure 2.1). Thereby the energy spectrum follows a so-called broken power law

$$F(E) = \frac{\mathrm{d}^2 N(E)}{\mathrm{d}E\,\mathrm{d}\Omega} \propto \left(\frac{E}{\mathrm{eV}}\right)^{-\gamma} \tag{2.1}$$

with a spectral index γ. The spectrum is referred to as broken, since distinct features lead to a change of the spectral index. The stepping at $E_k = 10^{15.5}\,\mathrm{eV}$ is known as the knee of

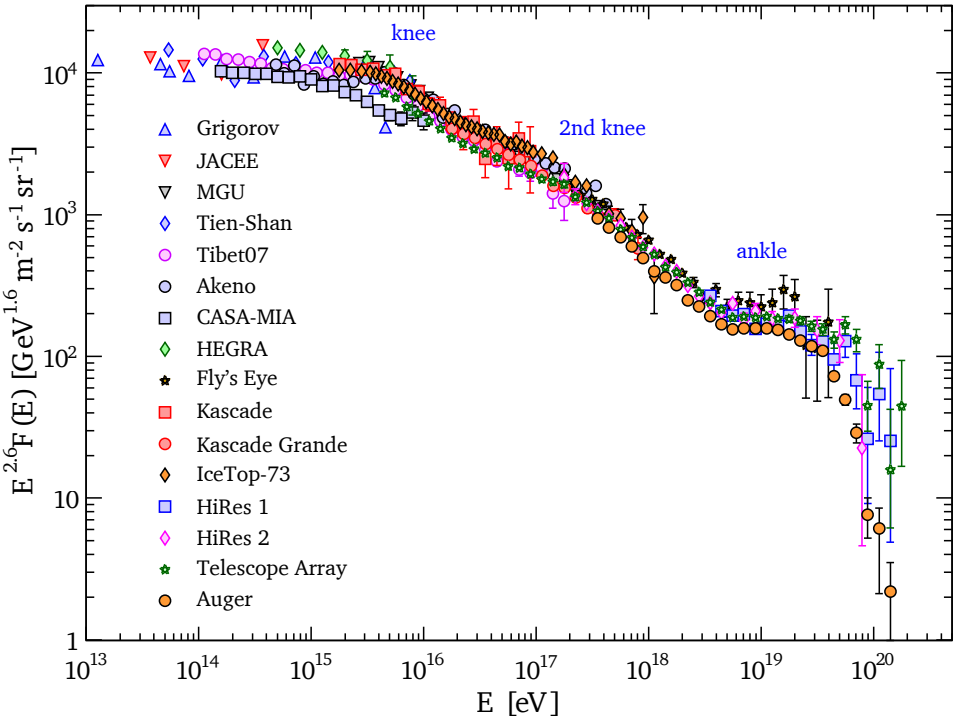

Figure 2.1: Differential all particle flux as a function of energy of cosmic rays. The displayed data has been obtained by air shower experiments. For better visibility of the features, the energy spectrum has been multiplied with $E^{2.6}$. Thus, the knee, the second knee and the ankle are emphasized. For energies $> 10^{20}$ eV the flux is suppressed. The origin of the suppression is still unknown. Taken from [22].

the spectrum at which the spectral index changes from $\gamma \approx 2.7$ to $\gamma \approx 3$ [23]. Around the second knee at $E_{2^{\text{nd}}\,k} = 10^{16.9}$ eV the spectrum hardens to $\gamma = 3.2$ up to the occurrence of the ankle at $E_a = 10^{18.7}$ eV [24]. After the ankle, the spectrum flattens to $\gamma = 2.6$ before the flux suppression sets in. The flux suppression is marked by the energy $E_{1/2} = 10^{19.6}$ eV at which the flux has fallen to 50 % of its value before the onset of the suppression.

Since cosmic rays are of unknown origin, many different models are discussed in the literature to explain the existence of the knee as it is believed to mark the transition of galactic to extragalactic cosmic rays [25]. A popular explanation is that each spectrum of the individual elements follows an individual power law with a cut off at high energies whereby a common spectral index and a cutoff energy proportional to the charge Z

$$E_c(Z) = Z\,E_c^p \tag{2.2}$$

with $E_c^p = E_k = 10^{15.5}$ eV for protons describes the data best (cf. e.g. poly-gonato model [25]). Thus, the knee marks the onset of the extinction of galactic sources up to $E_c(\approx 30) = 10^{17}$ eV which roughly coincides with the second knee under the assumption that ultra heavy elements are of minor importance. Other models relate the occurrence of the knee to a leakage of cosmic rays from the galaxy (e.g. Leaky Box model [26]), to interactions of cosmic rays with background particles (e.g. photo disintegration) or to new, not yet observed, interactions during the shower development in the atmosphere [25].

Due to the magnetic fields of the milky way, the charged particles are bent on circular paths with a characteristic radius, the Larmor radius

$$r_L = \frac{p}{Z\,e\,B} \approx \frac{10\,\mathrm{m}}{3}\left(\frac{p\cdot c}{\mathrm{GeV}}\right)\left(\frac{B}{\mathrm{T}}\right)^{-1} \quad . \tag{2.3}$$

Particles with energies of $E = E_a = 10^{18.7}$ eV yield a Larmor radius of > 1800 pc which exceeds the thickness of the galactic disk of ≈ 300 pc. Therefore, in a simplified view, these particles are no longer confined in the galaxy. Thus, the ankle is associated with a population of cosmic rays of extragalactic origin.

Finally, the end of the energy spectrum of cosmic rays is either a natural end to the acceleration capabilities of their sources or due to interactions with photons of the cosmic microwave background (CMB) which roughly coincides with a predicted cutoff above $6 \cdot 10^{19}$ eV. During propagation protons would suffer energy loss by forming $\Delta^+(1232)$ resonances which further decay to neutrons and pions

$$p + \gamma_{\mathrm{CMB}} \rightarrow \Delta^+ \rightarrow p + \pi^0 \tag{2.4}$$

$$p + \gamma_{\mathrm{CMB}} \rightarrow \Delta^+ \rightarrow n + \pi^+ \tag{2.5}$$

which in turn further decay. The neutrinos from the neutron and π^+ decays are of particular interest to measurements performed at IceCube and other neutrino experiments [27].

2.2 Acceleration mechanisms of cosmic rays

Since charged cosmic rays are deflected on their way through space, the question on their sources and production mechanisms is still open. Diffuse shock acceleration is a widely accepted acceleration model, already proposed by E. Fermi in 1949 [31]. Thus, the mechanism is also referred to as first-order Fermi acceleration. Shock waves of e.g. supernova remnants are preceded and followed by turbulent magnetic fields. By chance, low energy cosmic ray particles can be deflected in downstream direction upon crossing the shock area upstream and vice versa. Each deflection increases the energy of the cosmic ray whereby the total energy gain ΔE is

$$\Delta E \propto \beta_s \tag{2.6}$$

and thus proportional to the velocity β_s of the shock front. With increasing energy, chances increase that the particle escapes the shock region. The resulting energy distribution of the cosmic ray particles escaping the shock region is

$$\frac{\mathrm{d}N}{\mathrm{d}E} \propto E^{-\gamma} \tag{2.7}$$

which is a power law. This process can explain cosmic ray production in supernova remnants with a spectral index of $\gamma \approx 2$ up to energies of $E_{\mathrm{max}} \approx 10^{17}$ eV [1].

Similar to the Larmor radius in equation (2.3), a condition for successful acceleration of cosmic rays with an energy of E_{max} in diffusive shocks and one-shock acceleration of electric fields generated by rotating magnetic fields has been derived by G. Hillas

$$\left(\frac{E_{\mathrm{max}}}{1\,\mathrm{EeV}}\right) = 2 \cdot 1.08 \cdot Z \cdot \beta_s \cdot \left(\frac{B}{1\,\mu\mathrm{G}}\right)\left(\frac{R}{1\,\mathrm{kpc}}\right) \tag{2.8}$$

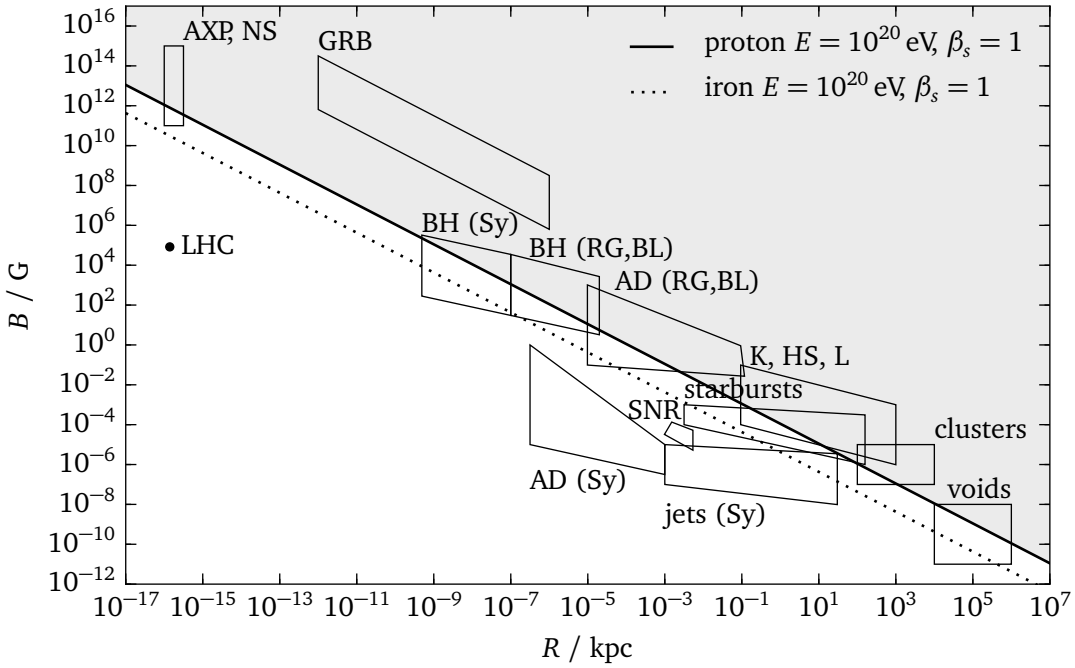

Figure 2.2: The Hillas plot signifying the parameter space of radius R and magnetic field strength B of source candidates of cosmic rays. The solid line signifies the lower boundary of the Hillas criterion given by equation (2.8) with $\beta_s = 1$ for 10^{20} eV protons. Thus, the shaded area above denotes the parameter region which presumably is allowed by the Hillas criterion. The dashed line corresponds to 10^{20} eV iron nuclei. The boxes mark regions of interests for astronomical objects that are: x-ray pulsars and magnetars (AXP), neutron stars (NS); super-massive black holes (BH) and central parsecs (AD) of active galaxies (low-power Seyfert galaxies (Sy), powerful radio galaxies (RG) and blazars (BL)); relativistic jets, knots (K), hot-spots (HS), and lobes (L) of powerful active galaxies (RG and BL); non-relativistic jets of low-power galaxies (Sy); gamma-ray bursts (GRB); galaxy clusters and intercluster voids and supernova remnants (SNR). The dot marks the Large Hadron Collider (LHC) at CERN with a circumference of 27 km and 8.3 T field strength. Adapted from [28].

with the radius of the source R, its magnetic field strength B, the charge number Z of the cosmic ray and the shock front velocity β_s. This is often referred to as Hillas criterion. For other acceleration mechanisms, β_s denotes the acceleration efficiency. Typical values for supernova remnants are $R = 1\,\mathrm{pc}$ and $B = 100\,\mu\mathrm{G}$ which yields in $E_{\max} \approx 10^{17}$ eV already cited above.

Thus, supernova remnants are disfavored as candidates for ultra-high-energy cosmic rays (UHECRs) with $E > 10^{18}$ eV. G. Hillas was the first to compare source candidates in the parameter space of source radius R and magnetic field strength B in a graphical view. An example for a so-called Hillas plot can be found in figure 2.2. The lines denote the solutions for $E = 10^{20}$ eV protons and iron nuclei for shocks with $\beta_s = 1$. All candidates above the line are possible sources as e.g. active galactic nuclei (AGN, cf. BH, AD, etc. in figure 2.2) which are widely discussed in literature.

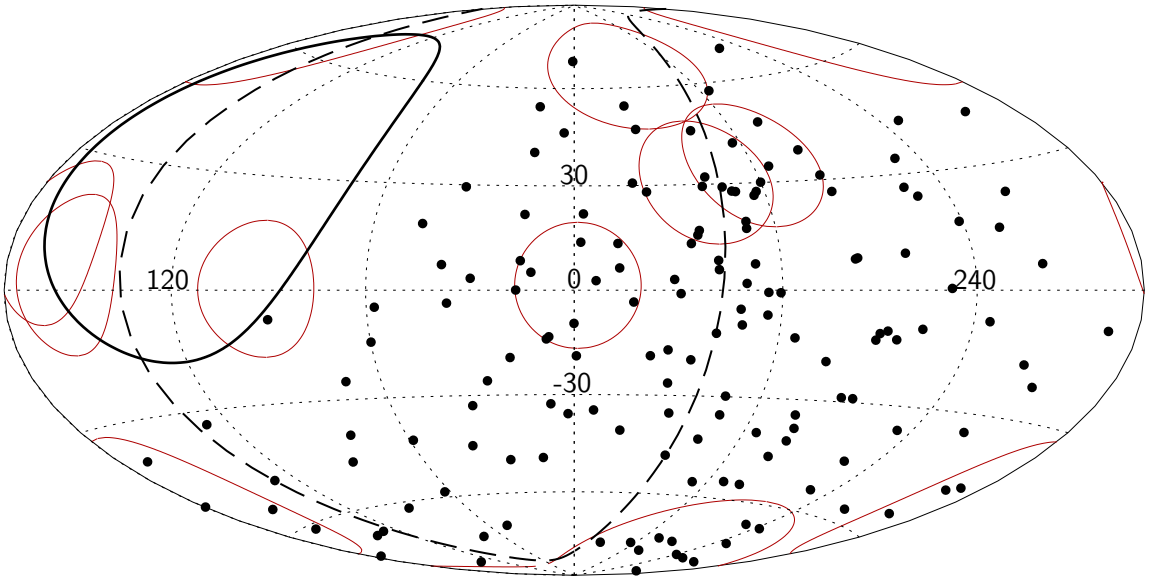

Figure 2.3: Map in galactic coordinates of the arrival directions of events, denoted by the black dots, with $E \geq 58\,\mathrm{EeV}$ measured by the Pierre Auger Observatory [29]. The red circles signify region of interests of 18° radius around active galactic nuclei (taken from the Swift-BAT catalog [30]) which are brighter than $10^{44}\,\mathrm{erg\,s^{-1}}$ and closer than 130 Mpc. By an auto-correlation analysis from 155 cosmic rays, 62 event pairs could be successfully matched to the AGNs while 32.5 are expected from isotropy. The chance probability for this observation given isotropy is $p = 1.3\,\%$.

An example for a search for source candidates is presented in [29, 32] which has been conducted by the collaboration of the Pierre Auger Observatory. There, the arrival directions of the most energetic cosmic rays, which are least likely to be deflected by galactic magnetic fields, with $E \geq 58\,\mathrm{EeV}$ have been associated on a statistical basis to the position of very bright AGNs (cf. figure 2.3) by means of an auto-correlation analysis. From the selected 155 cosmic rays, 62 event pairs could be successfully matched to regions of interest of 18° in size around the candidate AGNs while 32.5 are expected from isotropy. The chance probability of this observation is $p = 1.3\,\%$ under the assumption of isotropic arrival directions and thus unfortunately merely a hint for AGNs as sources of UHECRs. Other similar directed searches for anisotropy have been conducted e.g. by the Telescope Array [33] with similar results.

Most recent results of statistical analyses of the arrival direction of cosmic rays, so-called undirected searches, revealed a large-scale anisotropy at high energies $E > 4\,\mathrm{EeV}$ by the reconstruction of a dipole component [34]. The dipole has been observed at a right-ascension and declination of $(\alpha, \delta) = ((95 \pm 13)°, (-39 \pm 13)°)$ with an amplitude of 0.073 ± 0.015 and a chance probability of $p = 6.4 \cdot 10^{-5}$ for $E > 8\,\mathrm{EeV}$ under the hypothesis that the data is solely produced by a dipole. The hypothesis applies to the whole sky although only a fraction of 85 % can be seen by the Pierre Auger Observatory. The dipolar anisotropy could originate from extra-galactic turbulent magnetic fields or an inhomogeneous matter distribution in our local extragalactic neighborhood. This interesting result could help to reveal the origin of cosmic rays.

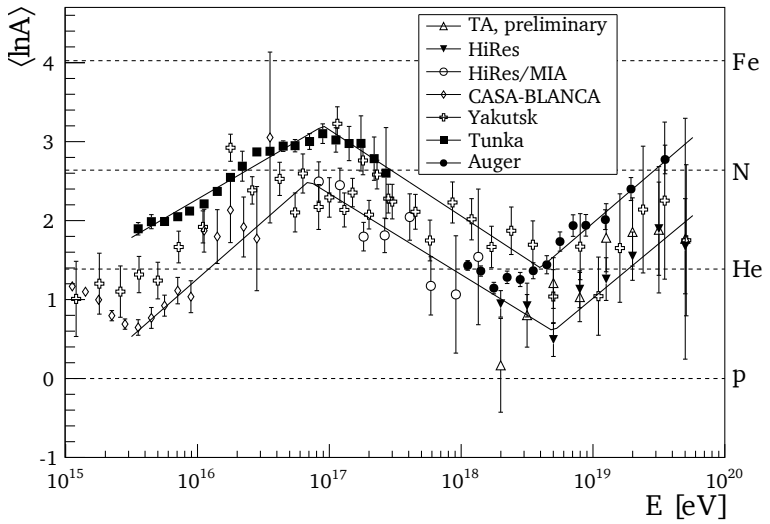

Figure 2.4: Average logarithmic atomic mass of high energy cosmic rays derived from air shower measurements with optical detectors for the EPOS 1.99 interaction model. To guide the eye, the upper and lower boundaries of the presented data are sketched as lines. These lines can also be understood as estimates on the experimental systematics on the logarithmic mass. Figure taken from [35].

2.3 Chemical composition

The chemical composition of cosmic rays can be measured by direct measurements which have shown that around $E = \mathbb{O}(1\,\mathrm{GeV})$ cosmic radiation mainly consists of charged nuclei [1] whereby $\approx 79\,\%$ are free protons, approximately 15 % are helium nuclei.

Due to the low flux at higher energies $E > 10^{15}\,\mathrm{eV}$, only indirect measurements of cosmic rays by means of extensive air showers are possible and therefore, the determination of the particle species can only be performed on a statistical basis. Yet, a detailed measurement of the chemical composition of ultra-high-energy cosmic rays would help to constrain astrophysical models regarding the sources of cosmic rays and the flux suppression [36]. As presented in figure 2.4, measurements hint that the chemical composition becomes heavier above the knee at $E_k = 10^{15.5}\,\mathrm{eV}$ and reaches a maximum at the second knee which can be understood as heavier particles accelerated to higher energies (cf. equation (2.8)). Above the second knee, the composition becomes lighter corresponding to the onset of an extragalactic cosmic ray population. Remarkably, again an increase in mass appears above the ankle at $E_a = 10^{18.7}\,\mathrm{eV}$ which could mark the maximum energy of extra-galactic accelerators rather than the GZK effect. Thus, a detailed measurement of the chemical composition is of great interest and currently in the focus of a major upgrade of the Pierre Auger Observatory [36, 37].

2.4 Extensive air showers

When entering the atmosphere of the Earth, high energy cosmic rays interact with the air molecules and produce numerous secondary particles. These secondaries are subject to further interactions and decays and develop into so-called extensive air showers (EAS) which travel in

form of a pancake with nearly the speed of light towards ground. The amount of matter of the atmosphere traversed by the EAS is denoted by the slant depth X

$$X(h) = \int_h^\infty \rho(h')\mathrm{d}h' \tag{2.9}$$

$$= \int_h^\infty \rho_0 e^{-h'/h_0}\mathrm{d}h' \approx 1000\,\mathrm{g\,cm^{-2}}\, e^{-h/h_0} \tag{2.10}$$

for perpendicular shower incidence with the air density $\rho_0 = 1.35\,\mathrm{kg\,m^{-3}}$ and the reference height $h_0 = 7.25\,\mathrm{km}$. For inclined showers, the amount of traversed matter is increased

$$X(h,\theta) \approx X(h)\frac{1}{\cos\theta} \tag{2.11}$$

with the zenith angle θ relative to the surface normal. Thus, the atmosphere corresponds to roughly 11 hadronic interaction lengths $X_0^{\mathrm{hadr}} = 90.1\,\mathrm{g\,cm^{-2}}$ and roughly 27 electromagnetic radiation lengths $\lambda_{\mathrm{em}} = 36.6\,\mathrm{g\,cm^{-2}}$ [22], respectively.

2.4.1 Heitler model

A very simple but illustrative model of EAS is the Heitler model [38] which has been originally proposed for purely electromagnetic cascades but can be extended to the Heitler-Matthews model for hadronic cascades [39].

2.4.1.1 Electromagnetic showers

In the following, the term particle refers to electrons e^-, positrons e^+ or photons γ. EAS initiated by electrons or photons are referred to as electromagnetic showers and are mainly driven by two processes: ionization loss of electrons and positrons and pair production of electrons and positrons by photons (cf. figure 2.5). Hence, these two processes are competing resulting in a particle energy loss of

$$\frac{\mathrm{d}E}{\mathrm{d}X} = -\alpha(E) - \frac{E}{\lambda_{\mathrm{em}}} \tag{2.12}$$

with the ionization loss $\alpha(E)$ described by the Bethe-Bloch formula, which depends logarithmically on the energy, and the second term introducing the energy loss due to conversions. A primary particle with the energy E_0 converts after one splitting length $X_{\mathrm{em}} = \lambda_{\mathrm{em}} \ln 2$ into two secondaries with the energy $E_0/2$. The height of this first interaction is referred to as X_0. The splitting length is about the same length after the electrons loose half their energy due to bremsstrahlung

$$E(X) = E_0\, e^{-X/\lambda_{\mathrm{em}}} \quad \text{with} \quad X_{\mathrm{em}} = \lambda_{\mathrm{em}} \ln 2 \tag{2.13}$$

$$\Rightarrow \frac{E(X_{\mathrm{em}})}{E_0} = \frac{1}{2} \quad . \tag{2.14}$$

Continuing the splitting and bremsstrahlung processes $j = X/X_{\mathrm{em}}$ times, the number of particles in the shower derives to

$$N(X) = 2^j = 2^{X/X_{\mathrm{em}}} = e^{X/\lambda_{\mathrm{em}}} \tag{2.15}$$

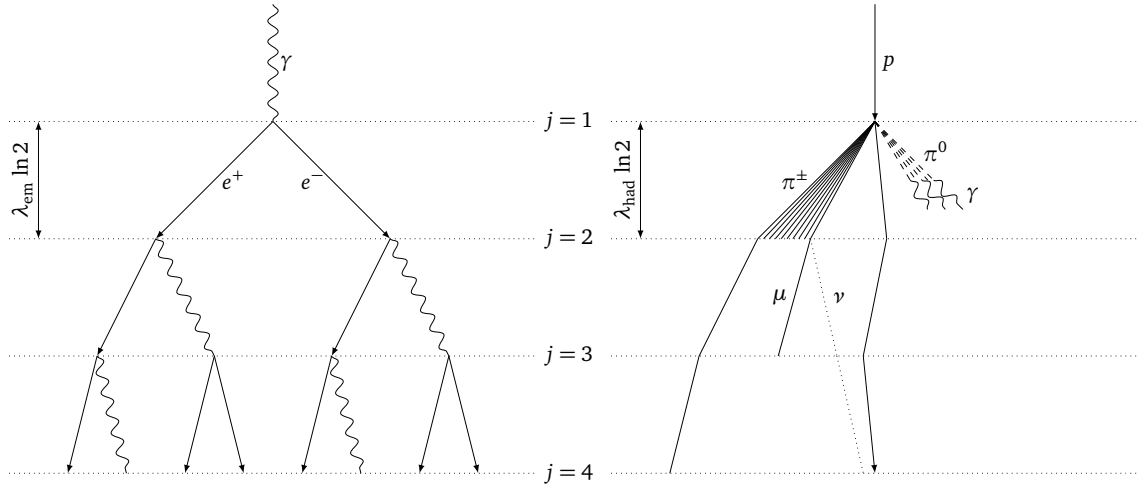

Figure 2.5: Schematic views of extended air showers. Left: electromagnetic cascade of a primary photon converting into an electron-positron pair. The secondary photons undergo further pair production processes whereas the secondary electrons and positrons loose energy by radiation. By convention, the energy of a particle is equally divided between the two secondary particles. Right: hadron shower initiated by a proton. The straight lines denote charged pions which interact. Further charged pions are created until their energy falls below E_c^π and decay to muons. The dotted lines are neutral pions which immediately decay into two photons each initiating electromagnetic sub showers (not shown). Not all pion lines are shown. Adapted from [39].

and the energy of the particles of the last generation to

$$E(X) = \frac{E_0}{N(X)} = \frac{E_0}{e^{X/\lambda_{\mathrm{em}}}} \quad . \tag{2.16}$$

Thus, the energy drops rapidly and ionization loss prevails at the energy at which the particles loose the same amount of energy to ionization and pair production

$$\alpha(E) = \frac{E}{\lambda_{\mathrm{em}}} \quad . \tag{2.17}$$

This energy is referred to as critical energy $E_c^{\mathrm{em}} \approx 86\,\mathrm{MeV}$. Therefore, with equation (2.16), the maximum number of particles in a shower is given by

$$N_{\max}(E_0) = \frac{E_0}{E_c^{\mathrm{em}}} \quad . \tag{2.18}$$

With equation (2.15), the slant depth of the shower maximum is given by

$$X_{\max}^e(E_0) = \lambda_{\mathrm{em}} \ln\left(\frac{E_0}{E_c^{\mathrm{em}}}\right) \tag{2.19}$$

which is a very important observable in air shower measurements. Summarizing, the very simple Heitler model already illustrates that the number of particles in a shower is proportional

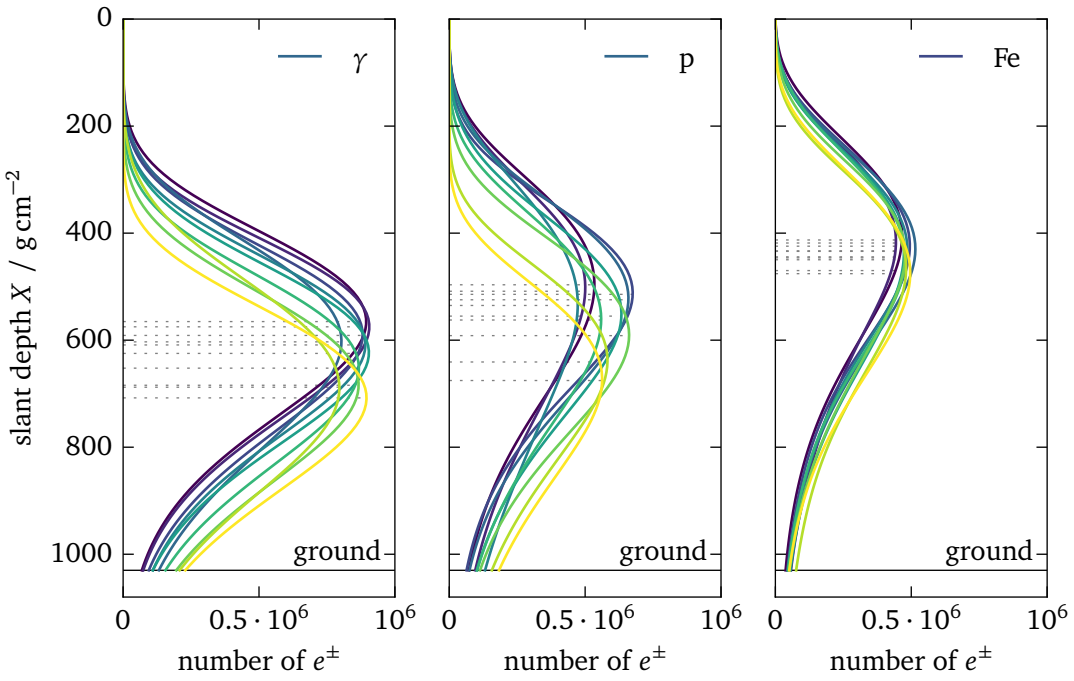

Figure 2.6: Longitudinal profiles for vertical ($\theta = 0°$) γ, proton and iron primary cosmic rays with an energy of $E = 10^{15}$ eV, simulated with the CONEX program [40, 41, 42] and the hadronic interaction model EPOS-LHC [43]. The dashed lines denote the atmospheric depth of the shower maximum $X_{\max}$. As discussed in section 2.4.1.2, the $X_{\max}$ is smaller for heavier nuclei due to the superposition of sub-showers for each nuclear constituent. Thus, the variance of the $X_{\max}$ also decreases for heavier nuclei. The longitudinal profiles satisfy the Gaisser-Hillas formula (cf. equation (2.20)).

to the energy of the primary particle and the depth of the shower maximum rises logarithmically with energy.

Considering the energy spectrum of the particles in an EAS, parameterizations for the longitudinal shower profile $N(X)$ have been developed from cascade theory [1]. The most recent is the famous Gaisser-Hillas formula [44]

$$N(X) = N_{\max} \cdot \left(\frac{X - X_0}{X_{\max} - X_0} \right)^{(X_{\max} - X)/\Lambda} \exp\left(\frac{X_{\max} - X}{\Lambda} \right) \tag{2.20}$$

which is the standard formula to use to fit measured longitudinal profiles. Here, the parameter Λ is just a fit parameter but could be understood as a mean interaction length. Simulated example showers resembling the Gaisser-Hillas formula are presented in figure 2.6 for different primary particles.

2.4.1.2 Hadronic showers

The main difference of hadronic showers, initiated for instance by protons, is that a considerable amount of hadrons is produced. After traversing one interaction length $X_{\text{had}} = \lambda_{\text{had}} \ln 2$

(analogously to equation (2.14)), the primary particle produces n_{ch} charged pions with a total energy of $\frac{2}{3}E_0$ and $\frac{1}{2}n_{\mathrm{ch}}$ neutral pions with a total energy of $\frac{1}{3}E_0$ (cf. figure 2.5). Furthermore kaons ($K^{\pm}$, K^0) are produced with a fraction of 10 % which either decay to muons ($K^{\pm}$ to 64 %) or to multiple pions. The neutral pions directly decay to $2 \cdot \frac{1}{2}n_{\mathrm{ch}} = n_{\mathrm{ch}}$ photons which carry each $E_0/3\,n_{\mathrm{ch}}$ of the total energy. Consequently, the charged pions roughly carry E_0/n_{ch} of the energy E_0 of the primary particle and the total energy converted to charged pions is $\left(\frac{2}{3}\right)^j E_0$ after j generations. The total number of pions produced up to generation j is given by

$$N_\pi = (n_{\mathrm{ch}})^j \quad . \tag{2.21}$$

It has been shown that a value of $n_{\mathrm{ch}} = 10$ is accurate within a factor of two for pions with kinetic energies between 1 GeV and 10 TeV [39]. Therefore, the energy of the pions in generation j derives to

$$E_\pi = \frac{E_0}{\left(\frac{3}{2}n_{\mathrm{ch}}\right)^j} \tag{2.22}$$

and decreases down to a critical value of E_c^π. Similarly to the critical energy E_c^{em} of electromagnetic showers, here, the production of further $\pi^{\pm}$ ceases and the pions decay. From equation (2.22), the number of generations to reach E_c^π is

$$j = \frac{\ln\left(\frac{E_0}{E_c^\pi}\right)}{\ln\left(\frac{3}{2}n_{\mathrm{ch}}\right)} = \underbrace{\frac{\ln n_{\mathrm{ch}}}{\ln\left(\frac{3}{2}n_{\mathrm{ch}}\right)}}_{=\beta} \frac{\ln\left(\frac{E_0}{E_c^\pi}\right)}{\ln n_{\mathrm{ch}}} \tag{2.23}$$

$$\Rightarrow j \approx 0.85 \log_{10}\left(\frac{E_0}{E_c^\pi}\right) \quad \text{and} \quad \beta \approx 0.85 \quad \text{with} \quad n_{\mathrm{ch}} \approx 10 \tag{2.24}$$

which results into values of $j = 3 \ldots 6$ for a value of $E_c^\pi = 20\,\mathrm{GeV}$ which only slightly decreases with increasing E_0. Since below E_c^π the pions decay into muons, the muon number of an EAS is given by

$$N_\mu = N_\pi = (n_{\mathrm{ch}})^j \tag{2.25}$$

$$\Leftrightarrow \ln N_\mu = \ln N_\pi = j\,\ln n_{\mathrm{ch}} \quad . \tag{2.26}$$

Using equation (2.23) yields

$$\ln N_\mu = \frac{\ln\left(\frac{E_0}{E_c^\pi}\right)}{\ln\left(\frac{3}{2}n_{\mathrm{ch}}\right)} \ln n_{\mathrm{ch}} = \beta\,\ln\left(\frac{E_0}{E_c^\pi}\right) \tag{2.27}$$

$$\Rightarrow N_\mu = \left(\frac{E_0}{E_c^\pi}\right)^\beta \tag{2.28}$$

with $\beta \approx 0.85$. With the number of muons N_μ, the energy of the hadronic component of the shower is $N_\mu\,E_c^\pi$. Each photon generated by a π^0 decay invokes an electromagnetic shower developing in parallel. Due to conservation of energy, the fraction of energy converted into electromagnetic cascades is given by

$$\frac{E_{\mathrm{em}}}{E_0} = \frac{E_0 - N_\mu\,E_c^\pi}{E_0} = 1 - \left(\frac{E_0}{E_c^\pi}\right)^{\beta-1} \quad . \tag{2.29}$$

For instance, at $E_0 = 10^{17}$ eV, the fraction is 90 %. The first interaction diverts one third of the energy E_0 into the electromagnetic component generating $\frac{1}{2} n_{\mathrm{ch}}$ neutral pions from which n_{ch} photons are produced. Thus, to first order only, the depth of the shower maximum of hadronic showers is

$$X_{\mathrm{max}}^{\mathrm{had}}(E_0) \propto X_{\mathrm{had}} + X_{\mathrm{max}}^{e}\left(\frac{E_0}{3\,n_{\mathrm{ch}}}\right) \tag{2.30}$$

$$\propto X_{\mathrm{had}} + \lambda_{\mathrm{em}} \ln\left(\frac{E_0}{3\,n_{\mathrm{ch}}\,E_c^{\mathrm{em}}}\right) \quad . \tag{2.31}$$

As a consequence, hadronic showers develop earlier in the atmosphere.

The calculations above can be extended from protons to nuclei with an atomic number A considering that the binding energy of the nucleons is much smaller than the primary energy E_0 and behave like a superposition of A independent hadronic showers with an energy $E_0^A = E_0/A$. The number of muons is then

$$N_\mu^A = A\left(\frac{E_0}{E_c^\pi A}\right)^\beta = \left(\frac{E_0}{E_c^\pi}\right)^\beta A^{1-\beta} \approx \left(\frac{E_0}{E_c^\pi}\right)^\beta A^{0.15} \tag{2.32}$$

and thus slightly increased for heavier elements. The opposite applies to the shower maximum

$$X_{\mathrm{max}}^{A}(E_0) \propto X_{\mathrm{had}} + \lambda_{\mathrm{em}} \ln\left(\frac{E_0}{3\,n_{\mathrm{ch}}\,E_c^{\mathrm{em}} A}\right) \tag{2.33}$$

$$\propto X_{\mathrm{max}}^{\mathrm{had}}(E_0) - \lambda_{\mathrm{em}} \ln A \tag{2.34}$$

where the depth of the shower maximum is decreased. This is also clearly recognizable in figure 2.6.

This has important implications for chemical composition measurements. By measuring both the total energy of the air shower and the depth of the shower maximum, the atomic mass number of the cosmic ray particle can be determined on a statistical basis (cf. figure 2.4). Due to the intrinsic fluctuations of X_{max}, the uncertainties on this calculation are large but the significance can be improved by including the muon number N_μ into the analysis as well. Therefore, the muon number is indeed an important observable and demands further investigation in dedicated measurements.

CHAPTER 3

The fluorescence detection technique

The standard method for the measurement of the longitudinal profile of extensive air showers (EAS), as introduced in the previous chapter, is the fluorescence detection technique by means of optical telescopes which are sensitive in the appropriate wavelength regime. These telescopes have a large field of view of $\mathbb{O}(10^\circ \times 10^\circ)$ and use mirrors for the collection of the faint fluorescence light produced by the showers in the atmosphere. Traditionally, the cameras of fluorescence telescopes are equipped with photomultiplier tubes which are gas-filled compartments enclosing several dynodes at a high voltage of $\mathbb{O}(1\,\mathrm{kV})$ for the amplification of photo-electrons created by the incoming photons on a photo-reactive surface [2, 3, 4, 5, 6, 7]. These devices have a high quantum efficiency of typically 30 %.

3.1 Fluorescence yield

As already discussed above in section 2.4.1, the fraction of energy of the primary particle of an EAS converted into the electromagnetic component is $\mathbb{O}(90\,\%)$. The secondary charged particles of this component suffer continuous energy loss due to ionization described by the Bethe-Bloch formula. Therefore, this energy is deposited in excitation states of the air molecules, mainly molecular nitrogen N_2 [47]. The main contribution comes from particles with energies $< 1\,\mathrm{GeV}$ with a maximum between 10 MeV and 50 MeV just below the critical energy of electrons $E_c^{\mathrm{em}} = 86\,\mathrm{MeV}$ at which ionization loss becomes the dominant process [48]. The energy deposit is a function of the slant depth X

$$\frac{\mathrm{d}E_{\mathrm{dep}}}{\mathrm{d}X} \propto \alpha(E)\,N(X) \tag{3.1}$$

and thus can also be described by the Gaisser-Hillas formula in equation (2.20). The ionization loss $\alpha \approx 2\,\mathrm{MeV\,g^{-1}\,cm^2}$ has a small energy dependence which will be ignored at this stage. However, not the total energy E_0 of the EAS is deposited, but

$$\int \frac{\mathrm{d}E_{\mathrm{dep}}}{\mathrm{d}X}\,\mathrm{d}X = E_0 - E_{\mathrm{inv}} \tag{3.2}$$

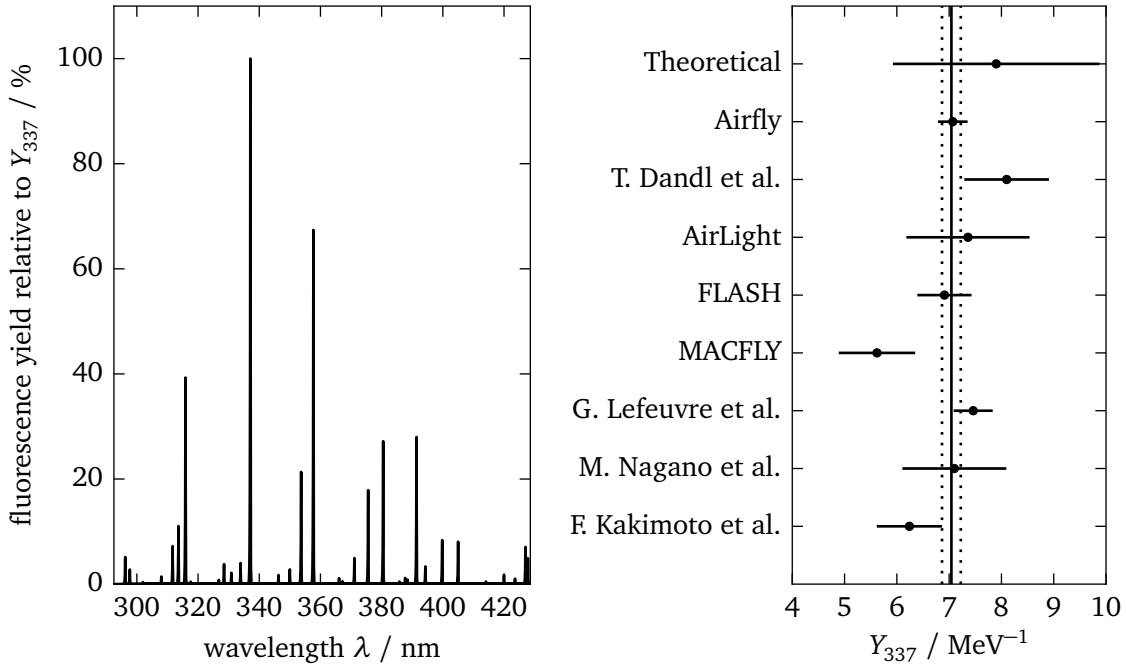

Figure 3.1: Left: fluorescence spectrum measured by the Airfly collaboration [45] in dry air at 800 hPa and 293 K relative to the maximum fluorescence yield value Y_{337}. Right: fluorescence yield measured by various experiments with corrections applied for the 337 nm band in dry air at 800 hPa and 293 K. The theoretical value has been obtained by Monte Carlo simulations and was not used for the calculation of the mean. The straight line denotes the result of a χ^2 fit of a constant to all values except the theoretical value. The found value is $Y_{337} = (7.04 \pm 0.18)\,\mathrm{MeV}^{-1}$ with a $\chi^2/\mathrm{ndf} = 1.22$. Data taken from [46].

since not all particles can be stopped in the atmosphere. The invisible energy E_{inv} due to e.g. muons and neutrinos from the hadronic shower component can be determined by air shower simulations [47].

When the molecules de-excite, the deposited energy is released as isotropically emitted ultraviolet light between 290 nm and 420 nm. The spectrum of the fluorescence light is presented in figure 3.1. Due to the fact that the fluorescence light is emitted isotropically, the EAS can be observed from the side and by multiple telescopes at the same time. The number of emitted photons is proportional to the energy deposit

$$\frac{\mathrm{d}^2 N_\gamma}{\mathrm{d}X\,\mathrm{d}\lambda} = Y(\lambda, p, T, u)\,\frac{\mathrm{d}E_{\mathrm{dep}}}{\mathrm{d}X} \tag{3.3}$$

with the proportionality factor $Y(\lambda, p, T, u)$, i.e. the fluorescence light yield, which is a function of the wavelength λ, the air pressure p, the air temperature T and the humidity u. Hence, some of the excited molecules may loose their energy due to collisions with other molecules. This quenching process introduces a dependence on the gas pressure since the collision rate depends on the air density [45]. Measurements have shown that the dependence of the fluorescence yield on the deposited energy portion is negligible [49]. Since the fluorescence yield is highest

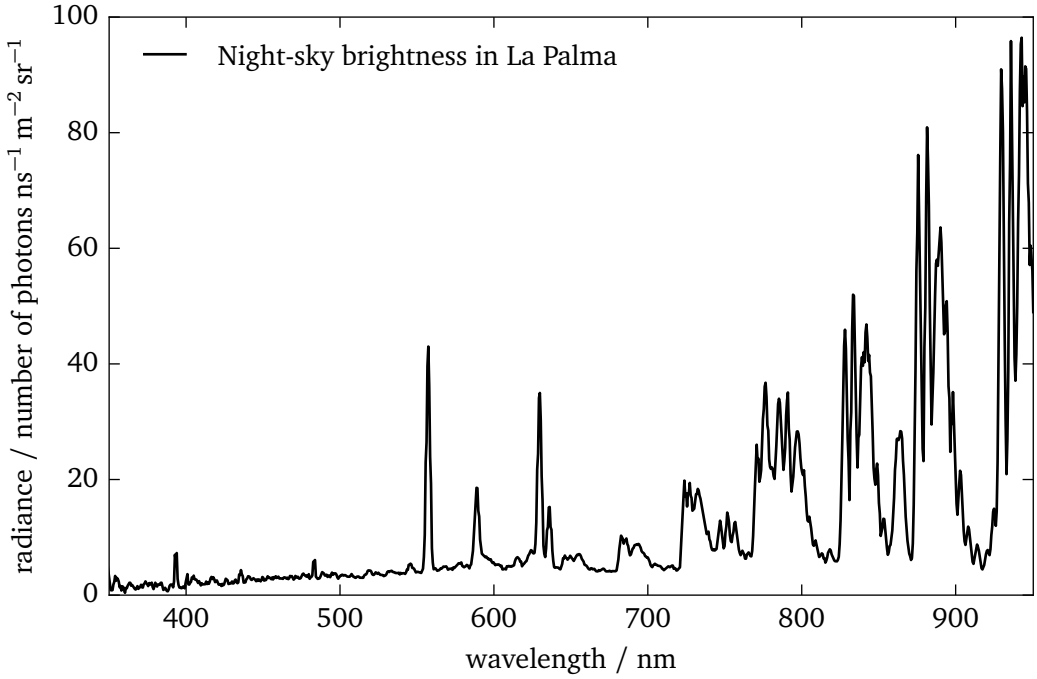

Figure 3.2: Night sky brightness measured on La Palma. The data was obtained by the analysis of 427 CCD images recorded with the Isaac Newton Group of telescopes during moonless nights with the sun $< 18°$ below the horizon (astronomical limit). Data taken from [51] and converted from micro-Jansky per square arcsecond.

at a wavelength of 337 nm, this emission line is taken as reference and is often discussed in the literature [46]. A compilation of multiple results of Y_{337} can be found in figure 3.1. It has an absolute value of

$$Y_{337} = (7.04 \pm 0.18)\,\mathrm{MeV}^{-1} \tag{3.4}$$

implicating that per each deposited 1 MeV approximately 7 fluorescence photons are generated. A parameterization of Y_{337} has been developed in [50].

3.2 Night sky brightness

Since the fluorescence light of EAS is faint, the night sky brightness (NSB) is a considerable source of background noise. Measurements have shown, that the NSB can vary by several orders of magnitude depending on the environmental conditions [52]. The main contributions to the NSB are airglow, zodiacal light, diffuse starlight, the moon and, in urban areas, light pollution [51].

Airglow is emitted by air molecules in the upper atmosphere, which are excited during day by the ultraviolet sunlight, and mainly contributes a continuum in the 260 nm to 380 nm regime and several spectral lines from NO_2 emission in the regime of 500 nm to 650 nm [51]. Since

airglow is induced by the sun, it changes with solar activity leading to an increase of ≈ 0.5 mag during the solar maximum. The surface brightness for the airglow in S_{10} units is

$$S_{10}^{(\text{airglow})} = 145 + \frac{130}{1.2}(S_\odot - 0.8) \quad \text{with} \quad S_\odot = 0.8 \ldots 2.0 \tag{3.5}$$

$$\approx 145 \ldots 275 \tag{3.6}$$

depending on the solar activity. The number S_{10} equals to the number of 10^{th} magnitude stars within one square degree, i.e. 27.78 mag arcsec^{-2}. Thus in contrast to the magnitude, the S_{10} values are scaled linearly and can be added up; a value of 10 corresponds to a ten times smaller surface brightness than a value of 100. From these units, the surface brightness can be calculated

$$\frac{I}{\text{mag arcsec}^{-2}} = 27.78 - 2.5 \log_{10}(S_{10}) \quad . \tag{3.7}$$

Zodiacal light is sunlight scattered by interplanetary dust and can contribute up to half to the NSB. Its wavelength spectrum is roughly similar to the wavelength spectrum of the sun. The surface brightness decreases with the observation latitude β

$$S_{10}^{(\text{zodiacal})} = \begin{cases} 140 - \sin(|\beta|) & \beta < 60^\circ \\ 60 \end{cases} \quad . \tag{3.8}$$

For the city of Aachen at $\beta = 50.7^\circ$, a value of $S_{10}^{(\text{zodiacal})} = 139$ can be found.

In the vicinity of stars, starlight scattered in the atmosphere significantly brightens the night sky. Furthermore, there is an extragalactic light contribution of $\approx 1\,\%$ ($S_{10} < 5$). Depending on the atmospheric conditions, the moon can contribute $S_{10} > 400$ to the NSB [53].

Light pollution is caused by man-made light, mainly sodium- and mercury-vapor and incandescent street lamps, which is scattered in the troposphere of the Earth. Typical mercury street lamps emit at 436 nm. For rural areas, the light pollution can be as low as $S_{10} = 20$.

Summing all contributions up, a conservative estimate for the NSB (excluding urban light pollution) is $S_{10}^{(\text{nsb})} = 439$ corresponding to a surface brightness of $I_{\text{nsb}} \approx 21$ mag arcsec^{-2}. An absolute measurement of the spectral night sky brightness on the island of La Palma is presented in figure 3.2. The integration of this spectrum weighted with the perception of the human eye yields a night sky photon flux of ≈ 0.5 ns^{-1} (8 mm pupil diameter, $\pm 60^\circ$ field of view, CIE 1931 color space tristimulus values).

3.3 The Pierre Auger Observatory

The Pierre Auger Observatory is the world's largest ultra-high-energy cosmic ray detector. It is located in Argentina in the providence of Mendoza in Malargüe east of the Andes on a large plateau covering an area of over 3000 km^2 with 1660 water Cherenkov stations with a spacing of 1.5 km, i.e. the surface detector (SD), and 27 fluorescence telescopes at five sites, i.e. the fluorescence detector (FD) [6, 54]. A schematic layout of the Pierre Auger Observatory can be found in figure 3.3. Areal photos taken during night are presented in figures 3.4 and 3.5. Due to this hybrid design, the complementary information of both detectors can not only improve the accuracy of the measurements but can also be used to calibrate both detectors with each other. In particular, the precise energy measurement of the FD can be used to calibrate a

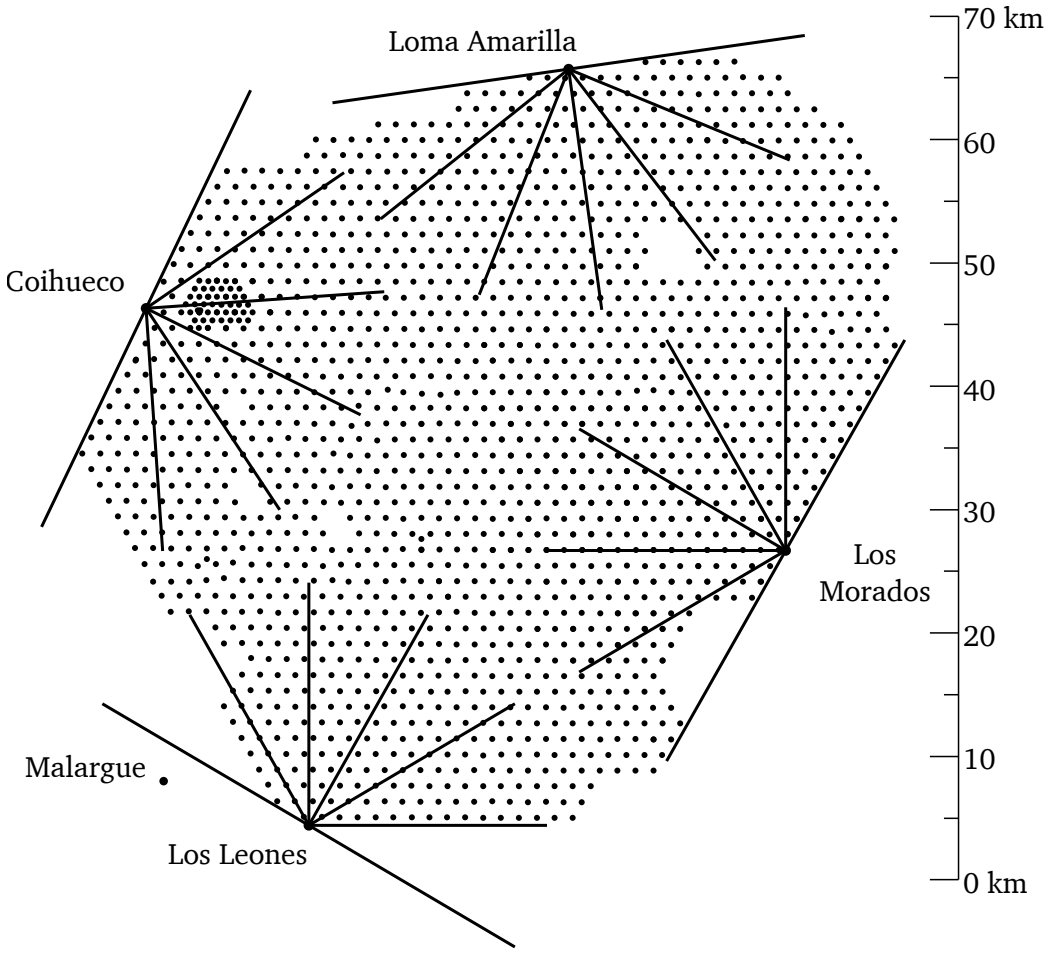

Figure 3.3: Layout of the Pierre Auger Observatory. Each dot represents a water Cherenkov station placed on a grid with a 1.5 km spacing. The grid is irregular at some places due to landmarks and owner-rights. The straight lines denote the field of view borders of the fluorescence telescopes. The three telescopes of the low-energy extension HEAT (cf. section 3.3.2), located near Coihueco, are not shown here. Original courtesy of D.Ṽeberic.

shower energy estimator for the SD improving the energy reconstruction for SD only measurements. Furthermore, the Pierre Auger Observatory is an ideal testbed for detector research and development which e.g. made the development of a cosmic ray radio detector (AERA [55]) or a subsurface muon detector array (AMIGA [56]) possible.

3.3.1 The surface detector

The individual stations of the surface detector (SD) of the Pierre Auger Observatory consist of light tight polyethylene tanks of 3.6 m diameter and 1.2 m height containing 12 000 l of purified water [54]. The interior is lined with Tyvek 1025D, which is a diffusive reflector with roughly 33 % specular reflectivity and 17 % diffusive reflectivity. The Cherenkov light produced by the secondary particles of the EAS in the water of the tank is recorded with three 9” photomultiplier

Figure 3.4: Areal photo including a fluorescence telescope building (Los Morados) of the fluorescence detector of the Pierre Auger Observatory. Each building contains six telescopes and is accompanied by a large communications antenna. Photo courtesy of S.Šaffi.

Figure 3.5: Areal photo including a water Cherenkov station of the surface detector of the Pierre Auger Observatory. Photo courtesy of S.Šaffi.

tubes. Due to the large area of the observatory and the large number of stations, the stations were designed to be self-sustaining. For this, the tank is complemented by a solar-power-system, a GPS receiver, readout electronics and a communications antenna for the handling of trigger requests and the transfer of data. The solar-power system provides a power of 10 W on average.

In contrast to the fluorescence detection technique, the lateral particle distribution, i.e. the footprint of the shower on the ground, is measured. The shower detection efficiency of the SD reaches 100 % for energies above $3 \cdot 10^{18}$ eV for zenith angles $\theta < 10°$ [6]. The data from mul-

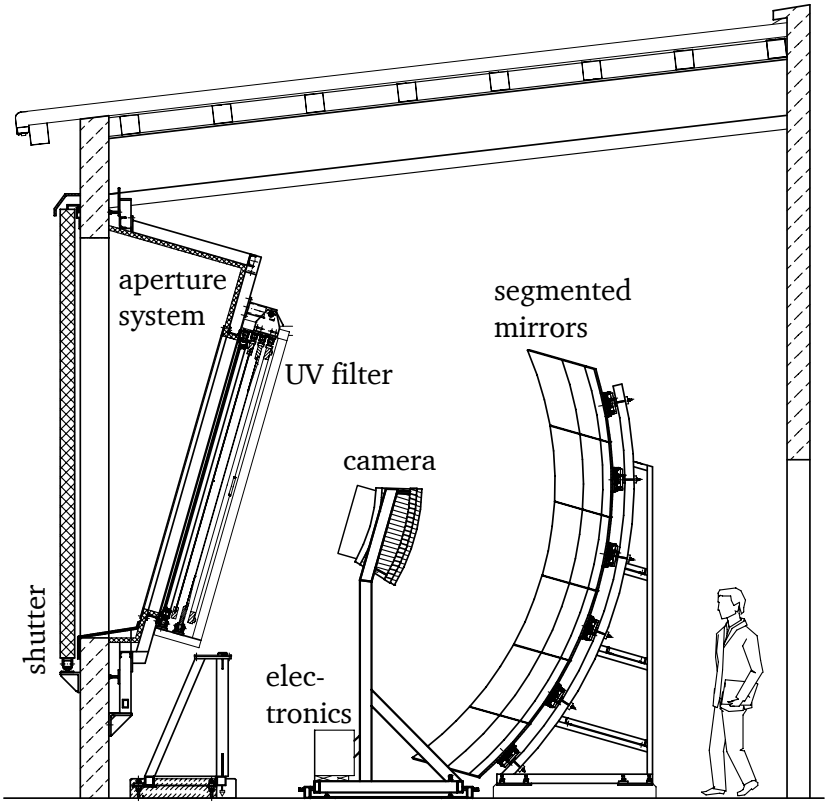

Figure 3.6: Schematic view of the Schmidt-telescopes of the fluorescence detector of the Pierre Auger Observatory. Taken from [6].

tiple triggered stations is used to fit a lateral distribution function to reconstruct the EAS core position and the particle density S_{1000} at a distance of 1000 m from the core. This observable serves as energy estimator for the energy E_0 of the primary particle. The uncertainty on the energy is $\approx 10\,\%$ with an angular resolution better than $\approx 1^\circ$ [57, 58].

3.3.2 The fluorescence detector

The fluorescence detector consists in total of 27 telescopes in four telescope buildings (Loma Amarilla, Los Leones, Los Morados and Coihueco) with six telescopes each and three HEAT telescopes near Coihueco. The telescopes of the detector extension HEAT (High Elevation Auger Telescopes) are tilted 30° degrees upwards to measure lower energy showers which develop earlier and therefore have the shower maximum higher in the atmosphere.

The telescopes are Schmidt telescopes [6]. A schematic of the optical baseline design and the mechanics of the telescopes is provided in figure 3.6. The telescopes have an entrance aperture of 2.2 m diameter with an ultraviolet pass filter made from Schott M-UG6 which blocks a considerable amount of the night sky brightness. The transmittance of the filter is 83 % at 370 nm [59]. Additionally a ring of tiles made from BK7 corrects the path of far off-axis rays to improve the imaging quality of the telescope to achieve the design goal spot size of 0.5° [60]. The ring has an inner radius of 0.85 m. Behind the aperture, a segmented anodized aluminum mirror with 36 rectangular or 60 hexagonal tiles and a total area of 3.8 m × 3.8 m focuses the

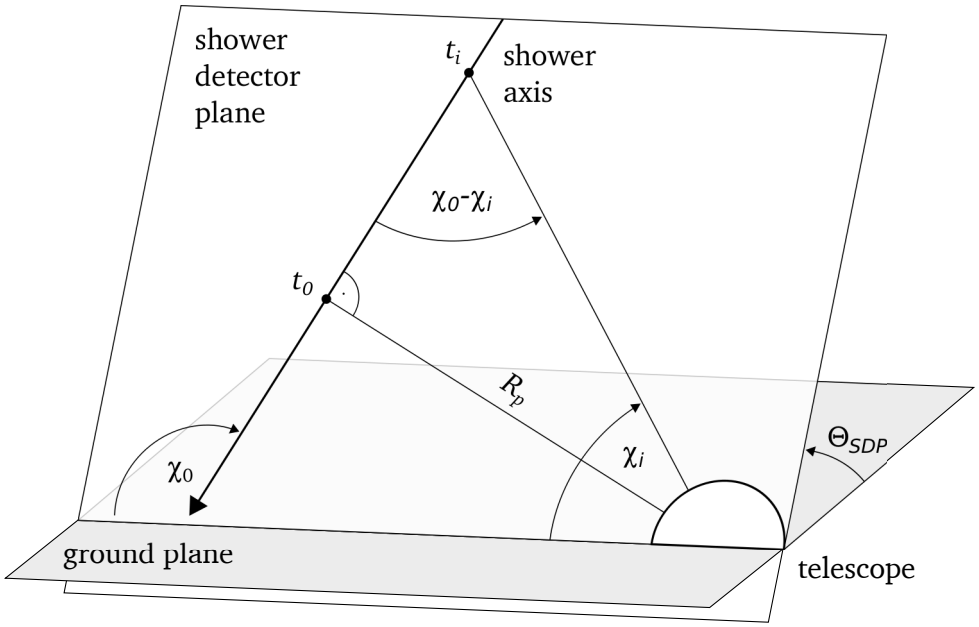

Figure 3.7: Schematic view of the shower detector plane. The plane is an important auxiliary construct for the geometrical reconstruction of the air shower. Adapted from [6].

light beam onto the camera [6]. The reflectivity has been measured to exceed 90 % at 370 nm. The radius of curvature of the mirror is 3.4 m resulting in a wide field of view of 30.0° × 28.1°. The camera is built up by a matrix of $22 \times 20 = 440$ Photonis XP3501 photomultiplier tubes with eight amplification stages and hexagonal windows of 40 mm diameter. The tubes are mounted on a curved aluminum support frame with a radius of curvature of 1.7 m. To minimize the dead space between the pixels, so-called Mercedes stars made from aluminized Mylar foil have been installed which implement the shape of Winston cones. Thus, Monte Carlo simulations testify an increase of the light collection efficiency of the camera from 70 % to 93 % [59]. The photomultiplier tubes have a quantum efficiency of ≈ 30 % at the peak wavelength of 420 nm [61]. Due to the large dimensions of the camera of 93 cm × 86 cm, a large fraction of ≈ 21 % of the aperture is obstructed. The ray-tracing simulations show that the transmission efficiency of the optical system up to the photomultiplier tubes is 55 %.

In comparison to the surface detector with a duty cycle of nearly 100 %, the fluorescence detector can only be operated during moonless nights. In total, a duty cycle of 15 % could be achieved [62]. However, the upgrade plans of the Pierre Auger Observatory include an upgrade of the FD electronics to enable measurements during twilight by reducing the gain of the photomultiplier tubes [37]. This leads to a theoretical increase of the astronomically possible duty cycle from 19 % to 29 % neglecting bad weather periods, power cuts and other environmental influences.

3.3.3 Extensive air shower reconstruction

The shower detector plane (SDP) is an important auxiliary construct for the geometrical reconstruction of an EAS with only one telescope. A schematic of the SDP is presented in figure 3.7.

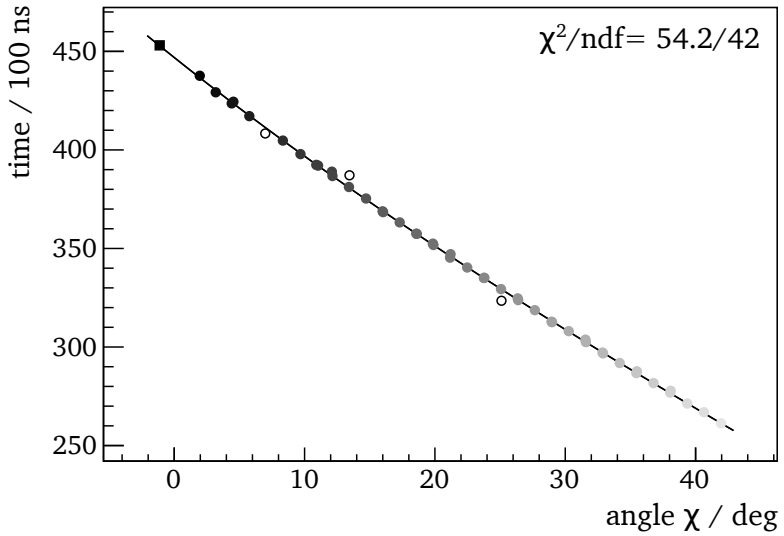

Figure 3.8: Peak light signal arrival time of an EAS recorded by the FD of the Pierre Auger Observatory. Each dot represents a pixel of an FD telescope and its shade the arrival time (early = light shades, late = dark). A fit of equation (3.9) is used to determine the geometry of the shower. The hollow dots denote timing information of surface detector stations which significantly improve the fit result. Event 15346477, taken from [62].

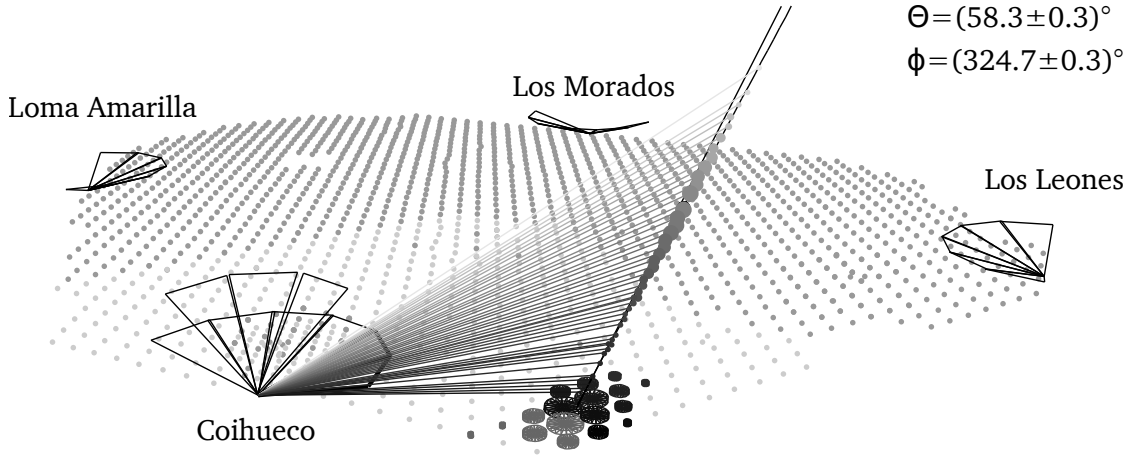

Figure 3.9: Schematic of a reconstructed EAS measured with the Pierre Auger Observatory. Due to the hybrid detector design, the EAS is measured simultaneously by the surface- and the fluorescence detector. The light incident directions on the telescopes are shown as shaded lines. The signal height of the telescopes and surface detector stations are denoted by markers of different size in a logarithmic scale. Event 15346477, taken from [62].

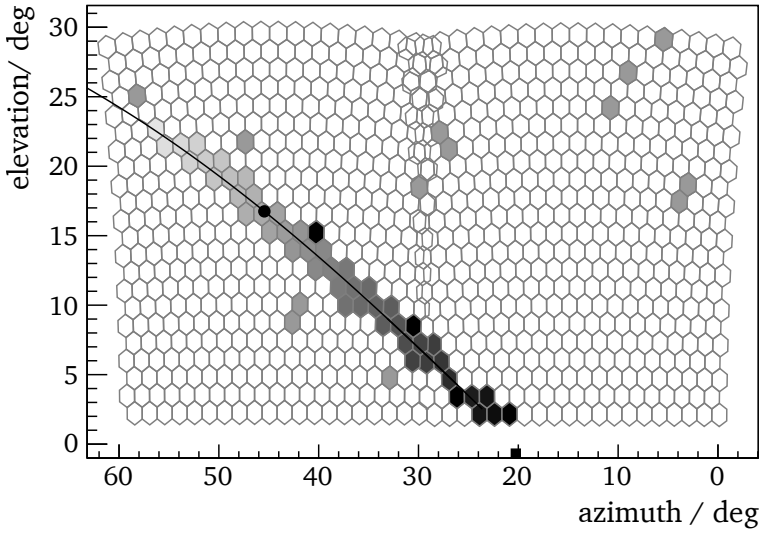

Figure 3.10: Camera view of an EAS recorded by two telescopes of the Coihueco telescope station. The peaking time of the pixels is denoted by the shading (early = light shades, late = dark). The straight line represents the shower detector plane (cf. figure 3.7). Event 15346477, taken from [62].

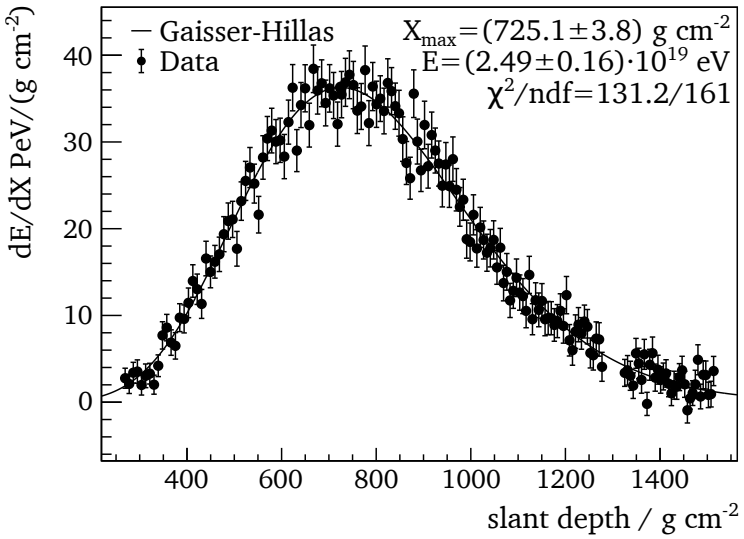

Figure 3.11: Longitudinal profile of an EAS recorded by the FD of the Pierre Auger Observatory. The dots represent the number of photons per 100 ns time bin recorded by a pixel of the camera. Due to the fact that the shower can be seen over the duration of several time bins in a single pixel, the number of data points exceeds the number of triggered pixels. The line is a fit of the Gaisser-Hillas formula to the data (cf. equation (2.20)). Event 15346477, taken from [62].

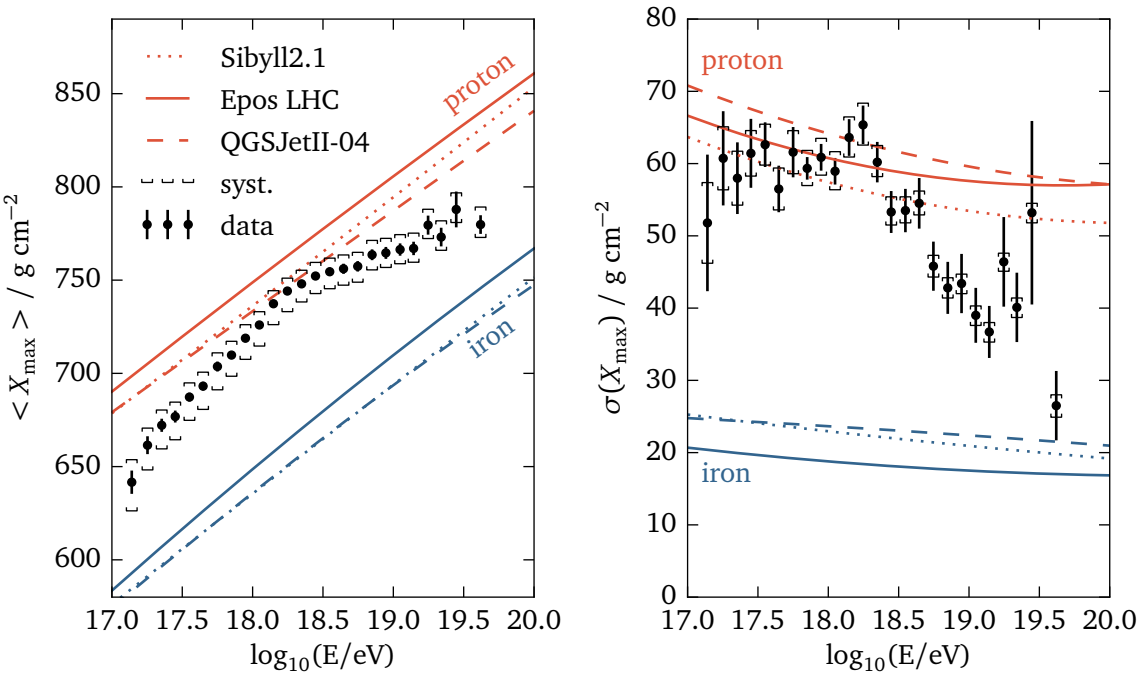

Figure 3.12: Moments of the shower maximum X_{max} measured by the Pierre Auger Observatory. The vertical bars denote the statistical and the vertical caps the systematical uncertainties. The lines represent the moments obtained by Monte Carlo simulations for proton and iron nuclei. Data taken from [63].

The axis of the EAS is extended to a plane to the observing telescope with an angle χ_0 between the axis and the ground in the SDP. Then, the shower distance R_p can be obtained by a fit of

$$t_i(\chi_i) = t_0 + \frac{1}{c} R_p \tan\left(\frac{\chi_0 - \chi_i}{2}\right) \tag{3.9}$$

to the recorded arrival time t_i of the peak signal in the PMT i with an elevation angle χ_i in the SDP. Obviously, the fit can be improved by including data points from the surface detector into the fit since they have a large leverage. Figure 3.8 presents the geometric reconstruction of an event recorded with the Pierre Auger Observatory including information from the FD and from the SD. A schematic of the geometry of the event is presented in figure 3.9 and a camera view of the FD telescopes which recorded this event is given in figure 3.10.

With the results of the geometrical reconstruction of the shower, the detected light is backtraced from the aperture of the telescope to the shower axis. The number of detected photons n_i by the PMT i is given by

$$n_i = \int \frac{\epsilon_{atm}(\lambda)\,\epsilon_{tel}(\lambda)}{4\pi\, r_i^2} \left(\frac{\mathrm{d}^2 N_\gamma}{\mathrm{d}X\,\mathrm{d}\lambda}\right)_i \mathrm{d}\lambda \tag{3.10}$$

$$= \int \frac{\epsilon_{atm}(\lambda)\,\epsilon_{tel}(\lambda)}{4\pi\, r_i^2} Y(\lambda, p, T, u) \left(\frac{\mathrm{d}E_{dep}}{\mathrm{d}X}\right)_i \mathrm{d}\lambda \tag{3.11}$$

with the distance between the telescope and the point on the shower axis r_i, the atmospheric transmittance $\epsilon_{atm}(\lambda)$, the efficiency of the telescope $\epsilon_{tel}(\lambda)$, and the fluorescence yield Y. By

inversion, the energy deposit in the field of view of the telescope as a function of the atmospheric depth can be determined to which the Gaisser-Hillas formula (cf. equation (2.20)) is fitted to reconstruct the whole profile including the parts not visible to the telescope. The fit results yield also the shower maximum $X_{\max}$ with a resolution of $\approx 20\,\mathrm{g\,cm^{-2}}$ [62] which is an important observable (cf. section 2.4.1.2). Figure 3.11 presents the longitudinal profile reconstructed for the example event. A measurement performed by the Pierre Auger Observatory of the mean and variance of the $X_{\max}$ as a function of energy can be found in figure 3.12. By integration of the energy deposit, the electromagnetic energy E_{em} of the EAS can be calculated. The energy of the primary particle E_0 can then be estimated by means of Monte Carlo simulations yielding a parametrization for the compensation of the invisible energy [64]

$$\frac{E_{\mathrm{em}}}{E_0} = 0.959 - 0.082\,E_{\mathrm{em}}^{-0.15} \tag{3.12}$$

on average for a mixed composition of protons and iron nuclei. Additionally, the light recorded by the telescope is contaminated by Cherenkov light, either direct light emitted in forward direction or scattered. This contribution has to be corrected for on an event by event basis when calculating the primary particle energy [50]. Additional corrections have to be implemented to model Rayleigh and Mie scattering. Rayleigh scattering is scattering of light on the molecules of the air and thus depends on its density and on the photon wavelength. The cross section is proportional to λ^{-4}. At sea level, the cross section for Rayleigh scattering is $\sigma = 1.673 \cdot 10^{-26}\,\mathrm{cm^2}$ [65] at 400 nm which corresponds to a mean free path length of $\approx 17\,\mathrm{km}$ at 20 °C and 1013 hPa. The distribution of the scattering angle θ is proportional to $\cos^2\theta$. Mie scattering is scattering of photons on aerosols in the air. The wavelength dependence is often parameterized with the so-called Ångström formula [66]. The angular distribution of the Mie scattered light is strongly peaked in forward direction [67]. Therefore, a continuous monitoring of the atmosphere above the array is crucial to successful data analysis.

In summary, the fluorescence detector has full trigger efficiency for energies above $E \geq 10^{19}\,\mathrm{eV}$. The statistical uncertainty on the reconstructed energy is better than 10 %. Major contributions to the systematical uncertainty on the energy measurement of the FD are the fluorescence yield (3.6 %), the aerosols optical depth of the atmosphere (6.2 %), the absolute calibration of the telescopes (9.9 %), the longitudinal profile reconstruction (6.5 %) and the invisible energy (3 %). In total, a systematic uncertainty of 14 % has been reported [68].

The trigger system of the FD is divided into several levels [69]. The first trigger level is a simple pixel threshold trigger. A moving average of the last $n = 4 \ldots 16$ ADC samples is compared to a 14 bit threshold value for each pixel. The threshold value is dynamically adjusted to maintain a trigger rate of 100 Hz to compensate for changing signal background. The second trigger level searches for tracks in the first level triggers generated during the last 1 µs. A track is identified if 5 adjacent pixels are triggered in one of 108 track-like patterns. At this point, the trigger rate per telescope is already reduced from 10 Hz to 0.1 Hz. The final step is the level three trigger for the rejection of lightning. It has been found, that lightning produces level one triggers with high multiplicities in 100 ns coincidence intervals. Thus, events with a multiplicity > 25 are rejected which rejects 99 % of all lightning events. The multiplicity of the first level trigger can be obtained without a complete readout of the ADCs, thus this decision process is very fast. In a second step, for the remainder of these events, the whole signal trace is read out to check the chronological order of signal peaking times. This second step also removes background events from random pixel triggers and muons. The fraction of rejected EAS by the third level trigger with an energy of $E > 10^{18}\,\mathrm{eV}$ is 0.6 % [70]. The trigger rate

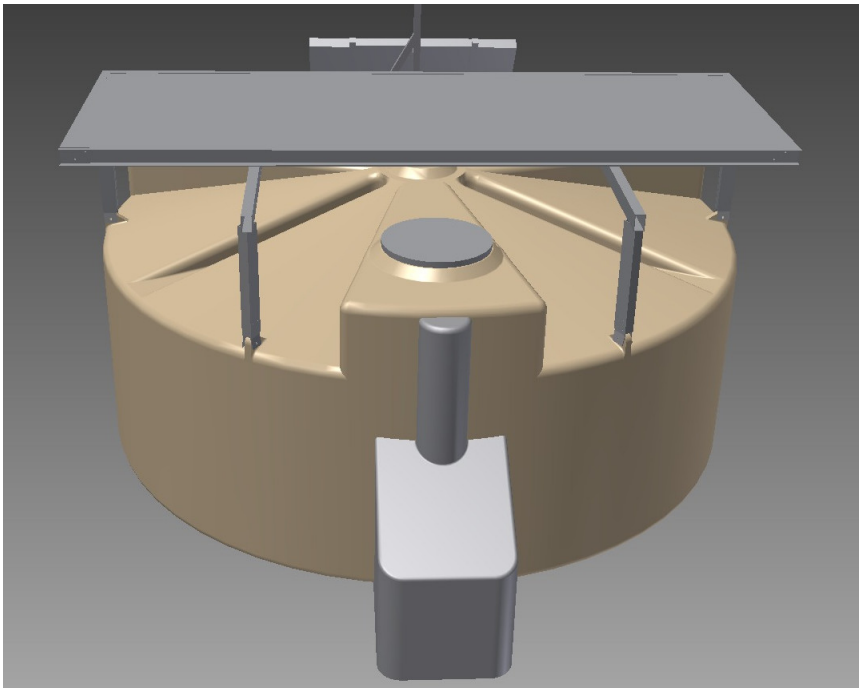

Figure 3.13: Computer drawing of a module of the AugerPrime surface detector upgrade of the Pierre Auger Observatory. A schematic of the inside of the compartment mounted on top of the water Cherenkov station is provided in figure 3.14. Image courtesy of the Pierre Auger Collaboration.

per telescope building is now 0.01 Hz on average. Further trigger stages are implemented to create hybrid events between multiple telescope buildings and the surface detector.

3.3.4 The Upgrade of the Pierre Auger Observatory AugerPrime

The Pierre Auger Observatory began a major upgrade of its detectors with the focus on improved measurements of the chemical composition of cosmic rays with the surface detector which up to now could only be measured with considerable uncertainties [37]. Referred to as AugerPrime, the surface detector will be upgraded by installing a $4\,\mathrm{m}^2$ plastic scintillator detector on top of each water Cherenkov station (cf. figure 3.13). Furthermore, the electronics of the tank will be improved by increasing the sampling frequency from 40 MHz with 10 bit ADCs to 120 MHz with 12 bit ADCs. The number of readout channels is also increased for the readout of the scintillator detector and one additional small PMT (< 30 mm diameter) will be installed in the water Cherenkov tank to enhance the dynamic range.

The scintillator detector itself consists of two $2\,\mathrm{m}^2$ modules with each 12 bars of 1.6 m length, 10 cm width and 1 cm thickness produced by the Fermi National Accelerator Laboratory (FNAL) [71] (cf. figure 3.14). These bars are extruded including a diffusive coating to prevent light leakage and four tunnels over the whole length for inserting a 1 mm thick wavelength shifting fiber. The blue light of the scintillator (≈ 430 nm) is shifted to green (≈ 500 nm). The shifting process also helps to trap the scintillator light inside the fiber for the transport to the photomultiplier. Each fiber is 6.3 m long and routed through two adjacent bars to improve the uniformity of the detector (non-uniformity $< 6\,\%$) and each fiber end is spliced to

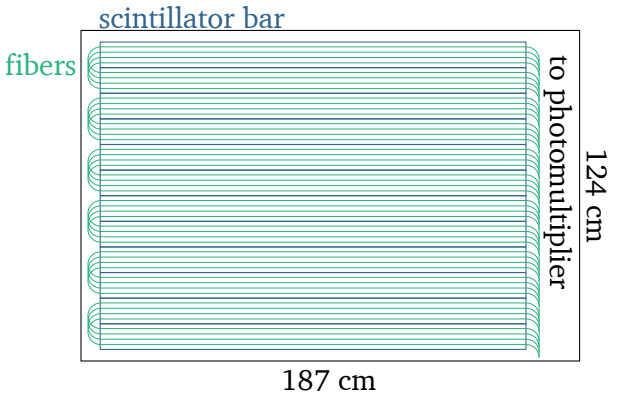

Figure 3.14: Schematic of one half of the compartment mounted on top of the water Cherenkov station. It contains 1.6 m long scintillating bars produced with each four tunnels for the routing of wavelength shifting fibers. Each fiber is laid through two adjacent modules and the two fiber ends are spliced to the photomultiplier. The bending radius of the fibers is 5 cm to keep light loss to a minimum. Adapted from [37].

the photomultiplier. The fibers are laid without gluing for easier handling in case of a defect of the fiber. As photomultipliers traditional photomultiplier tubes and silicon photomultipliers are in discussion. The dynamic range of the detector is claimed to be sufficient to measure 1 to 20 000 minimal ionizing particles (MIPs) whereby the position of the peak due to MIPs in the pulse height spectrum of the recorded photomultiplier data is resolved with an accuracy of 1.5 % [37].

The predicted resolution on the number of muons N_μ is 18 % for 10 EeV and 8 % for 100 EeV EAS. The resolution has been achieved by the utilization of the novel concept of shower universality which predicts that the electromagnetic part of hadronic showers is fully determined by the shower age $s = 3X/(X + 2X_{\max})$ and the primary energy E_0 [72, 73].

In summary, the upgrade of the Pierre Auger Observatory will be a big step forward to answering the remaining questions of cosmic rays, mainly their chemical composition, their sources and finally their acceleration mechanisms in combination to the explanation of the observed flux suppression. The construction of the upgrade will be started in mid 2016 and put into service until 2018.

Chapter 4

Silicon photomultipliers

Silicon photomultipliers (SiPMs) are pixelated photon detectors for the detection of light on a single photon basis and can be considered the successor of photomultiplier tubes (PMTs) for many use cases.

PMTs are evacuated compartments with a photo-reactive entrance window emitting single electrons upon photon incidence due to the photoelectric effect [74]. The initial photon is accelerated by means of an electric field through a concatenation of dynodes used to form the field. Due to a high field strength in the kilovolt regime, the electrons gain energy at each stage and eventually release further electrons when hitting a dynode. The resulting electron cloud yields a measurable current proportional to the number of incident photons. Thus, these devices have to be operated with a bias voltage of $O(1\,\mathrm{kV})$ and require a lot of space due to the elongated dynode structure. Furthermore, these devices can be harmed when operated with

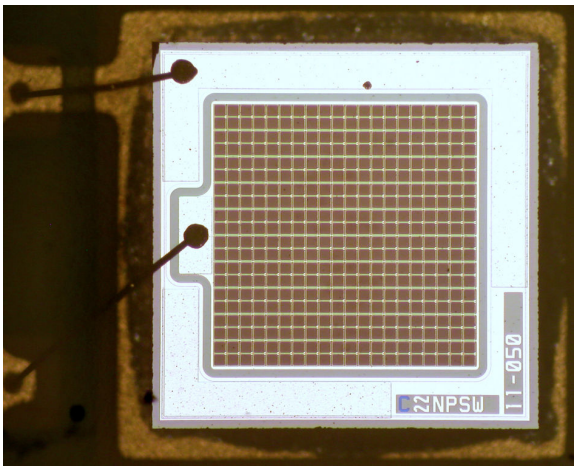

Figure 4.1: Microscope image of a Hamamatsu S12571-50P silicon photomultiplier. The device in the SMD package has a pitch of $1 \times 1\,\mathrm{mm}$ and a cell pitch of $50\,\mu\mathrm{m}$ resulting in a total number of cells of 400.

high light intensities such as day light. Nevertheless, PMTs have a large dynamic range, large sensitive areas up to several square centimeter and a high quantum efficiency of typically 35 %. Hence, PMTs are a mature technology and are therefore used in many experiments.

Silicon photomultipliers translate this concept to a silicon based device [8]. A photograph of a SiPM is presented in figure 4.1. SiPMs consist of an array of avalanche photodiodes, referred to as cells, operated in the Geiger mode. This implies that upon incidence of a photon, each cell produces a standard signal, i.e. a nominal standard charge. The sum of these standard signals is again proportional to the number of impinging photons under the assumption each cell is hit only once. Hence, due to the cellular structure, the dynamic range of the SiPMs is limited by the number of cells since each cell can only detect one photon at a time. Furthermore, SiPMs have a higher dark noise of $\mathbb{O}(100\,\mathrm{kHz\,mm^{-2}})$ compared to PMTs. It depends on the case of application whether this is problematic or not. Additionally, the properties of the SiPM depend on the ambient temperature, thus the bias voltage has to be adjusted continuously to compensate this effect. In contrast to PMTs, the dimensional requirements of SiPMs are very low since they are thin and just slightly larger than their sensitive area. Typical sizes are 1 mm × 1 mm, 3 mm × 3 mm and arrays offering up to $O(1\,\mathrm{cm^2})$ of sensitive area. SiPMs are operated by relatively low voltages of $< 100\,\mathrm{V}$ and are not harmed by high luminosities which renders them very robust. At the time of completion of this thesis, the photon detection efficiency of commercially available SiPMs surpasses the quantum efficiency of PMTs with values of $>$ 50 % [75, 76].

In the following, the basic properties of p-n junctions, Geiger-mode avalanche photodiodes and SiPMs will be discussed.

4.1 P-n junctions

A p-n junction is a two-terminal device with a boundary between an n-type and a p-type semiconductor [77]. They are fundamental to modern semiconductor applications and thus to the understanding of other semiconductor devices. The term n-type corresponds to a doped material with a higher electron than hole concentration n_d compared to the base material. In contrast, p-type materials are doped with a higher hole than electron concentration n_a. The electrons and holes are also often referred to as donors and acceptors. Typically, in a semiconductor electrical conductivity is prohibited by a band gap between the so-called valence band E_v below the Fermi level E_F and the conduction band E_c above the Fermi level. At absolute zero temperature, in the valence band all possible electron states are filled and contribute to the chemical bonding. The Fermi-level E_F denotes the energy of a state whose chance of being occupied is 50 % at thermal equilibrium. Here, the conduction band E_c is only partially filled, thus can contribute to the conductivity of the material. In summary, the band gap $E_g = E_c - E_v$, which has to be overcome by electrons contributing to conductivity, is in the order of a few electronvolts for semiconductors at absolute zero ($E_g = 1.169\,\mathrm{eV}$ for silicon). The band gap decreases with temperature [77]

$$E_g(T) = E_g(0) - \frac{\alpha T^2}{T + \beta} \tag{4.1}$$

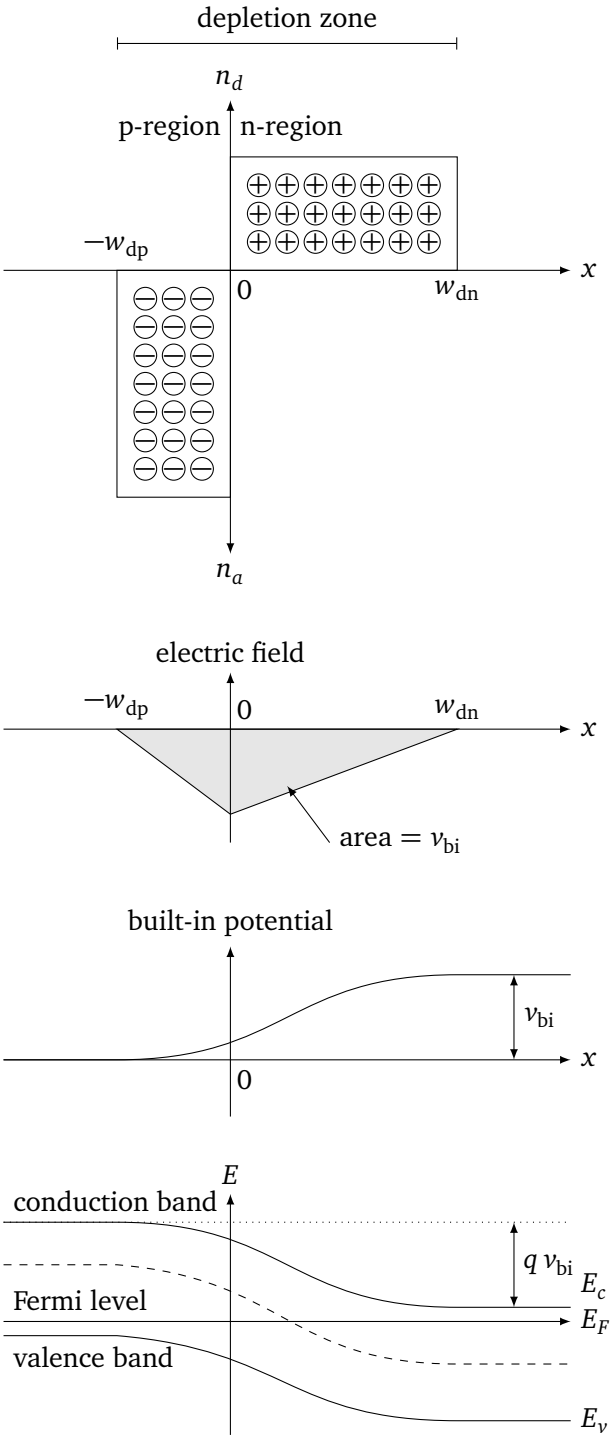

Figure 4.2: Schematic of an abrupt p-n junction in thermal equilibrium. From top to bottom: 1) space charge distribution, 2) electric field distribution, 3) distribution of the built-in potential v_{bi} and 4) energy bands. Since the Fermi level E_F has to be constant, the conduction and valance bands are shifted at the junction. Adopted from [77].

with $\alpha = 4.9 \cdot 10^{-4}\,\mathrm{eV\,K^{-1}}$ and $\beta = 655\,\mathrm{K}$ for silicon and thus is slightly reduced to $E_g(300\,\mathrm{K}) = 1.123\,\mathrm{eV}$ at room temperature. The number of electrons in the conduction band of a semiconductor is given by [77]

$$n_e = \int_{E_c}^{\infty} N(E)\,F(E)\,\mathrm{d}E \tag{4.2}$$

with the lowest possible energy state E_c, the total number of states $N(E)$ at energy E

$$N(E) \propto (E - E_c)^{1/2} \tag{4.3}$$

and the Fermi-Dirac-distribution $F(E)$ of the occupancy of states

$$F(E) = \frac{1}{1 + e^{(E-E_F)/k_B\,T}} \tag{4.4}$$

with the Fermi-level E_F, the Boltzmann constant k_B and the temperature T.

Now, if semiconductors are doped with n-type or p-type impurities, new energy states are introduced within the band gap [77]. For p-type semiconductors, the acceptors are vacant valence electrons. Thus, the Fermi level is decreased and lies closer to the valence band. For n-type semiconductors, the Fermi level is increased since electrons are more abundant and it lies closer to the conduction band.

At the junction of the p-type and the n-type semiconductor, the electrons tend to drift to the p-doped side and recombine with the holes and vice versa [77]. Since the two Fermi levels must align, the conduction and valence bands are shifted. The area in which the recombination takes place is denoted as depletion zone. Due to the charge shift, the n-doped side is positively and the p-side negatively charged constituting an electric field opposing the diffusion process. In thermal equilibrium, the potential difference corresponding to the electric field is the built-in voltage

$$v_{\mathrm{bi}} = \frac{k_{\mathrm{B}}\,T}{q} \ln\left(\frac{n_a\,n_d}{n_i^2}\right) \tag{4.5}$$

with the charge of a single charge carrier q, the donor and acceptor concentrations n_a and n_d and the intrinsic charge carrier density n_i of the non-doped semiconductor. The width of the depletion zone is given by

$$w_d = \sqrt{\frac{2\epsilon_{\mathrm{Si}}\epsilon_0}{q\,n}\left(v_{\mathrm{bi}} - \frac{2\,k_B T}{q}\right)} \tag{4.6}$$

with the charge carrier concentration $n \approx n_a$ if $n_d \ll n_a$ (and vice versa), the dielectric constant ϵ_0 and the dielectric constant of silicon $\epsilon_{\mathrm{Si}} \approx 12$. The capacity of the depletion region is then given by

$$c_d = \frac{\epsilon_{\mathrm{Si}}\epsilon_0}{w_d} \quad . \tag{4.7}$$

A schematic of a p-n junction and its properties is presented in figure 4.2.

The application of a reverse bias voltage v_{bias}, contributes to the built-in voltage v_{bi} and thus increases the width of the depletion zone

$$w_d = \sqrt{\frac{2\epsilon_{\mathrm{Si}}\epsilon_0}{q\,n}\left(v_{\mathrm{bi}} + v_{\mathrm{bias}} - \frac{2\,k_B T}{q}\right)} \tag{4.8}$$

at the cost of the depletion zone capacitance c_d (cf. equation (4.7)) [77].

By increasing the reverse bias voltage v_{bias}, the electric field strength is increased and the p-n junction becomes susceptible to breakdown phenomena of which the avalanche multiplication is here of particular interest [77]. If the electric field in the depletion zone is high enough, charge carriers can multiply by impact ionization leading to a current increase. The ionization rate, i.e. the number of electron hole pairs generated by a charge carrier per unit distance, is qualified by a constant

$$\alpha_n = \frac{1}{n\, v_n} \frac{\mathrm{d}n}{\mathrm{d}t} \tag{4.9}$$

with the charge carrier velocity v_n, and analogously for holes α_p. It can be found, that the ionization rate strongly increases with increasing electric fields. In silicon, the threshold energy for impact ionization is 3.6 eV for electrons and 5.0 eV for holes. Thus the electric field must be high enough to facilitate these carrier energies. During the avalanche, each charge carrier is multiplied by a factor

$$M = \left\{ 1 - \int_0^{w_d} \alpha_p \exp\left[- \int_0^x \left(\alpha_p - \alpha_n \right) \mathrm{d}x' \right] \mathrm{d}x \right\}^{-1} \tag{4.10}$$

$$= \left\{ 1 - \int_0^{w_d} \alpha \, \mathrm{d}x \right\}^{-1} \quad \text{for} \quad \alpha = \alpha_n = \alpha_p \tag{4.11}$$

which reaches infinity if the integral yields 1. This can be interpreted as an initial electron which gets accelerated and creates one additional electron hole pair. The hole gets accelerated in the opposite direction and in turn creates an electron hole pair of which the electron is accelerated towards the starting position of the initial electron. Thus, the process repeats itself indefinitely. The breakdown voltage is proportional to the width of the depletion zone [77]

$$v_{\text{break}} \propto w_d \quad . \tag{4.12}$$

Since the depletion zone width is more or less constant as a function of temperature, the electric field is also constant.

However, with increasing temperature and in high field strengths, the more energetic charge carriers loose a part of their energy to the lattice due to scattering. Hence, these carriers must pass a higher potential difference before acquiring enough energy to initiate the avalanche breakdown which leads to a considerable decrease of the ionization rate. As a consequence, the breakdown voltage increases with increasing ambient temperature.

4.2 Geiger-mode avalanche photodiodes

In general, Geiger-mode avalanche photodiodes (GAPDs) are basically p-n junctions which can be brought to an avalanche breakdown by the absorption of optical photons within the electric field region which creates the initial electron hole pair. This enables photon detection on a single photon level. Furthermore, a so-called quenching resistor R_q is connected in series to the junction for a passive self-quenching of the avalanche breakdown. A schematic of an example structure of a GAPD is presented in figure 4.3. With rising bias voltage v_{bias}, the size of the depletion zone and the electric field strength increase which is beneficiary to the probability that the initial carriers successfully initiate an avalanche breakdown. Thus, the photon detection efficiency of the device increases with the excess over the breakdown voltage

$$v_{\text{ov}}(T) = v_{\text{bias}} - v_{\text{break}}(T) \tag{4.13}$$

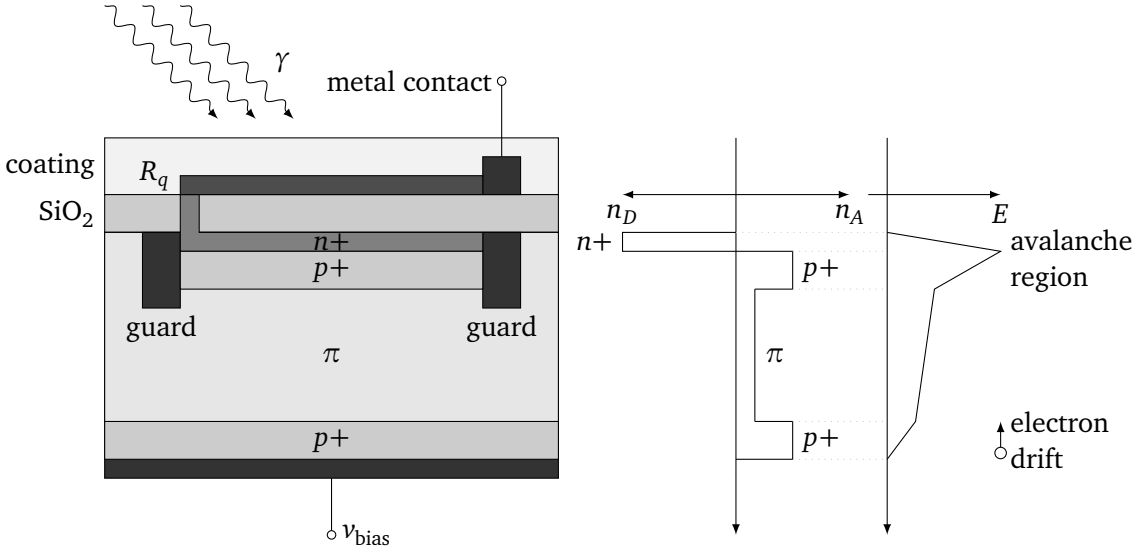

Figure 4.3: Schematic of the architecture of a Geiger-mode avalanche photodiode (GAPD). The structure is known as "reach-trough" structure which is a popular way to connect the front with the back side of the diode. Following the path of light, the first layer is the quenching resistor R_q which is either nontransparent and occupies only a small part of the GAPD or a transparent metal film. The next layer is a SiO_2 of $\approx 15\,\mu m$ thickness which acts as insulator between the metal contacts and the diode. The heavily doped $n+$ layer of $\approx 1\,\mu m$ thickness is connected to the quenching resistor and marks the begin of the avalanche region. Below, there is a heavily doped $p+$ layer also a few micrometers thick. Thus, the depletion zone forms between the $n+$ and $p+$ layer. Incoming photons can either be absorbed directly in the depletion zone (blue light) or below in the lightly n-doped π layer (green to orange light) which has a thickness of $\approx 300\,\mu m$. Adapted from [78].

whereby, as mentioned above, the breakdown voltage depends on the ambient temperature T. When the GAPD breakdown is initiated, a self-sustaining avalanche develops due to satisfaction of the avalanche condition (cf. equation (4.11)) [79]. The leading edge of the avalanche current signal marks the arrival time of the photon with great precision in the order of several $\mathbb{O}(10\,ps)$. The current through the diode as a function of time t is given by

$$i_d(t) = \frac{v_d(t)}{R_d} \tag{4.14}$$

with the voltage drop over the diode $v_d(t)$ and the internal diode resistance R_d attributed to the resistance of the bulk silicon material [79]. A typical value for the diode resistance is $R_d = 1\,k\Omega$. The current falls logarithmically to a steady-state value i_f with a time constant, referred to as the quenching time constant

$$\tau_d = (c_d + c_s)\, R_d \tag{4.15}$$

with the capacitance of the depletion zone c_d and the stray capacitance of the surrounding material c_s. Thus, the GAPD can be modeled as capacitor with a resistance R_d connected in parallel [79]. The equivalent circuit is presented in figure 4.4. Under the assumption, that

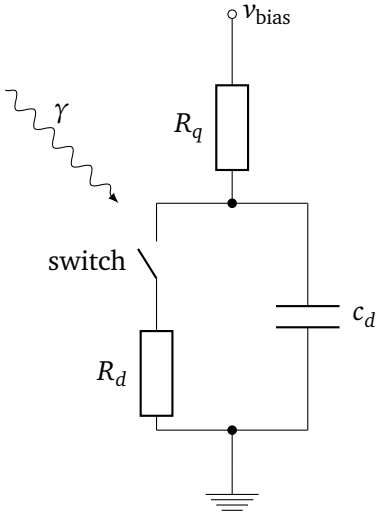

Figure 4.4: Equivalent circuit of a GAPD as proposed in [79]. The avalanche is initiated by closing the switch which drains the capacitance c_d over the internal resistance R_d. After the avalanche is quenched, the switch is considered opened again and the capacitance can be recharged over the quenching resistor R_q. Parasitic capacitances, resistances and inductances are not shown. Adapted from [79].

$c_s \approx 0$ and $c_d \approx 0.1\,\text{pF}$, the quenching time constant is $\tau_d \approx 100\,\text{ps}$. This can also be understood as the dead time of the diode during which the GAPD can not detect further impinging photons. The steady-state current i_f is the current which flows through the whole GAPD when it is conducting and corresponds to a steady-state voltage drop v_f

$$i_f = \frac{v_{\text{ov}}}{R_d + R_q} \tag{4.16}$$

$$v_f = v_{\text{break}} + R_d\, i_f \tag{4.17}$$

with the quenching resistor R_q which is in the order of $\mathbb{O}(100\,\text{k}\Omega)$ [79]. For the values given above, the steady-state current and voltage derive to $i_f \approx 15\,\mu\text{A}$ and $v_f - v_{\text{break}} \approx 15\,\text{mV}$ for an over-voltage of $v_{\text{ov}} = 1.5\,\text{V}$. At this stage, the capacitance of the diode is considered depleted. Since the current is small, only few charge carriers take part. The impact ionization process is a statistical process, so chances are high that the ionization rate α drops spontaneously and the avalanche stops. Furthermore, the electric field in the diode is weakened substantially which also lowers the ionization rate α. At some point, the holes do not multiply anymore since their energy threshold for impact ionization is higher than for electrons. Thus, the quenching condition $M \to \infty$ (cf. equation (4.11)) is not satisfied any more. The avalanche develops in direction to the current flow and finally stops. Experimentally, the multiplication factor M has been found to depend on the current flowing during the breakdown [80]

$$\frac{1}{M} \propto i \quad . \tag{4.18}$$

In practice, the quenching resistor should be chosen so that $i_f < 100\,\mu\text{A}$ [79, 81]. Breakdowns initiated given $v_{\text{break}} < v < v_f$ can be initiated but are not self-sustaining.

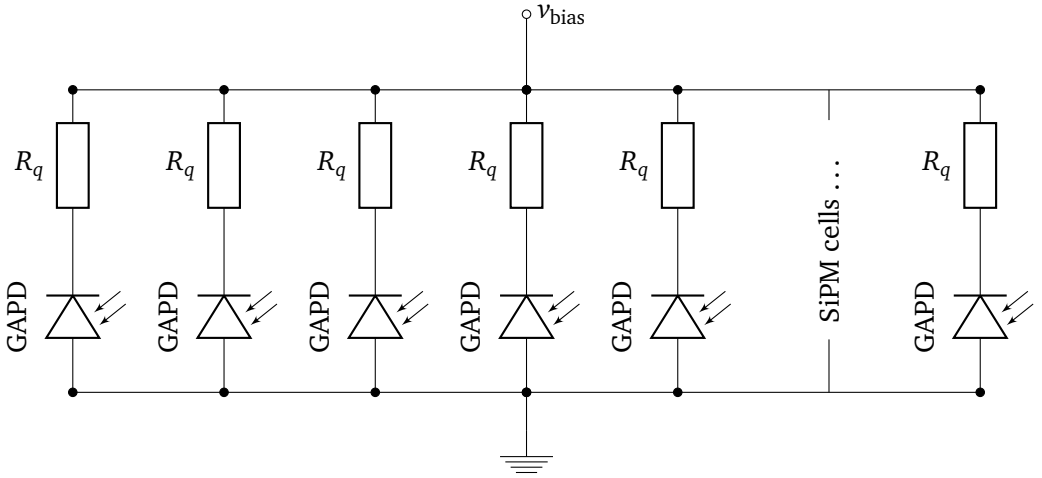

Figure 4.5: Schematic of a SiPM with GAPDs connected in parallel. Depending on the cell pitch of e.g. 10 µm, 25 µm, 50 µm or 100 µm and the total size of the SiPM, models with 100, 400, 900, 3600, 14 400 cells or more are available. Besides the recovery time constant, the number of cells situated on a SiPM has a great influence on its dynamic range.

Now that the avalanche stopped, the depletion zone can be replenished. Since, the quenching resistor is connected in series to the diode, the recharge can be modeled analogously to a capacitor

$$v_d(t) = v_{\text{ov}}\left(1 - e^{-t/\tau_{\text{rec}}}\right) \tag{4.19}$$

with the time after the breakdown t and the recovery time constant

$$\tau_{\text{rec}} = (c_d + c_s)\, R_q \tag{4.20}$$

which yields $\tau_{\text{rec}} \approx 10\,\text{ns}$. In good approximation, the diode can be considered fully charged after $5\tau_{\text{rec}}$ since $(v_d(5\tau_{\text{rec}}) - v_{\text{ov}})/v_{\text{ov}} < 1\,\%$ is sufficiently small. If another photon is absorbed during this time window and after a time t after the breakdown, the GAPD can break down prematurely with a reduced signal $\propto v_d(t)/v_{\text{ov}}$ which can be understood by calculating the total charge of the current signal

$$q_d = (c_d + c_s)\, v_{\text{ov}} \tag{4.21}$$

$$\Rightarrow q_d(t) = (c_d + c_s)\, v_d(t) \quad . \tag{4.22}$$

The value of q_d/e corresponds to the gain g of the GAPD, i.e. the multiplication in electrons from the one initial charge carrier pair induced by one incident photon. Typical values for the gain g are in the order of $\mathbb{O}(1 \cdot 10^6)$ which is comparable to the gain of PMTs. Furthermore, since the charge is completely drained, the signal gain g is equal for photons regardless of their energy which qualifies the denomination Geiger mode.

4.2.1 Arrays of Geiger-mode avalanche photodiodes

Eventually, silicon photomultipliers (SiPMs) are arrays of GAPDs connected in parallel. The single GAPDs on a SiPM are also referred to as cells. A schematic is presented in figure 4.5.

Following the discharge and recharge of the capacitor equivalent circuit, the current signal i_{pe} of a SiPM rises with

$$i_{\mathrm{pe}}(t) \propto \left(1 - e^{-t/\tau_d}\right) \tag{4.23}$$

until t_{max}, which corresponds the maximum current $i_{\mathrm{max}} = i_f \approx v_{\mathrm{ov}}/R_q$, is reached (cf. equations (4.15) and (4.17)). Then the current falls off with

$$i_{\mathrm{pe}}(t) \propto e^{-(t-t_{\mathrm{max}})/\tau_r ec} \tag{4.24}$$

while the GAPD recharges (cf. equation (4.19)). The integral of the current signal equals to q_d (cf. equation (4.22)).

4.3 Temperature dependence of the breakdown voltage

As discussed above, the breakdown voltage of GAPDs and therefore also of SiPMs changes with temperature. In small temperature ranges $< 50\,^{\circ}\mathrm{C}$ the breakdown voltage dependence of the temperature is linear in good approximation. Based on a reference breakdown voltage at e.g. $T_0 = 25\,^{\circ}\mathrm{C}$, the breakdown voltage as a function of temperature is

$$v_{\mathrm{break}}(T) = v_{\mathrm{break}}(T_0) + \beta\ (T - T_0) \tag{4.25}$$

with the progression coefficient β. Typical values are $\beta = 56\,\mathrm{mV\,K^{-1}}$ for Hamamatsu devices [10, 82]. By adjusting the breakdown voltage v_{break} with the ambient temperature, the gain $g = q_d/e$ remains constant since $g \propto v_{\mathrm{break}}$ (cf. equation (4.22)).

4.4 Photon detection efficiency

The photon detection efficiency (PDE) of SiPMs is a compound quantity of multiple constituents and a function of the photon wavelength λ and the angle of incidence θ with respect to the surface normal

$$PDE(\lambda, \theta) = \epsilon_{geom}\, \epsilon_{\mathrm{trig}}\, \epsilon_{\mathrm{trans}}(\theta)\, QE(\lambda) \quad . \tag{4.26}$$

First, not the complete chip area can be considered sensitive with respect to impinging photons. The single cells on a SiPM are separated by electrical wiring, electrical separation and possibly optical barriers and therefore loose a fraction of their sensitive area to the quenching resistor which is traditionally made from polysilicon and placed on top of the cells. Newer models feature a metal film quenching resistor which, albeit covering a larger fraction of the cell area, is considered transparent. Due to these geometrical reasons, the fraction of the SiPM area sensitive to photons is referred to as geometrical fill factor ϵ_{geom}.

Commonly, the silicon surface of SiPMs is coated with a transparent resin or glass in newer models to protect the sensitive silicon from corrosion and mechanical stress which makes the devices very durable. Furthermore, the refractive index of silicon is high ($n = 4.7 + 0.2\mathrm{i}$ at 450 nm [85]) and the additional optical boundary with $n \approx 1.5$ provides a less harsh optical transition from air into the SiPM. Nevertheless, multi-layer Fresnel reflections take place lowering the transmission efficiency $\epsilon_{\mathrm{trans}}(\theta)$ for inclined light with the result that it rapidly drops to zero for $\theta > 70°$. The measurements performed in [86, 87] confirm a simple analytical model generically developed in [88]. A more detailed discussion and derivation of an analytical formula for ϵ_{geom} is presented below in section 5.3.2.

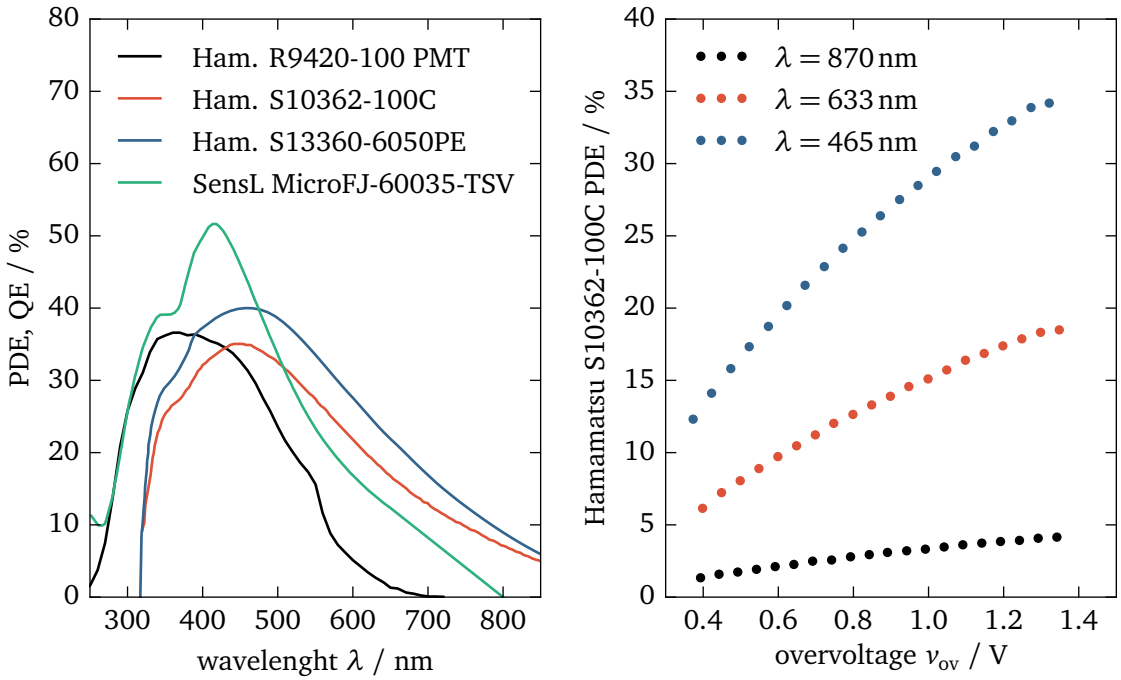

Figure 4.6: Left: quantum efficiency (QE) of a Hamamatsu R9420-100 PMT as a function of wavelength λ compared to the PDE of various SiPMs: Hamamatsu S10362-100C at $v_{ov} = 1.3\,V$ (released Nov. 2009), Hamamatsu S13360-6050PE at $v_{ov} = 3\,V$ (released Oct. 2015) and a SensL MicroFJ-60035-TSV at $v_{ov} = 5\,V$ (released March 2016) at room temperature. The values are for perpendicular light incidence and have been taken from the datasheets [83, 84]. It is apparent, that the PDE could be increased significantly over time in comparison to the earliest models. Right: photon detection efficiency of the Hamamatsu S10362-100C as a function of the over-voltage. Data taken from [10].

When the photon finally enters the GAPD, the probability of absorption and creation of the initial pair of charge carriers necessary to initiate the avalanche is the quantum efficiency $QE(\lambda)$. It is a function of the photon wavelength since the absorption depth of the photon depends on its wavelength. Depending on the depth of absorption, the initial charge carrier pair might be created outside the depletion zone where the electric field is too weak to accelerate it to sufficiently high energies before it gets absorbed.

The probability of an avalanche breakdown emerging from this first charge carrier pair is given by ϵ_{trig}. It is also a function of the over-voltage v_{ov} explaining the increase of the PDE with increasing over-voltage [89]. The PDE as a function of the wavelength and the over-voltage for distinct devices is presented in figure 4.6.

4.5 Noise phenomena

SiPMs are subject to several noise phenomena worth of consideration: thermal noise, optical crosstalk and afterpulsing whereby optical crosstalk and afterpulsing are also referred to as

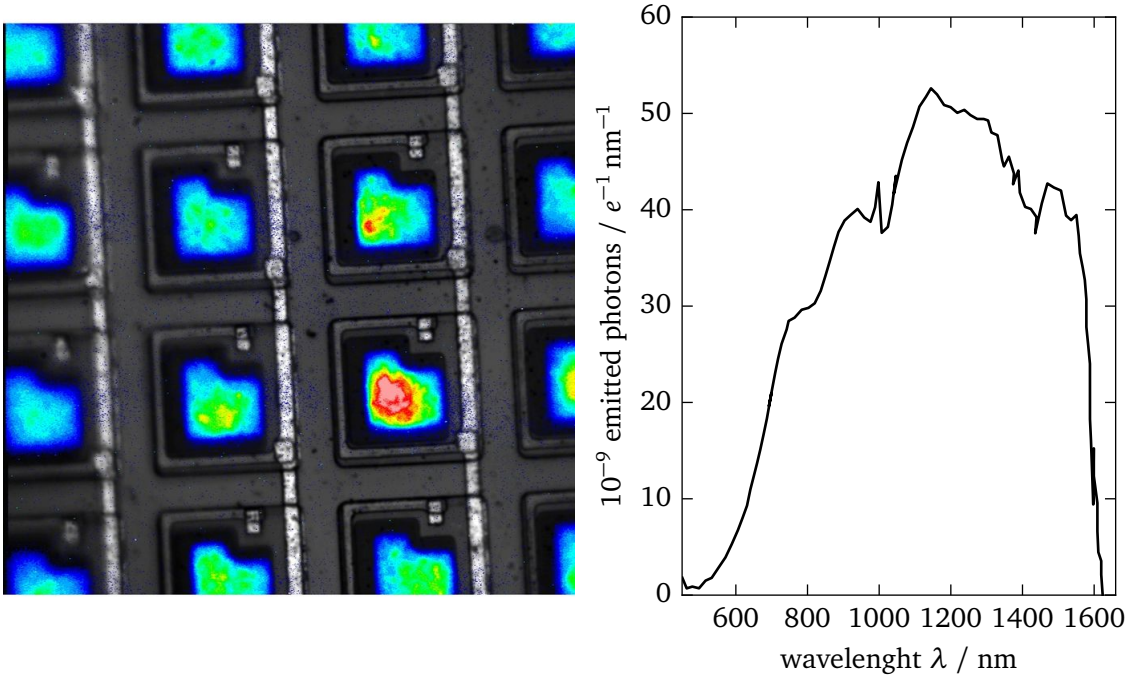

Figure 4.7: Left: photograph of a prototype SiPM from MEPhI and Pulsar enterprise overlayed with a measurement of the intensity of light emitted by optical crosstalk. Taken from [92]. Right: measured differential light emission spectrum from silicon avalanches. The relative uncertainty for any point of this spectrum is $< 25\,\%$. Data taken from [93].

correlated noise due to the fact that these phenomena only appear in the presence of a primary avalanche breakdown. Analogously to the PDE, the probabilities of occurrence of noise rise with higher over-voltages. Besides thermal noise, these probabilities are constant if the over-voltage is kept constant as a function of temperature (cf. equations (4.13) and (4.25)). This is very important for a stable operation of SiPMs.

4.5.1 Thermal noise

By thermal excitation, charge carriers can be created inside the depletion region and accidentally trigger an avalanche breakdown. Since the SiPM cells are operated in Geiger mode, the resulting signal is indistinguishable from photon induced breakdowns. A typical rate of newer devices is $f_{\text{th}} = 100\,\text{kHz}$ per square millimeter sensor area [90]. This value is the result of continuous improvements made to the manufacturing processes and materials over the last years. Additionally, the amount of thermal noise can be reduced significantly by cooling. With every 10 °C temperature drop, the thermal noise rate drops by a factor of two [91].

4.5.2 Optical crosstalk

Optical crosstalk is the phenomenon of correlated coincident avalanche breakdowns in the neighborhood of the original triggered cell. The coincident breakdowns are induced by pho-

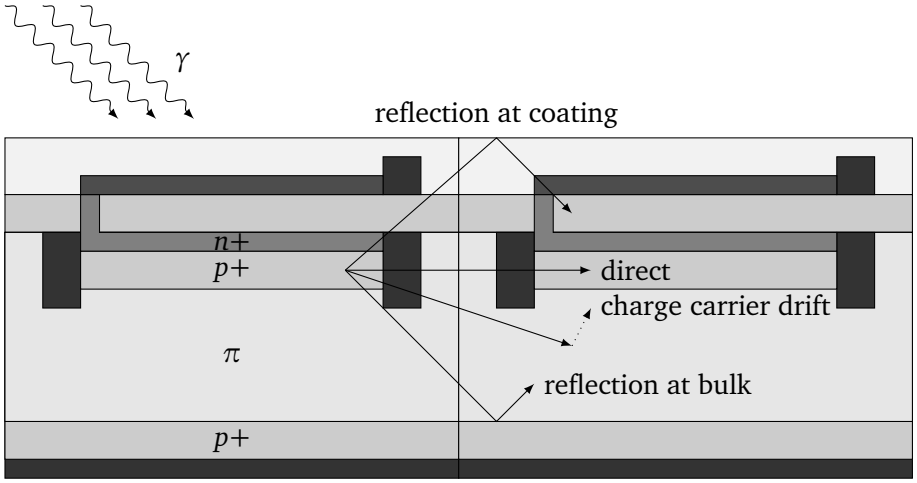

Figure 4.8: Schematic of possible paths of optical crosstalk photons. Due to the high difference of the refractive indexes between the silicon and the coating, a transmission of optical crosstalk photons through the coating to a neighboring cell is discouraged. In case the optical crosstalk photon creates charge carriers outside the avalanche region (cf. figure 4.7), the trigger is delayed by the travel time of the newly created charge carriers.

tons created during the original avalanche [93, 94]. A typical value for the probability of the occurrence of at least one optical crosstalk is

$$p_{\mathrm{ct}} = (27.3 \pm 0.1)\,\% \tag{4.27}$$

for a Hamamatsu 3 mm × 3 mm SiPM with 100 µm cell pitch operated at an over-voltage $v_{\mathrm{ov}} = (1.31 \pm 0.01)\,\mathrm{V}$ at a temperature of $T = (1.0 \pm 0.1)\,^{\circ}\mathrm{C}$ [95]. Possible mechanisms for the generation of the light are bremsstrahlung and band transitions [93]. Although for each avalanche charge carrier only $\mathbb{O}(10^{-5})$ photons are created, the high gain of SiPMs of $\mathbb{O}(10^{6})$ leads to a considerable amount of secondary photons created in the wavelength regime between 500 nm and 1600 nm [93]. A fraction of $< 1\,\%$ of the light of the lower end of this wavelength regime can also exit the SiPM (cf. figure 4.7) [92].

These secondary photons can either be transmitted directly to a neighboring cell or be reflected at the top material border of the silicon or the SiPM coating or at the bottom material border (cf. figure 4.8). In case of direct transmission, only the four nearest neighbors tend to be reached [96]. The light bounced off the bottom material border can get absorbed prematurely in the bulk of the GAPD creating an charge carrier pair slowly diffusing to the avalanche region leading to a trigger delayed by several nanoseconds [97]. However, the contribution of delayed crosstalk to the correlated noise is found to be low in comparison to afterpulsing.

4.5.3 Afterpulsing

Afterpulses are delayed triggers in the original triggered cell created by the release of charge carriers trapped at material impurities during the avalanche [8]. The time difference between the initial pulse and the afterpulse follows an exponential distribution. Experimentally, two types of afterpulsing with the probabilities $p_{\mathrm{ap,f}}$ and $p_{\mathrm{ap,s}}$ have been found with a short time

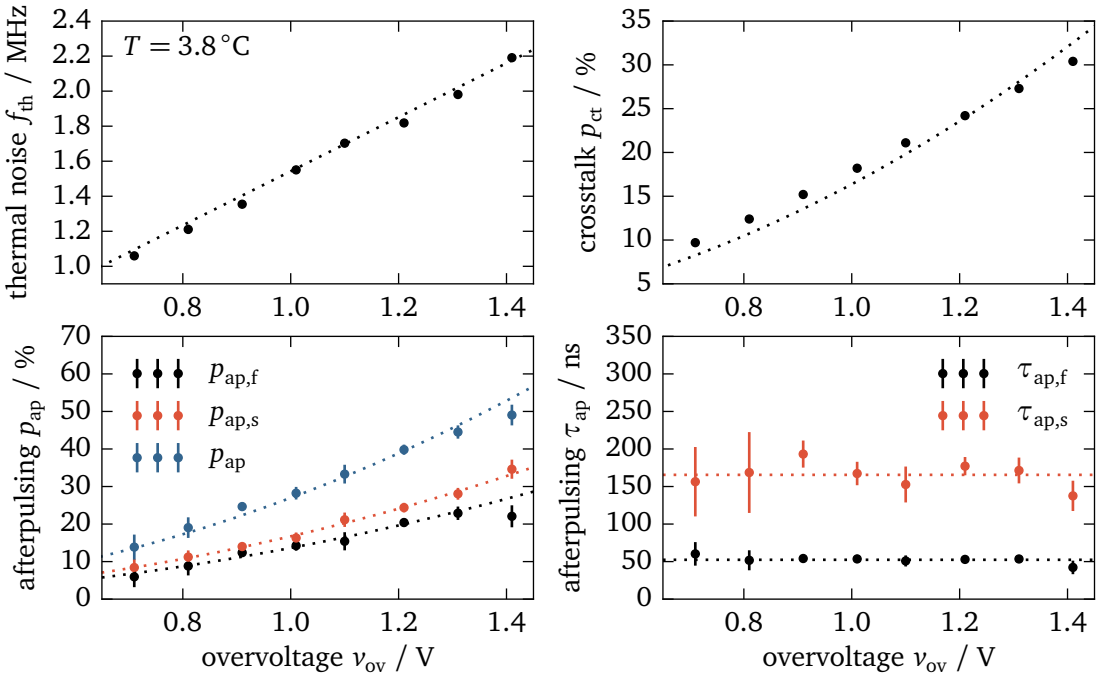

Figure 4.9: Measured over-voltage dependency of the thermal noise f_{th}, the optical crosstalk probability p_{ct}, the afterpulsing probabilities $p_{ap,f}$, $p_{ap,s}$ and the afterpulsing time constants $\tau_{ap,f}$, $\tau_{ap,s}$ for a Hamamatsu S10362-33-100C SiPM at a temperature of $T = (3.76 \pm 0.03)\,°C$. The over-voltage dependence of the thermal noise is signified by a dotted best fit straight line $f_{th}(v_{ov}) = a\,v_{ov}$. In case of the correlated noise, a quadratic behavior is expected and thus the best fit of $p_{ct,ap}(v_{ov}) = a\,v_{ov}^2$ is shown. The mean afterpulsing time constants are $\tau_{ap,f} = (52.4 \pm 3.2)\,ns$ and $\tau_{ap,s} = (166 \pm 10)\,ns$. Data taken from [95].

constant $\tau_{ap,f} = \mathbb{O}(10\,ns)$ and a long time constant $\tau_{ap,s} = \mathbb{O}(100\,ns)$. For the same device as mentioned above, the following values have been found

$$\tau_{ap,f} = (52.4 \pm 3.2)\,ns \tag{4.28}$$
$$\tau_{ap,s} = (166 \pm 10)\,ns \tag{4.29}$$
$$p_{ap,f} = (23 \pm 2)\,\% \tag{4.30}$$
$$p_{ap,s} = (28 \pm 2)\,\% \tag{4.31}$$
$$\tag{4.32}$$

whereby the joint probability for afterpulsing can be obtained by

$$p_{ap} = 1 - (1 - p_{ap,f})(1 - p_{ap,s}) = (45 \pm 2)\,\% \quad . \tag{4.33}$$

Although the afterpulsing probabilities depend on the applied over-voltage, the afterpulsing time constants are stable within the margin of uncertainties [95].

The over-voltage dependency of the properties discussed above is presented for one Hamamatsu SiPM model in figure 4.9. Due to the fact, that the gain g is proportional to the over-voltage v_{ov}, the number of charge carriers which possibly induce correlated noise also rises.

Furthermore, the avalanche probability ϵ_{trig} is also proportional to the over-voltage. Resulting, the probabilities for correlated noise

$$p_{\text{ct,ap}} \propto v_{\text{ov}}^2 \tag{4.34}$$

increase quadratically with the over-voltage whereas thermal noise is expected to increase linearly [89, 91].

Since optical crosstalk occurs instantaneously, only thermal noise and afterpulsing contribute to the dark noise trigger rate of a SiPM. It is often characterized by

$$f_{\text{dark}} = (1 + p_{\text{ap}}) f_{\text{th}} \quad . \tag{4.35}$$

4.5.4 Gain variations

The avalanche breakdown is a stochastic process. Thus, the gain varies from avalanche to avalanche breakdown by $\mathbb{O}(1\,\%)$ [98]. This phenomenon is referred to as excess noise. Furthermore, not all cells on the SiPM are equal in terms of electrical wiring length and other parasitic effects such as capacitances. In particular, the gain of cells at the borders of the active area of the SiPM are known to have a slightly reduced gain. It can be lower by about 10 % [10].

4.6 Dynamic range

Due to the cellular substructure of the SiPM, its dynamic rage is intrinsically limited. For a number of coincident impinging number of photons n_γ, the number of cells triggering is given by

$$n_{\text{trig}}(n_\gamma) = n_{\text{cell}} \left(1 - e^{-p\, n_\gamma / n_{\text{cell}}}\right) \text{ p.e.} \tag{4.36}$$

with the probability of detection $p \approx PDE \left(1 + p_{\text{ct}} + p_{\text{ap}}\right)$ as discussed above and the total number of cells on the SiPM n_{cell}. The number of cell triggers n_{trig} is given in units of photon equivalents p.e. and corresponds to the total signal charge q divided by the gain g. Therefore, n_{trig} in general is a decimal number. At the lower limit of the dynamic range, the limited statistics and correlated noise intrinsically lead to high fluctuations on the number of triggering cells. For coincident photons and assuming the triggering over all is a Poisson process, the relative uncertainty on the number of triggered cells is given by

$$\sigma^2_{\text{trig,rel}} = \frac{n_{\text{trig}}(n_\gamma)}{n^2_{\text{trig}}(n_\gamma)} = \frac{1}{n_{\text{trig}}(n_\gamma)} \quad . \tag{4.37}$$

Furthermore, for a small number of photons $n_{\text{trig}}(n_\gamma)$ can be approximated by

$$n_{\text{trig}}(n_\gamma) \approx n_{\text{cell}}\, p\, n_\gamma \quad . \tag{4.38}$$

If e.g. a relative uncertainty $\sigma_{\text{trig,rel}} < 1\,\%$ is required, the lower limit of the dynamic range is given by

$$n_\gamma > \frac{1}{n_{\text{cell}}\, p\, \sigma^2_{\text{trig,rel}}} \approx 8 \tag{4.39}$$

for a SiPM with $n_{\text{cell}} = 3600$ cells and a photon detection efficiency of $PDE \approx 35\,\%$.

At the upper limit of the dynamic range, the device saturates at a certain number of effectively triggering cells which makes higher photon intensities indistinguishable from each other [100].

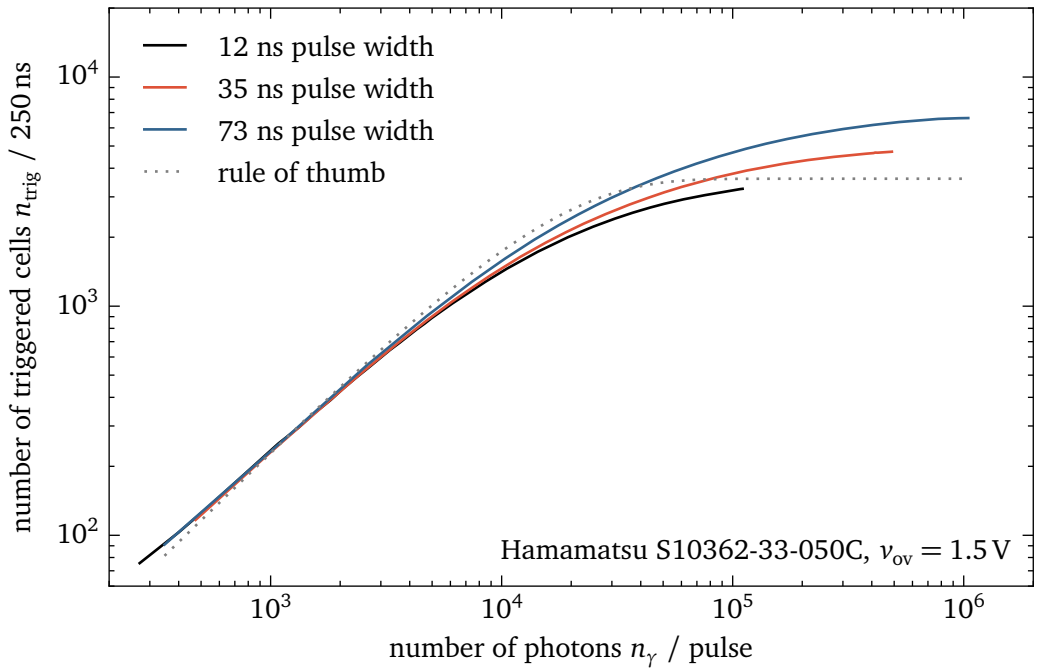

Figure 4.10: Number of effectively triggered cells in an integration window of 250 ns as a function of the number of impinging photons n_γ on the SiPM sensitive area measured for a Hamamatsu S10362-33-050C SiPM. The dotted line denotes the rule of thumb of equation (4.36) with $n_{cell} = 3600$, $PDE = 24\,\%$ $p_{ct} = 12\,\%$ and $p_{ap} = 21\,\%$. The photons originate from a 480 nm LED driven by Gaussian pulses with various pulse widths (12 ns, 35 ns and 73 ns) and pulse heights. Data taken from [99].

However in practice, the light pulses to be detected by SiPMs are of finite length. Thus, cells can start their recovery process and might be fully recharged before the next photon hits. Figure 4.10 presents a measurement of the dynamic range of a Hamamatsu S10362-33-050 3 mm × 3 mm SiPM with 3600 cells operated at an over-voltage of $v_{ov} = 1.5\,V$ and room temperature. Apparently, the measured dynamic range differs substantially from the rule of thumb introduced above (cf. equation (4.36)) and it is not trivial to analytically predict the exact response of the SiPM when exposed to light [100, 101, 102, 103, 104]. Therefore, a simulation of the response of SiPMs respecting certain background and photon signal shapes in spectrum, intensity and time has to be developed. Such a simulation framework is G4SiPM which will be presented in the following chapter.

CHAPTER 5

The silicon photomultiplier simulation G4SiPM

Since silicon photomultipliers (SiPMs) are powerful and versatile photon detectors capable of single photon resolution and providing a large dynamic range, the interest in these devices grows rapidly. At the time of this thesis, SiPMs are being discussed to be employed at the CTA experiment [105, 106, 107], in the upgrade of the MEG dark matter detector [108] and at the LHC, CERN for the LHCb experiment [109]. At the CERN experiment CMS, SiPMs are already installed in the gas drift velocity monitoring and the hadron outer calorimeter [110, 111]. Therefore, the necessity for a dedicated, versatile SiPM simulation is given. The simulation package G4SiPM has been developed for this purpose [12]. Here, the prefix "G4" denotes the reference of G4SiPM to the open source C++ simulation framework Geant4 which is widely established in particle physics. G4SiPM implements certain constructs of Geant4 to make it integrable into existing Geant4 detector simulations. In the following, the main aspects and the inner workings of Geant4 are introduced before discussing the details of the G4SiPM Monte Carlo code.

5.1 Introduction to Geant4

Geant4 (for GEometry ANd Tracking) is a C++ framework for simulating the passage of particles through matter and their interaction with it [11]. The most important features of Geant4 are:

- tracking of fundamental particles through matter
- modular lists of physics processes i.e. lists of particle interactions
- definition of detector geometries and electromagnetic fields
- definition of materials with their chemical and physical properties
- response of sensitive detector elements to the passage of particles
- generation of detector readouts and storage of particle tracks
- visualization of the detector and particle trajectories

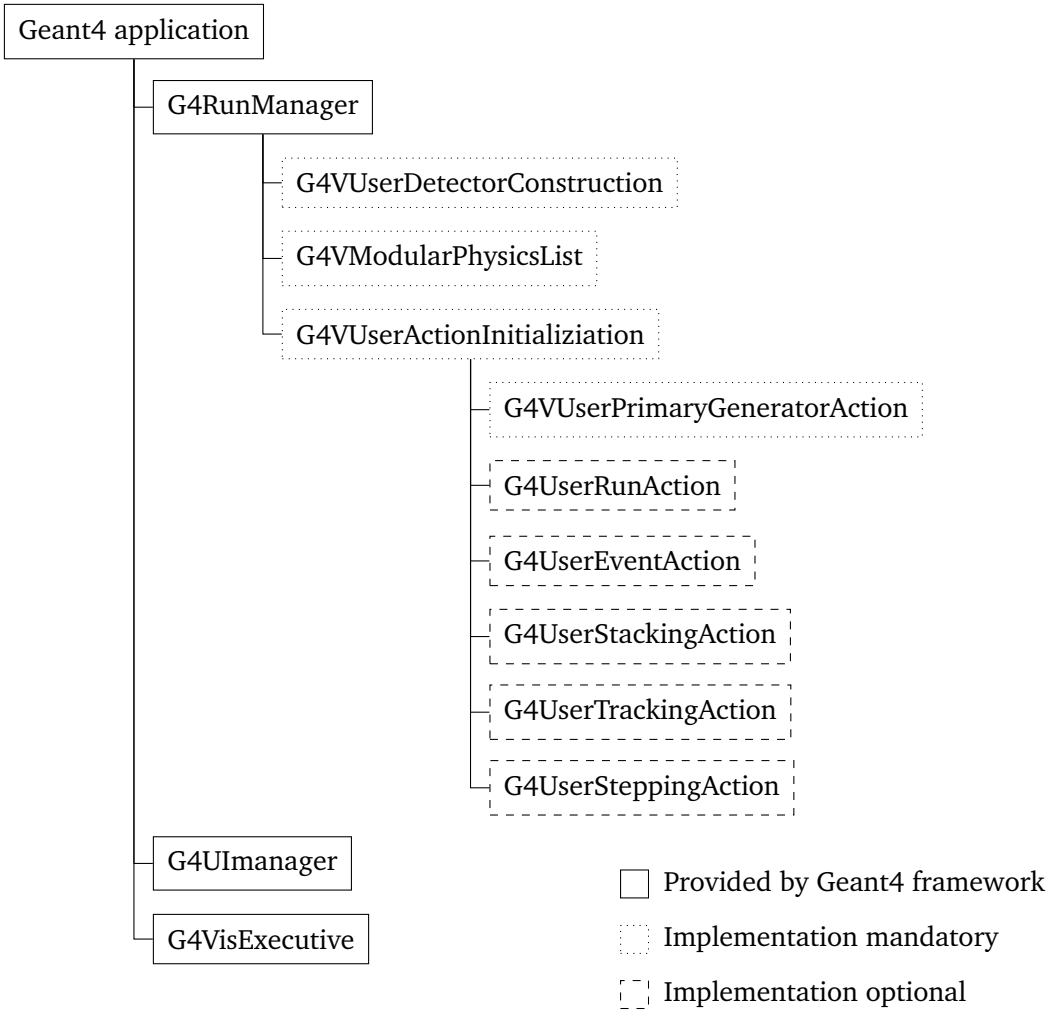

Figure 5.1: Schematic overview of a Geant4 application. Mandatory and optional parts are to be implemented by the application programmer. The components “G4UImanager" and “G4VisManager" are for the end-user interaction.

Geant4 is the successor of Geant and Geant3 originally developed at CERN written in Fortran released 1974 and 1982, respectively [112]. Thereafter in 1994, two groups at CERN and KEK, Japan, joined their efforts in a formal proposal named RD44 to completely rewrite the Geant3 code in the contemporary programming language C++ with an object oriented approach for improved maintainability and extensibility. Since then, the Geant4 project is maintained by the international Geant4 collaboration.

Geant4 is a framework. Thus, there are three types of users: the framework provider, i.e. the Geant4 collaboration, which maintains the code and adds case-specific features to the Geant4 code base, the application programmer and the end user.

The application programmer is essential to every Geant4 detector simulation and requires a strong background in the C++ programming language. The programmer composes the framework parts of Geant4 to an executable program including a detailed detector description (cf. figure 5.1).

A detector in Geant4 consists of so-called solids. Each solid has a distinct geometry, e.g. sphere, tube, pyramid, etc. From a solid and a material, a logical volume is created. Geant4 is equipped with a large database of predefined materials from the NIST database [113, 114, 115]. Physical properties as e.g. the refractive index have to be supplied by the application programmer and are stored in so-called material properties tables. Finally, the logical volume is used to create a physical volume which defines the point in space at which this part of the detector will be placed. Furthermore, the logical and physical volumes can reference elements higher (parent) or lower (children) in the hierarchy of volumes. Child volumes are considered to be enclosed by the parent volume and thus must not protrude. The highest volume in the hierarchy is the world volume and defines the space in which particles are simulated.

The end user executes the simulation while controlling run time parameters as e.g. the primary particle energy. Geant4 also provides basic functionality for visualization and a command line interface. The commands of the command line interface can be comprised to simple scripts for batch execution.

5.1.1 Geant4 run execution

A run in Geant4 consists of the simulation of one or more events. After each run, the detector is set back to its initial state. Each event refers to the simulation of one or more primary particles. Primary particles are fundamental particles created by the primary generator action with a certain kinetic energy, position, momentum direction, polarization and time.

The execution of a run is initiated by the command

```
/run/beamOn n
```

entered either in the command line interface or in a batch processing file with the number of events n. Before the n new events are created, the run action is invoked which can be used to prepare data structures for the recording of the simulated data. Subsequently at least one primary vertex, comprised by a point in space and time and a particle type, must be created by the "G4VUserPrimaryGeneratorAction". The tracking of the particles in space is performed step by step. The step length corresponds to the minimum mean interaction length required by the physics processes. A new step is added to the track of the particle and the physics processes are invoked which might change the properties of the particle or even create secondary particles. Upon completion of each step, a user intervention method of the "G4UserSteppingAction" is called which could be used to monitor certain properties of the particle for the duration of its simulation. The tracking of a particle stops, if the particle leaves the world volume, if it is at rest or if it is destroyed. The latter can be done manually by one of the user intervention methods. If no more particles have to be tracked, the event is considered completed. In a user intervention method of the "G4UserEventAction", the application programmer can invoke the digitization mechanism of Geant4 which is introduced later in this chapter. Finally, the output files should be closed properly. If no more runs have to be simulated, the Geant4 application exits. A sequence diagram of a Geant4 simulation can also be found in figure 5.2.

5.1.2 Geant4 hits and digitization

Logical volumes of the detector construction in Geant4 can be provided with a user implemented sensitive detector, an instance of "G4VSensitiveDetector". Each time a particle traverses the logical volume, its sensitive detector is invoked and the application programmer can

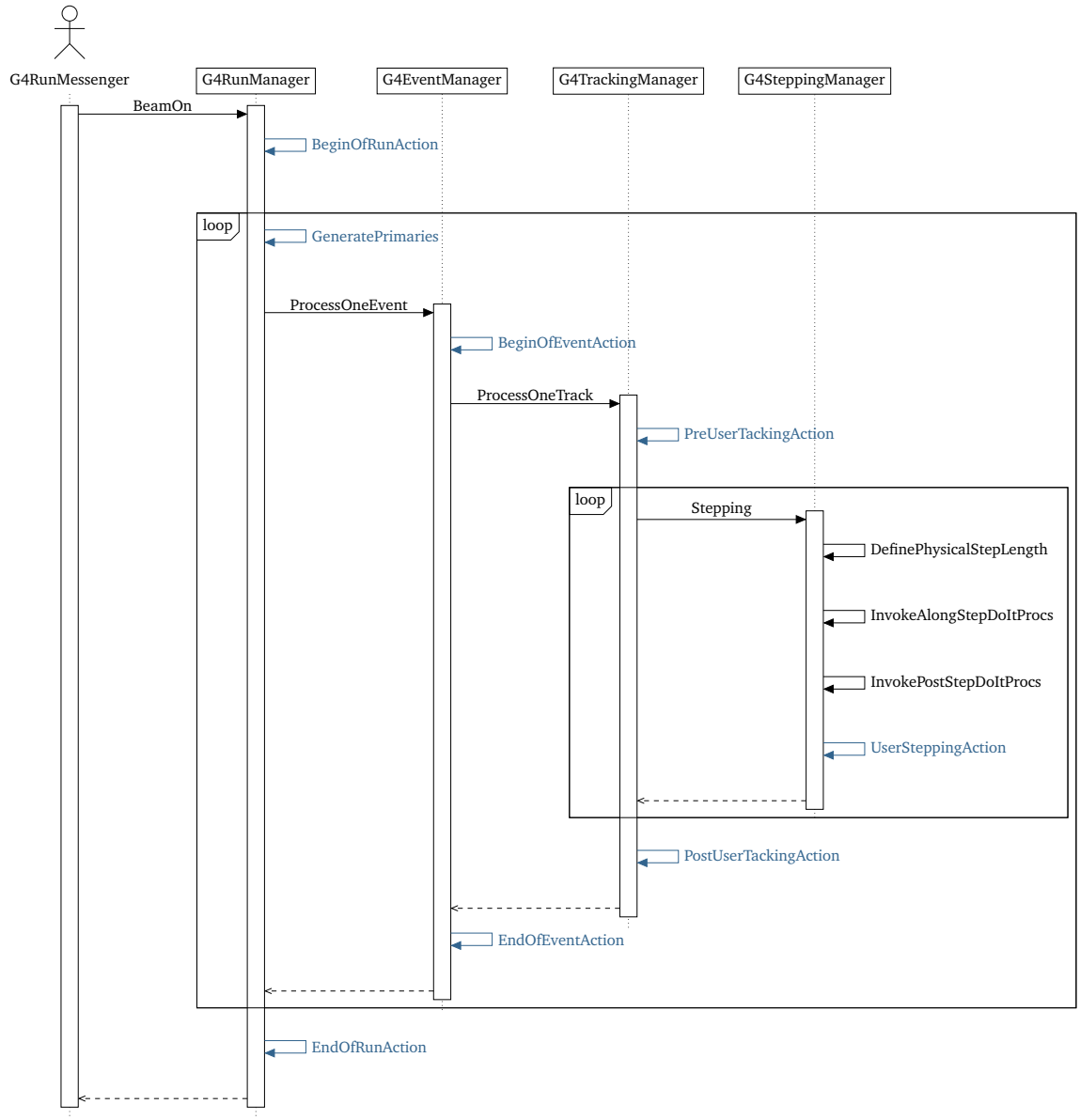

Figure 5.2: Simplified sequence diagram of the execution of a Geant4 application. The colored arrows and labels denote the invocation of the corresponding user action whose implementation is optional.

record the particle properties of interest. The recorded properties are stored in “G4VHit” objects and filled into a “G4VHitCollection”, i.e. a list of all “G4VHit” objects created during one event. Since the response of the sensitive detector may depend on certain properties of the particle, the application programmer can implement a sensitive detector filter “G4VSDFilter” which will be queried before. Hits will only be created in case of a positive return value. Upon completion of the event, the application programmer is responsible for saving the hit collection to a file.

So far, the hits only contain true Monte Carlo values. To compile a more realistic detector

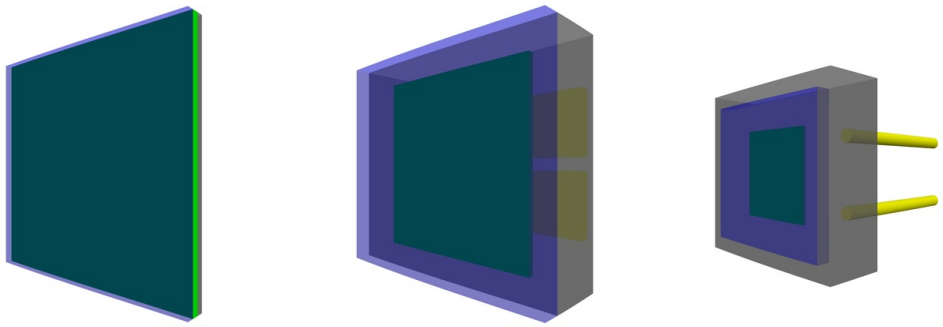

Figure 5.3: Screenshots of the G4SiPM simulation with one “G4Sipm” instance embedded in a “G4SipmHousing”. Left: the default housing simply creates the coating in front of the silicon chip and a ceramic bulk behind the chip. Middle: SMD variant produced by Hamamatsu for reflow soldering [14]. Right: Ceramic variant produced by Hamamatsu with pins for soldering.

response including e.g. uncertainties on the measurement and noise, the hits can be further processed during the digitization stage of Geant4 by the implementation of a “G4VDigitizerModule” which creates “G4VDigi” objects contained in a so-called “G4VDigiCollection”. At the end of the digitization, the application programmer is again responsible for the persistence of the created collections to the hard-disk.

5.2 G4SiPM object classes

Similarly to Geant4, G4SiPM is a framework and provides the means to create Geant4 simulations with SiPMs as sensitive parts of the detector geometry. Nevertheless, all classes are highly interlinked to minimize the application programmer effort.

5.2.1 Object class: G4Sipm

The “G4Sipm” class is responsible for the creation of solids, logical and physical volumes for the detector construction. Additionally, it registers a sensitive detector and a digitizer module to Geant4. Since in most simulations more than one SiPM would be placed in the detector construction, all instances are uniquely identified by an integer id. The same id is used for the name of the hits and digi collections. The physical representation of the silicon chip of a SiPM is a cuboid of silicon.

5.2.2 Object class: G4SipmHousing

This class wraps the bare silicon created by the “G4Sipm” class in a housing (cf. figure 5.3). The most simple housing consists of a cuboid of ceramic behind and an cuboid of epoxy in front of the silicon chip. Here, the epoxy acts as the coating which is required to correctly resemble the angular dependency of the detection efficiency of SiPMs. Due to this construction, multiple reflections between air, the coating and the silicon can occur. Light, which is reflected by the SiPM by either direct or multiple reflection, can trigger other detector elements or lead to a

dispersion of the photon signal. The incorporation of these effects is essential to a detailed detector simulation.

5.2.3 Object class: G4SipmModel

All phenomenological properties of the SiPM are stored in the "G4SipmModel" class. New models can be implemented by either sub-classing "G4SipmModel" or by the creation of a configuration file

```
name = HamamatsuS12573...
numberOfCells = 3600
cellPitch = 100 * micrometer
biasVoltage = 65.0 * volt
[...]
```

which is a simple text file. Since most quantities have a unit, the corresponding unit name of the CLHEP library, which is used for the handling of units in Geant4, can be stated.

The "G4SipmPropertiesFileModel" class used for the parsing of the text files can also handle tables which is useful for e.g. for the configuration of the photon detection efficiency as a function of the photon wavelength. These tables are formatted with tabulators as column separators which makes the whole file editable with spreadsheet programs.

5.2.4 Object class: G4SipmVoltageTraceModel

The "G4SipmVoltageTraceModel" holds the properties important to the generation of voltage traces. The actual amplitude of a 1 p.e. pulse a_{pe} in volts, the rise and fall time constants of the signal τ_{rise} and τ_{fall}, the constant voltage offset of the baseline v_0 and the electronics noise are unique to the readout circuit [116]. These properties are also configurable in the aforementioned properties file.

Each SiPM cell trigger is converted to a voltage trace pulse

$$v_{\mathrm{trig}}(t) = \begin{cases} 0 & t < 0 \\ a_{\mathrm{pe}}\, g \left(1 - \exp^{-t/\tau_{\mathrm{rise}}}\right) \exp^{-t/\tau_{\mathrm{fall}}} & t \geq 0 \end{cases} \tag{5.1}$$

as a function of the time after the breakdown t and the simulated gain $g \in [0,1]$ of the SiPM cell.

5.2.5 Object class: G4SipmGainMapModel

Tiny differences in the electrical wiring, border effects or defects in the silicon substrate lead to fluctuations of the gain of a SiPM cell, which are modeled by the excess noise σ_{pe}. Two models are predefined. The first model simply varies the gain by generating random values from a normal distribution with mean one and variance σ_{pe}

$$p(g, \sigma_{\mathrm{pe}}) = \frac{1}{\sigma_{\mathrm{pe}}\sqrt{2\pi}}\, e^{-\frac{(g-1)^2}{2\sigma_{\mathrm{pe}}^2}} \quad . \tag{5.2}$$

A typical value is $\sigma_{\mathrm{pe}} = 10\,\%$.

Complementary, the second model takes into account that cells at the edge of the SiPM surface could behave differently compared to the cells in the inner parts. Under the assumption

the gain is highest in the center and lowest at the edges, the gain is modeled by a 2D Gaussian distribution as a function of the coordinate on the SiPM surface [117]. A combination of both models can be implemented by the application programmer.

5.2.6 Object class: G4SipmSensitiveDetector

The "G4SipmSensitiveDetector" is attached to the silicon logical volume of the "G4Sipm". It is automatically activated when a photon traverses the silicon volume and records the hit SiPM cell, time and other particle properties in form of a "G4SipmHit". Other particles are ignored, but it has been shown that SiPMs are susceptible to radiation damage [118, 119]. In any case, optical photons are absorbed at this point by stopping the Geant4 track programmatically. In contrast to the so-called optical photons, gammas are considered as fundamental particles in Geant4 and are not treated by geometrical optics. These and other fundamental particles possibly pass the SiPM.

To identify the photon hit position with a cell on the SiPM, the cells in G4SiPM are enumerated by a unique cell identifier

$$id = i\sqrt{n_{\text{cell}}} + j \tag{5.3}$$

with the number of cells n_{cell} on the SiPM and the integer coordinates of a cell i, j. Technically, this enumeration only applies to quadratic devices with $\sqrt{n_{\text{cell}}}$ being an integer number. The coordinates i, j are integer Cartesian coordinates. For a given incident position x, y relative to the center of the silicon chip, the cell coordinates can be derived to

$$i = \left\lfloor \frac{x + \frac{d}{2}}{d_{\text{cell}}} \right\rfloor \quad \text{and} \quad j = \left\lfloor \frac{y + \frac{d}{2}}{d_{\text{cell}}} \right\rfloor \tag{5.4}$$

with the device pitch $d = d_{\text{cell}}\sqrt{n_{\text{cell}}}$ and the cell pitch d_{cell}. The coordinates are valid if

$$0 \geq i < \sqrt{n_{\text{cell}}} \quad \text{and} \quad 0 \geq j < \sqrt{n_{\text{cell}}} \quad . \tag{5.5}$$

With future developments, exotic hexagonal or circular sensitive areas might become available. For these devices, the numbering scheme of the cells has to be adapted by the application programmer.

5.2.7 Object class: G4SipmSensitiveDetectorFilter

The sensitive detector filter is responsible for the activation of the "G4SipmSensitiveDetector". A positive decision is made if two criteria are met.

Initially, when a photon hits the SiPM silicon in G4SiPM, it is checked whether the photon hits the sensitive area of a cell. Commonly, the borders of the cells of SiPMs are insensitive due to electrical wiring, electrical separation and possibly optical barriers between the single cells [8] which has a diminishing effect on the photon detection efficiency. To respect the fill factor ϵ_{geom} of the device, the outer parts of the cell is considered blind. With the cell coordinates stated in equation (5.4), the center of the cell is given by

$$x_c = \left(i + \frac{1}{2}\right) d_{\text{cell}} - \frac{d}{2} \quad \text{and} \quad y_c = \left(j + \frac{1}{2}\right) d_{\text{cell}} - \frac{d}{2} \tag{5.6}$$

and thus the borders of the active area of each cell can be derived to

$$x_{1,2} = x_c \pm \frac{d_{\text{cell}}}{2}\sqrt{\epsilon_{\text{geom}}} \quad \text{and} \quad y_{1,2} = y_c \pm \frac{d_{\text{cell}}}{2}\sqrt{\epsilon_{\text{geom}}} \quad . \tag{5.7}$$

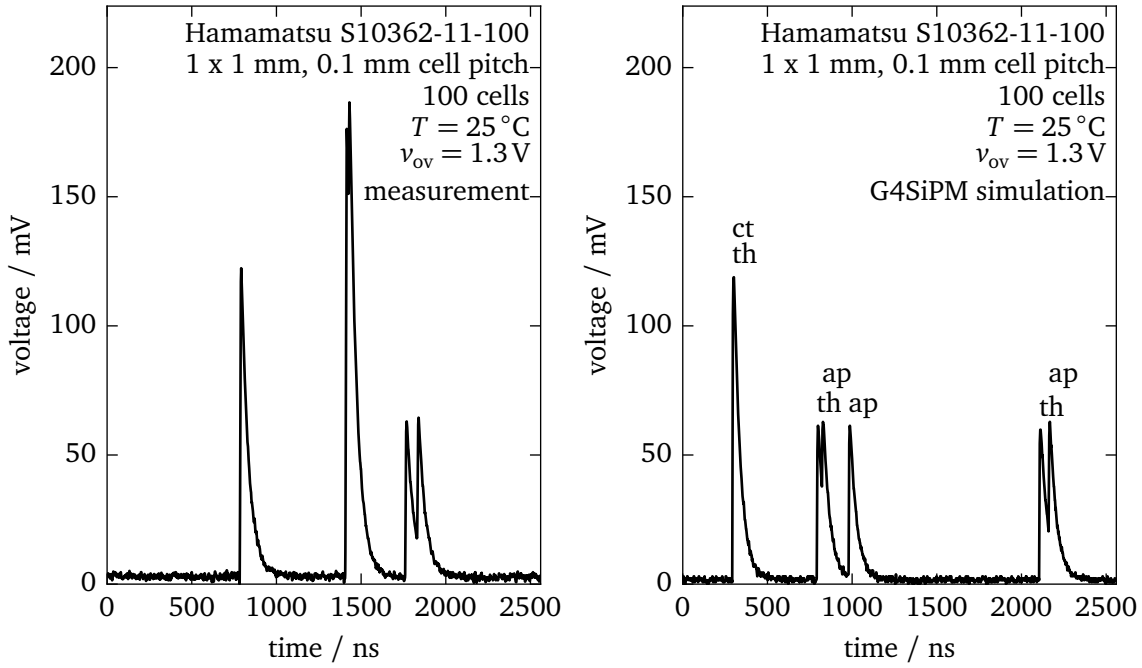

Figure 5.4: Left: measured voltage trace of dark noise of a Hamamatsu 1 mm × 1 mm SiPM with 100 cells. The measurement has been obtained with a CAEN FADC [120] and a custom-made amplifier [121] at room temperature. Right: simulated dark noise trace of the same SiPM model obtained by G4SiPM. The labels denote the origin of the voltage pulse: thermal noise (th), optical crosstalk (ct) and afterpulsing (ap).

Finally, for acceptance of the photon due to geometrical reasons, the conditions

$$x_1 \leq x < x_2 \quad \text{and} \quad y_1 \leq y < y_2 \tag{5.8}$$

have to be met.

Secondly, the photon detection efficiency is taken into account. Besides the fill factor, the reflectivity of the material boundaries between the air, the coating and the silicon have already been simulated by Geant4 during the tracing of the photons. Thus, the photon detection efficiency as given by the manufacturer is revised upwards. The details of this algorithm are discussed below in section 5.3.2.

5.2.8 Object class: G4SipmDigitizer

The "G4SipmDigitizer" is one of the most central parts of G4SiPM. It implements the simulation of thermal and correlated noise as well as the triggering mechanism on a single cell basis as described below in section 5.3.2. Triggers are represented by "G4SipmDigi" objects which are filled into the "G4SipmDigiCollection" for further processing.

5.2.9 Object class: G4SipmVoltageTraceDigitizer

After the completion of the digitization of the SiPM signal, the voltage trace can be derived from the list of triggers. For this, all SiPM triggers are converted to pulses using the voltage

pulse parameterization of the "G4SipmVoltageTraceModel" and added up to a complete voltage trace

$$v(t) = \sum_i v_i(t) + v_0 \tag{5.9}$$

plus the constant voltage offset v_0. The time t is given in discrete steps of e.g. 1 ns. To incorporate white noise, the resulting voltages $v(t)$ are smeared separately for each t by multiplying a random factor picked from a Gaussian distribution with mean one and variance σ_{el}. A simulated trace in comparison to a measured SiPM signal is presented in figure 5.4.

5.2.10 Object class: G4SipmUiMessenger

The UI messenger provides control commands which influence the execution of G4SiPM. For instance, parts of the simulation as e.g. the simulation of thermal noise or the whole digitization can be switched off. These commands are available via the Geant4 command line interface.

5.2.11 Testing

Automated testing is very important when developing libraries or frameworks [122]. Unit tests in particular are small programs which run small pieces of code and compare the result to a certain expectation. These tests can also easily be used to exploit the implementation regarding special cases. At a higher level, integration tests are used to test the source code at larger scope. The purpose of testing is not only to ensure the correctness of the implementation during the development phase but also that it is not broken later by minor changes.

G4SiPM uses the Google Test library [123] and has 135 unit and integration tests in total with a total code coverage of 85 %. A good practice is to ensure a code coverage of $> 80\,\%$ [124].

5.3 SiPM model

The SiPMs in G4SiPM are represented by a phenomenological model with phenomenological input quantities which can either be determined in the laboratory or be taken from existing publications [10, 82, 95, 125]. Thus, G4SiPM is explicitly not an electrical simulation at semiconductor level as for instance the code presented in [92]. Instead, the triggering of the SiPM is simulated on a single cell level for correct modeling of the recovery behavior and also the creation of correlated noise. Besides many predefined SiPM model implementations for widely used devices from Hamamatsu [83] and SensL [84], the user can define new SiPM models by means of simple text configuration files. A list of the properties can be found in table 5.1. Furthermore, the performance properties of the SiPM can be interpolated for a setting of v_{bias} and T which has not been supplied by the user.

5.3.1 Operating points

Since many properties of the SiPM depend on the over-voltage v_{ov} which in turn depends on the bias voltage v_{bias} and the ambient temperature T the performance properties, i.e. e.g. the photon detection efficiency and correlated noise probabilities, are defined for an operating point $\vec{p} = (T_{\text{ov}}, v_{\text{ov}})$. Here, the ambient temperature T and the bias voltage v_{bias} are referred to as operational parameters. The more operating points and corresponding performance parameters

Property	Symbol	Unit
Geometrical and package properties		
Number of cells	n_{cell}	
Cell pitch	d_{cell}	µm
Fill factor	ϵ_{geom}	%
Coating thickness	d_{coat}	mm
Coating refractive index	n_{coat}	
Operational parameters		
Ambient temperature	T	°C
Bias voltage	v_{bias}	V
Relative fluctuation of the gain	σ_{pe}	%
Dead time	τ_{dead}	ns
Operating point		
Temperature	T_{ov}	°C
Over-voltage	v_{ov}	V
Performance properties for operating points		
Breakdown voltage	v_{break}	V
Spectral photon detection efficiency	$PDE(\lambda)$	%
Thermal noise rate	f_{th}	kHz
Probability of fast afterpulsing	$p_{\text{ap,f}}$	%
Probability of slow afterpulsing	$p_{\text{ap,s}}$	%
Time constant of fast afterpulsing	$\tau_{ap,f}$	ns
Time constant of slow afterpulsing	$\tau_{ap,s}$	ns
Probability of optical crosstalk	p_{ct}	%
Recovery time constant	τ_{rec}	ns

Table 5.1: List of properties which comprise an SiPM model in G4SiPM. The geometrical and package parameters are fixed during run time. Each operating point is defined by its ambient temperature T_{ov} and v_{ov}. Upon change of the operational parameters, the two best fitting operating points are selected as basis for a linear interpolation of the performance parameters. More sophisticated interpolation mechanisms can be implemented. The $PDE(\lambda)$ is given for perpendicular light incidence in air. All listed properties can be configured in one single SiPM properties file.

are supplied for a SiPM model, the more freely T and v_{bias} can be chosen and the better is the interpolation of the performance parameters between operating points. For this, the geometrical distance between the operating points $\vec{p}_i$ and the operational parameters $\vec{p} = \left(T, v_{\text{bias}} - v_{\text{break,i}}\right)$ is calculated

$$\Delta_i = |\vec{p}_i - \vec{p}| = \sqrt{\left(T_{\text{ov,i}} - T\right)^2 + \left(v_{\text{ov,i}} - \left(v_{\text{bias}} - v_{\text{break,i}}\right)\right)^2} \tag{5.10}$$

with the breakdown voltage $v_{\text{bias,i}}$ of operating point i. Thus, the two best matching operating points $\vec{p_1}$ and $\vec{p_2}$ have the two smallest distances Δ_p. The performance properties are then interpolated linearly as a function of T if $T_{\text{ov,1}} \neq T_{\text{ov,2}}$ or as a function of v_{bias} otherwise. Here, the linear interpolation is a conservative choice but the application programmer can easily implement the preferred behavior or extend the mechanism to a two-dimensional interpolation.

5.3.2 Phenomenological model

The photon detection efficiency is defined by

$$PDE(\lambda, \theta) = \epsilon_{\text{geom}}\, \epsilon_{\text{trig}}\, \epsilon_{\text{trans}}(\theta)\, QE(\lambda) \tag{5.11}$$

with the geometrical fill factor ϵ_{geom}, the trigger probability ϵ_{trig}, which is the probability for the primary electron hole pair to create an avalanche, the transmission efficiency from air into the silicon $\epsilon_{\text{trans}}(\theta)$ as a function of the angle of incidence and the quantum efficiency $QE(\lambda)$ [126]. The geometrical fill factor is respected as described above in section 5.2.7.

Furthermore, the PDE is reduced for photons impinging at non normal angles due to multilayer Fresnel reflections at the coating and the silicon chip [86, 87]. Since more than two optical media are involved (air, coating and silicon), higher order combinations of transmission and reflection occur. The reflectivity $r(\theta, n_1, n_2)$ and the transmittance $t(\theta, n_1, n_2)$ of optical boundaries under an incidence of θ with the angle of refraction $\sin\eta = n_1/n_2 \sin\theta$ can be calculated by the Fresnel equations [127]

$$r(\theta, n_1, n_2) = \frac{1}{2}\left(r_p(\theta, n_1, n_2) + r_s(\theta, n_1, n_2)\right) \tag{5.12}$$

$$t(\theta, n_1, n_2) = 1 - r(\theta, n_1, n_2) \tag{5.13}$$

with the reflectivity r_s for perpendicularly polarized light and r_p for parallel polarized light

$$r_s(\theta, n_1, n_2) = \left| \frac{n_1 \cos\theta - n_2 \sqrt{1 - \left(\frac{n_1}{n_2}\sin\theta\right)^2}}{n_1 \cos\theta + n_2 \sqrt{1 - \left(\frac{n_1}{n_2}\sin\theta\right)^2}} \right|^2 \tag{5.14}$$

$$r_p(\theta, n_1, n_2) = \left| \frac{n_2 \cos\theta - n_1 \sqrt{1 - \left(\frac{n_1}{n_2}\sin\theta\right)^2}}{n_2 \cos\theta + n_1 \sqrt{1 - \left(\frac{n_1}{n_2}\sin\theta\right)^2}} \right|^2 \quad . \tag{5.15}$$

The first order of transmission into the silicon is a product of the transmission of light from air to the coating $t(\theta, n_{\text{air}}, n_{\text{coat}}) \equiv t_{12}(\theta)$ and from the coating to the silicon $t(\eta, n_{\text{coat}}, n_{\text{Si}}) \equiv t_{23}(\eta)$:

$$\epsilon^{(1\text{st})}_{\text{trans}}(\theta) = t_{12}(\theta)\, t_{23}(\eta) \quad . \tag{5.16}$$

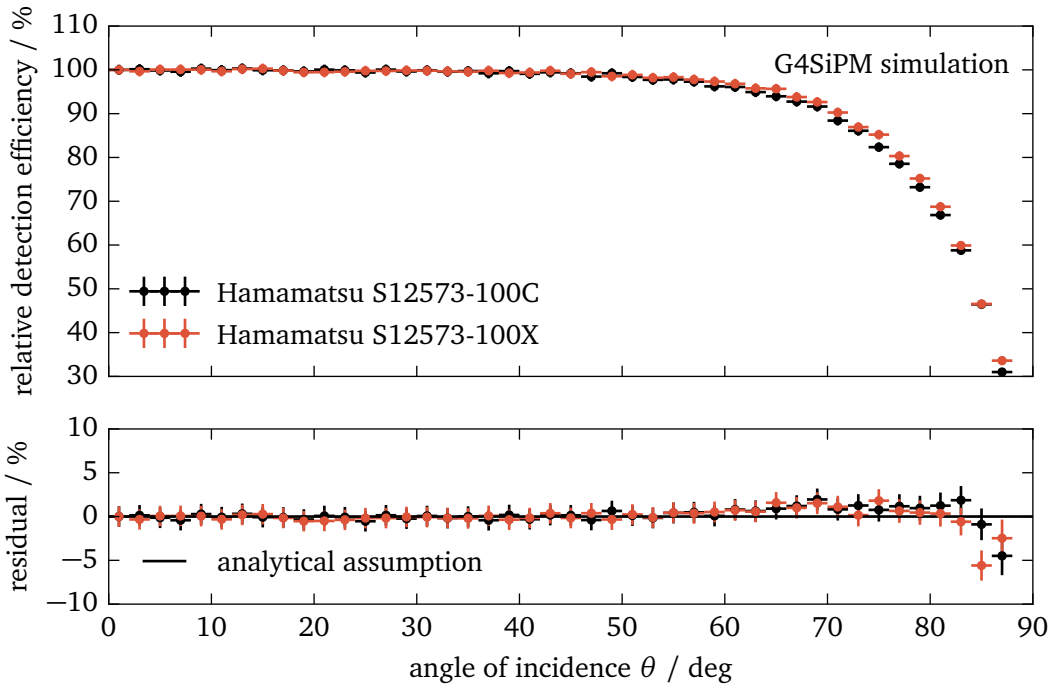

Figure 5.5: Simulated photon detection efficiency of the Hamamatsu S12573-100C with an epoxy coating with $n_{\text{coat}} = 1.55$ and of the Hamamatsu S12573-100X with an silicone coating with $n_{\text{coat}} = 1.41$ [14, 90]. The solid line has been acquired by the analytical formula of the multi-layer Fresnel transmission $\epsilon_{\text{geom}}(\theta)$ stated in equation (5.19). The indexes of refraction of air and silicon are $n_{\text{air}} = 1+172 \cdot 10^{-6}$ [22] and $n_{\text{si}} = 4.6784 + 0.1485\text{i}$ at $\lambda = 450\,\text{nm}$ [85].

The next order of transmission to the silicon involves a reflection at the coating silicon boundary $r(\eta, n_{\text{coat}}, n_{\text{Si}}) \equiv r_{23}(\eta)$ back to the coating air boundary. If it is again reflected there $r(\eta, n_{\text{coat}}, n_{\text{air}}) \equiv r_{21}(\eta)$, the photon has another chance to penetrate the silicon. The complete term of the second order process is given by

$$\epsilon_{\text{trans}}^{(\text{2nd})}(\theta) = t_{12}(\theta)\, r_{23}(\eta)\, r_{21}(\eta)\, t_{23}(\eta) \quad . \tag{5.17}$$

From here, higher orders are easily constructed by adding additional multiplicands of $r_{23}(\eta)\, r_{21}(\eta)$. This can be continued to an infinite series

$$\epsilon_{\text{trans}}(\theta) = t_{12}(\theta) \left[\sum_{i=0}^{\infty} (r_{23}(\eta)\, r_{21}(\eta))^i \right] t_{23}(\eta) \tag{5.18}$$

$$= \frac{t_{12}(\theta)\, t_{23}(\eta)}{1 - r_{23}(\eta)\, r_{21}(\eta)} \tag{5.19}$$

with the substitution $\eta = \sin^{-1}(n_1/n_2 \sin\theta)$. Here, n_1 is the index of refraction of air n_{air}, n_2 the index of refraction of the coating n_{coat} and n_3 the index of refraction of silicon n_{si}, respectively. A G4SiPM simulation example for the angular dependence of the PDE and the calculation of the corresponding $\epsilon_{\text{trans}}(\theta)$ are presented in figure 5.5.

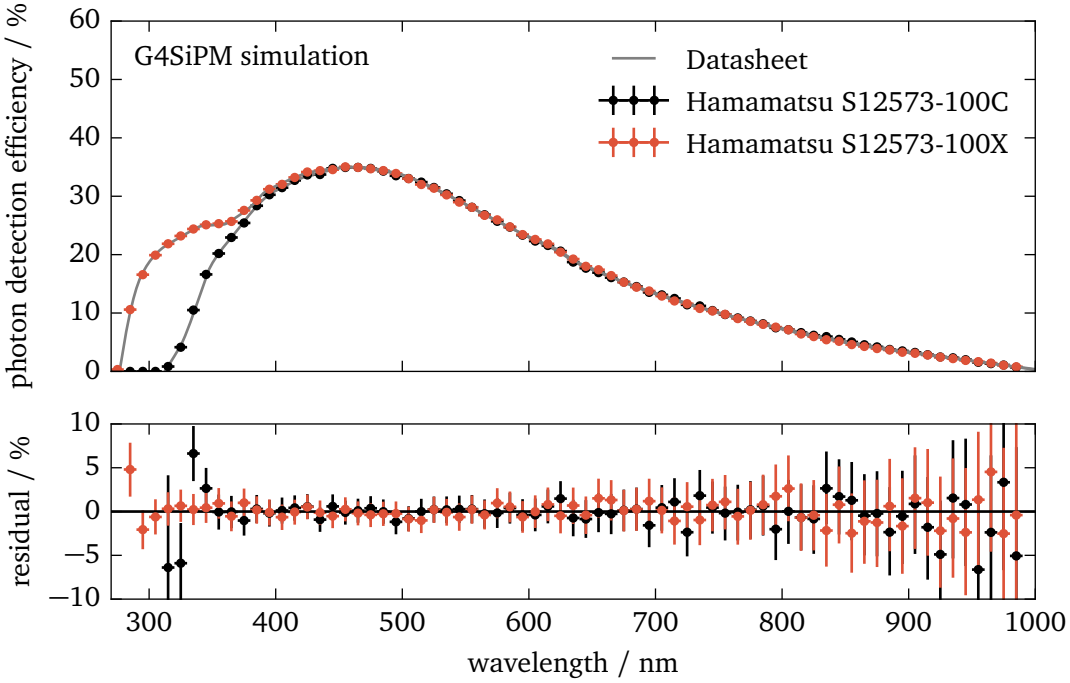

Figure 5.6: Simulated photon detection efficiency of the Hamamatsu S12573-100C with epoxy coating and of the Hamamatsu S12573-100X with silicone coating for improved UV detection efficiency at an over-voltage of $v_{ov} = 1.4\,\mathrm{V}$. The solid lines represent the seed PDE taken from the datasheets [14, 90].

Since the fill factor ϵ_{geom} and the reflections at the boundary surfaces are already taken into account, the photon is accepted as detected with an upward revised probability of

$$p = \frac{PDE(\lambda)}{\epsilon_{geom}\,\epsilon_{trans}(\theta)} \tag{5.20}$$

with the PDE supplied by the user $PDE(\lambda)$ which traditionally is measured as a function of the photon wavelength for perpendicular light incidence. An example reproducing the input PDE in G4SiPM is shown in figure 5.6. All successfully detected photons are written as hits to a separate hit collections for each simulated SiPM. At this stage, the ray-tracing of the photons is considered completed and the photon tracks are stopped. All further simulation steps regarding the electrical model and the correlated noise are performed during the digitization stage of Geant4.

Even if operated in the dark, SiPM cells can break down accidentally due to thermal- and secondary correlated noise [8]. To simulate the SiPM with dark noise on a single cell basis, a chronologically sorted trigger queue is created (cf. figure 5.7). Each cell trigger from the photon tracking gets sorted into the queue along with the creation process (photon, thermal, crosstalk or afterpulse) the cell identifier and the exact point in time.

Subsequently, triggers from thermal noise are added to the queue. For this, the time difference between two consecutive thermal noise triggers is picked from an exponential distribution

$$p_{th}(\delta t) = f_{th}\,\exp^{-f_{th}\,\delta t} \tag{5.21}$$

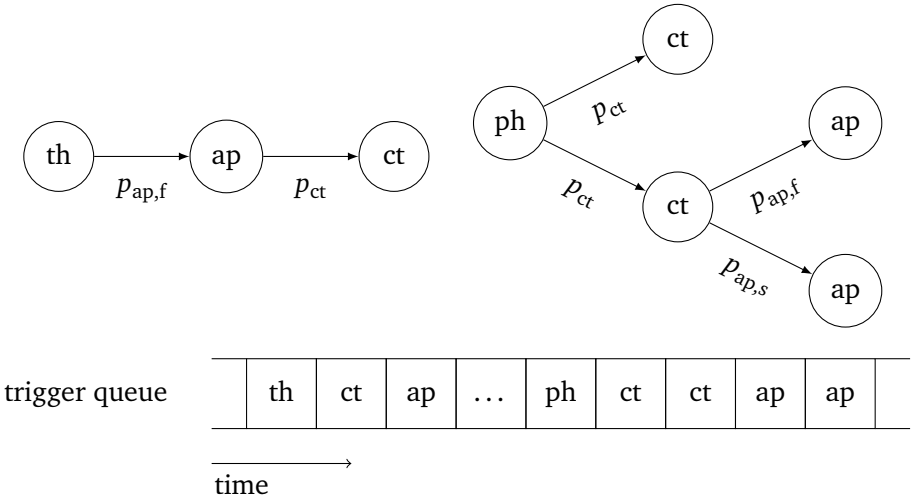

Figure 5.7: Top: sketch of two possible trigger histories sorted into the chronologically sorted trigger queue implemented in G4SiPM. The label "th" denotes thermal noise triggers, "ph" photon, "ct" optical crosstalk and "ap" after-pulsing. Bottom: sketch of the trigger queue. The recharge status of each cell determined by the time passed after the preceding trigger in the same cell. While traversing the queue, all triggers are handled in an equal manner and correlated noise triggers are added subsequently. This implies that correlated noise can in turn create further correlated noise triggers.

which yields uniformly distributed points in time. This approach prevents floating point accuracy problems for very large time windows in contrast to generating the times from a uniform distribution directly. The cell identifier is diced uniformly.

Thermal noise is added to the trigger queue in a time window considerably larger than the time window in which the photons have been simulated to allow the Monte Carlo model to reach a steady state. The time window is increased by

$$t_{\pm} = n_{\mathrm{th},\pm} \frac{n_{\mathrm{cell}}}{f_{\mathrm{th}}} \tag{5.22}$$

to both sides with an arbitrary, configurable multiplicand $n_{\mathrm{th},\pm}$ allowing each cell to have $n_{\mathrm{th},\pm}$ thermal noise induced breakdowns on average before and after the arrival of the photons. A value of $n_{\mathrm{th},\pm} \approx 10$ has been found to be sufficient. Later, the output saved to the hard-disk can be clipped to the photon time window.

From now on, the G4SiPM trigger queue is traversed. For each trigger, regardless of its origin, correlated noise, as described in the following, is computed.

The number of crosstalk triggers succeeding a single cell trigger is picked from a binomial distribution

$$P_{\mathrm{ct}}(k) = \binom{n}{k} q^k (1-q)^{n-k} \tag{5.23}$$

with n trials and the probability

$$q = 1 - (1 - p_{\mathrm{ct}})^{1/n} \tag{5.24}$$

given $P_{\mathrm{ct}}(0) = 1 - p_{\mathrm{ct}}$.

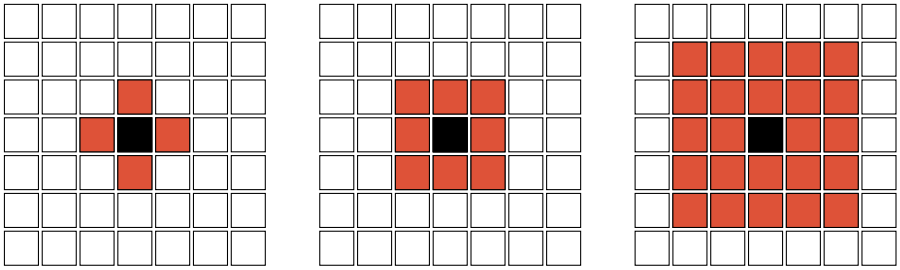

Figure 5.8: Possible scenarios for the considered neighbors (shaded) for optical crosstalk from a seed cell (center). Left: the preferred model with four nearest neighbors [96]. Here, the number of shells is $n_s = 0$ by convention. Middle: one complete shell $n_s = 1$ with eight nearest neighbors. Right: two shells $n_s = 2$ including the second nearest neighbors.

For the optical crosstalk by default the $n = 4$ nearest neighboring cells are considered in G4SiPM since it has been shown to fit experimental data best [96]. The number of nearest neighbors can be increased to include all nearest neighbors $n = 8$, the second nearest $n = 24$, and so on. Depending on the number of shells n_{shell} to include, the number of possible neighbors derives to

$$n = 4\, n_{\text{shell}}\,(n_{\text{shell}} + 1) \quad . \tag{5.25}$$

By convention, the number of neighbors is $n = 4$ for $n_{\text{shell}} = 0$. An example is given in figure 5.8.

For each afterpulsing component $p_{\text{ap,f}}$ and $p_{\text{ap,s}}$ separately, the number of afterpulsing triggers is picked from a Poisson distribution

$$P_{\text{ap}}(k) = \frac{\lambda^k}{k!} e^{-\lambda} \tag{5.26}$$

with the mean

$$\lambda = -\ln\left(1 - p_{\text{ap}}\right) \tag{5.27}$$

given $P_{\text{ap}}(0) = 1 - p_{\text{ap}}$.

In principle, the GAPDs can be modeled as a capacitor with a capacitance of C_d (cf. figure 4.4 in section 4.2) [79]. The breakdown is a spontaneous discharge of the capacitance with the intrinsic GAPD resistance R_d connected in parallel. Now, in the equivalent circuit, the capacitance C_d is fully drained and the voltage over the diode recharges with the quenching resistance R_q in series according to

$$v_{\text{d}}(t) = v_{\text{ov}}\left(1 - e^{-t/\tau_{\text{rec}}}\right) \tag{5.28}$$

with the characteristic recharge time constant $\tau_{\text{rec}} = C_d R_q = \mathbb{O}(10\text{ns})$. Since the gain g is proportional to the diode voltage, it recharges accordingly. In G4SiPM, the gain of a cell is set to zero after a breakdown and the cell is considered dead in the time window τ_{dead}. If $t > \tau_{\text{dead}}$, new triggers are accepted with a reduced gain $g(t) \propto v_{\text{d}}(t)$. In G4SiPM the gain g is a relative quantity, thus the maximum value is $g(t \to \infty) = 1$. Since the probabilities p for correlated noise are proportional to the square of the diode voltage, successive correlated noise is generated with a reduced probability $p\, g(t)^2$ under the assumption $p = 0$ at $v_{\text{ov}} = 0$.

In summary, the following parameters are required by G4SiPM for a successful ray tracing: $PDE(\lambda)$ and ϵ_{geom}. However, for the noise simulation, f_{th}, p_{ct}, $p_{\text{ap,f}}$, $p_{\text{ap,s}}$, $\tau_{\text{ap,f}}$, $\tau_{\text{ap,s}}$ and τ_{rec} are required. If desired, all parameters can be supplied as a function of v_{ov} and T.

In terms of computing costs, 1 ms of dark noise of a 3600 cell SiPM can be generated in less than 1 second (< 5 seconds including voltage trace, cf. figure 5.4) with a memory usage of less than 350 MB (single 3 GHz CPU) [12].

5.4 Validation of the G4SiPM model

To ensure the validity of the predictions being made by the G4SiPM Monte Carlo code, the simulation results have been compared to several measurements. The results of these measurements yield the phenomenological parameters needed for G4SiPM and have been obtained with analysis procedures similarly to those described in the following [95]. The analysis makes use of a peak detection algorithm to determine the point in time and peak height of the avalanche breakdowns of SiPMs [82, 128]. From the peak heights, the number of photon equivalents can be computed. After successful analysis, the obtained parameters are fed into the G4SiPM simulation. Since here, the trigger times and peak heights are known from the simulation, the trigger finding algorithm can be bypassed. Finally, the results of the analysis of the Monte Carlo simulation are compared to the input parameters.

5.4.1 Trigger analysis procedure of dark noise

A standard method is the evaluation of the dark noise of SiPMs operated in the dark. Thus, dark noise arises solely from thermal noise. Correlated noise contributes to the dark noise whereas optical crosstalk, since it occurs instantly, increases only the height of the pulses. Since afterpulses are delayed triggers, new triggers are created which increases the dark noise rate. Thus, in first order, the dark noise rate is given by

$$f_{\text{dark}} = \left(1 + p_{\text{ap}}\right) f_{\text{th}} \quad . \tag{5.29}$$

A common approach for the determination of the thermal noise rate and the properties of afterpulsing is the measurement of the distribution of time delays δt between thermal noise triggers and the subsequent trigger.

For a correct determination of afterpulsing from dark noise, it is mandatory to investigate the combinatorics of these processes because the probability of occurrence of triggers due to thermal noise and correlated noise depends on their development history. Since the primary triggers of dark noise are generated by thermal noise, thermal noise has to be selected with a good purity from the data. As already mentioned above, the probability distribution of the time difference between thermal noise triggers is given by

$$p_{\text{th}}(\delta t) = f_{\text{th}}\, e^{-\delta t\, f_{\text{th}}} \quad . \tag{5.30}$$

Thus, the characteristic time constant is $\tau_{\text{th}} = f_{\text{th}}^{-1}$. A similar distribution applies for the fast and slow afterpulsing component. Thus in general the following applies

$$p(\delta t) = \frac{1}{\tau}\, e^{-\delta t/\tau} \quad . \tag{5.31}$$

If the time offset between a trigger and its predecessor is large enough, the probability is high that the trigger is a thermal noise trigger. Given the afterpulsing time constants $\tau_{\text{ap,f}}$ and $\tau_{\text{ap,s}}$ are smaller than the thermal noise time constant τ_{th}, a reasonable value for the required time

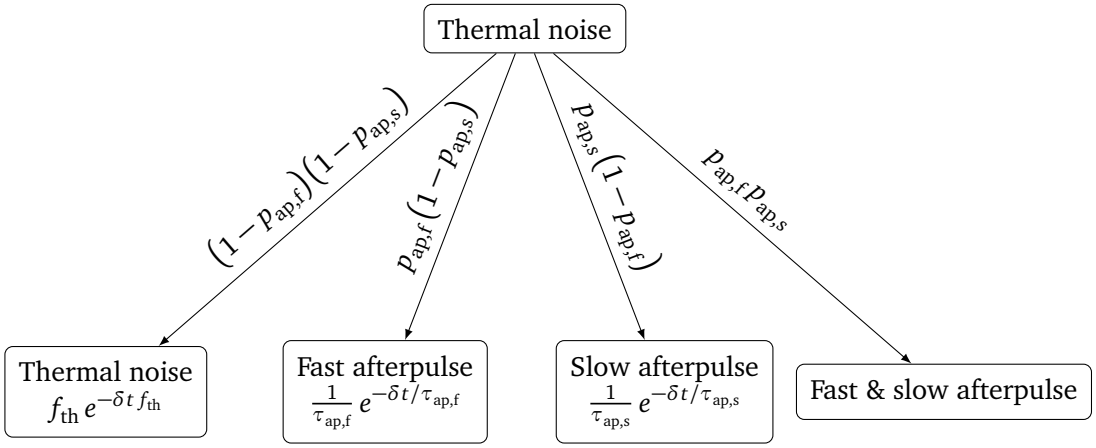

Figure 5.9: Decision tree of dark noise triggers after an initial thermal noise trigger without coincident optical crosstalk since it changes the probabilities of the subsequent triggers. The paths denote the probability of occurrence of a succeeding thermal noise trigger, fast afterpulsing, slow afterpulsing and, in higher order, fast and slow afterpulsing at the same time.

of noiselessness is $\approx \tau_{\mathrm{th}}$. Furthermore, the pulse height is required to be between 0.5 p.e. and 1.5 p.e. to discard crosstalk in the initial trigger which would deteriorate the analysis. From here, different scenarios can arise: the initial thermal noise trigger is succeeded after δt by a second thermal noise trigger, a fast afterpulse or a slow afterpulse while the other two are absent in the time frame δt. Figure 5.9 presents possible histories of thermal noise triggers and other subsequent triggers and their probabilities. The probability for a subsequent trigger occurring after a time δt or later is then given by the integral of equation (5.31)

$$P(\delta t) = \int_{\delta t}^{\infty} p(\delta t)\mathrm{d}t \tag{5.32}$$

$$= \int_{\delta t}^{\infty} \frac{1}{\tau}\, e^{-t/\tau}\mathrm{d}t = e^{-\delta t/\tau} \quad . \tag{5.33}$$

Now, in case of two possible outcomes i and j for a subsequent trigger, the probability distribution for outcome i to occur under the absence of j and vice versa is given by

$$P_{i,j}(\delta t) = p_i(\delta t) \int_{\delta t}^{\infty} p_j(\delta t)\mathrm{d}t + p_j(\delta t) \int_{\delta t}^{\infty} p_i(\delta t)\mathrm{d}t \tag{5.34}$$

$$= \left(\frac{1}{\tau_i} + \frac{1}{\tau_j}\right) e^{-\delta t/\tau_i} e^{-\delta t/\tau_j} \tag{5.35}$$

which can be extended to three cases i, j, k analogously

$$P_{i,j,k}(\delta t) = \left(\frac{1}{\tau_i} + \frac{1}{\tau_j} + \frac{1}{\tau_k}\right) e^{-\delta t/\tau_i} e^{-\delta t/\tau_j} e^{-\delta t/\tau_k} \quad . \tag{5.36}$$

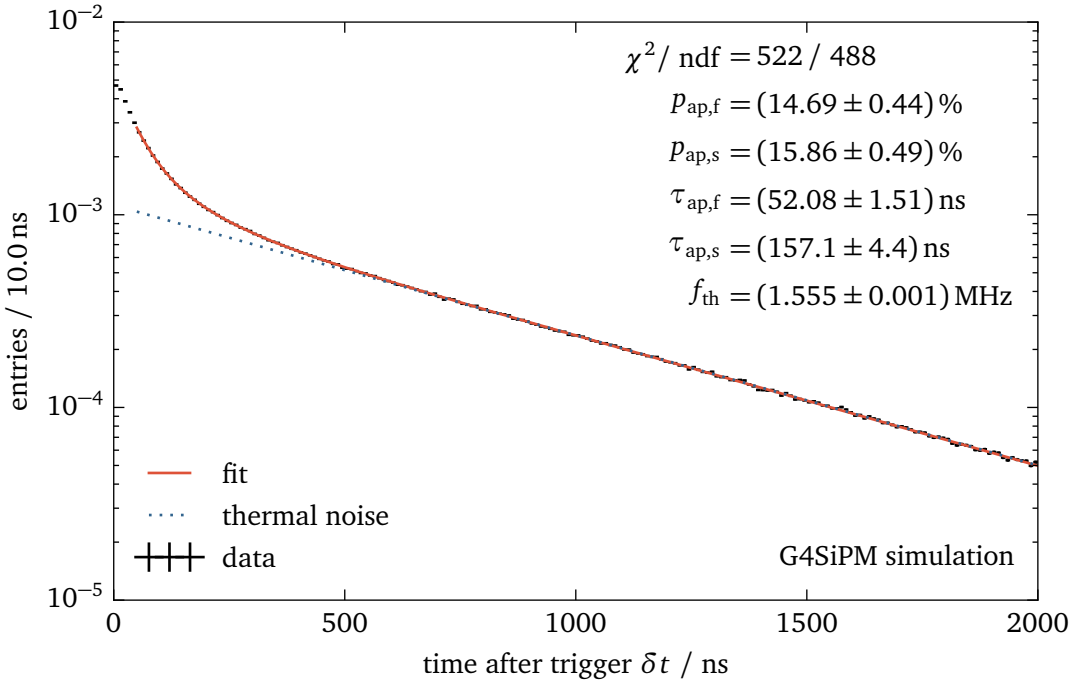

Figure 5.10: Analysis of dark noise simulated with G4SiPM by means of the time difference δt between a thermal noise trigger and the subsequent trigger. The simulated SiPM is a Hamamatsu S10362-33-050C at $v_{\mathrm{ov}} = 1\,\mathrm{V}$ and $T = 3.8\,^{\circ}\mathrm{C}$. The input parameters have been taken from [95]: $f_{\mathrm{th}} = (1.55 \pm 0.01)\,\mathrm{MHz}$, $p_{\mathrm{ap,f}} = (14.3 \pm 1.3)\,\%$, , $p_{\mathrm{ap,s}} = (16.3 \pm 1.5)\,\%$, $\tau_{\mathrm{ap,f}} = (52.4 \pm 3.2)\,\mathrm{ns}$ and $\tau_{\mathrm{ap,s}} = (166 \pm 10)\,\mathrm{ns}$. The line denotes a fit of equation (5.37) to the simulated data.

By plugging in the probabilities of the scenarios presented in figure 5.9, the following probability distribution for δt after a pure thermal noise trigger can be obtained

$$
\begin{aligned}
P_{\mathrm{dn}}(\delta t) = a\,&\left(1 - p_{\mathrm{ap,f}}\right)\left(1 - p_{\mathrm{ap,s}}\right) e^{-\delta t\, f_{\mathrm{th}}} \\
&+ p_{\mathrm{ap,f}}\left(1 - p_{\mathrm{ap,s}}\right)\left(\frac{1}{\tau_{\mathrm{ap,f}}} + f_{\mathrm{th}}\right) e^{-\delta t/\tau_{\mathrm{ap,f}}}\, e^{-\delta t\, f_{\mathrm{th}}} \\
&+ p_{\mathrm{ap,s}}\left(1 - p_{\mathrm{ap,f}}\right)\left(\frac{1}{\tau_{\mathrm{ap,s}}} + f_{\mathrm{th}}\right) e^{-\delta t/\tau_{\mathrm{ap,s}}}\, e^{-\delta t\, f_{\mathrm{th}}} \\
&+ p_{\mathrm{ap,s}}\, p_{\mathrm{ap,f}}\left(\frac{1}{\tau_{\mathrm{ap,s}}} + \frac{1}{\tau_{\mathrm{ap,f}}} + f_{\mathrm{th}}\right) e^{-\delta t/\tau_{\mathrm{ap,f}}}\, e^{-\delta t/\tau_{\mathrm{ap,s}}}\, e^{-\delta t\, f_{\mathrm{th}}}
\end{aligned}
\tag{5.37}
$$

with an artificial amplitude a. Although this probability distribution is correctly normalized to one, the artificial amplitude a can be used to account for the dead and recovery time of SiPMs and inefficiencies of peak finding algorithms for small $\delta t < 10\,\mathrm{ns}$.

A reconstructed δt distribution is presented in figure 5.10 for a Hamamatsu S10362-33-050C at $v_{\mathrm{ov}} = 1.01\,\mathrm{V}$ over-voltage and $T = 3.8\,^{\circ}\mathrm{C}$ ambient temperature. The fit has been obtained by first fitting only the thermal noise component ($p_{\mathrm{ap,f}} = p_{\mathrm{ap,s}} = 0$) in the regime $\delta t > 600\,\mathrm{ns}$, then secondly the slow afterpulsing component ($p_{\mathrm{ap,f}} = 0$) for $\delta t > 300\,\mathrm{ns}$ and feeding the

partial results as start parameters to the final fit of the full probability distribution as stated in equation (5.37). The input quantities could be successfully reconstructed within the margins of their uncertainties.

With upcoming new generations of SiPMs the dark noise is reduced dramatically (almost no afterpulsing, <10 % optical crosstalk, <50 kHz mm^{-2}, see e.g. [129]). This implicates that the measurement time has to be increased substantially for sufficient statistics.

5.4.2 Analysis procedure of optical crosstalk

Since optical crosstalk is quasi coincident to its seed trigger, the pulse height distribution in photon equivalents of the initial thermal noise triggers including crosstalk is measured. Analogously to the procedure described above, only pulses with a time of noiselessness of $\approx \tau_{\mathrm{th}}$ is required to minimize the effects of preceding correlated noise in the analysis. Here, no restriction regarding the pulse height of the initial triggers is made.

As discussed above, the number of first order optical crosstalk triggers k for a single cell trigger follows a binomial distribution (cf. equation (5.23)). Hence, the probability of a cascade of n crosstalk triggers can be obtained by applying the binomial distribution repeatedly [96]. For higher order generations of optical crosstalk triggers, an empirical approximation using a modified Erlang distribution has been found in [130] to describe the data best. The probability distribution for the number of crosstalk triggers n including higher orders is proportional to

$$P_{\mathrm{ct}}(n) \propto \frac{(q\,n)^{n-1}}{((n-1)!)^{\nu}} \tag{5.38}$$

with

$$q = p\,e^{-p} \tag{5.39}$$

containing the Poisson probability p and a shape parameter ν which increases the probability of higher multiplicities for $\nu > 1$ or decreases it for $\nu < 1$. Since fractional photon equivalents x can be measured, the pulse height distribution for each multiplicity n is Gaussian distributed due to excess noise σ_{pe} and electronics noise σ_{el} with mean $\mu_{\mathrm{pe}}(n)$ and variance $\sigma_{\mathrm{pe}}(n)$

$$\mu_{\mathrm{pe}}(n) = n\,g + \mu_0 \tag{5.40}$$

$$\sigma^2_{\mathrm{pe}}(n) = n\,\sigma^2_{\mathrm{pe}} + \sigma^2_{\mathrm{el}} \tag{5.41}$$

with the gain g and an arbitrary offset μ_0. The complete pulse height distribution function is then given by

$$P_{\mathrm{pe}}(x) = a\sigma_{\mathrm{pe}}(1)\sum_{n=1}^{\infty}\frac{P_{\mathrm{ct}}(n)}{\sigma_{\mathrm{pe}}(n)}\,e^{-\left(x-\mu_{\mathrm{pe}}(n)\right)^2/\sigma^2_{\mathrm{pe}}(n)} \tag{5.42}$$

with an arbitrary amplitude a to account for the proportionality factors of $P_{\mathrm{ct}}(n)$ [130]. In practice, the sum can be broken off early depending on the highest multiplicity measured in the data.

From a fit of the data to $P_{\mathrm{pe}}(x)$ the crosstalk probability p_{ct} can be calculated

$$p_{\mathrm{ct}} = \frac{1}{\kappa_{\mathrm{ct}}}\frac{\sum_{n=2}^{\infty}P_{\mathrm{ct}}(n)}{\sum_{n=1}^{\infty}P_{\mathrm{ct}}(n)} \tag{5.43}$$

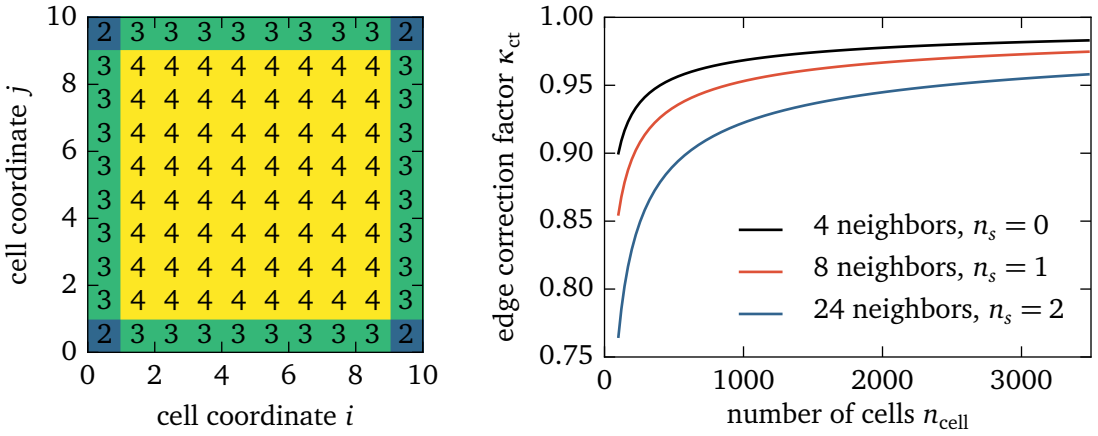

Figure 5.11: Left: schematic cell grid of a SiPM with denoted number of possible neighbors $n_{n,cell}$ for optical crosstalk based on four nearest neighbors. See also figure 5.8. Right: the edge correction factor κ_{ct} as a function of the number of cells n_{cell} on the SiPM for multiple number of shells.

which is the probability of at least one crosstalk trigger. The factor κ_{ct} accounts for the reduced number of possible neighbors for cells near the edge of the device by summing up the number of possible neighbors of each cell $n_{neig}(i)$ for the whole device

$$\kappa_{ct} = \sum_{i=1}^{n_{cell}} \frac{n_{neig}(i)}{n_{cell} n} \tag{5.44}$$

divided by the number of total neighbors neglecting border effects (cf. equation (5.25)). An example for this calculation is presented in figure 5.11.

Figure 5.12 presents a simulated pulse height spectrum, often referred to as finger spectrum, for a Hamamatsu S10362-33-050C at $v_{ov} = 1.01\,\mathrm{V}$ over-voltage and $T = 3.8\,^{\circ}\mathrm{C}$ ambient temperature. The fit successfully reproduces the input quantities.

Similar to afterpulsing, optical crosstalk is reduced in newer generations. The reduction has been achieved by introducing optical trenches between the cells at the expense of the geometrical fill factor. Thus, the PDE of these devices is significantly lower. Furthermore, the absence of optical crosstalk makes the calibration of the gain with dark noise more challenging due to a significant loss of statistics of in the multiple photon equivalent regime in the pulse height spectrum.

5.4.3 Summary of validation results

The δt and pulse height distributions have been simulated for a series of over-voltages v_{ov} for the Hamamatsu S10362-33-050C SiPM. The results are presented in figure 5.13 whereby the dots represent the analysis results and the dotted lines the expectation. In summary, the thermal noise and the crosstalk probability match the expectation with a relative difference of better than 2 %. The residual of the reconstructed afterpulsing probabilities to the input is better than 5 %. The afterpulsing time constants degrade systematically with increasing over-voltages down to a residual of 15 % whereby the fast time constant is reconstructed better than

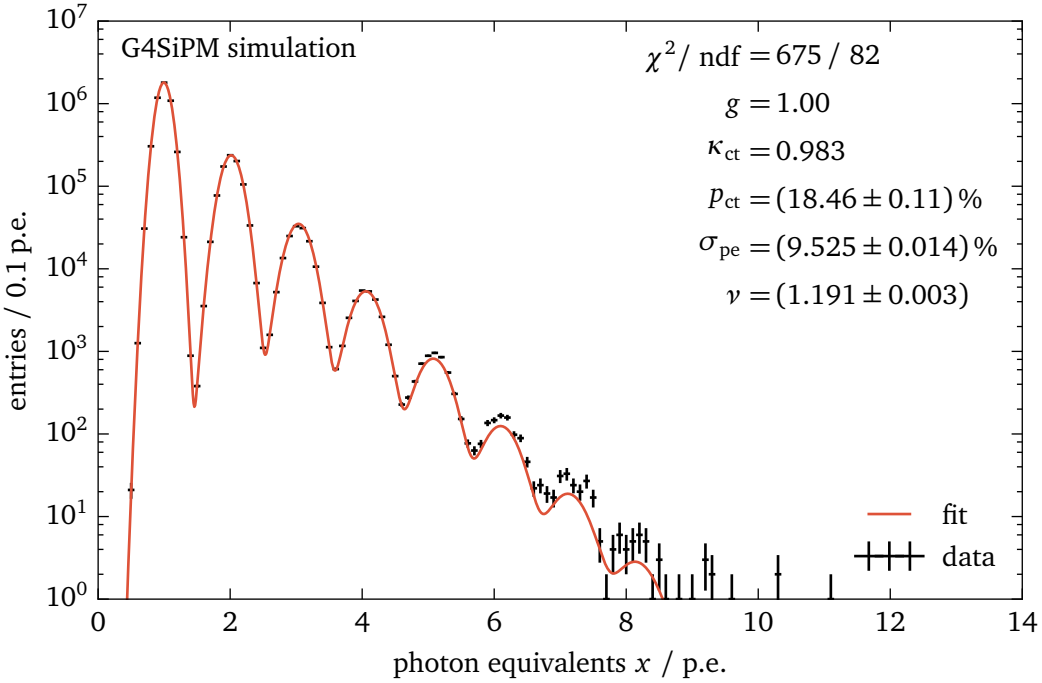

Figure 5.12: Analysis of dark noise simulated with G4SiPM by means of the pulse height in photon equivalents of a thermal noise trigger. The simulated SiPM is a Hamamatsu S10362-33-050C at $v_{ov} = 1\,\mathrm{V}$ and $T = 3.8\,^{\circ}\mathrm{C}$. The input parameter has been taken from [95]: $p_{ct} = (18.2 \pm 0.1)\,\%$. The expectation for the gain is $g = 1$ and for the excess noise $\sigma_{pe} = 10\,\%$ with $\sigma_{el} = \mu_0 = 0$. The line denotes a fit of equation (5.42) to the simulated data.

the slow time constant. Possible reasons are the lack of robustness of the fit, since it has six free parameters, and the correlation between the long afterpulsing time constant $\tau_{ap,s}$ and the thermal noise constant τ_{th}; a smaller value of $\tau_{ap,s}$ can be easily compensated by a slightly smaller value of τ_{th}. Although the influence of the time constants on the χ^2 has been found to be very low, the global minimum χ^2 is systematically offset to smaller time constants.

5.4.4 Dynamic range

To demonstrate the ability of the G4SiPM package to predict the response of the SiPM for a wide incoming photon flux range and for different photon arrival time distributions, simulation results of the dynamic range have been compared to a dedicated measurement of the same model (cf. figure 4.10 in section 4.6). Details on the measurement can be found in [99]. The properties of the used Hamamatsu-S10362-33-050C for G4SiPM have been taken from [10, 82, 95, 116]. The light source was an LED with $\lambda = 485\,\mathrm{nm}$ driven by a custom-made pulser developed in the electronics workshop of the III. Physikalisches Institut A, RWTH Aachen University by F. P. Zantis. Primarily, the irradiation of the LED has been characterized using a calibrated PIN diode from Hamamatsu. Secondly, the pulsed LED is used to illuminate the SiPMs with light pulses of varying intensity and length. The SiPM is operated in a cooling box for temperature controlled measurements. The readout electronics consists of a readout circuit proposed

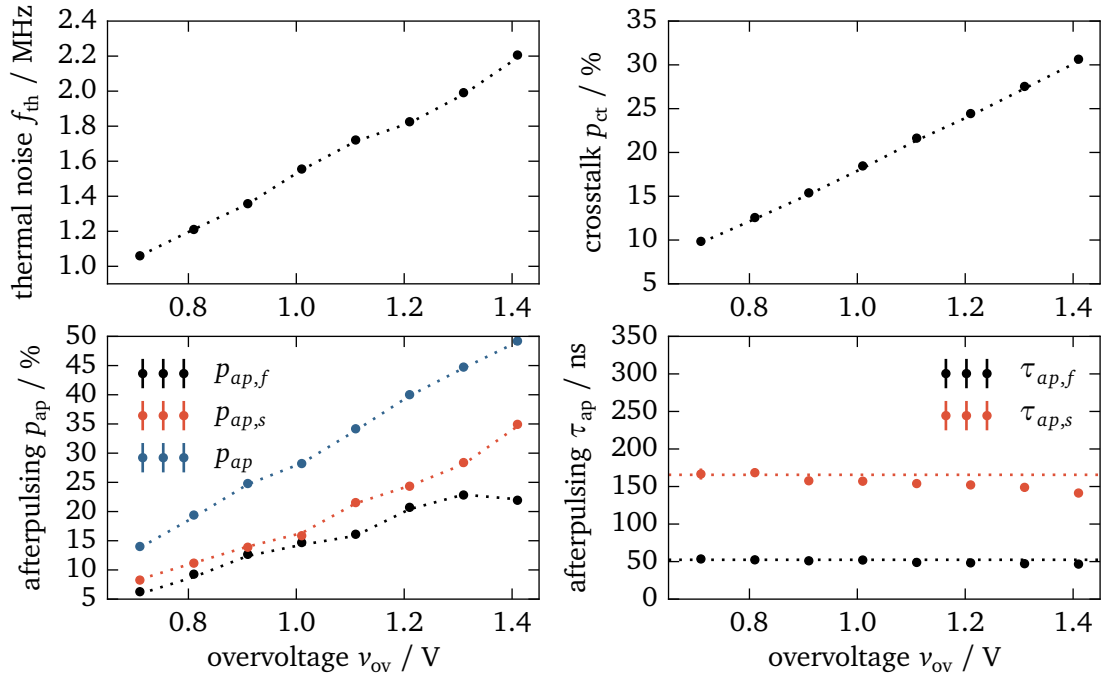

Figure 5.13: Reconstructed SiPM parameters as a function of over-voltage. The input parameters have been taken from [95] (Hamamatsu S10362-33-050C at $T = 3.8\,°C$, cf. figure 4.9 in section 4.5). The dotted lines denote the input values. In case of the thermal noise and the optical crosstalk probability, the residual between the reconstructed and the input parameters is better than 2 %, in case of the afterpulsing probabilities better than 5 %. The reconstructed afterpulsing time constants decrease systematically with over-voltage down to a residual of −15 %.

by the manufacturer Hamamatsu and a charge-to-digital converter. Finally, the number of effectively triggered SiPM cells within a certain integration window was measured as a function of the number of photons per pulse. As presented in figure 5.14, G4SiPM can successfully reproduce the dynamic range measurement of a Hamamatsu device for a certain LED pulse width and over-voltage within 5 %. The systematic offset is attributed to the uncertainties in the calculation of the emitted number of photons as a function of the LED voltage applied by the custom-made pulser. Since the PIN diode current is only a measure for the mean number of photons, the exact shape of the LED light pulse can only be approximated by measuring the voltage pulse fed into the LED.

Given the SiPM parameters as obtained in the laboratory or from the datasheets, G4SiPM can be used to simulate SiPMs over large range of over-voltages, temperatures and light intensities. The phenomenological model of G4SiPM has been verified by analyzing the simulated data in the same manner as the corresponding measurements in the laboratory. Furthermore, the model has been successfully exploited over the entire dynamic range of one specific SiPM model. With the exception of the afterpulsing time constants, which tend to be reconstructed systematically too small, all SiPM parameters could be reproduced at a 5 % level or better with small systematic offsets. Thus, G4SiPM is the ideal toolkit to test the feasibility of SiPMs when developing new detectors and optimizing their design with Geant4 Monte Carlo simulations.

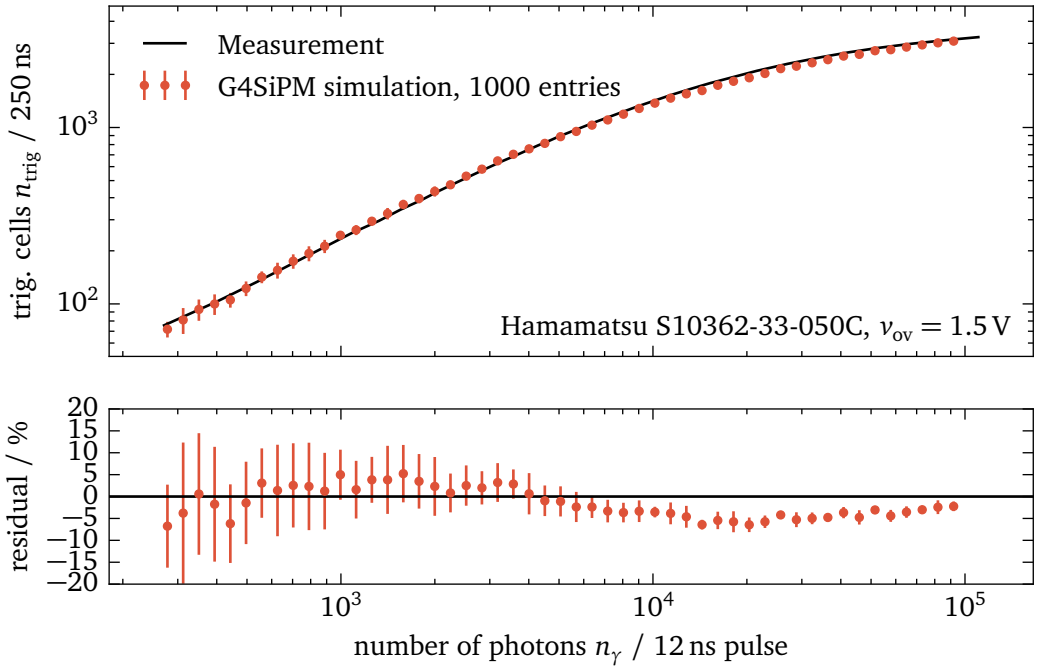

Figure 5.14: Simulated dynamic range of a Hamamatsu S10362-33-050C SiPM at $v_{ov} = 1.5\,V$ and $T \approx 0\,°C$. The measurement (line) of the dynamic range and the reference input parameter have been taken from [99]. Besides some fluctuations due to statistics, the residual between the measurement and simulation is below 5 %. The largest uncertainty is given by the shape of the LED light pulse as a function of time since it can not be resoled by the measurement of the average PIN diode current.

Ultimately, G4SiPM can help to make crucial decisions regarding the required PDE, number of cells and sensor size of the SiPMs.

5.5 Applications

The G4SiPM package already has been used in other simulation studies [131, 132, 133] and is also included in the GODDeSS software package (Geant4 Objects for Detailed Detectors with Scintillators and SiPMs) [134, 135]. Very recently, efforts are being made to use the G4SiPM package in the software framework Offline of the Pierre Auger Collaboration [136].

In the following, the usage of the G4SiPM package for the simulation of a muon detector with scintillating tiles is presented.

5.5.1 Simulation of a scintillating tile with silicon photomultiplier readout

The AMD (Aachen Muon Detector) has been developed in the context of the upgrade of the Pierre Auger Observatory [137]. Scintillating tiles of 30 cm × 30 cm × 0.5 cm in size are placed into a steel housing of 3.64 m × 3.64 m total area which is built to carry one water Cherenkov tank. Since the inner of the housing has struts made from steel I-beams necessary for the

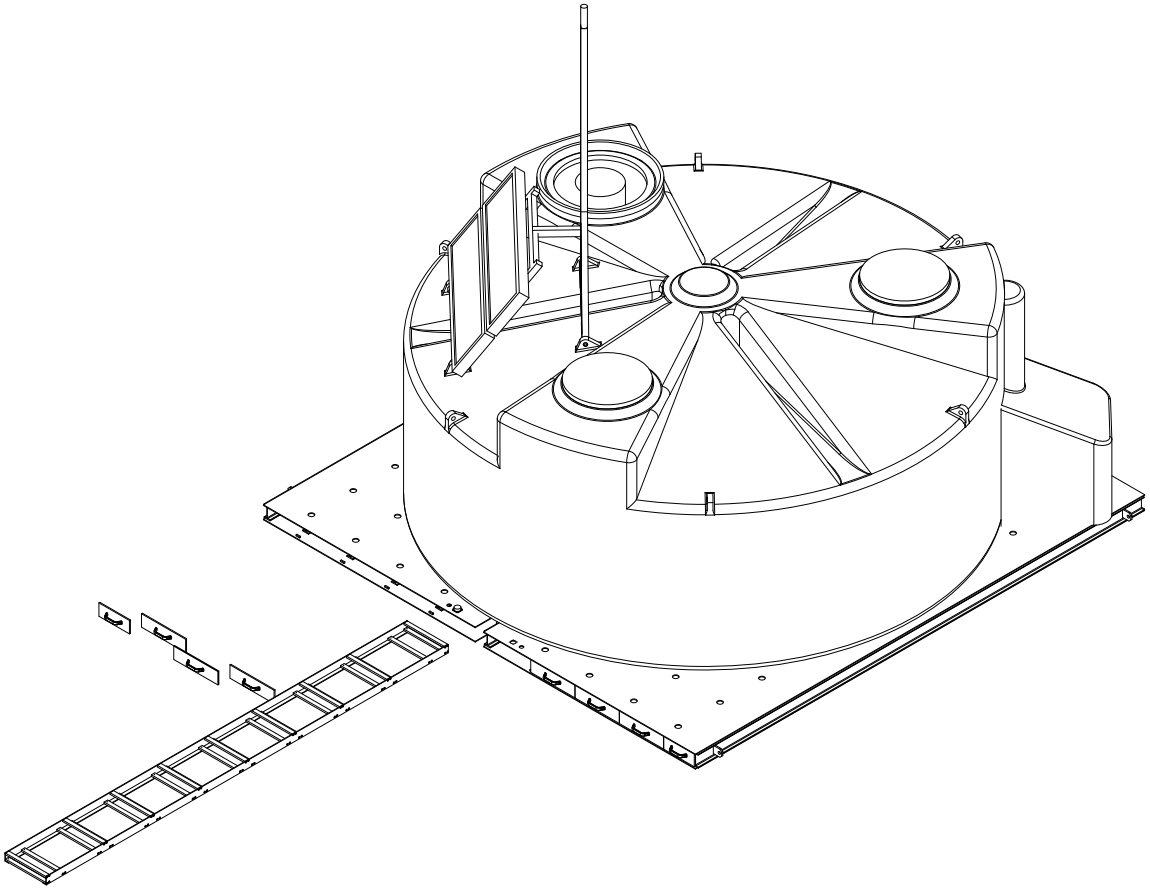

Figure 5.15: Schematic view of the AMD detector and, placed on top of it, a water Cherenkov tank of the surface detector of the Pierre Auger Observatory. The mechanics are made of large sheets of steel and steel I-beams for support. Between the inner I-beams is enough space to slide in eight trays which take eight scintillator tiles each. The space between the two uttermost I-beams is left empty. The tiles are not shown here. In total, one AMD stations has 64 scintillator tiles with wavelength shifting fibers and SiPM readout. The side faces of the detector are then closed off by steel covers which seal the interior from ambient light, water and dust. Technical drawings courtesy of B. Philipps (RWTH Aachen University).

support, eight tiles make up one tray, eight trays one complete station. Therefore, each station is equipped with 64 tiles in total with a total instrumented area of 44 %. For practicality reasons, the housing is split into two parts. A wavelength shifting fiber of 1 mm diameter (Saint-Gobain BCF-92 [138]) with a mirrored end is embedded in a loop shape into each scintillator tile. When it exits the tile, a special connector splices the wavelength shifting fiber to a clear waveguide of the same refractive index (Saint-Gobain BCF-98 [138]). The eight clear waveguides of each tray are routed to one side of the steel housing where each is optically connected to each one 1 mm × 1 mm SiPM, a Hamamatsu S12651-050P with $p_{ct} = 5\,\%$ crosstalk and $p_{ap}<1\,\%$ afterpulsing [9]. A schematic of the mechanics with an illustration of a water Cherenkov tank can be found in figure 5.15.

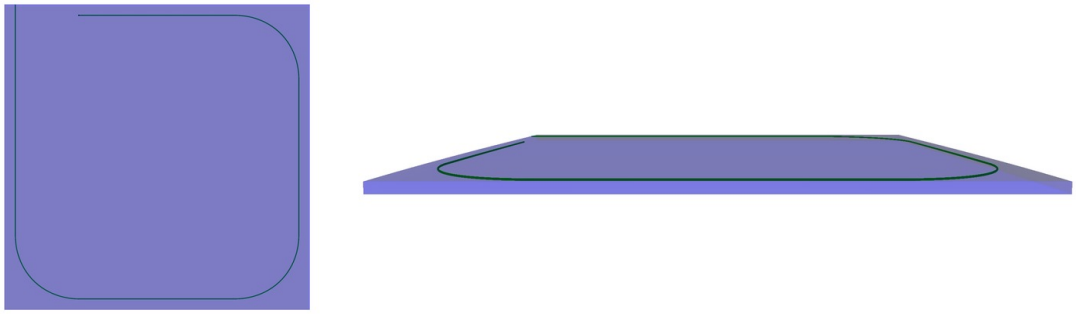

Figure 5.16: Screenshots of the Geant4 simulation of the scintillating tiles of the AMD. Left: front view showing the sigma shaped fiber. Right: view from the side. As shown here, the fiber is installed close to the surface of the tile rather than in the middle. This has the advantage that the trenches for the fiber can be milled into the scintillator tile and the fiber can be glued easily. Furthermore, it has been found that the collection efficiency of the fiber is largest when placed near the surface.

5.5.1.1 Readout electronics

Due to the tiled design, the detector has a good spatial resolution which is important for the exact determination of the material overburden of the water Cherenkov tank traversed by a muon. Also, the number of particles passing each tile can be reconstructed measuring the signal height of the SiPMs. The SiPMs are read out with two EASIROC ASICs which 32 channels each [139]. It has a fast and a slow shaping signal lane for each channel. The fast shaper is used for the threshold trigger. In case of a successful trigger, the slow shaper is used to integrate the signal over a long period of time which is in the order of the expected event length. Due to the specific signal height of one photon equivalent, the number of photons and therefore the number of particles can be reconstructed.

5.5.1.2 Results of the AMD detector simulation

The task of the simulation is now to determine the number of photons to be expected from muons and other charged particles which reach the ground. For this, a dedicated Geant4 simulation on the basis of G4SiPM has been developed and is currently in the stage of the transition to the GODDeSS package for the detector construction. A sample of 100 000 muons with kinetic energies of $E_{\text{kin}} = 10^{-1.5}$ MeV to $E_{\text{kin}} = 10^{5.75}$ MeV, distributed logarithmically, and incidence angles of $\vartheta = 0°$ to $\vartheta = 90°$ have been simulated isotropically over the whole surface of the AMD without the overburden of the water Cherenkov tank. For each simulation, the number of detected photons is available for each SiPM as a number of photon equivalents. To safe computing time, the correlated noise simulation of the 64 SiPMs has not been performed since the effects of the low optical crosstalk of $p_{ct} = 5\,\%$ and quasi non-existing afterpulsing of $p_{ap} < 1\,\%$ are negligible for this basic analysis. The number of photon equivalents for muons which actually hit scintillator tiles is compared to possible threshold values $n_{\gamma,\text{thresh}}$. A setting of $n_{\gamma,\text{thresh}} = 7.5$ p.e. yields a detection efficiency of $> 90\,\% \cdot 44\,\% \approx 40\,\%$ for minimal ionizing particles for the complete detector (the total instrumented area is 44 %) and is expected to almost completely reject the dark noise of the SiPMs (cf. figure 5.17). The efficiency of de-

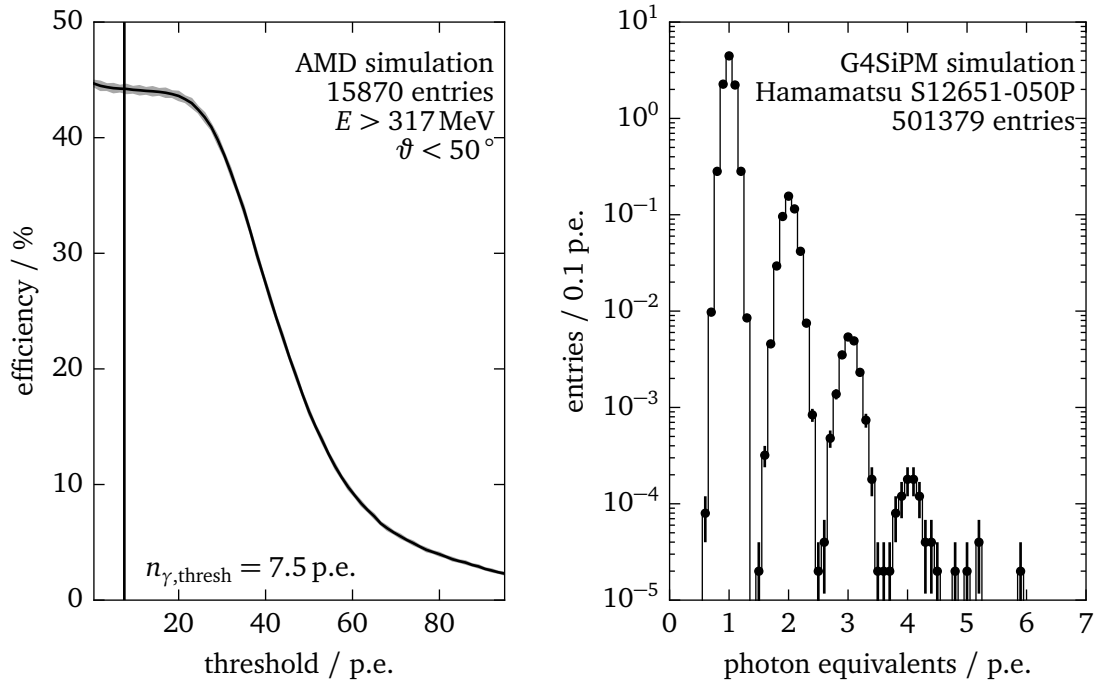

Figure 5.17: Left: simulated trigger efficiency of a simple threshold trigger as a function of the threshold in number of coincident photons for muons with $E > 3\,m_\mu = 317\,\mathrm{MeV}$ (minimum ionizing particles) and $\theta < 50°$. The detector has a very high trigger efficiency up to the point at which the MIP signal distribution falls off. The vertical line denotes the trigger threshold which has been chosen and is sufficient to cut off $> 99.9\,\%$ of the dark noise of the SiPMs. For inclined muon incidence, tracks through the lateral faces of the tile can fulfill the trigger criterion. Right: simulated dark noise of the Hamamatsu S12651-050P 1 mm × 1 mm SiPM. Due to the fact that this device has very low correlated noise, the dark count spectrum falls very steeply.

tection as a function of the particle incidence position and as a function of the kinetic energy and incidence angle can be found in figure 5.18. It is expected, that the number of photon equivalents x follows a Landau distribution [22]

$$p(x) = \frac{1}{\pi}\int_0^\infty e^{-t\log t - xt}\sin(\pi t)\,dt \approx \frac{1}{\sqrt{2\pi}}\exp\left\{-\frac{1}{2}(x+e^{-x})\right\}. \tag{5.45}$$

since the energy deposit of the muons also follows a Landau distribution due to the fact that the scintillator tiles are too thin to stop the particles. Furthermore, the Landau distribution is folded with a Gaussian distribution due to the production and transportation processes of the photons and the photon detection of the SiPMs. This has very important implications for the analysis of the simulations and later of the data of the detector because the moments of the Landau distribution (mean, variance, etc.) are not defined [140, 141]. As auxiliary quantities, the most probable value μ_{mpv}, i.e. the maximum of the distribution, and a scale parameter σ

$$x \to \frac{x - \mu_{\mathrm{mpv}}}{\sigma} \tag{5.46}$$

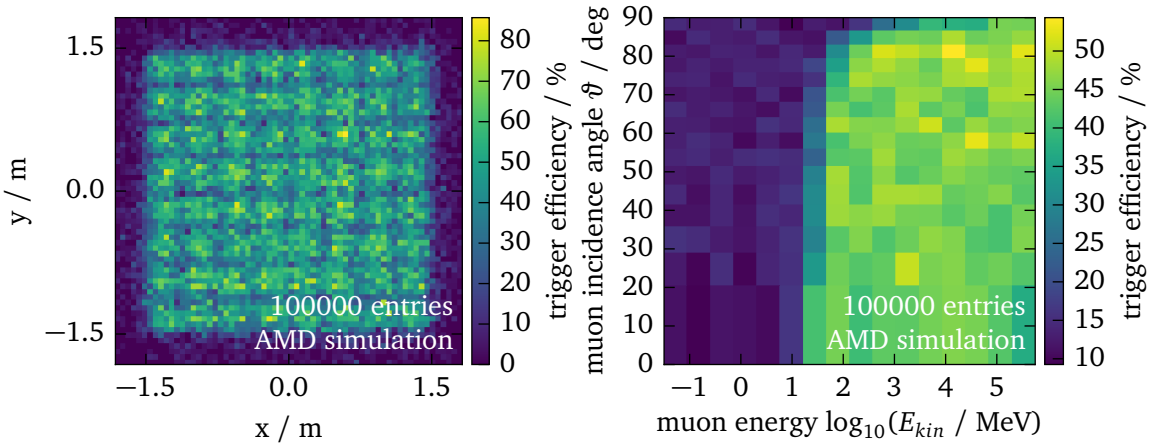

Figure 5.18: Left: simulated trigger efficiency of the AMD detector as a function of the point of incidence of a muon. For these simulations, muons with a kinetic energy of $E_{\text{kin}} = 10^{-1.5}$ MeV to $E_{\text{kin}} = 10^{5.75}$ MeV and incidence angles of $\vartheta = 0°$ to $\vartheta = 90°$ have been simulated. The trigger threshold has been set to $n_{\gamma,\text{thresh}} = 7.5$ p.e.. Right: simulated trigger efficiency as a function of the kinetic energy E_{kin} and the angle of incidence ϑ of the particles.

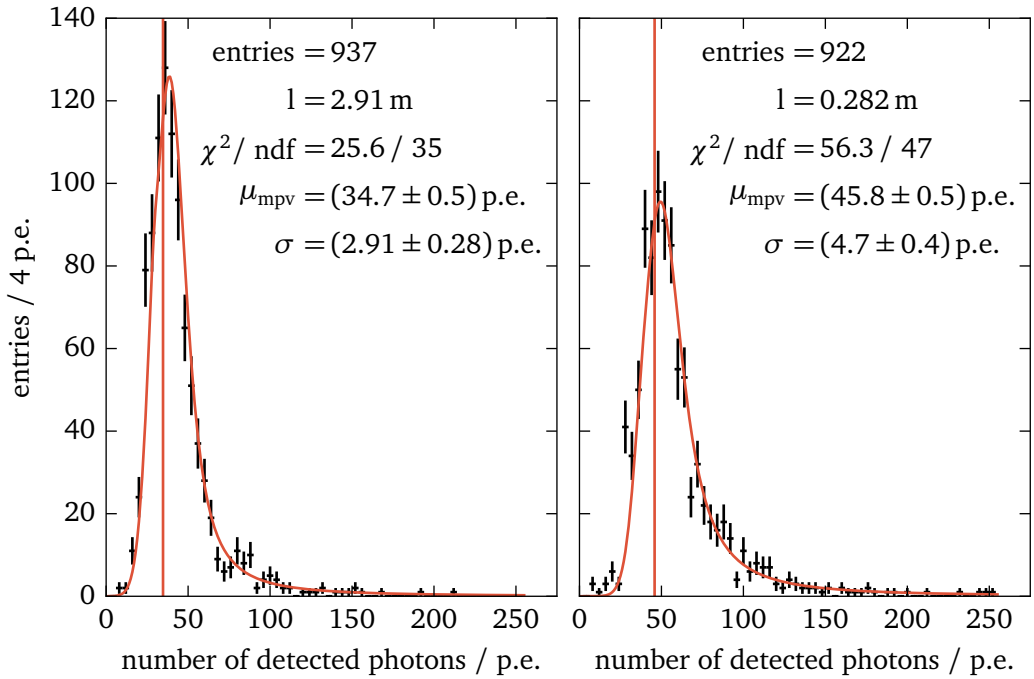

Figure 5.19: The number of photons detected by the SiPM for the shortest and longest clear waveguide length l. The distributions can be approximated by the convolution of a Landau and a Gaussian distribution since the energy deposit follows a Landau distribution. Processes, such as photon production, the photon transportation and the photon detection efficiency of the SiPMs are Gaussian distributed. The fitted distribution is denoted as (red) curve, the reconstructed MPV μ_{mpv} as vertical line.

are introduced. The distributions of the measured photons for muons with $E_{\text{kin}} > 3\,m_\mu$ and $\theta < 50°$ is presented in figure 5.19.

As discussed above, the detector simulations yield very promising results. In combination with the overburden of the water Cherenkov tank used as shielding against electrons, the AMD would effectively measure the muon content of extensive air showers. First studies with simulated showers are presented in [132]. Furthermore, a dissertation on this topic is to be released in the near future [142].

CHAPTER 6

Baseline design and commissioning of FAMOUS

FAMOUS is a refracting telescope. Many mirror telescope designs, that offer a wide field of $> 10°$ opening angle, require the focal plane to be placed in the path of light leading to an obstruction which in turn significantly reduces the total aperture area of the telescope [143]. Since FAMOUS is a prototype platform for the test of SiPMs in fluorescence telescopes and requires a lot of new developments regarding the electronics and the mechanics, the dimensional constraints can be lifted significantly if the focal plane is kept outside the light path. With the commercial availability of large, thin plastic lenses made from UV transparent Acrylic, a simple refracting optical system instead of a multi-mirror approach has been chosen [144].

The most important part of the optical system of FAMOUS is the Fresnel lens which refracts the incoming light onto a focal plane composed of 61 circular pixels arranged in a hexagonal layout. Each pixel is a special light funnel, a so-called Winston cone, which concentrates the light onto the SiPM, and has a circular field of view of $\approx 1.5°$ of the sky resulting in a total field of view of $\approx 12°$ opening angle. Optionally, an ultraviolet light pass filter can be placed between the Winston cone and the SiPM to reduce light from the night sky brightness. The whole system is enclosed by a telescope tube mounted on an altitude-azimuth mount, i.e. a two-axis mount allowing the rotation about the horizontal axis and the angle of elevation of the pointing direction [143]. Mechanical drawings of the telescope are presented in figure 6.1.

In the following, the optical elements and sensors which build up the telescope will be discussed in detail including first characterization measurements.

6.1 Fresnel lens

The concept of Fresnel lenses has already been proposed in 1748 by G. de Buffon [147] and later built by the French physicist J. Fresnel for light houses along the French coast [148]. To minimize weight and light loss due to bulk absorption, a Fresnel lens is divided into concentric, annular sections, so-called grooves, while the bulk material of each section is reduced to the minimum possible. To further simplify the construction, the light-facing shape of the grooves is planar instead of curved. Thus, the original lens surface is only resembled closely for a large number of grooves. A schematic of the construction principle is provided in figure 6.2.

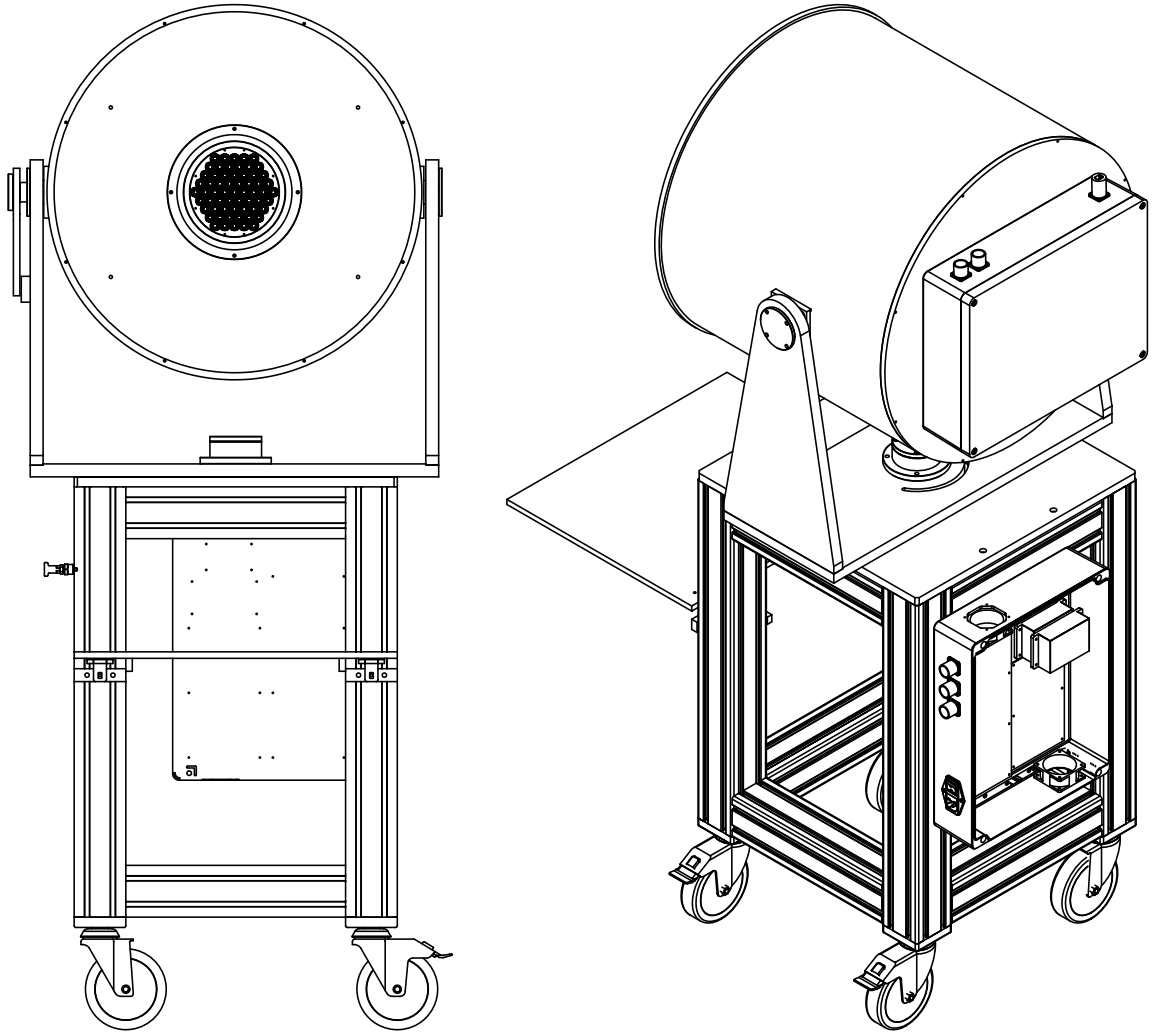

Figure 6.1: Mechanical design of the fluorescence telescope FAMOUS. The main element is a large aluminum tube with 570 mm diameter. The focal plane is held by a special inset which can be exchanged easily for a better focus. The Winston cones are glued into a common base plate. On the back side, the whole focal plane is enclosed by an aluminum box. A part of the power supply of the telescope is situated in the lower compartment to reduce the weight and dimensions of the box behind the tube. Thus the construction does not interfere with the altitude-azimuth mount. Technical drawings courtesy of B. Philipps (RWTH Aachen University).

The Fresnel lens of FAMOUS is a commercial Fresnel lens from ORAFOL Fresnel Optics GmbH [13], the SC-943 model, with an aperture of $d = 502.1\,\text{mm}$ diameter and a nominal focal length of $f = 502.1\,\text{mm}$ at $\lambda = (546 \pm 27)\,\text{nm}$. Thus, the lens has an f-number of

$$n_f = \frac{f}{d} = 1 \tag{6.1}$$

crucial for a wide field of view and closely meets the design goal of $f = 510\,\text{mm}$ [149]. Furthermore, 10 grooves per millimeter are situated on the 2.5 mm thin lens. The large number

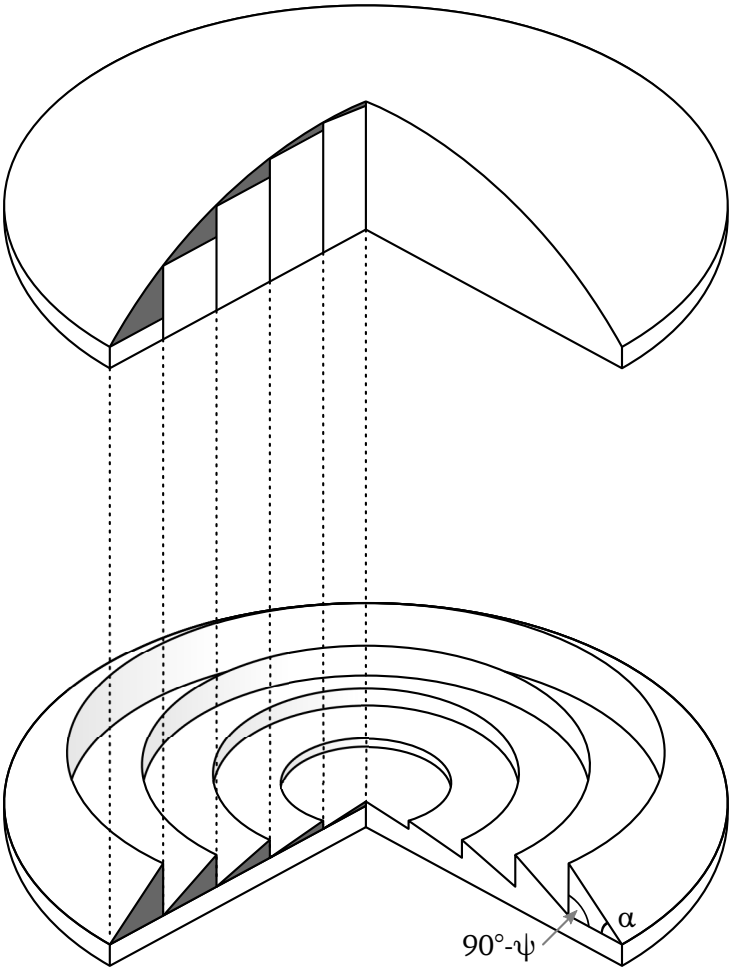

Figure 6.2: The basic construction principle of a Fresnel lens. The surface of the lens is divided into concentric sections (grooves) of equal width. For each section, the bulk material is removed which leads to an overall reduced thickness and weight of the lens. The effect on the image quality due to the cutting of bulk material is small since it is of minor importance to the optics of the lens. Nevertheless, light might be refracted into the wrong direction at the perpendicular faces of the grooves. This can be partly compensated by bending each groove individually either by adjusting the slope angle α or the draft angle ψ which otherwise is always $\psi = 90°$. Adapted from [145].

of grooves is beneficial to the imaging quality. The surface of the lens follows the shape of a parabolic lens to compensate spherical aberration [144]. The lens is made from UV transparent Acrylic which is important for the detection of fluorescence light [144]. A plot of the internal transmittance of the material can be found in figure 6.3. A conventional plano-convex lens of the same diameter and f-number would have a thickness of roughly 250 mm and therefore would be too heavy to be manageable.

A major disadvantage of Fresnel lenses is the deteriorated image quality due to the fragmentation into planar grooves and false refractions. This can be partly overcome by adjusting the angles of the front facing and perpendicular planes of each groove separately. A detailed ray-

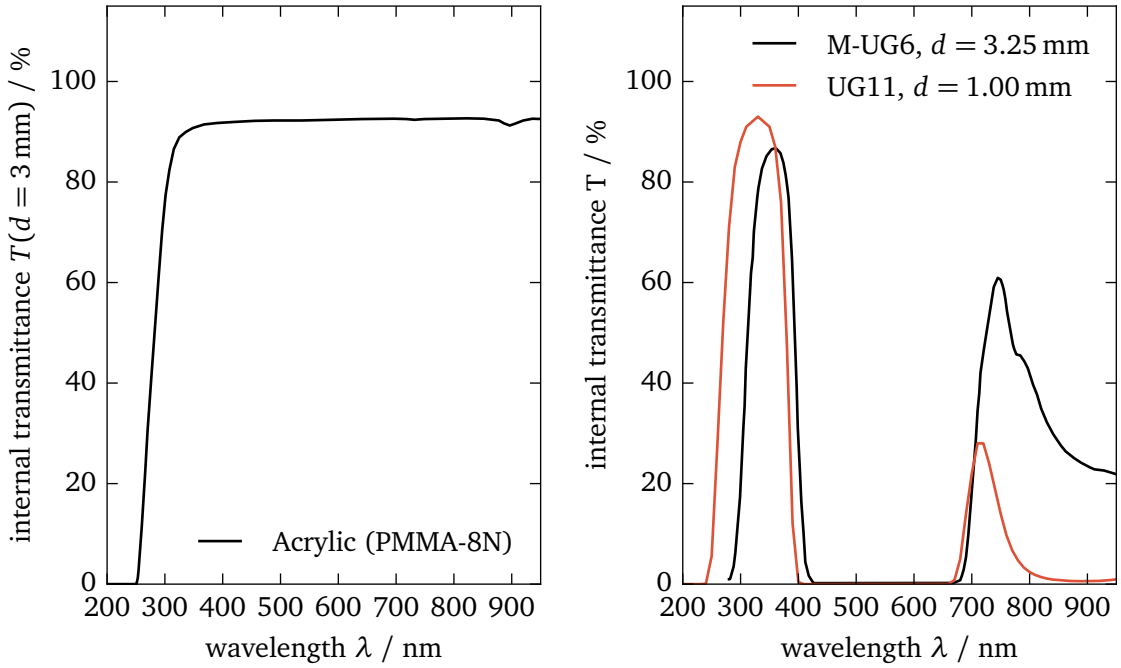

Figure 6.3: Left: internal transmittance of the Acrylic PMMA-8N [144] used for the Fresnel lens of FAMOUS measured for a thickness of 3 mm. The material becomes transparent for wavelengths $\lambda > 300\,\mathrm{mm}$ which is ideal for the measurement of fluorescence light. Right: transmittance of UG11 [146] and the predecessor M-UG6 as used in the fluorescence telescopes of the Pierre Auger Observatory [6]. The UG11 has a maximum transmittance of 93 % at $\lambda = 330\,\mathrm{nm}$ compared to M-UG6 with 87 % at $\lambda = 361\,\mathrm{nm}$ since it is with 1 mm versus 3.25 mm much thinner.

tracing study on this topic has been performed in [150]. For the Fresnel lens of FAMOUS, the so-called draft angle, i.e. the tilt angle of the perpendicular face of the grooves (cf. figure 6.2), is given by

$$\psi(\rho) = 3^\circ + 0.0473^\circ\,\mathrm{mm}^{-1}\,\rho \tag{6.2}$$

as a function of the radial distance ρ from the optical axis whereby the lower limit $\psi_0 = 3^\circ$ is given by the manufacturing process [144, 150].

The image of an infinitely distant point source yields the so-called point spread function whose size can be measured by the aberration radius r_{90} and has to be small enough for the application in FAMOUS. A measurement of the aberration radius r_{90} is described in the following.

6.1.1 Measurement of the point spread function

Besides the simplification which is performed when constructing a Fresnel lens, the loss in image quality must be acceptable. For FAMOUS, the limiting factor is the size of the Winston cones with an entrance radius of $r_1 = 6.71\,\mathrm{mm}$. Due to the fact, that the faint fluorescence light of the extensive showers will behave like a moving point source, the imaging quality of a point source object is investigated by the evaluation of the produced point spread function (PSF),

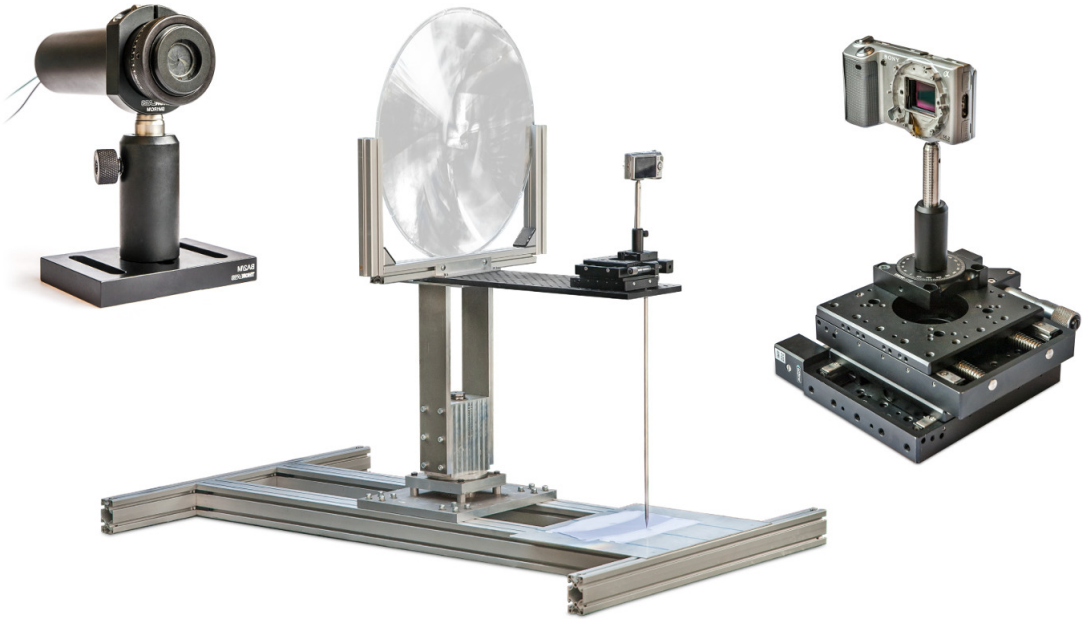

Figure 6.4: Photographs of the main parts of the setup for the measurement of the PSF of the Fresnel lens. Adapted from [150]. Left: the green LED used for the measurements in placed inside a light-tight tube behind a pinhole adjustable iris. Middle: the Fresnel lens is fixed in a frame and mounted onto a rotary table. The camera is situated behind the lens on its optical axis on the same rotary table. Right: the position of the camera can be finely tuned by means of translational stages.

i.e. the distribution of the light on the image plane. A measurement of the size of the PSF is achieved by means of the aberration radius r_{90} which encircles 90 % of the energy contained in the PSF. The measurements have been taken in the scope of the thesis in [150] and will be re-evaluated due to an improved compatibility of the used libraries.

6.1.1.1 Measurement setup

The PSF of the lens has been measured using a commercial camera from Sony, the NEX-5 [151]. It is a system camera with a large CMOS sensor with 4592 × 3056 pixels in the APS-C format with a dimension of 22.8 mm × 14.8 mm. The term system camera means that the lens of the camera is interchangeable. For this measurement, no lens is needed and it is made advantage of the very small obstruction due to the enclosure of the camera.

As light source, a green LED with $\lambda = 550\,\text{nm}$ behind a pinhole aperture in $\approx 20\,\text{m}$ distance to the lens has been used [150]. The whole setup has been placed in a windowless dark service corridor. The camera was mounted behind the lens on translational stages for micrometer adjustments of the lens to camera distance and the shift with respect to the optical axis for measurements with inclined light incidence. The measurements with inclined light incidence have been performed by mounting the lens camera compound on a rotary table. Measurements for incidence angles $\theta_{\text{in}} = 0°$, 2°, 4°, 6°, 8°, 10° and 12° with up to 100 individual photographs have been performed. An overview over the measurement setup is given in figure 6.4.

The photographs are recorded in the proprietary raw format ARW of the manufacturer to have maximum precision. With the newest version of the open source library LibRaw version

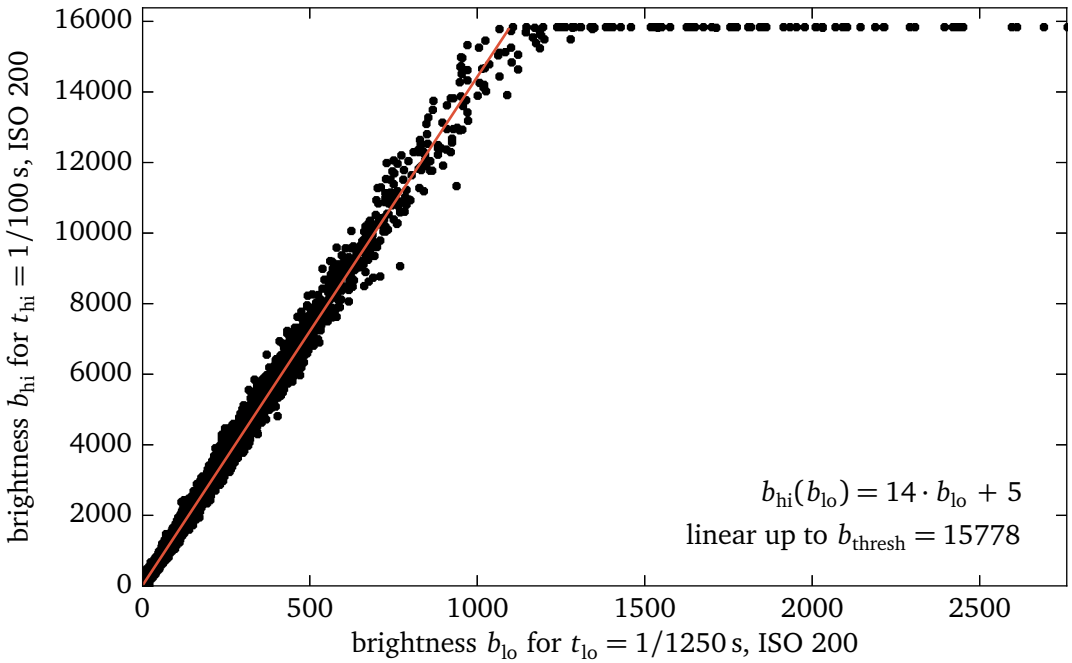

Figure 6.5: Brightness values of the pixels of image b_{hi} versus the brightness value of image b_{lo} of the same image pixel. The factor of exposure of the two images is $t_{hi}/t_{lo} = 12.5$. The linear fit has been used to determine the maximum usable brightness of $\approx 15\,000$.

0.17, 14 bit read out of raw files is supported (previous version only 8 bit) whereby only the information of the green pixels is processed further since the LED emits green light [152]. The read out brightness is given in units of ADC counts in a range of 0 to 2^{14}. To eliminate the originally red and blue pixels containing no information, the size of the image is reduced by a factor of four so that sixteen adjacent pixels are combined to one. In that way no interpolation of the Bayer pattern is necessary, i.e. the sensor color filter array used to produce color images. The black point, i.e. the ADC count of the darkest pixel, is subtracted automatically on import. Additionally, a dark frame has been recorded right before the measurement with the LED turned off. This dark frame is also subtracted from the image prior further processing.

6.1.1.2 Image stacking

Since the dynamic range of the camera is not large enough to record the PSF with a good resolution of both the peak and the tails, all images have been recorded twice at ISO 200, the first with an integration time of $t_{hi} = 1/100\,s$, the second with $t_{lo} = 1/1250\,s$. Thus, the second image is a factor of

$$f = \frac{t_{hi}}{t_{lo}} = 12.5 \tag{6.3}$$

darker than the first. Exemplary in figure 6.5, the brightness values $b_{i,hi}$ of all pixels of the brighter image are plotted against the corresponding brightness $b_{i,lo}$ of the same pixel in the dark image. At a certain point, the values of the brighter image saturate whereby the values of

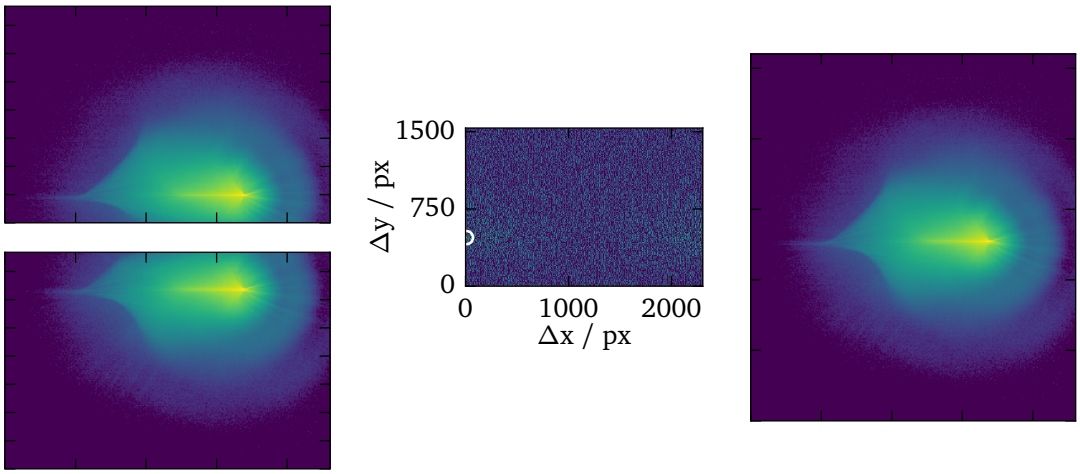

Figure 6.6: Left: the upper and the lower photograph of the PSF for a light incidence of $\theta_{\text{in}} = 6°$. The peak of the PSF should be visible in both images. All color scales are scaled logarithmically for better readability. Middle: The computed normalized cross-correlation. The relative shift between the two images is marked by the global maximum of the cross-correlation. Due to the structure of the images, many high cross-correlation values can be found, but the maximum is reliably at the correct position (marked by a white circle in the lower left corner). Right: The stitched image of the two images using the point of maximum cross-correlation. In the overlap region, the mean between the two images ensures a smooth transition.

the darker image are still rising. This breakpoint can be identified with a linear fit at $b_{\text{thresh}} = 15\,000$. Thus, a so-called high dynamic range (HDR) image can be obtained by setting the brightness to

$$b_i = \begin{cases} b_{\text{i,hi}} & b_{\text{i,hi}} < b_{\text{thresh}} = 15\,000 \\ b_{\text{i,lo}} \frac{t_{\text{hi}}}{t_{\text{lo}}} & \text{otherwise} \end{cases} \tag{6.4}$$

with a total dynamic range of roughly 17.5 bit.

6.1.1.3 Background noise subtraction

A small patch either in the upper left or lower left corner of 500×400 pixels is considered signal free. To the background noise contribute residual ambient brightness, stray light of the LED light of walls and mechanical structures and any residual intrinsic noise of the image sensor which could not be removed neither by black point nor the dark frame subtraction. Thus, the mean background b_{noise} is given by the mean brightness of the 500×400 pixel patch and subtracted from all brightness values b_i. Values $b_i < 0$ are kept to ensure an overall mean background of zero. Furthermore, the standard deviation of the brightness values $\sigma_{b,\text{noise}}$ is calculated and stored for the uncertainty calculation. A typical value is $b_{\text{noise}} = (2 \pm 4)$ counts.

6.1.1.4 Image stitching

For incidence angles $\theta_{\text{in}} > 6°$, the height of the PSF exceeds the sensor area. Thus, one image of the upper and one image of the lower part of the PSF is recorded (cf. figure 6.6 left) and

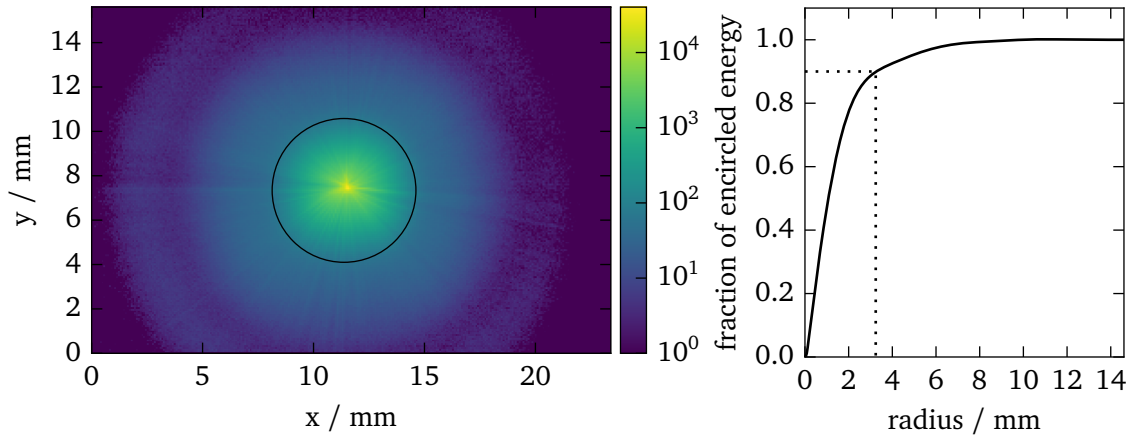

Figure 6.7: Left: exemplary measurement for perpendicular light incidence at $z = 513\,\mathrm{mm}$. The circle denotes the measured $r_{90} = \left(3.24 \pm 0.03(\mathrm{stat})^{+0.65}_{-0.43}(\mathrm{sys})\right)$ mm. Also visible are star-like structures in the PSF. Their origin is discussed below in chapter 7. Right: the encircled energy of the photograph on the left as a function of the size of the circle.

combined using the phase correlation between the two images [153, 154]. Given the two input images b_a, b_b, the discrete 2D Fourier transform of both images is calculated

$$\mathbf{B}_a = \mathscr{F}\{b_a\},\ \mathbf{B}_b = \mathscr{F}\{b_b\} \quad . \tag{6.5}$$

From these, the so-called cross-power spectrum by taking the complex conjugate of $\mathbf{B}_b$ is calculated for each pixel

$$C_i = \frac{B_{i,a}\, B^*_{i,b}}{|B_{i,a}\, B^*_{i,b}|} \tag{6.6}$$

and transformed back

$$c = \mathscr{F}^{-1}\{C\} \tag{6.7}$$

to obtain the normalized cross-correlation (cf. figure 6.6 center). The peak point

$$i_{\max} = \arg\max_i\{c\} \tag{6.8}$$

determines the point of maximum correlation between the two images and denotes the relative shift Δx, Δy in number of pixels of the second image to the first. This method has been found far more reliable than a simpler approach by stitching the images at the position of the peak of the PSF. An example for this process is given in figure 6.6.

6.1.1.5 Measurement of the size of the point spread function

A quantity measuring the size of the PSF is the so-called aberration radius r_{90}, i.e. the radius of a circle which encloses 90 % of the energy in the image. The energy in the image plane is obtained by the integral of the brightness values b_i of the image

$$I = \sum_i^N b_i \quad . \tag{6.9}$$

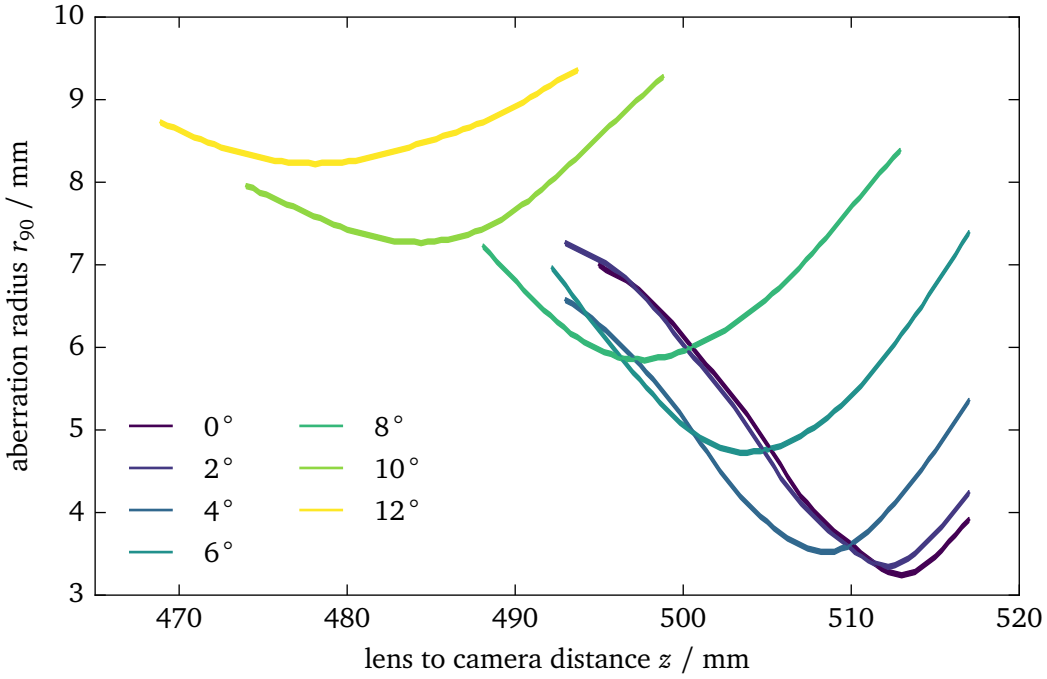

Figure 6.8: Measured aberration radius r_{90} as a function of the lens camera distance z for distinct incidence angles θ_{in}. The statistical uncertainties are signified by the line width, for the systematical uncertainty cf. figure 6.9.

The center of gravity of the PSF

$$x_c = \frac{1}{I}\sum_{i}^{N} b_i\, x_i \tag{6.10}$$

$$y_c = \frac{1}{I}\sum_{i}^{N} b_i\, y_i \tag{6.11}$$

$$\tag{6.12}$$

with the position x_i, y_i of the pixel i along the x- and y-axis is also referred to as centroid. The centroid is used as center of the circle. Now, with respect to the centroid position, the brightnesses b_i are ordered into a set

$$\mathbf{R} = \{b_1(r_1), \ldots, b_i(r_i), \ldots, b_N(r_N) | r_{i-1} \leq r_i\} \tag{6.13}$$

by their radius

$$r_i = \sqrt{(x_i - x_c)^2 + (y_i - y_c)^2} \quad . \tag{6.14}$$

The aberration radius r_{90} (here, the number does not denote the index) can be found by integrating the set $\mathbf{R}$ until 90 % is reached

$$\sum_{r_1}^{r_{90}} b_i \equiv 0.9\, I \quad . \tag{6.15}$$

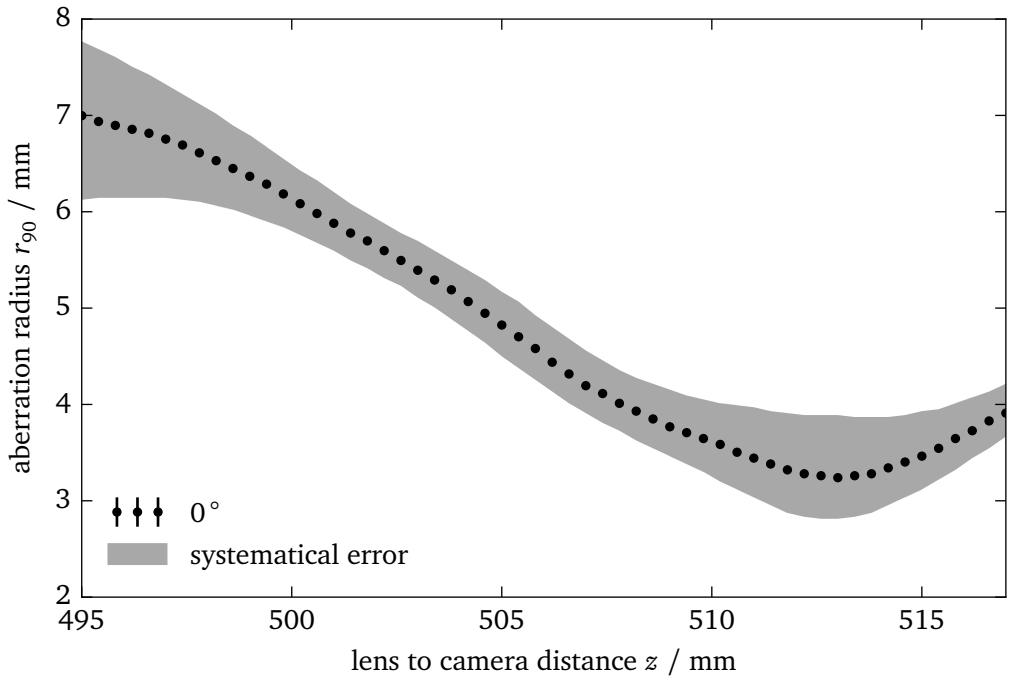

Figure 6.9: Measured aberration radius r_{90} as a function of the lens camera distance z and angle of incidence $\theta_{in} = 0°$ with the systematical error shown as shaded area. The error-bars of the statistical uncertainties are not visible here.

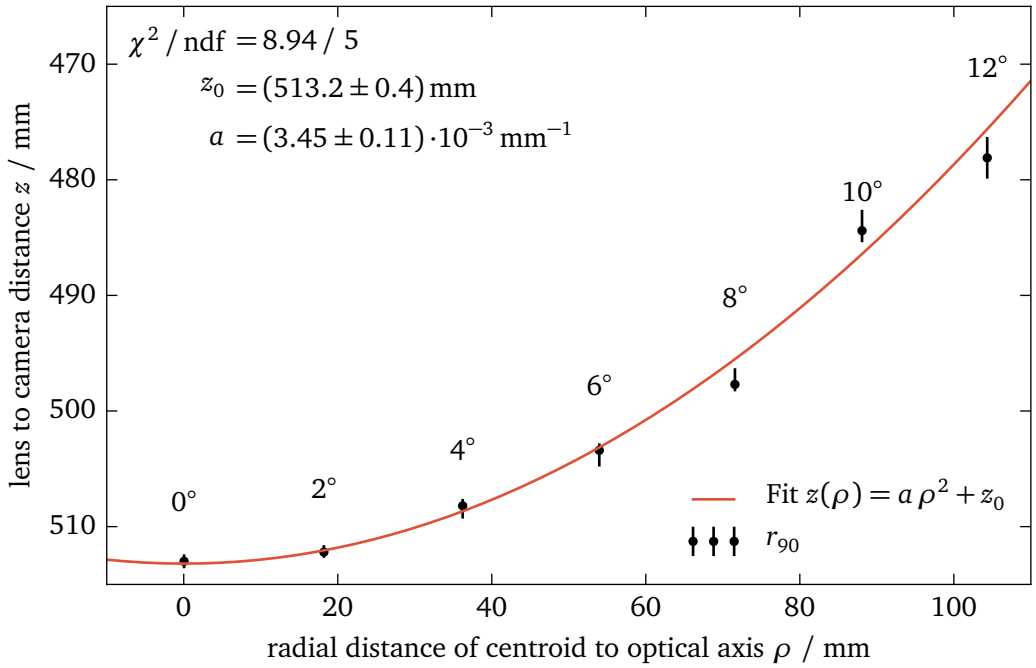

Figure 6.10: The lens-camera-distance z as a function of the distance of the centroid on the image plane x. The data are fitted to a parabola to reveal the curvature of field.

Due to the high number of pixels on the sensor and the usage of the full dynamic range, the statistical error due to spontaneous fluctuations of the pixel readout is very small, in the order of $\mathbb{O}(1\,\%)$. The highest uncertainty in the determination is therefore the noise subtraction described above. To estimate the systematic uncertainty on r_{90}, the calculation of r_{90} is performed with $b_i - \sigma_{b,\text{noise}}$ and $b_i + \sigma_{b,\text{noise}}$. The deviation from the original result of r_{90} is taken as standard deviation and is in the order of $\mathbb{O}(10\,\%)$. An exemplary measurement is presented in figure 6.7.

The results of the measurements of the PSF as a function of the lens camera distance z and the angle of incidence θ are presented in figures 6.8 and 6.9. The overall best value has been determined to

$$r_{90} = \left(3.24 \pm 0.03(\text{stat})^{+0.65}_{-0.43}(\text{sys})\right)\,\text{mm} \quad . \tag{6.16}$$

Additionally, with the radial distance of the centroid of the PSF from the optical axis, denoted as ρ, the curvature of field can be determined (cf. figure 6.10). The fit of a parabola to the positions of the minima of r_{90} for each measured incidence angle θ_{in} yields

$$z(\rho) = (3.45 \pm 0.11) \cdot 10^{-3}\,\text{mm}^{-1}\,\rho^2 + (513.2 \pm 0.4)\,\text{mm} \quad . \tag{6.17}$$

This formula describes a rotationally symmetric image plane perpendicular to the optical axis at which the PSF is smallest for every incidence angle. The optimal lens focal plane distance for perpendicular light incidence can be calculated to

$$z(0) = (513.2 \pm 0.4)\,\text{mm} \quad . \tag{6.18}$$

This result has also been found by the Geant4 ray-tracing simulations discussed below in chapter 7. The r_{90} obtained by the ray-tracing simulation is roughly 1 mm smaller compared to the measurement. Here, a possible explanation is that each groove of the Fresnel lens contributes an airy function to the PSF as discussed in [150]. Lastly, the origin of the star-like structures which can be seen in the example images given in figures 6.6 and 6.7 are caused by the optical aberrations as also discussed below in chapter 7.

6.2 Focal plane

The focal plane of FAMOUS is an array of 61 pixels on a symmetric hexagonal grid around a central pixel. Each pixel of FAMOUS consists of a light concentrator made from polished aluminum in the mechanical workshop of the III. Physikalisches Institut A, RWTH Aachen University, an optional UV pass filter and an SiPM. A photograph of the front and back side of the focal plane is provided in figure 6.11. Though the mechanics of the focal plane allow to focus the lens, this distance is currently fixed to 507.89 mm which is a compromise setting for large incidence angles. More details can be found in section 7.1.1.

6.2.1 Winston cones

The light concentrator is a rotationally symmetric Winston cone, also referred to as compound parabolic concentrator [158]. Its walls are of parabolic shape with the focal point of the parabola lying in the exit plane. A schematic of the Winston cones of FAMOUS is presented

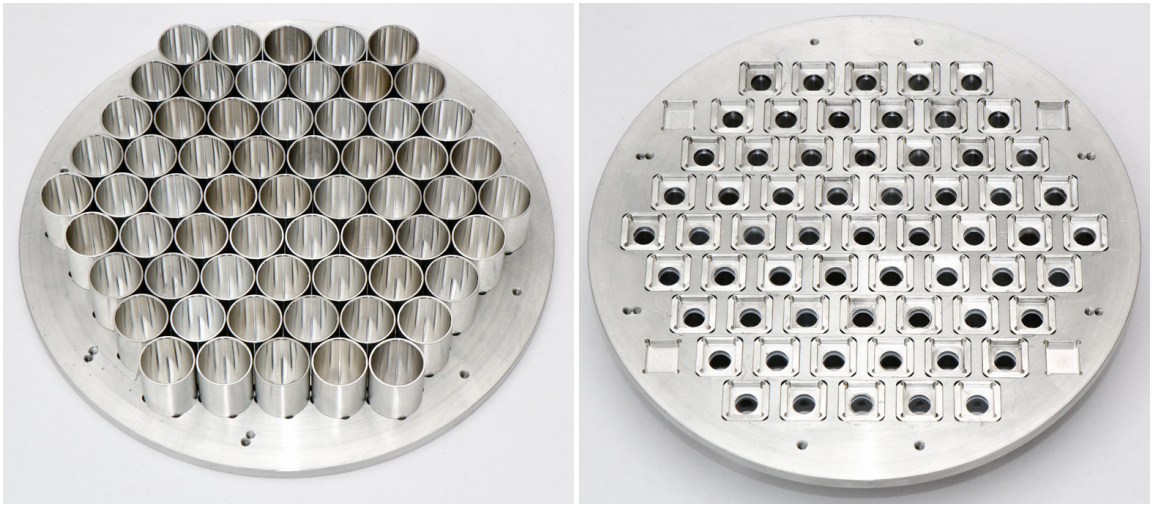

Figure 6.11: Left: front view of the 61 pixel focal plane of FAMOUS. The single Winston cones have a wall thickness of approximately 0.69 mm and are glued on a common base plate. Right: back side of the focal plane. The rectangular indentations provide enough space for the UV filter and the SiPM. Additionally, four indentations for the placement of unlit SiPMs are provided, which would be used for noise monitoring. The small holes are threads for mounting purposes. Photos courtesy of L. Middendorf (RWTH Aachen University).

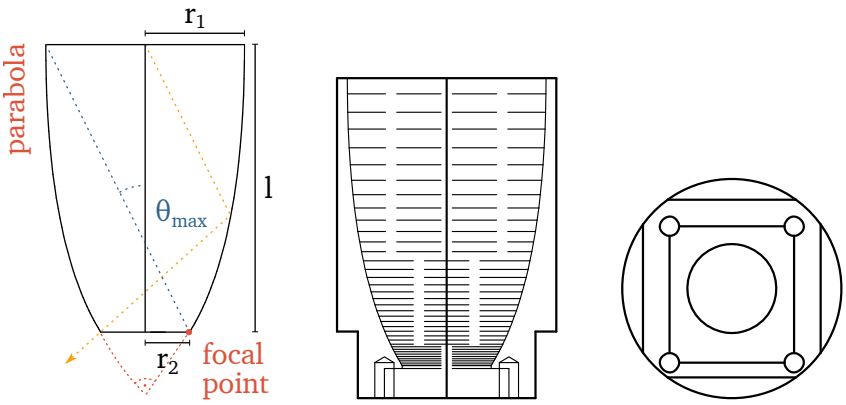

Figure 6.12: Left: the construction principle of Winston cones. The walls of the Winston cone are parabolas tilted with respect to the optical axis so that the focal points lie in the exit plane. Thus, light with an incidence angle of θ_{max} is reflected to the opposite side towards the focal point and can leave the cone whereas light with larger incidence angles will be reflected back towards the entrance. Middle: technical drawing of the Winston cones of FAMOUS. The entrance and exit radii are $r_1 = 6.71\,\text{mm}$ and $r_2 = 3\,\text{mm}$ corresponding to $\theta_{max} = 26.56°$. The wall thickness of the cones is approximately 0.69 mm. Right: back view. The inset at the back is deep enough to fully incorporate the UG11 filter and the SiPM. Due to the asymmetry of the SiPM package, the inset is also shifted with respect to the optical axis to position the sensitive area of the SiPM in the center of the cone exit.

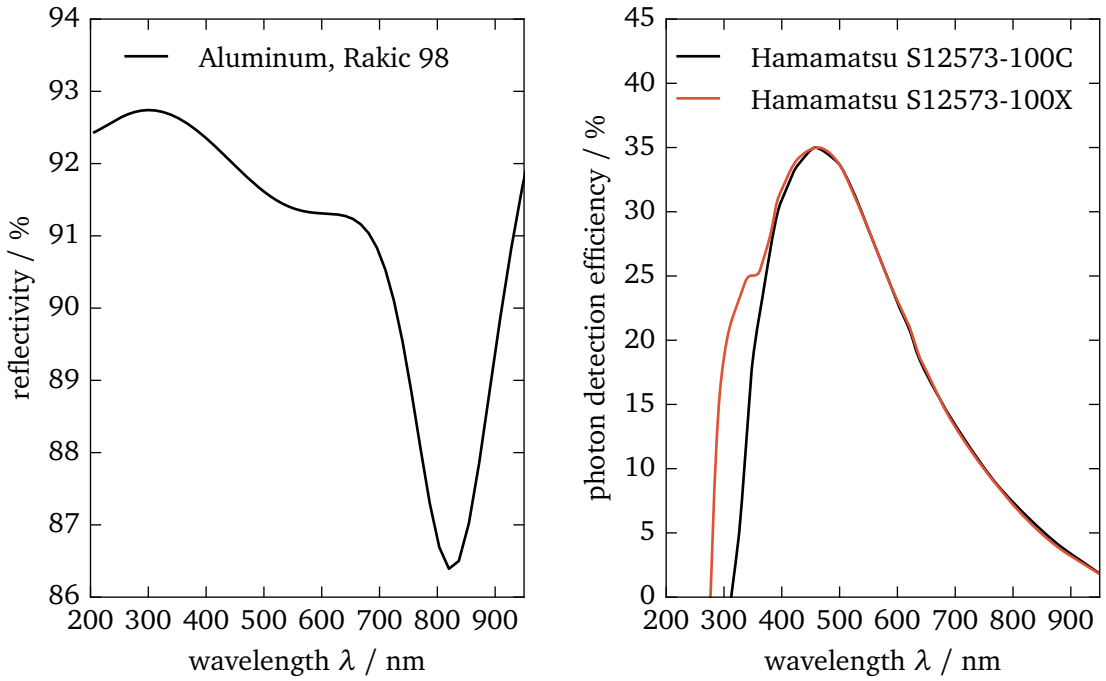

Figure 6.13: Left: reflectivity of bare aluminum as a function of the wavelength [155]. It has been shown that oxidation, which builds a protective layer of ≈ 30 µm over time, reduces the reflectivity by ≈ 1.5 % at 220 nm and less than 0.3 % at 550 nm [156, 157]. Right: photon detection efficiency of the Hamamatsu S12573-100C SiPM as a function of the photon wavelength [14].

in figure 6.12. The concentrator is the mathematical optimal concentrator since it transmits 100 % of the incoming light up to a sharp cut-off angle θ_{max}

$$\sin\theta_{\text{max}} = \frac{r_2}{r_1} \tag{6.19}$$

whereas r_1 and r_2 are the radii of the entrance and the exit aperture, respectively. The Winston cone of FAMOUS has an entrance radius of $r_1 = 6.71\,\text{mm}$ and an exit radius of $r_2 = 3\,\text{mm}$ resulting in a cut-off angle of $\theta_{\text{max}} = 26.56°$ [159]. The length of the Winston cone is given by

$$l = \frac{r_1 + r_2}{\tan\theta_{\text{max}}} = 19.43\,\text{mm} \quad . \tag{6.20}$$

Ray-tracing simulations of the Winston cone including the reflectivity of aluminum and surface roughness (cf. figure 6.13 left) yield a transmission efficiency of ≈ 90 % up to θ_{max} (cf. section 7.1.2).

The mechanics of the light concentrator feature a rectangular inset at the exit which can retain the optional UV pass filter and the SiPM (cf. figure 6.12, right). The UV pass filter is a Schott UG11 filter of 1 mm thickness [146]. It has a refractive index of $n = 1.585$ at $\lambda = 365\,\text{nm}$ and a high transmittance of 93 % at $\lambda = 330\,\text{nm}$. It is the successor of the M-UG6 filter which is installed in the fluorescence telescopes of the Pierre Auger Observatory [6]. A plot of the internal transmittance can be found in figure 6.3. The filter is transparent for

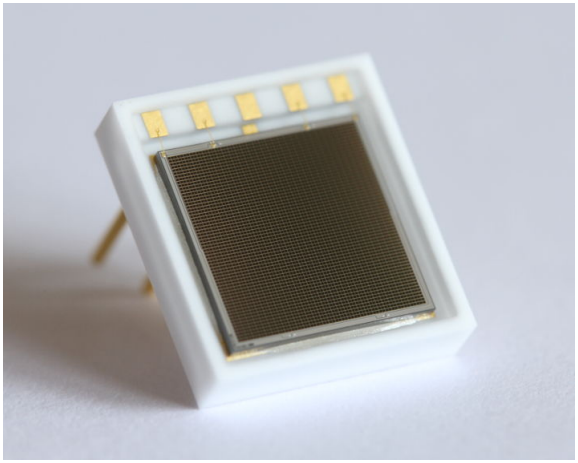

Figure 6.14: Photograph of the Hamamatsu S12573-100X SiPM. Photo courtesy of L. Middendorf (RWTH Aachen University).

wavelengths from 250 nm to 400 nm and again from 680 nm. The transmittance in the red to infrared regime unfortunately is intrinsic to these glasses due to the colorants. Nevertheless, the successor product UG11 has been improved significantly compared to M-UG6 benefiting the night sky background suppression.

6.2.2 Silicon photomultipliers

The SiPM is a Hamamatsu S12573-100X 6 mm × 6 mm SiPM with 2 × 2 channels which are read out separately [14]. The SiPM is a special issue with a silicone coating, which has a better UV transmission efficiency compared to the epoxy coating usually applied for the ceramic package. The SiPM has a high photon detection efficiency of 35 % at 450 nm, almost no afterpulsing and a low dark count rate of $f_{\text{dark}} \approx 2\,\text{MHz}$ compared to its predecessors (cf. figure 6.13 and table 6.1). The optical crosstalk at the recommended over-voltage $v_{\text{ov}} = 1.4\,\text{V}$ is $p_{\text{ct}} = 35\,\%$.

The SiPMs are already calibrated by the manufacturer. The manufacturer supplies the recommended bias voltage v_{bias}, the dark noise rate f_{dark} and the gain g for each of the four channels of one SiPM. The recommended bias voltage is given for $T = 25\,^{\circ}\text{C}$ and for an over-voltage of $v_{\text{ov}} = 1.4\,\text{V}$. It ranges between $v_{\text{bias}} = 65.45\,\text{V}$ and $v_{\text{bias}} = 66.08\,\text{V}$ with an average sample standard deviation of the four channels of $\sigma_{\text{v,bias}} = 26\,\text{mV}$ which corresponds to an average gain deviation of $\sigma_g = \sigma_{\text{v,bias}}/v_{\text{ov}} \approx 2\,\%$ and is negligible. The same applies to the dark noise rate with a mean of $\mu_{\text{f,dark}} = 722\,\text{kHz}$ and an average sample deviation of $\sigma_{\text{f,dark}} = 27\,\text{kHz}$.

Figures 6.15 and 6.16 present the recommended bias voltages and dark noise rates averaged per device and their sample standard deviation. Of the purchased batch of 68 SiPMs the two worst devices regarding the on-device bias voltage deviation and two representative samples, which have been used for other measurements, have been sorted out before equipping the focal plane of FAMOUS.

Parameter	Value
Size of active area	6 mm × 6 mm
Number of channels	2 × 2
Number of cells n_c	3600
Cell pitch	100 µm
Fill factor ϵ_{geom}	78.5 %
Operating voltage v_{bias}	≈ 65 V
Recommended over-voltage v_{ov}	1.4 V
Operating temperature	0 °C - 40 °C
Bias voltage progression factor β	60 mV K^{-1}
Package	Ceramic
Window	Silicone
Window refractive index	1.41
Spectral response range	270 nm - 900 nm
Photon detection efficiency PDE	35 % at 450 nm
Dark count rate f_{dark}	2 MHz
Gain g	$2.8 \cdot 10^6$
Crosstalk probability p_{ct}	35 %
Afterpulsing probability p_{ap}	< 1 %
Recovery time τ_{rec}	≈ 23 ns

Table 6.1: Table of important specifications of the Hamamatsu S12573-100X [14]. A photograph of the device is presented in figure 6.14.

6.3 Power supply unit

The 64 channel power supply unit of FAMOUS has been developed in the electronics workshop of the III. Physikalisches Institut A, RWTH Aachen University by F. P. Zantis and D. Louis and is made especially for applications which possibly expose the SiPMs to high continuous luminous intensities and thus is ideal for the application in fluorescence and Cherenkov telescopes [15]. It has been designed for autonomous operation which means it automatically adjusts the bias voltage v_{bias} for changes in ambient temperature T with a progression factor β

$$v(T) = v_{\text{bias}}(T = 25\,^{\circ}\text{C}) + \beta\, T \quad . \tag{6.21}$$

This behavior is implemented in a microcontroller which communicates via Ethernet with the user. The user can set the bias voltage v_{bias} at a reference temperature of $T = 25\,^{\circ}$C and the bias voltage progression factor β individually for each channel. A photograph of the first partly assembled power supply can be found in figure 6.17.

A very important feature of the power supply is the integrated current monitor with a 12 bit ADC. With every readout cycle of the microcontroller, the current flow of each channel is measured. Should it exceed a value of ≈ 1 mA, the bias voltage of the SiPM is set to zero to protect

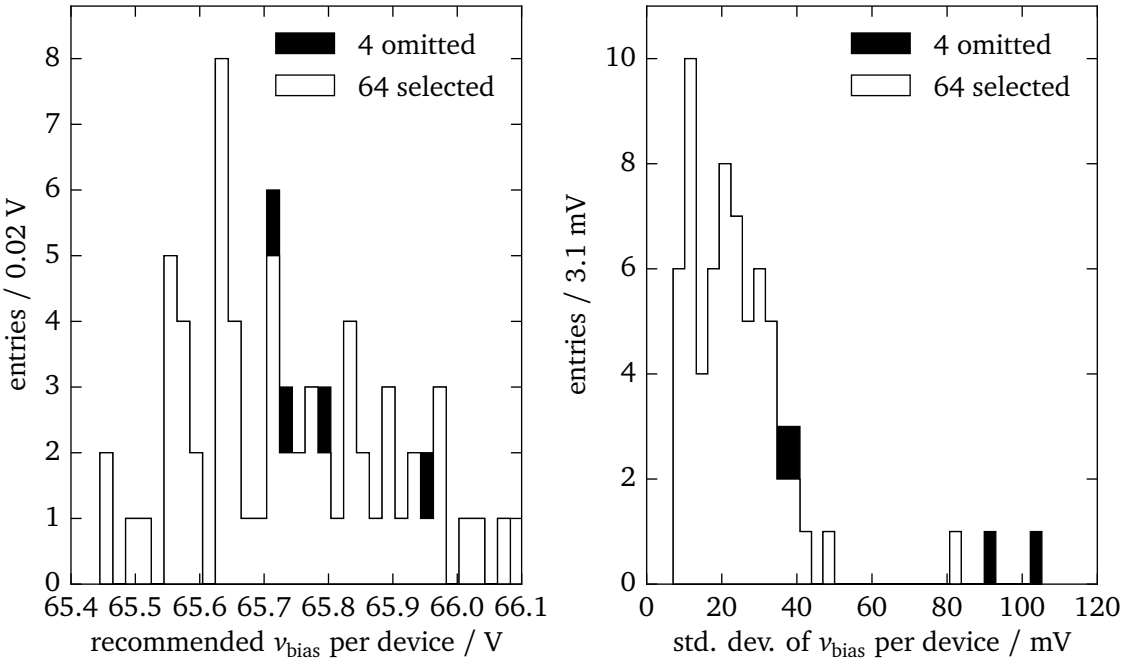

Figure 6.15: Left: mean recommended bias voltage per device of the Hamamatsu S12573-100X batch delivered for FAMOUS. Right: sample standard deviation of the bias voltages of the four channels for each device. The parts of the distribution which are marked black, have not been installed; here, these are the two worst devices and two which have been used for test measurements. Taken from the measurement reports delivered by the manufacturer.

the SiPM and the readout electronics. Furthermore, the current values are available for readout. To compute the current flow from the ADC counts c of the current monitors, which range from 0 to 4095, those values have to be converted by a calibration

$$i(c) = i_c\, c + i_0 \tag{6.22}$$

with the slope i_c and the offset i_0. The calibration constants are presented in figure 6.18. In contrast to the approximately equal calibration slopes i_c, the calibration offsets have a large spread due to component tolerances. The measured current flow has been used to track the trails of stars through the field of view of FAMOUS as discussed in chapter 9.

6.4 Readout electronics

The readout electronics is in the process of development at the point of completion of this thesis. It will be built based on the TARGET7 chip developed for the Cherenkov Telescope Array (CTA) collaboration [107, 161]. The TARGET is an application specific integrated circuit (ASIC) which has been specifically designed to read out signals recorded by SiPMs in cameras of Cherenkov telescopes. The current generation TARGET7 has been proposed for the small-sized and medium-sized dual-mirror telescopes of CTA.

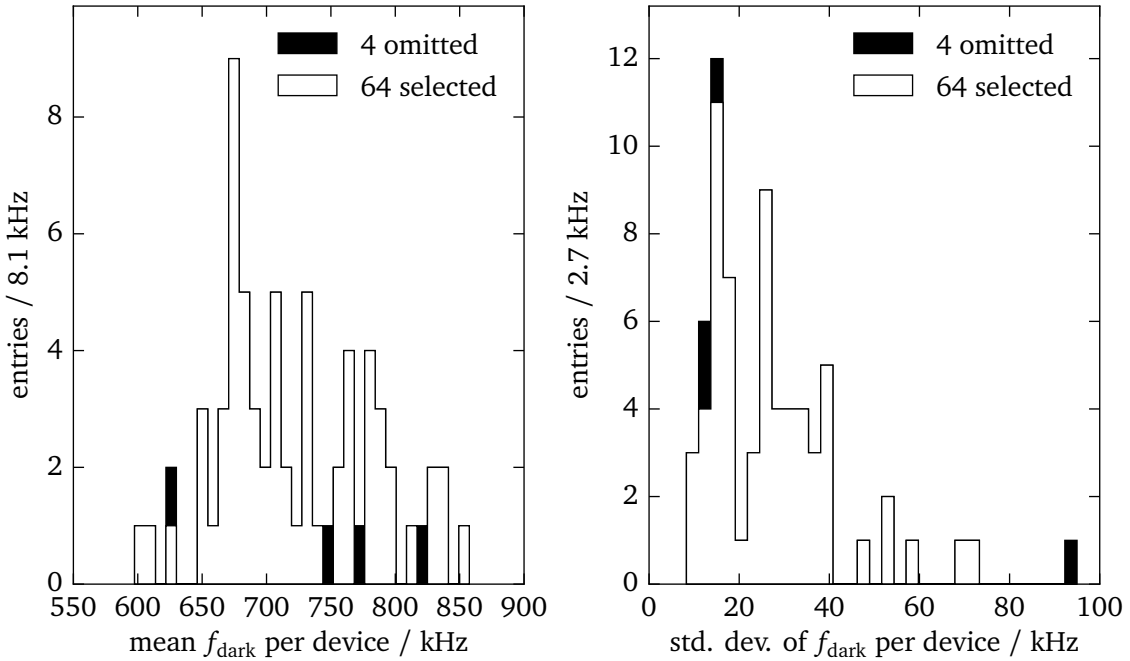

Figure 6.16: Left: mean dark noise rates per device of the Hamamatsu S12573-100C batch delivered for FAMOUS. Right: sample standard deviation of the dark noise rates of the four channels for each device. Taken from the measurement reports delivered by the manufacturer.

One chip has 16 readout channels which are digitized with a high rate of 0.5 Gsps to 1 Gsps (Giga-samples per second). Furthermore, logic has been built in to achieve a self-triggering of the readout on the sum of four adjacent camera pixels. The data is continuously digitized in a 32 cell switched capacitor array which then is buffered to a storage array of 512 blocks with 16 384 switched capacitor cells in total. This results in a total signal trace length of 16.384 µs to 32.758 µs depending on the sampling rate. Due to this design, the maximum trigger latency is in the order of the trace length which makes the ASIC also an ideal candidate for the use in fluorescence telescopes. Here, the duration of the light signal in one pixel is in the order of $\mathbb{O}(1\,\mu\text{s})$ and much longer compared to the Cherenkov telescopes with $\mathbb{O}(1\,\text{ns})$.

6.5 Night sky camera

The night sky camera is a QHY5L-II-C CMOS camera from QHYCCD with 1280 × 960 pixels and USB readout originally intended for taking photographs of planets and stars with optical telescopes [162]. A photograph of the camera can be found in figure 6.19. It has a 4.8 mm × 3.6 mm large APTINA MT9M034 CMOS sensor with a high quantum efficiency of 74 %. Color information is recorded by means of a so-called Bayer filter mounted in front of the chip. A Bayer filter is a mosaic of red, green and blue colored glasses with a ratio of 50 % green, 25 % red and 25 % blue to resemble the perception of the human eye. The gains g_r, g_g, g_b of the red, green and blue pixels can be controlled individually. Additionally, the exposure

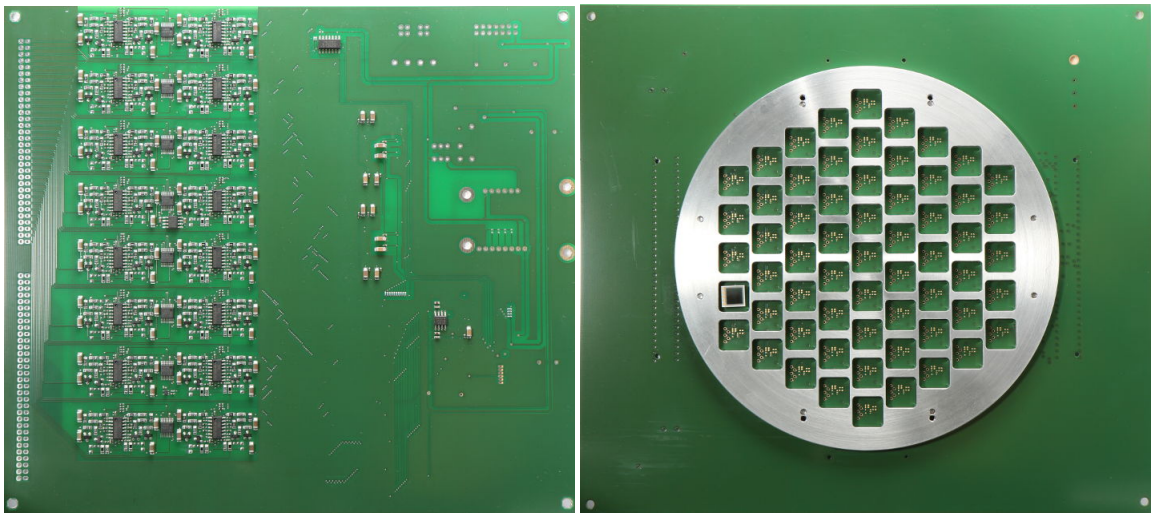

Figure 6.17: Left: photograph of the partially equipped 64 channel power supply of FAMOUS (May 2015). The patches of components on the left side are 32 SiPM bias voltage regulators. The other 32 regulators are situated on the top side of the PCB (printed circuit board). The $2 \cdot 64$ joints on the left border of the PCB are used for the connection of the focal plane PCB with 64 SiPMs (top joints) and 64 temperature sensors (bottom joints). The Ethernet RJ45 jack has been placed near the right border. The total dimensions of the PCB are 220 mm × 200 mm. Right: front view of the focal plane PCB with the base plate in which the Winston cones are to be glued and one SiPM (not soldered yet). The PCB provides mounting holds for fixation to the focal plane base plate which in turn is fixated to the telescope tube. Photos courtesy of L. Middendorf (RWTH Aachen University). For further details see also [15].

Parameter	Value
Sensor	APTINA MT9M034 CMOS
Number of pixels	1280 × 960
Sensor size	1/3” (4.8 mm × 3.6 mm)
Color filter	Bayer filter
Quantum efficiency	52 % blue, 62 % green, 58 % red
Readout	USB 2.0
Integration time	20 µs - 99 s
Image depth	8 bit or 12 bit
Lens mount	C-mount

Table 6.2: Table of important specifications of the QHY5L-II-C CMOS camera from QHY-CCD [162]. Due to the Bayer filter, the quantum efficiency is lower compared to the monochrome variant with 74 %.

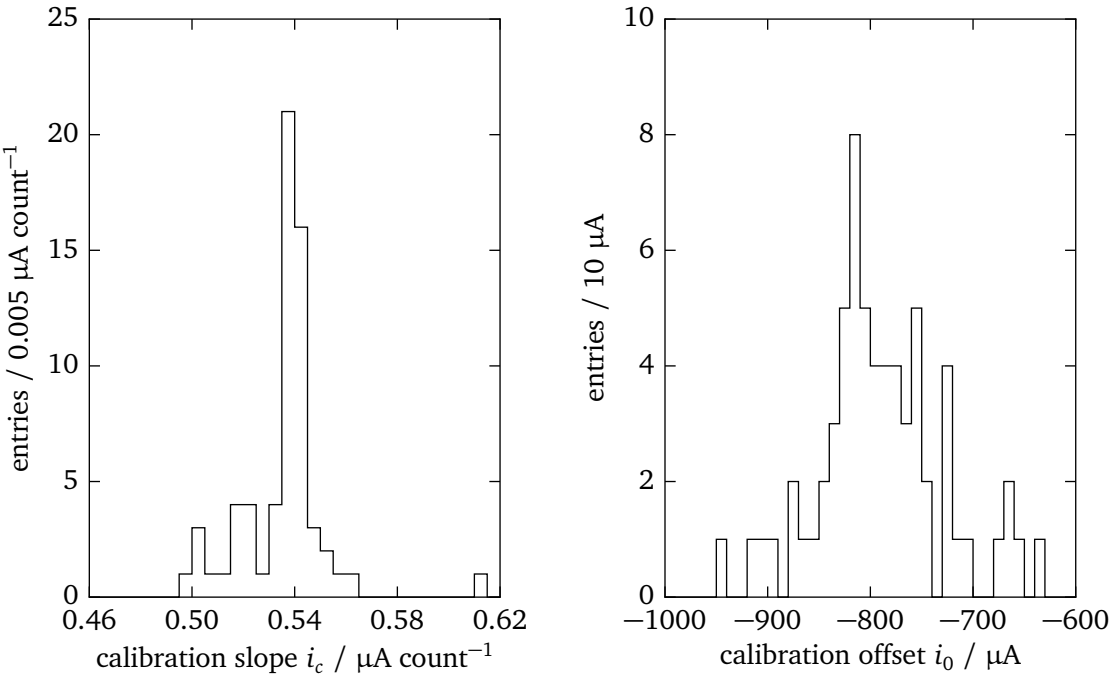

Figure 6.18: Left: measured slope for the ADC count to current conversion of the PSU [160] Right: measured offset for the ADC count to current conversion. The ADC count c of a channel is converted with $i(c) = i_c\, c + i_0$ to a current. The slopes are more or less equal with only a few outliers. In contrast, the variations of the offset are large.

Parameter	Value
Focal length	8 mm
Maximum sensor format	2/3" (8.8 m × 6.6 m)
Aperture size	f/1.4 - f/16
Working distance	100 mm - ∞
Lens mount	C-mount

Table 6.3: Table of important specifications of the fixed focal length lens MegaPixel #56-786 of Edmund Optics [163].

time of the photos can be finely adjusted. The camera also has a C-mount type lens mount widely used for small movie and microscope cameras. A fixed focal length lens with $f = 8$ mm from Edmund Optics, the MegaPixel #56-786, has been attached to the camera. The aperture of the lens can be adjusted in discrete steps from f/1.4 to f/16 and is kept constant at f/2.8 at which the sharpness of the lens is highest. In total, the field of view of this camera lens system is 33° × 25° and roughly two-fold of the field of view of FAMOUS. The system is then mounted on the tube parallel to the optical axis of the telescope with an angular uncertainty of approximately 1°. During measurements with FAMOUS, the night sky camera autonomously

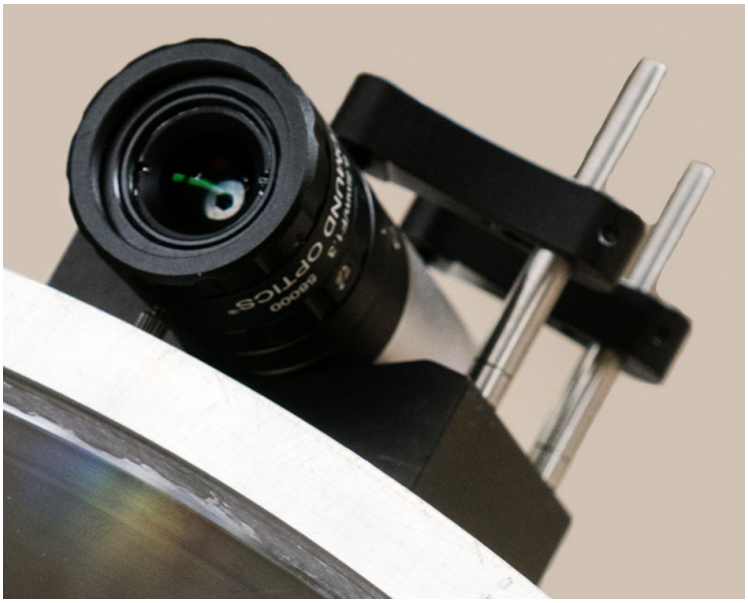

Figure 6.19: Photograph of the night sky camera of FAMOUS mounted on the telescope tube. Attached to the QHY5L-II-C CMOS camera is a fixed-focal-length lens from Edmund Optics. The sensor is read out continuously via USB and the photographs of the night sky are stored for further analysis of the visible stars in the field of view. The field of view is roughly two-fold of the field of view of FAMOUS.

takes photographs of the night sky, automatically adjusting the gain of the individual pixels and the integration time ensuring a good exposure of the photographs. These images are analyzed to detect the visible stars in the field of view of FAMOUS. Further specifications of the night sky camera can be found in tables 6.2 and 6.3. Details of the automatic exposure algorithm and the image analysis are discussed in chapter 8.

6.5.1 Measurement of the image distortion

Due to the small focal length, the image produced by the lens is subject to distortion, especially in the image corners. By photographing a known pattern, in this case a chessboard pattern with white and black tiles printed on a large sheet of paper in approximately 60 cm distance, prominent features can be recognized and used for distortion analysis as e.g. the corners between the chessboard tiles. Example photographs before and after the distortion correction can be found in figure 6.20. The image coordinates (in arbitrary units) used for the following calculations are x and y and can be transformed to pixel coordinates u and v with the so-called camera matrix

$$\begin{pmatrix} u \\ v \\ 1 \end{pmatrix} = \begin{pmatrix} f_x & 0 & c_x \\ 0 & f_y & c_y \\ 0 & 0 & 1 \end{pmatrix} \begin{pmatrix} x \\ y \\ 1 \end{pmatrix} \tag{6.23}$$

with the computed effective focal length f_x in x-direction, f_y in y-direction and the center of the photograph at $c_x = 639.5$ and $c_y = 479.5$. The relation between the apparent and expected position of these patterns can be divided into radial distortion and tangential distor-

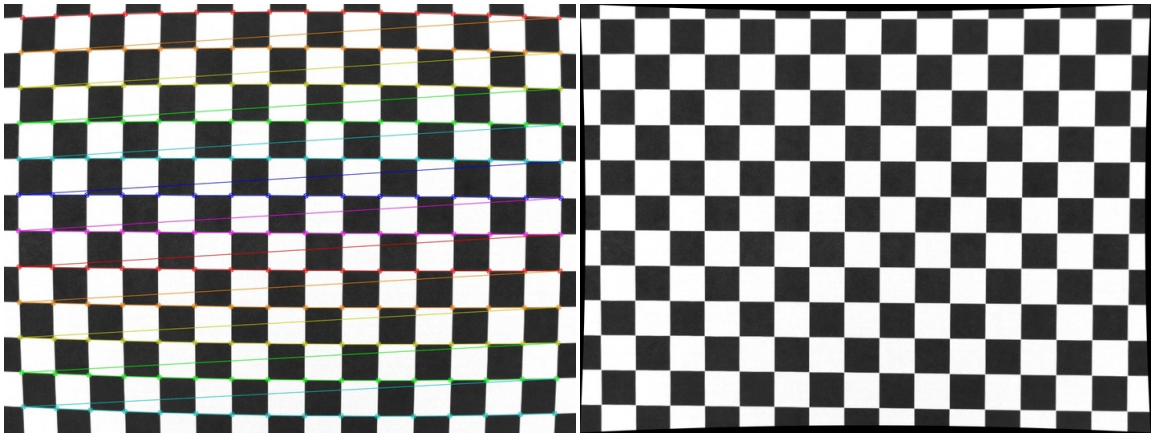

Figure 6.20: Left: photograph of a black and white chessboard pattern with found corners as colored circles for $f/2.8$. The position of the found corners is used to obtain the distortion parameters. Right: undistorted photograph before cutting the black borders.

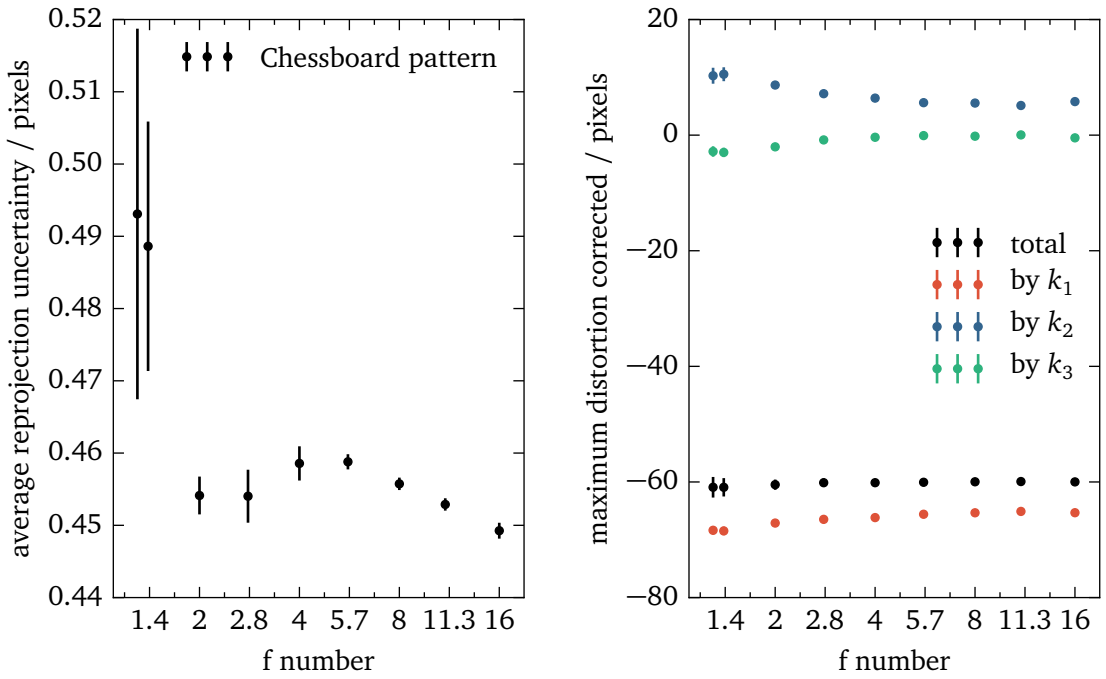

Figure 6.21: Left: average re-projection error of the distortion correction as a function of the aperture size ranging from $f/1.4$ to $f/16$. Six measurements with ten images each were performed for each data point. An aperture of $f/2.8$ will be used for the measurements with FAMOUS since the re-projection error is small and the sharpness of the lens high. Right: maximum distortion corrected by the radial distortion coefficients k_1, k_2, k_3 in pixels as a function of aperture size. The relation between the coefficients changes as whereby the total distortion slightly improves for smaller apertures.

tion [164, 165]. The corrected position (x', y') of a pixel (x, y) shifted by radial distortion can be calculated by

$$x' = x\left(1 + k_1 r^2 + k_2 r^4 + k_3 r^6\right) \tag{6.24}$$

$$y' = y\left(1 + k_1 r^2 + k_2 r^4 + k_3 r^6\right) \tag{6.25}$$

with the radial distortion parameters k_1, k_2, k_3 and $r^2 = x^2 + y^2$ [166]. The tangential distortion, which occurs when lens and sensor axes are not perfectly parallel aligned to each other, can be compensated by

$$x'' = x\prime + \left[2\,p_1\,x\,y + p_2\,(r^2 + 2\,x^2)\right] \tag{6.26}$$

$$y'' = y\prime + \left[p_1\,(r^2 + 2\,y^2) + 2\,p_2\,x\,y\right] \tag{6.27}$$

with the the tangential distortion parameters p_1, p_2. This image correction algorithm is implemented in the OpenCV library [167]. The library also has ready-to-use scripts for the determination of the distortion coefficients by analyzing multiple images or even a live feed of a camera.

The quality of the fit of the distortion coefficients is given by the average re-projection error which is the residual error between the corrected and expected positions when applying the correction to the analyzed images. Furthermore, the distortion pattern of the lens changes with the aperture. Figure 6.21 presents the measured re-projection error as a function of the aperture size. A good compromise between re-projection error, sharpness and exposure is the aperture $f/2.8$ which is used for the capturing of the night sky photographs. The determined distortion coefficients are

$$k_1 = -1.045 \pm 0.005 \tag{6.28}$$

$$k_2 = 2.262 \pm 0.164 \tag{6.29}$$

$$k_3 = -5.260 \pm 2.129 \tag{6.30}$$

$$f_x = f_y = 3589 \pm 5 \tag{6.31}$$

with a re-projection error of $(0.454 \pm 0.004)\,\mathrm{px}$. For this lens, the distortion coefficient k_1 has the highest influence and the tangential coefficients p_1 and p_2 are zero in all cases indicating that no misalignment between lens and sensor exists. The maximum shift in pixels is approximately 60 pixels or 5 % of the width of the photograph. This corresponds to an angular shift of

$$\alpha = \tan^{-1}\left(\frac{60\,\mathrm{px}\cdot 3.75\,\mu\mathrm{m\,px^{-1}}}{8\,\mathrm{mm}}\right) \approx 1.6^\circ \tag{6.32}$$

which is in the order of the field of view of one pixel of the FAMOUS telescope. In summary, the image quality of the night sky camera is sufficiently good for the use in FAMOUS and might be acceptable without the application of the image correction.

6.6 Environmental sensors unit

The environmental sensors unit of the FAMOUS telescope is used to monitor several ambient conditions which have an influence on the measurement. These include the ambient temperature, air pressure, relative humidity, luminosity and the absolute position. The sensors are read

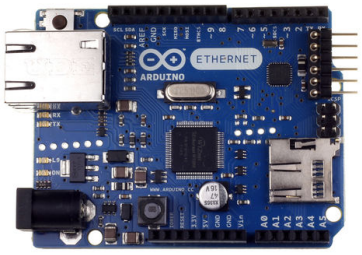

Figure 6.22: Photograph of the Arduino Ethernet micro-controller board. On the upper left is the RJ45 jack for the communication via Ethernet, in the lower left corner the power jack. The Ethernet functionality is implemented by a WIZnet W5100 chip [169]. The pins used for programming are situated on the upper right side of the PCB. On the lower right side, there is a slot for a flash memory card in the microSd format. Taken from [170].

out with an Arduino Uno microcontroller board and are made available to the user via Ethernet using the HTTP protocol. A first version of this unit with USB readout has been developed in [168].

6.6.1 Arduino Uno microcontroller board

The Arduino Uno is a microcontroller board based on the Atmel ATmega328P chip with a clock speed of 16 MHz and 32 kB of flash memory [171]. It has 14 digital input and output pins and 6 analogue input pins which can be digitized with a 10 bit ADC. This special version, the Arduino Ethernet, is equipped with an RJ45 jack instead of an USB jack. Power has to be supplied separately via a power connector. The Ethernet functionality is provided by the WIZnet W5100 chip which implements the TCP protocol which is the standard for Ethernet connections [169]. All these components are placed on a small 68.6 mm × 53.4 mm, nearly credit card sized, PCB (printed circuit board) (cf. figure 6.22). The programming of these devices is very convenient. The manufacturer supplies an IDE (integrated development environment), which is programmed in C-code, provides all necessary compilers and can flash the memory of the Arduino through the USB port or an FDTI converter which can be connected via the pins on the PCB.

The software for the Arduino Ethernet, the basis of the environmental sensor unit, reads out all sensors and derives the quantities of interest in SI units applying sensor specific conversion and calibration factors. The information is provided via the HTTP protocol which means, the user can use a normal web browser to get a reading from the device. The data are formatted in the human and machine readable JSON format which is a way of formatting data as plain text. More details on the readout software and the data format can be found in chapter 8.

6.6.2 Temperature and pressure sensor

The Adafruit BMP085 breakout board is equipped with the digital Bosch BMP085 pressure and temperature sensor [173]. The low power and low voltage sensor has been designed for the use in mobile devices such as smartphones and GPS outdoor equipment. The combined information of the pressure and the temperature can also be used to detect changes in the altitude with a

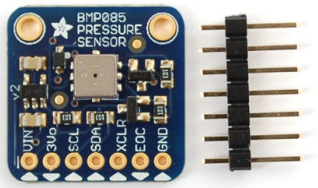

Figure 6.23: Photograph of the PCB with the Bosch BMP085 pressure and temperature sensor. The temperature sensor is used to improve the measurement of the pressure. Taken from [172].

Parameter	Condition	Value
Pressure range		300 hPa - 1100 hPa
Communication		I^2C
Operating voltage		3.3 V
Operating temperature	full precision	0 °C - 65 °C
	operational	−40 °C - 85 °C
Systematical uncertainty	pressure	±1 hPa
	temperature	±1 °C
Statistical uncertainty	pressure	±0.5 hPa
	temperature	±0.1 °C

Table 6.4: Table of important specifications of the Bosch BMP085 pressure and temperature sensor [173].

claimed precision of 0.25 m. The communication is performed via the I^2C standard. A photo and further specifications can be found in figure 6.23 and table 6.4.

6.6.3 Humidity sensor

The SparkFun HIH-4030 breakout is equipped with the Honeywell HIH-4030 humidity sensor [175]. It consists of a laser trimmed, polymer capacitive sensing element with hydrophobic filter layers which makes it suitable for use in harsh environments. Due to these filters, the drift of the humidity measurement is quoted as approximately 0.5 % per year at an ambient relative humidity of 50 % if operated between 0 °C and 50 °C. The sensor can also be operated outside this temperature range with a lifetime of < 50 h. The analogue voltage output of the sensor is nearly linear over the full relative humidity range. Given the input voltage $v_{\text{bias}} = 5$ V, the measured output voltage yields

$$v_{\text{out}}(h) = (0.0062\,h + 0.16)\; v_{\text{bias}} \tag{6.33}$$

Figure 6.24: Photograph of the PCB with the HIH-4030 humidity sensor breakout board from SparkFun Electronics. Taken from [174].

Parameter	Condition	Value
Humidity range		0 % - 100 %
Communication		analog
Operating voltage		5 V
Operating temperature	normal operation	0 °C - 50 °C
	lifetime < 50 h	−40 °C - 0 °C, 50 °C - 85 °C
Systematic uncertainty	humidity< 60 %	±5 %
	humidity ≥ 60 %	±8 %
Statistical uncertainty		±0.5 %

Table 6.5: Table of important specifications of the Honeywell HIH-4030 humidity sensor [175].

for a given ambient relative humidity h. The voltage is read out by the Arduino analogue input with a precision of 10 bit. A photo and further specifications can be found in figure 6.24 and table 6.5.

6.6.4 Luminosity sensor

The Adafruit TSL2561 luminosity sensor has been developed for general light sensing appliances, such as automatic illumination dimming, with a near-photopic response (human eye). For this it is equipped with two light diodes, the first for the detection of light in a broad wavelength regime of 300 nm to 1100 nm, the second for the red to infrared regime from 500 nm to 1100 nm [176]. Furthermore, the gain and integration time of the photo diodes are configurable to detect a wide range of light fluxes between 0.1 lx and 40 000 lx. Real world conditions range from starlit night with $\mathbb{O}(1\,\text{lx})$ to $> 100\,000$ lx during daytime. The precision is good enough to distinguish between moonless and moonlit nights with $\gtrsim 4$ lx. Additionally, it automatically removes 50 Hz and 60 Hz ripples from artificial lightning. The PCB is also equipped with a 16 bit ADC with the I^2C digital interface for communications. A photo and further specifications can be found in figure 6.25 and table 6.6. In FAMOUS, this sensor can be used to implement a failsafe which prevents switching on the telescope in daylight.

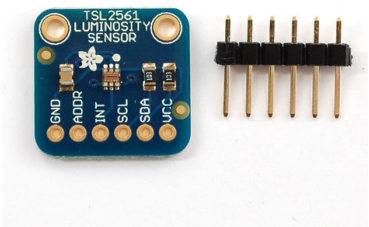

Figure 6.25: Photograph of the PCB of the TSL2561T luminosity sensor from Adafruit Electronics. Taken from [176].

Parameter	Channel	Value
Pressure range		0.1 lx - 10 000 lx
Communication		I^2C
Operating voltage		3.3 V
Operating temperature		−30 °C - 70 °C
Dark count		< 4 counts
Responsivity $t_{int} = 402$ ms	broadband	144 counts lx^{-1}
(incandescent light)	infrared	72 counts lx^{-1}
Responsivity $t_{int} = 402$ ms	broadband	9 counts lx^{-1}
(incandescent light, low gain mode)	infrared	4.5 counts lx^{-1}

Table 6.6: Table of important specifications of the TAOS TSL2561T luminosity sensor [177].

6.6.5 GPS receiver

The GPS shield from SparkFun can be used to connect GPS receivers to the Arduino [178]. Several types of receivers are supported by means of different connectors and a switch between DLINE and UART communication protocols. Furthermore, all wires of the Arduino are looped through which is useful here since the same shield can also be used to connect and mount the other sensors of the sensor unit of FAMOUS to the Arduino.

As GPS receiver, the GlobalSat EM406A GPS receiver has been used [180]. It has a SiRF Star III chipset with 20 channels and relatively fast signal acquisition times from cold start. Besides that, the package is with 30 mm × 30 mm × 10.5 mm very compact. The GPS module can also be used to get the current time of the day with a claimed precision of 1 µs. A photo and further specifications can be found in figure 6.26 and table 6.7.

6.6.6 Commissioning of the fully assembled environmental sensors unit

A photograph of the fully assembled environmental sensors unit can be found in figure 6.27. Long-running measurements in a temperature controlled laboratory have been performed to test the uncertainties of the measurements. In total, roughly 250 000 data points have been taken over several hours with a rate of 0.1 Hz. The deviations from the mean of 100 s intervals

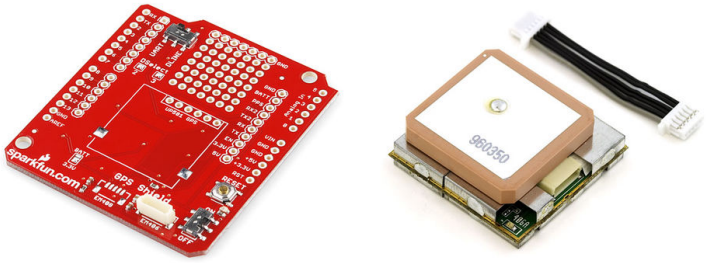

Figure 6.26: Photographs of the GPS shield from SparkFun (left) and the GlobalSat EM406A GPS receiver (right). The GPS shield is used to connect the GPS receiver to the Arduino. Furthermore, it can also host the other sensors since all wires of the Arduino are looped through. Taken from [178, 179].

Parameter	Value
Chipset	SiRF Star III, 20 channels
Communication	UART
Operating voltage	5 V
Operating temperature	−40 °C - 85 °C
Sensitivity	−159 dBm
Startup time	8 s - 42 s (warm / cold start)
Reacquisition time	0.1 s
Absolute position accuracy	±10 m
Relative position accuracy	±5 m

Table 6.7: Table of important specifications of the GlobalSat EM406A GPS receiver [180].

(100 data points) are presented in figures 6.28 and 6.29. Overall, the statistical uncertainties quoted by the manufacturers could be confirmed.

In case of the GPS position, the difference in longitude λ and latitude ϕ has been converted into a distance x in meters using the so-called Haversine formulae [181]

$$a = \sin^2(\Delta\phi/2) + \cos\phi_1 \cdot \cos\phi_2 \cdot \sin^2(\Delta\lambda/2) \tag{6.34}$$

$$c = 2\,\mathrm{atan2}(\sqrt{a}, \sqrt{a-1}) \tag{6.35}$$

$$x = R_e \cdot c \cdot \mathrm{sign}(\Delta\phi) \tag{6.36}$$

with the latitudes ϕ_1, ϕ_2, $\Delta\phi = \phi_1 - \phi_2$; longitudes λ_1, λ_2, $\Delta\lambda = \lambda_1 - \lambda_2$ and the earth radius $R_e = 6371\,\mathrm{km}$. Thus, the angular uncertainty of $\sigma_\lambda \approx \sigma_\phi \approx 0.7\,\mathrm{arcsec}$ corresponds to a maximum position uncertainty of $\approx 25\,\mathrm{m}$.

Summarizing, the environmental sensors unit will provide valuable information during data-taking. Albeit very cost efficient with a total cost of ≈ 150€, the precision of the used sensors is good. Furthermore, the unit is very compact and thus can be fixed anywhere at the telescope

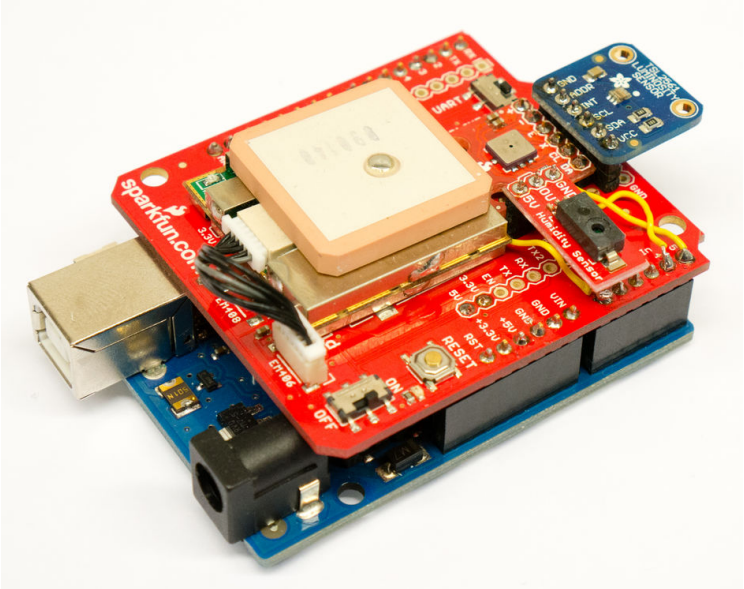

Figure 6.27: Photograph of the fully assembled environmental sensors unit placed on top of an Ardunino Uno with USB connector positioned on upper left side of the PCB.

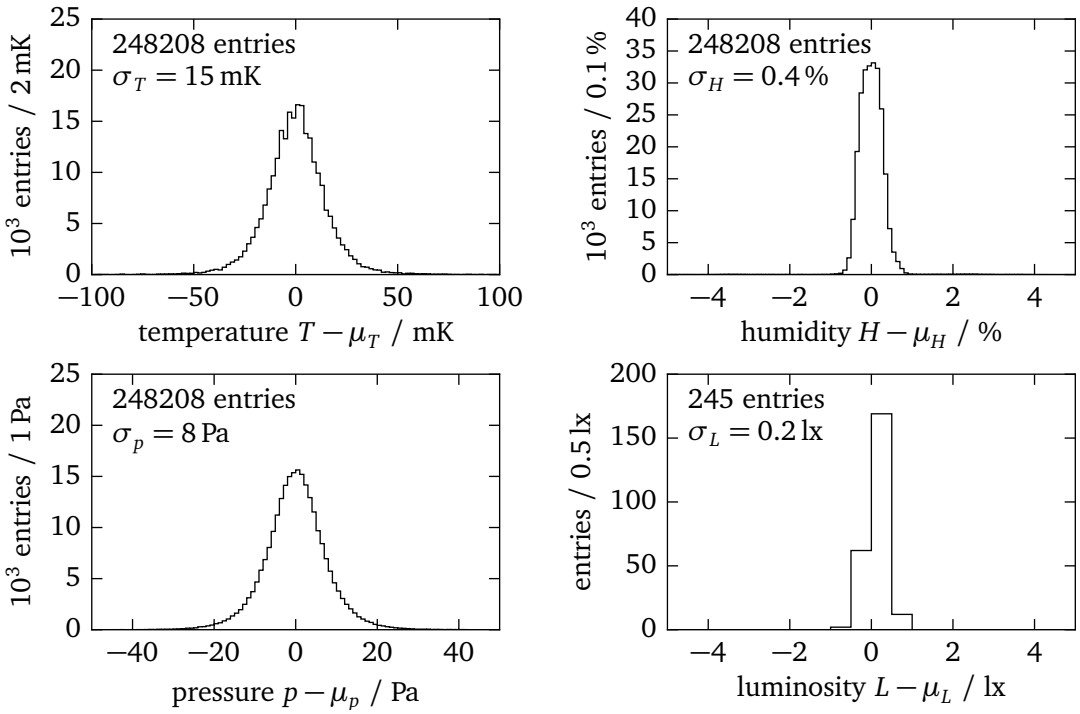

Figure 6.28: Measured uncertainties of environmental sensors.

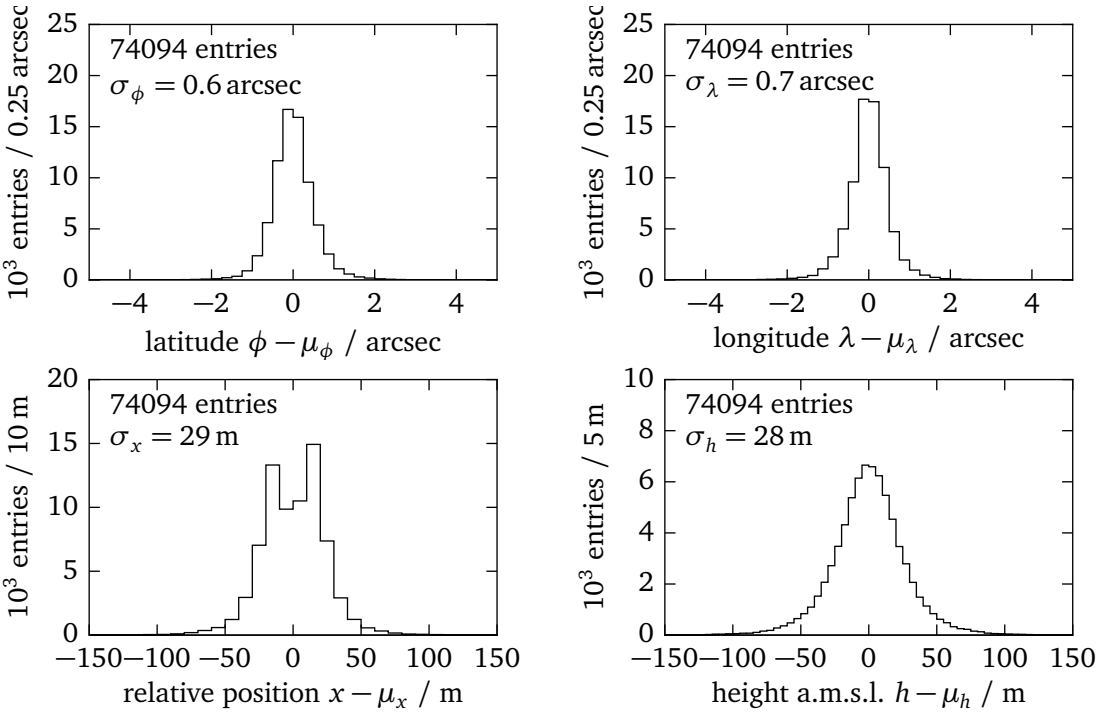

Figure 6.29: Measured uncertainties of the GPS location of the environmental-sensors unit.

tube and is operated self-dependently without any user interaction. The data can be obtained with very short delay of roughly 100 ms over the Ethernet connection in a human readable format. A full description of the firmware and the used data format can be found in chapter 8.

6.7 The seven pixel prototype FAMOUS-7

For first tests of the mechanics of the tube and especially the focal plane, a seven pixel version of the focal plane has been constructed since the SiPM power supply and the readout electronics could be constructed from existing components. Due to the fact that each SiPM has four channels, in total 28 signal cables had to be routed to the electronics placed in a NIM / VME combi crate from CAEN. The four signals of each SiPM have been summed up with fan-in-fan-out NIM modules. Since the fan-in-fan-out modules also provided several outputs of the same signal, two SiPM readouts could be tested at the same time. A photograph of the seven pixel focal plane can be found in figure 6.30. Several measurements with this prototype have been performed [182, 183].

6.7.1 Power supply unit

The power supply FTPC (Fiber Tracker Power Controller) is a NIM module that has been developed at the III. Physikalisches Institut B, RWTH Aachen University for the use in a time-of-flight spectrometer with scintillating fibers and SiPMs [121]. The power supply has eight channels and can provide up to 80 V for each SiPM separately. Additionally, four PT100 temperature sensors are available and are read out continuously for an automatic adjustment of the bias

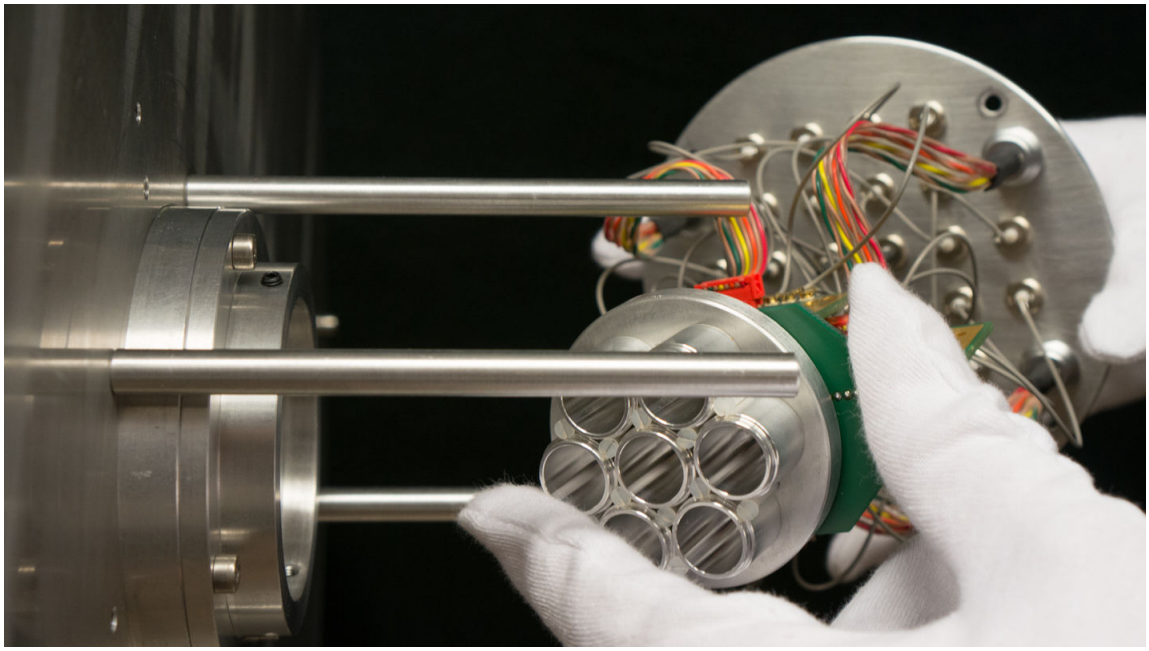

Figure 6.30: Photographs of the seven-pixel-focal-plane of FAMOUS-7 during the assembly. Here, the Winston cones have thicker walls and are hold in place by plastic screws instead of glue. Behind the focal plane are the amplifiers and the bias voltage, temperature sensor and signal cables.

voltage. These temperature sensors are located on amplifier boards also developed by the same institute. Each amplifier board can amplify the signal of two SiPMs. The data are read out via a serial connection established by a FTDI serial converter connected via USB. FTDI is the name of the company producing these converters and nowadays a synonym for USB to serial interfaces.

6.7.2 Readout electronics

The amplified SiPM signal is read out with two different electronics. The first variant uses the 16 channel QDC (charge-to-digital converter) V965 from CAEN with a 12 bit resolution [184]. A charge readout is triggered randomly with a frequency of 50 kHz and 200 ns integration time. This can be used to obtain finger spectra of dark noise which are important for calibration purposes.

The second variant uses two DRS4 evaluation boards, i.e. an ASIC with four channels using switched capacitor arrays which sample the SiPM with up to 5 Gsps [185, 186]. The evaluation boards can even be connected to each other which has been useful for the implementation of a camera wide trigger on two adjacent pixels. Additionally, the central pixel has been fed in both boards enabling the calibration of timing offsets between the two boards.

6.7.3 The IceAct Cherenkov telescope

The seven pixel prototype with the DRS electronics has been adopted for the use at the South Pole at the IceCube neutrino observatory to study its feasibility for the detection of cosmic rays using Cherenkov light beamed in forward direction of the extensive air shower (EAS) [187].

Figure 6.31: Left: photograph of the IceCube laboratory near the Scott-Amundsen South Pole station. Here, all data cables of the IceCube detector converge to the central data acquisition. The IceAct Cherenkov telescope prototype has been installed on the roof of this station in November 2015. Data taking is scheduled for the polar night beginning in May 2016. The trigger of the telescope is fed to IceCube to seek for coincidences with cosmic rays measured by the observatory [187] (image by Felipe Pedreros, IceCube/NSF). Right: photograph taken after the successful commissioning of the IceAct prototype telescope. By detecting the Cherenkov light of extensive air showers, it could provide a veto for the IceCube detector to select events from astrophysical neutrinos (image courtesy of J. Auffenberg, RWTH Aachen University).

The prototype with the name IceAct (IceCube Air Cherenkov telescope) has been successfully installed in November 2015 on the roof of the IceCube central data taking facility (cf. figure 6.31). After the commissioning, data of the dark noise of the focal plane have been taken to set a trigger threshold and to test the data link to the IceCube detector readout system. The link is provided by a data acquisition module of the IceCube observatory which provides IceCube trigger timestamps for comparison to self-triggered EAS events recorded by IceAct. After nightfall at the South Pole in May 2016, telescope lid has been opened and data taking has been started.

The aim of the prototype is to study the feasibility of such a telescope at the South Pole. If successful, the telescope can provide a veto for the IceCube detector to distinguish between atmospherical neutrinos created during the development of EASs and astrophysical neutrinos. Furthermore, fully equipped telescopes with 61 pixels could provide a cost-efficient extension of the field of view of the existing IceCube veto for inclined showers of which the number of recorded astrophysical neutrinos would greatly benefit. The estimated cost of each telescope is 10 000€ [187].

CHAPTER 7

Detector simulation of FAMOUS

Detector simulations are substantial to the understanding and improvement of experiments since they predict the response of the experiment given certain signals and can uncover shortcomings of the detector design.

In case of the telescope FAMOUS, the central part of the detector simulation is a detailed Geant4 model used for the ray-tracing of light through the optical system. By the simulation of parallel light beams, the efficiency of all optical components can be obtained separately.

Finally, simulations of extensive air showers (EASs) have been performed involving a chain of several simulation programs. Beginning with the simulations of EASs, the energy deposit in the atmosphere is simulated by the CONEX software [41]. This information is used by the Auger Offline software framework to simulate the emittance of fluorescence light along the axis of the shower and to track the light through the atmosphere to the telescope [188]. Then, this light can be traced through FAMOUS with the Geant4 simulation code developed in this thesis. As a result, the SiPM signals of EASs can be simulated and used to study trigger algorithms for an efficient self-triggering of the readout electronics which is currently under construction. A first approach of a trigger simulation and event reconstruction has been made in [133].

As discussed below in this chapter, especially the last simulation step is computationally intensive. Thus, a parameterization of the telescope FAMOUS has been derived which allows a quasi instantaneous prediction of the number of photons detected by the SiPMs of the camera of FAMOUS and the application of the aforementioned trigger simulation.

7.1 Ray-tracing simulations of FAMOUS

The ray-tracing simulation of the FAMOUS telescope implements all optical components of the telescope as well as mechanical features such as the telescope tube. Due to the modular software development approach, each component of the telescope can be simulated separately.

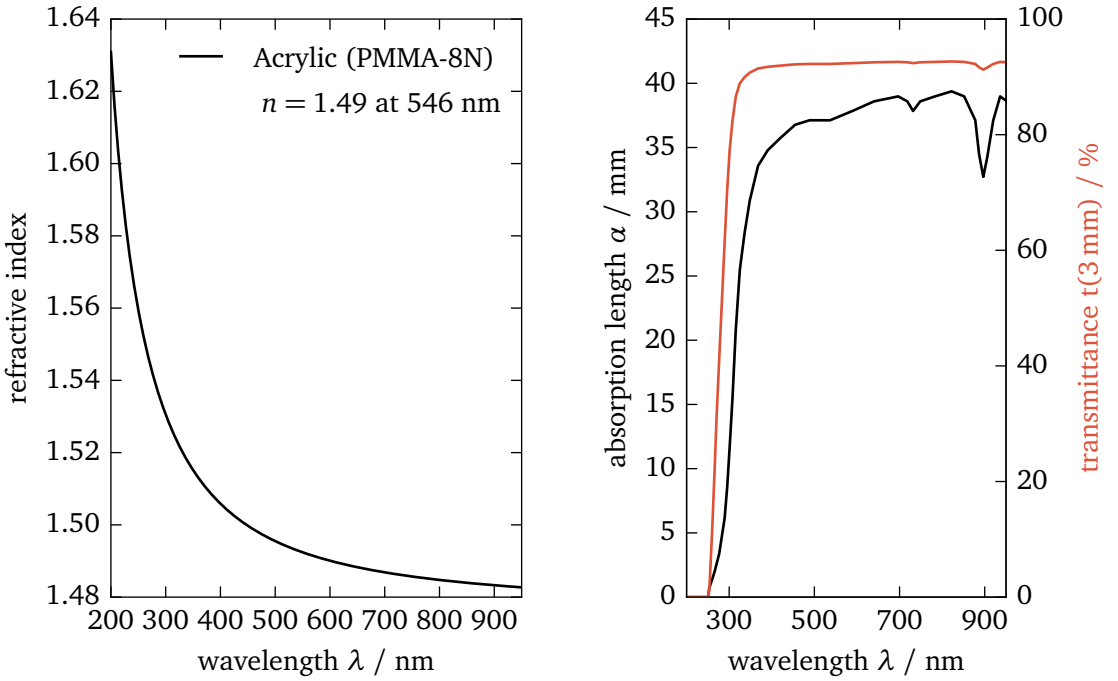

Figure 7.1: Left: refractive index of PMMA as a function of the photon wavelength λ. The data has been taken from [189] and matches the data used by the manufacturer of the lens [144]. Right: the absorption length for PMMA as a function of the photon wavelength. The values have been calculated from the internal transmittance measured by the supplier for a material thickness of 3 mm [144]. These values do not include losses due to reflections at optical boundaries.

7.1.1 Fresnel lens

The Fresnel lens is a compound object made from many concentric hollow cones, also referred to as grooves, placed on a common base plate (cf. section 6.1). The number of grooves per millimeter is given by n_g. The height of a conventional thick plano-convex lens at a certain radial distance ρ from the center of the lens relative to $\rho = 0$ is given by the so-called sagitta function [190]

$$s(\rho) = \frac{c\,\rho^2}{1+\sqrt{1-(1+k)\,c^2\,\rho^2}} + \sum_i a_i^{2i} \tag{7.1}$$

with the curvature c, the conic constant k and the aspheric parameters a_i. In principle, the aspheric parameters can be used to accurately optimize the lens which is beyond the scope of this thesis. The curvature c of the lens can be calculated by the lensmaker's equation with small corrections for the lens thickness d

$$c = \left[\frac{n_{\text{lens}} - n_{\text{air}}}{n_{\text{air}}}\left(f + \frac{n_{\text{air}}}{n_{\text{lens}}}d\right)\right]^{-1} \tag{7.2}$$

with the nominal focal length f of the lens and the refractive index of the lens n_{lens} and the refractive index of air n_{air} calculated for the reference wavelength of 546 nm [191]. The conic

constant k, also referred to as Schwarzschild constant, is a quantity used to describe conic sections whereby $k = 0$ refers to a sphere, $k = -1$ to a parabola and $k < -1$ to a hyperbola [190]. For lenses, a value of $k = -1$ is preferred since parabolic lens surfaces cancel spherical aberration. Using equation (7.1), the height of the i-*th* groove is given by

$$h_i = s\left((i+1)\, w_g\right) - s\left(i\, w_g\right) \quad \text{with} \quad w_g = n_g^{-1} \quad . \tag{7.3}$$

The height of the grooves increases with increasing i and thus with increasing ρ to resemble the original convex lens surface as close as possible.

For a detailed simulation, the refractive index as well as the absorption length of the lens material as a function of the photon wavelength have been implemented (cf. figure 7.1) using a Sellmeier equation [192]

$$n^2(\lambda) = 1 + \frac{0.99654\lambda^2}{\lambda^2 - 0.00787\,\mu\text{m}^2} + \frac{0.18964\lambda^2}{\lambda^2 - 0.02191\,\mu\text{m}^2} + \frac{0.00411\lambda^2}{\lambda^2 - 3.85727\,\mu\text{m}^2} \tag{7.4}$$

whereas the empirical constants for PMMA have been obtained from [189, 193]. This correctly models the dispersion of the light inside the material leading to chromatic aberrations.

To improve the light collection of rays far off the optical axis of the Fresnel lens, the perpendicular faces of the Fresnel lens can be tilted (cf. section 6.1). This so-called draft angle of the Fresnel lens of FAMOUS is

$$\psi(\rho) = 3^\circ + 0.0473^\circ\,\text{mm}^{-1}\,\rho \tag{7.5}$$

whereby the lower limit $\psi_0 = 3^\circ$ is given by the manufacturing process [144, 150].

7.1.1.1 Simulation of the size of the point spread function

A crucial property of lenses is the size of the point spread function, i.e. the distribution function of the energy of an indefinitely distant point light source in the image plane. For a perfect lens with circular aperture and no aberrations, this distribution function is a special diffraction pattern referred to as Airy pattern or Airy disk [194, 195]

$$I(\theta) = I_0 \left(\frac{2J_1(k\,a\sin\theta)}{k\,a\sin\theta} \right)^2 \tag{7.6}$$

with the wavenumber $k = 2\,\pi/\lambda$, the aperture radius a, the angle θ between the optical axis and the point in the image plane and the first kind and first order Bessel function J_1. The parameter I_0 is the maximum intensity for $\theta = 0$. This equation can be simplified by introducing the abbreviation

$$x = k\,a\sin\theta \approx \frac{2\pi}{\lambda}\, a\, \frac{r}{f} = \frac{\pi}{\lambda\, n_f}\, r \tag{7.7}$$

with the radial distance r from the optical axis and the f-number n_f of the lens. The f-number is the quotient of focal length f and aperture diameter d

$$n_f = \frac{f}{d} \quad . \tag{7.8}$$

An important observable for the image quality is the aberration radius r_{90}, i.e. the radius of a circle containing 90 % of the energy in the image plane (cf. section 6.1.1). The total energy contained in a fraction of the diffraction pattern can be obtained by integration

$$P(x) = P_0[1 - J_0^2(x) - J_1^2(x)] \tag{7.9}$$

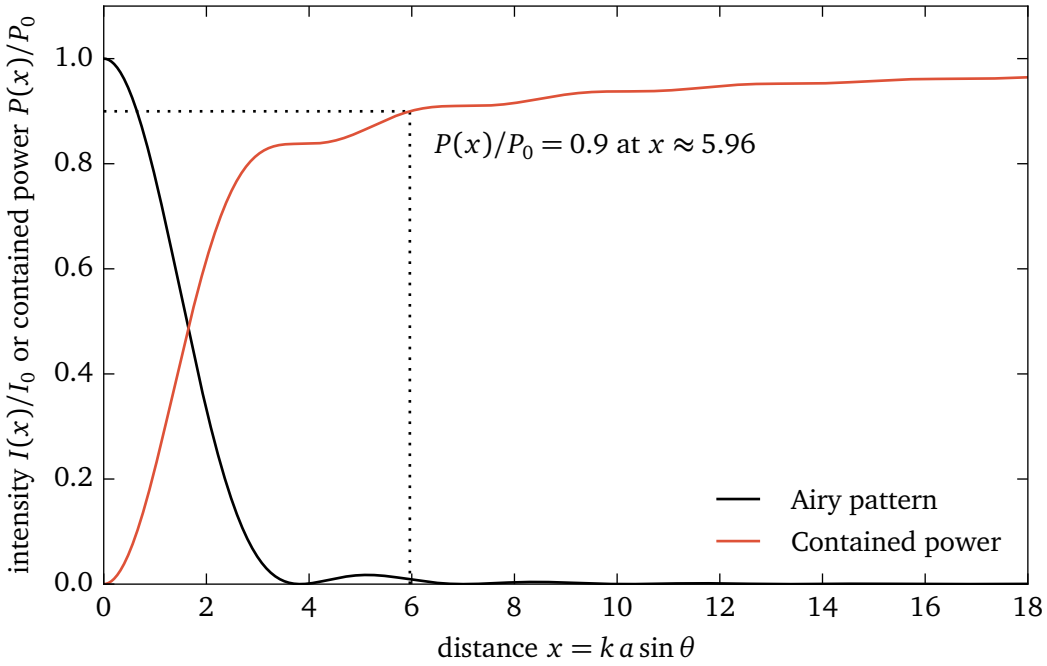

Figure 7.2: The calculated intensity distribution of a point light source at infinite distance in the image plane of a perfect lens with circular aperture, also referred to as Airy pattern. The independent variable x is a measure for the distance to the optical axis (cf. text). Marked by the dotted lines is the aberration radius r_{90} which corresponds to a circle containing 90 % of the energy in the image plane.

with the Bessel functions J_0 and J_1. A plot of the Airy pattern and its integral can be found in figure 7.2. It can be found that $P(\theta) = 0.9P_0$ for $x \approx 5.96$. By plugging in the values for the Fresnel lens of FAMOUS ($n_f = 1$, $\lambda = 546\,\text{nm}$) it can be derived that the perfect lens would produce a small aberration radius of $r_{90} = 1.04\,\mu\text{m}$. Consequently, the optimal lens focal plane distance is the distance at which r_{90} is minimal.

The aberration radius r_{90} can also be easily obtained by ray-tracing simulations. A large number of parallel, monochromatic rays has to be traced through the lens to the image plane. As a result, the directions $\vec{m}_i$ and intersection points $\vec{p}_i$ of each ray $i = 1, \ldots, N$ with the image plane are known. In analogy to the measurement, the mean position of all rays on the image plane yield the so-called centroid, i.e. the position of the image in the image plane

$$\vec{c} = \frac{1}{N} \sum_{i=1}^{N} \vec{p}_i \quad . \tag{7.10}$$

The radial distance of the ray intersection points and the centroid is $r_i = |\vec{c} - \vec{p}_i|$. By sorting all rays by their radial distance in ascending order into a list of length N

$$R = \{r_1, \ldots, r_i, \ldots, r_N | r_{i-1} \leq r_i\} \tag{7.11}$$

the aberration radius is given by the element $r_{90} = R(\lceil 0.9N \rceil)$. A best value of

$$r_{90} = (1.98 \pm 0.03)\,\text{mm} \tag{7.12}$$

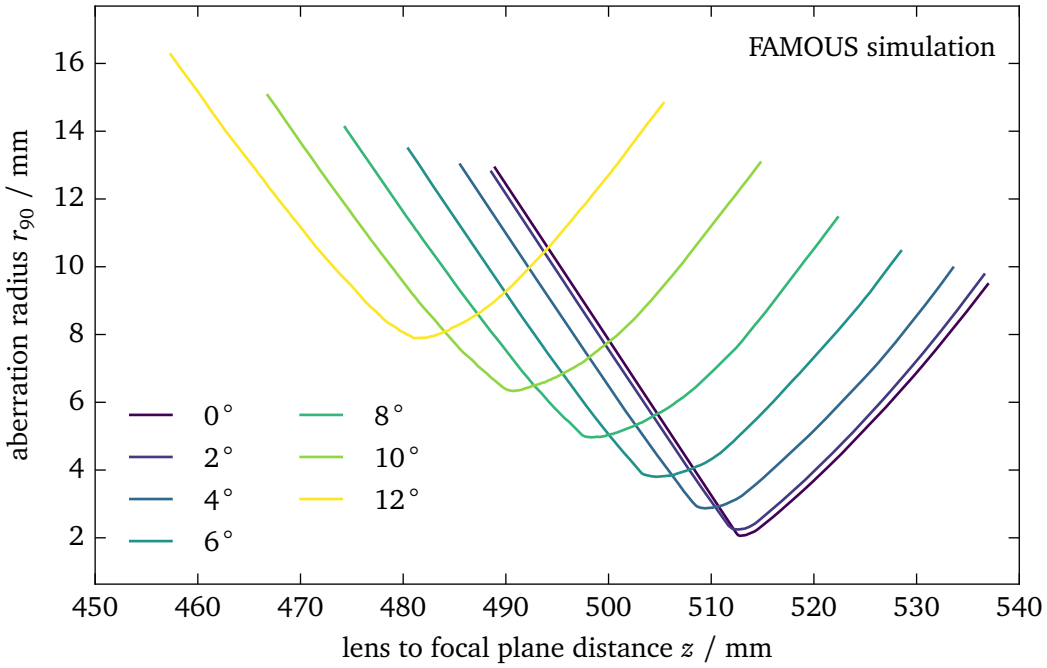

Figure 7.3: The simulated aberration radius r_{90} as a function of the lens to focal plane distance. For each line, one simulation with 10 000 rays has been performed. The information on point of incidence and ray direction has been used to calculate the value of r_{90} for different lens to focal plane distances z.

is found for the Fresnel lens of FAMOUS with $n_g = 10\,\mathrm{mm}^{-1}$ which is in agreement with previous studies [131, 149, 150]. This value is larger by three orders of magnitude compared to the value calculated by the Airy pattern which is to be expected due to the fragmented lens surface as each groove on the lens contributes its own Airy pattern to the point spread function (cf. [150]). The measurement of the aberration radius yields a slightly larger value of $(3.24 \pm 0.03)\,\mathrm{mm}$ (statistical uncertainty only) due to imperfections of the lens and diffraction at the grooves of the lens. The latter has been investigated in depth in [150]. Nevertheless, the aberration radius is small enough for the application in FAMOUS.

Since the directions $\vec{m}_i$ of the rays are known, the intersection points of the rays with an image plane at a different distance to the lens z can be calculated directly. Thus, the aberration radius r_{90} can be derived as a function of z without performing further simulations (cf. figure 7.3). Therefore, the optimal lens focal plane distance can be found by minimizing r_{90} as a function of z to obtain $r_{90,\mathrm{min}}$. Figure 7.4 presents the aberration radius $r_{90,\mathrm{min}}$ and its corresponding z as a function of the incidence angle as well as the transmission efficiency. Both quantities get deteriorated as the angle of incidence gets larger.

Lastly, with the distance ρ of the centroid from the optical axis, the curvature of field can be determined (cf. figure 7.5). A fit of a parabola to the minimum r_{90} for each simulated incidence angle yields

$$z(\rho) = (2.75 \pm 0.06) \cdot 10^{-3}\,\mathrm{mm}^{-1}\,\rho^2 + (513.0 \pm 0.1)\,\mathrm{mm} \quad . \tag{7.13}$$

Thus, the point of optimal focus for perpendicular light incidence is found for a lens focal plane

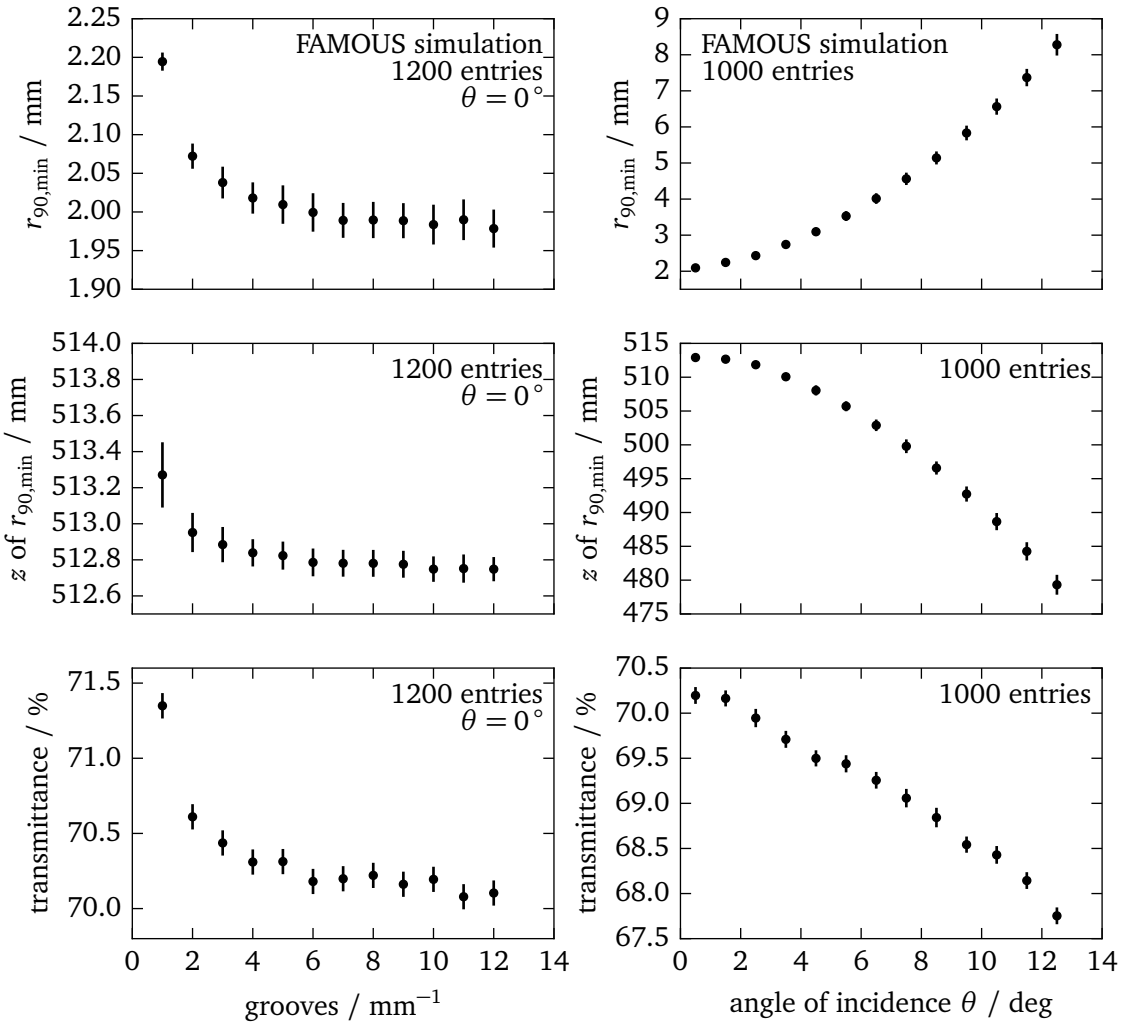

Figure 7.4: Left: minimum possible aberration radius $r_{90,\min}$, lens to focal plane distance z of $r_{90,\min}$ and the transmittance as a function of the number of grooves per millimeter simulated for the Fresnel lens of the FAMOUS telescope for perpendicular light incidence. The more grooves are situated on the lens, the closer the shape of the thick lens is reproduced. Thus, the aberration radius $r_{90,\min}$ asymptotically decreases to a value of $\approx 1.98\,\text{mm}$. The same applies to the lens to focal plane distance z which decreases to a value of $\approx 512.8\,\text{mm}$. However, the increased number of fringes reduces the transmittance. Right: the same quantities as a function of the angle of incidence θ of a parallel light beam on the Fresnel lens of FAMOUS for $n_g = 10\,\text{mm}^{-1}$. With increasing angles of incidence, the aberration radii increase and the transmission decreases signifying a degraded image quality.

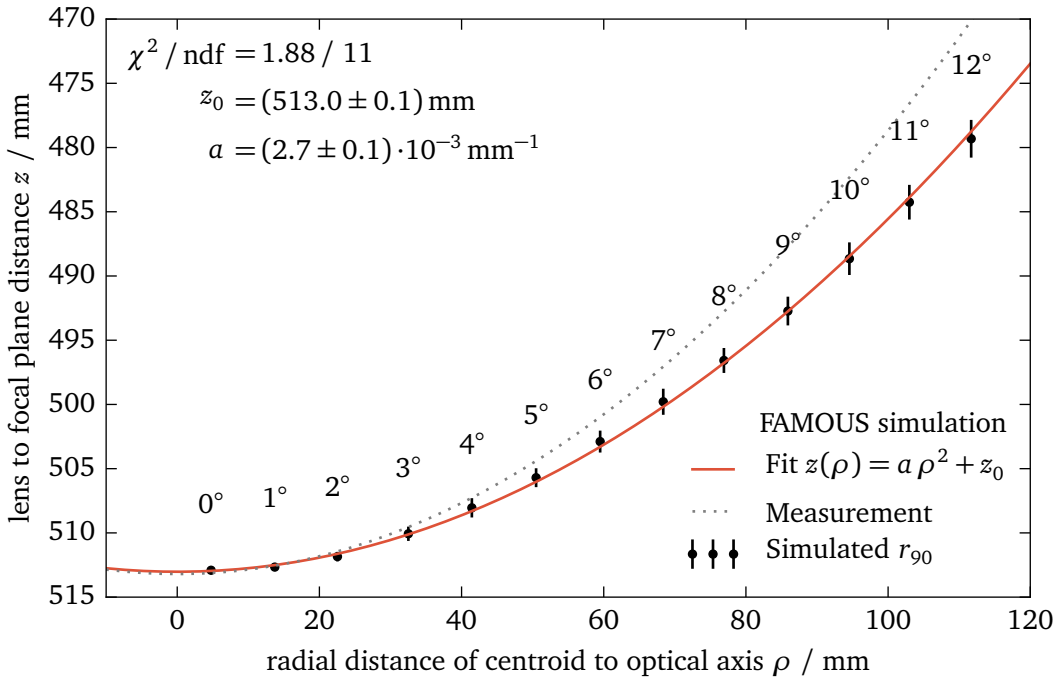

Figure 7.5: The simulated lens focal plane distance z as a function of the radial distance ρ of the centroid on the image plane with respect to the optical axis. A parabola is fitted to the data to reveal the curvature of field of the lens.

distance $z(0) = (513.0 \pm 0.1)$ mm. To closely match the measurement (cf. section 6.1.1), the nominal focal length of the Fresnel lens in the simulation has been optimized by reducing the f-number from 1 to

$$n_f = 0.9925 \quad . \tag{7.14}$$

If the value of r_{90} would not be sufficient for larger angles of incidence, the focal plane could be constructed to follow this parabola to ensure that each pixel is illuminated by the smallest point spread function possible. However, the curvature of field obtained by the simulations is smaller than the measured curvature of field. A possible explanation can be found either in the remaining, large systematical uncertainties of the measurement or the missing simulation of diffraction in Geant4.

7.1.1.2 Simulation of the optical aberrations of the Fresnel lens

To understand the structures apparent in the measured point spread functions (cf. section 6.1.1), the wavefront errors of the Fresnel lens can be determined. In optical theory, there is a functional relation between the wavefront error and the measurable point spread function [196]. For ray-tracing, the wavefront is a plane of equal optical path length of all simulated rays. The optical path length l is the geometrical path length s weighted with the refractive index n as a function of the position [197]

$$l = \int n(s)\mathrm{d}s \quad . \tag{7.15}$$

j	n	m	aberration	j	n	m	aberration
0	0	0	piston	11	4	-2	2nd oblique astigmatism
1	1	-1	vertical tilt	12	4	0	primary spherical
2	1	1	horizontal tilt	13	4	2	2nd vertical astigmatism
3	2	-2	oblique astigmatism	14	4	4	vertical quadrafoil
4	2	0	defocus	15	5	-5	vertical pentafoil
5	2	2	vertical astigmatism	16	5	-3	2nd vertical trefoil
6	3	-3	vertical trefoil	17	5	-1	2nd vertical coma
7	3	-1	vertical coma	18	5	1	2nd horizontal coma
8	3	1	horizontal coma	19	5	3	2nd oblique trefoil
9	3	3	oblique trefoil	20	5	5	oblique pentafoil
10	4	-4	oblique quadrafoil	21	6	-6	...

Table 7.1: Aberrations associated with the moments n and m of the Zernike polynomials [196, 198]. The index j is calculated according to the ANSI single indexing scheme (cf. equation (7.19)).

When the rays pass the lens, an initially planar wavefront gets bend to a spherical wavefront. Due to the groove structure of the lens, the rays have slightly different optical path lengths, which leads to a deviation from the perfect spherical wavefront. This deviation is referred to as wavefront aberration or wavefront error [196].

7.1.1.3 Description of wavefront aberrations with the Zernike polynomials

Wavefront aberrations can be expressed mathematically by means of the so-called Zernike polynomials [196] . These polynomials are a sequence of orthogonal polynomials as a function of the polar coordinates $\rho \in [0,1]$ and $\phi \in [0, 2\pi]$ which denote a point in the entrance aperture, i.e. the aperture of the Fresnel lens, with the radius of the aperture normalized to one. Thus, these coordinates are also referred to as pupil coordinates. The polynomials are

$$Z_n^m(\rho,\phi) = R_n^m(\rho)\cos(m\,\phi) \tag{7.16}$$

$$Z_n^{-m}(\rho,\phi) = R_n^m(\rho)\sin(m\,\phi) \tag{7.17}$$

with $n \geq m$. The radial polynomials R_n^m are given by

$$R_n^m(\rho) = \begin{cases} \sum_{k=0}^{(n-m)/2} \frac{(-1)^k (n-k)!}{k!((n+m)/2-k)!((n-m)/2-k)!}\rho^{n-2k} & n-m \text{ even} \\ 0 & \text{otherwise} \end{cases} \tag{7.18}$$

For an easier and unambiguous abbreviation of the indices m and n, an ANSI standard notation (American National Standards Institute) has been introduced which reduces the two indices m and n to a single indexing scheme with index j [198]

$$j = \frac{n(n-2)+m}{2} \quad . \tag{7.19}$$

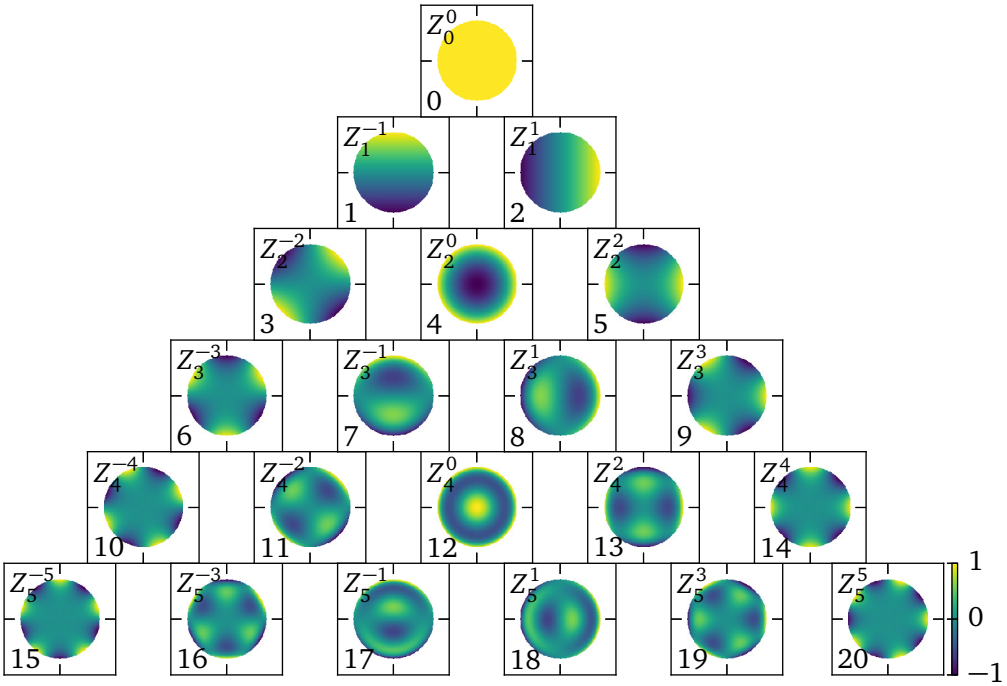

Figure 7.6: Zernike polynomials Z_m^n for the moments n, m given $n-m$ is even for the polar coordinates $\rho \in [0,1]$, $\phi \in [0, 2\pi]$. The number stated in the lower left corner of the plots is the ANSI index j (cf. table 7.1).

A table of indices and their associated optical aberration can be found in table 7.1. Figure 7.6 presents the Zernike polynomials of up to $j = 20$. Finally, any wavefront can be expressed as a weighted sum of Zernike polynomials [127]

$$W(\rho, \phi) = \sum_{j=0}^{N} \omega_j Z_j(\rho, \phi) \quad . \tag{7.20}$$

Traditionally, the wavefront error is expressed in number of photon wavelengths λ whereby the absolute value of the error is scaled by the corresponding weight ω_j.

The wavefront error of the Fresnel lens of FAMOUS has been simulated using the commercial program ZEMAX OpticStudio [199] which also has been used successfully to simulate and optimize the optics of the Fresnel lens [159]. Here, the wavefront is computed in discrete bins with Cartesian coordinates $x = \rho \cos\phi$ and $y = \rho \sin\phi$. Thus, the wavefront can be expressed as a matrix

$$\mathbf{W} = \sum_{j=0}^{N} \omega_j \, \mathbf{Z_j} = \mathbf{Z}\, \omega \tag{7.21}$$

with the Zernike polynomials $\mathbf{Z_j}$ calculated for the given grid of x and y. An ordinary least squares regression yields the weights ω_j

$$\hat{\boldsymbol{\omega}} = (\mathbf{Z}^T \mathbf{Z})^{-1} \mathbf{Z}^T \mathbf{W} \quad . \tag{7.22}$$

The results of these simulations for perpendicular and inclined light incidence are presented in figure 7.7. Two important results can be obtained from the wavefront simulations. Firstly,

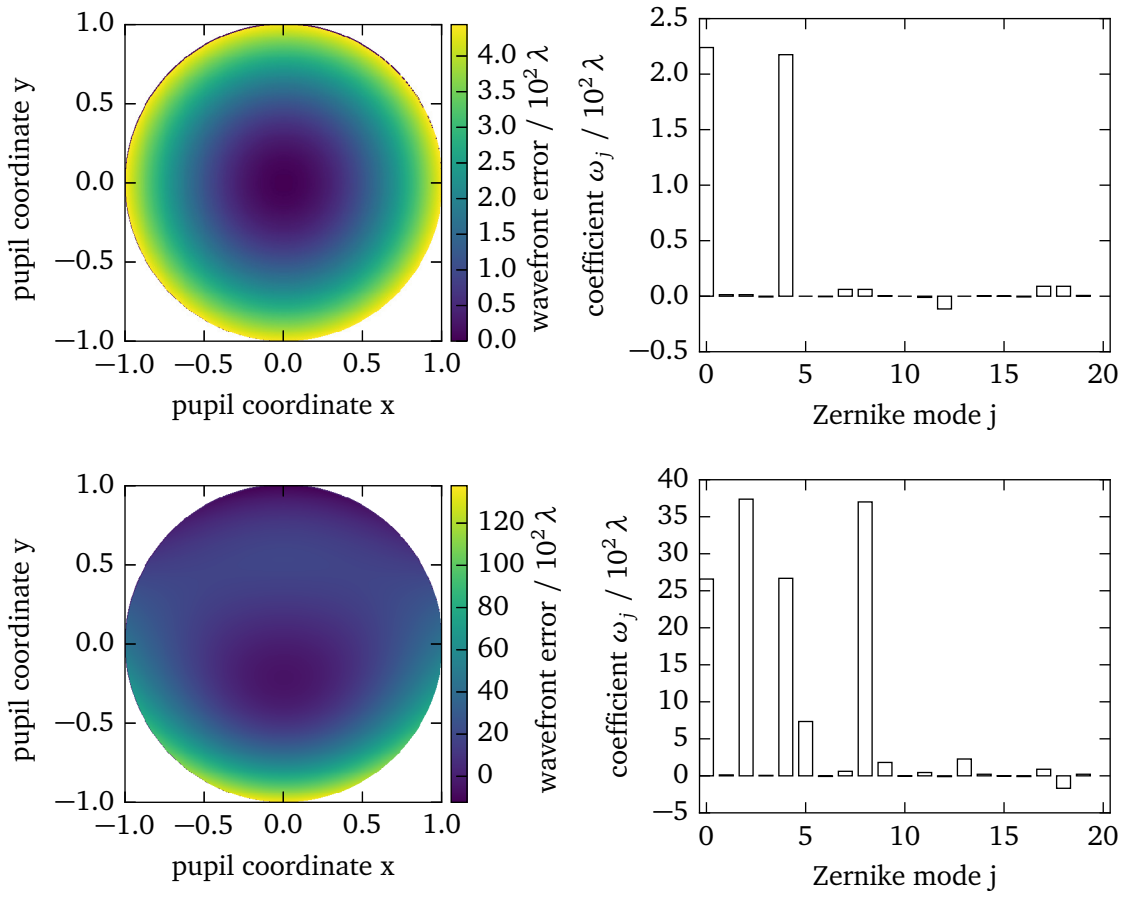

Figure 7.7: Wavefront error of the parabolic Fresnel lens of FAMOUS simulated with the commercial program ZEMAX OpticStudio [199] and decomposed into Zernike polynomials. Top: results for perpendicular light incidence. Here, the Fresnel lens only suffers from defocus which means, that the calculated focal length of the Fresnel lens differs from the effective focal length. Bottom: results for $\theta = 12°$ inclined light incidence. Additionally to the defocus, the lens suffers from coma which is expected. The contribution to the tilt is an artifact of the inclined light incidence and can be ignored. Furthermore, minor contributions can be seen for higher j, which would contribute to the star like structures seen in the measurements (cf. section 6.1.1). It is likely, that for the real pendant of the lens, the contributions of higher order aberrations is larger than simulated.

a large contribution for the component $j = 4$ corresponds to a defocus of the lens. This means that the optimal lens to focal plane distance is not equal to the focal length of the lens and has to be determined by means of measurements or simulations as discussed previously. Secondly, for inclined light incidence, the components corresponding to astigmatism and coma gain importance and contribute to the aberration radius r_{90}. For inclined light incidence, the circular image of a point source appears distorted into a wedge shaped structure due to coma. This effect increases with inclination which potentially spreads the light over several pixels. All these effects are correctly reproduced in the Geant4 simulation of the Fresnel lens.

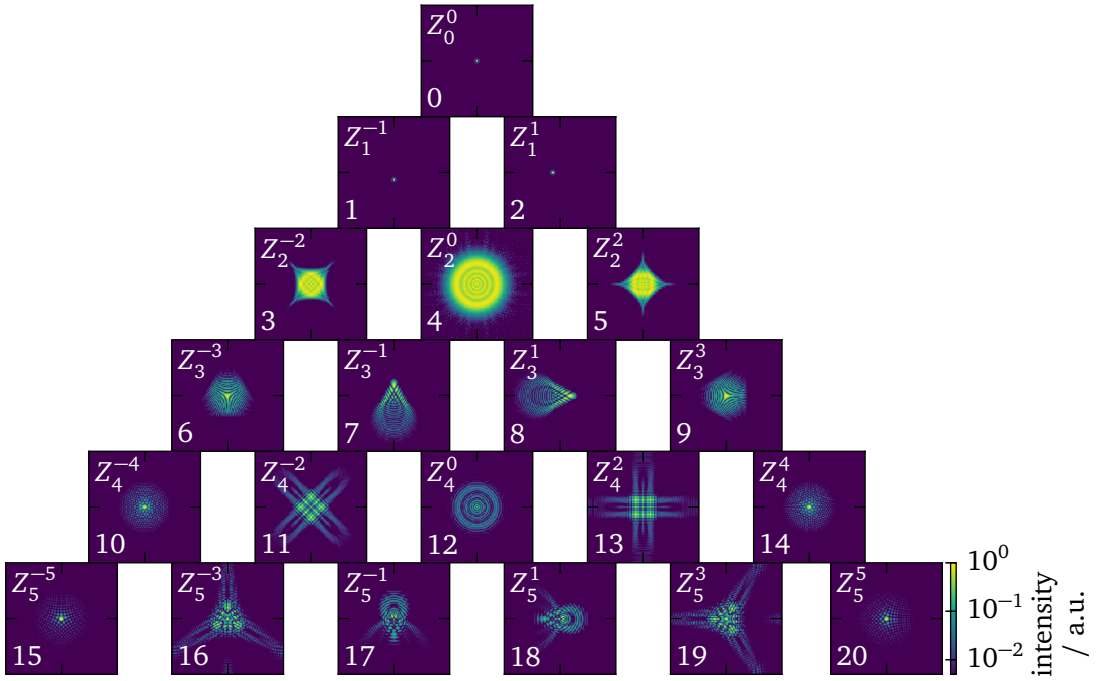

Figure 7.8: Zernike polynomials Z_m^n transformed into point spread functions for the moments n, m given $n-m$ is even for the polar coordinates $\rho \in [0,1]$, $\phi \in [0, 2\pi]$. The number stated in the lower left corner of the plots is the ANSI index j (cf. table 7.1).

7.1.1.4 Calculation of the point spread function

Now, the wavefront can be used to calculate the pupil function

$$P(\rho,\phi) = \alpha(\rho,\phi)\exp(i\,k\,W(\rho,\phi)) \tag{7.23}$$

with the wavenumber k and a pupil mask $\alpha(\rho,\phi)$ which is in our case $\alpha = 1$ but could be used to introduce an obstruction of the aperture as for example in some mirror telescope designs [127]. The Fourier transform of the pupil function yields the point spread function

$$PSF(\rho,\phi) = |\mathscr{F}(P(\rho,\phi)|^2 \quad . \tag{7.24}$$

The point spread functions of the single Zernike polynomials are presented in figure 7.8. The star like structures for $j > 11$ already have been seen in the measurement (cf. section 6.1.1). Thus, although all mechanical features of the Fresnel lens of FAMOUS are of circular nature, small mechanical deformations can contribute to the higher order wavefront aberrations which are expressed by the apparent star like structures. These high order aberrations possibly originate from surface imperfections, which are not rotationally symmetric, or scratches.

7.1.2 Winston cones

The circular Winston cones of the telescope FAMOUS have the purpose of increasing the sensitive area of the SiPMs to increase the signal, i.e. the fluorescence light of EASs, over the SiPM

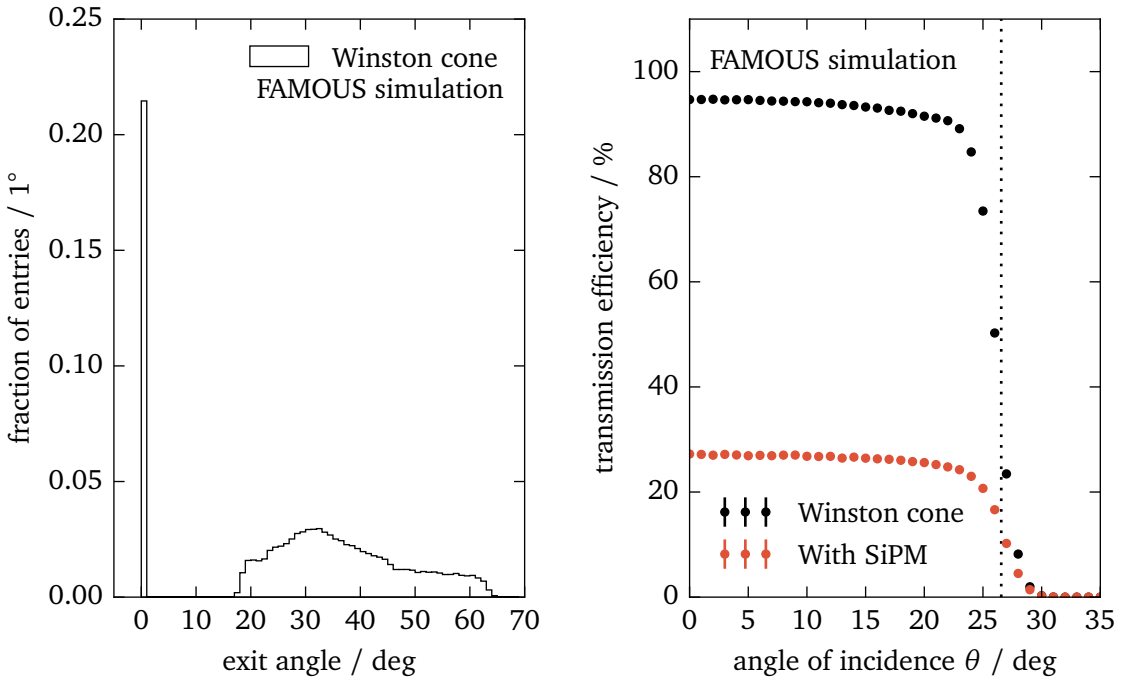

Figure 7.9: Left: simulated exit angle distribution for perpendicular light incidence. Light entering in the central area of the entrance of the cone can pass the cone directly, light entering trough the outer areas has to be reflected at least once leading to a large exit angle which could be a challenge if paired with a SiPM. Right: the transmission efficiency as a function of the angle of incidence simulated for a Winston cone of FAMOUS ($r_1 = 6.71\,\text{mm}$, $r_2 = 3.00\,\text{mm}$) at a wavelength of $\lambda = 550\,\text{nm}$. Near the corresponding maximum acceptance angle of $\theta_{\text{max}} = 26.56°$, the transmission efficiency of the cone rapidly drops to zero. The lower points denote a simulation performed in conjunction with the FAMOUS SiPM Hamamatsu S12573-100X placed at the exit. The PDE of the SiPM at this wavelength is $PDE(550\,\text{nm}) = 29\,\%$.

noise ratio. At the same time, the amount of background light is reduced by blocking stray light. The latter is achieved by construction, due to a maximum acceptance angle

$$\theta_{\text{max}} = \arcsin\left(\frac{r_2}{r_1}\right) \tag{7.25}$$

with the radius of the entrance r_1 and the radius of the exit r_2 [158]. The length of the Winston cone is given by

$$l = \frac{r_1 + r_2}{\tan\theta_{\text{max}}} \quad . \tag{7.26}$$

More information on the construction principle of Winston cones can be found in section 6.2 and in [131, 149, 158].

Light with incidence angles larger than θ_{max} can not pass the cone and is reflected back through the entrance. Yet, a small portion of this light might be transmitted due to naturally occurring surface imperfections of the polished aluminum. Additionally, it is expected that the aluminum develops a thin layer of aluminum oxide which might introduce a small loss

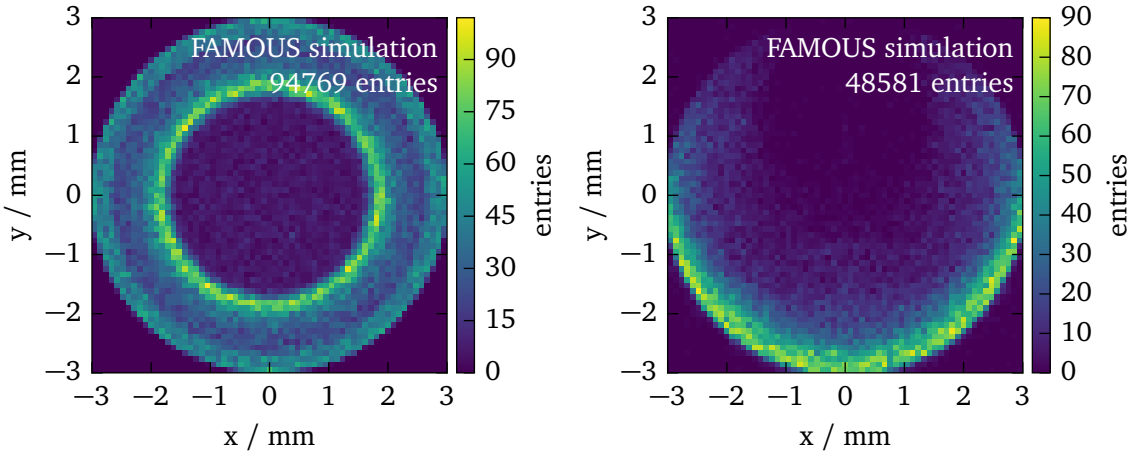

Figure 7.10: Left: exit positions of light rays for a parallel beam of 100 000 rays with an angle of incidence of $\theta = 0°$ with respect to the optical axis of the cone. Right: exit positions of the rays for a parallel beam of 100 000 rays with an angle of incidence of $\theta = \theta_{max} = 26.56°$ originating from the lower border of the Winston cone entrance.

of reflectivity $\approx 15\,\%$ [157] which is not included in the simulations. To model surface imperfections, the Geant4 framework simulates micro-facets by adding randomized tilts to the surface normal when calculating the angle of reflection [200]. The tilt angle is picked from a Gaussian distribution with mean zero and the standard deviation equal to a user chosen value σ_α. In this case, the standard deviation of the angle has been set to $\sigma_\alpha = 0.45°$ to match the measurements performed in [157].

The Winston cones of FAMOUS have an entrance radius of $r_1 = 6.71\,\text{mm}$ and an exit radius of $r_2 = 3.00\,\text{mm}$ which corresponds to $l = 19.43\,\text{mm}$ and $\theta_{max} = 26.56°$. Figure 7.9 presents the transmission efficiency as a function of the angle of incidence and the exit angle distribution for perpendicular light incidence. As expected, the transmission efficiency drops to zero for angles around θ_{max}. The portion of the light, which enters the Winston cone in the central region of the entrance area, passes the cone without reflection, whereas the other portion gets reflected at least once and reaches the exit under larger angles of up to 60°. This can present a challenge for the SiPM due to the intrinsic reflectivity of its surface for inclined light (cf. figure 5.5 in section 5.3.2) but the effect has been found to be almost negligible. Thus, the Winston cone is a good option for increasing the light collection area of the SiPM. The exit locations of the rays are presented in figure 7.10. For inclined light incidence, the exit light is focused to a small region of the exit area which can pose a problem for high incoming light fluxes. This effect is automatically included in the simulation of the full telescope by using G4SiPM for the simulation of the SiPMs (cf. chapter 5).

7.1.3 FAMOUS telescope

The simulation of the Fresnel lens and the Winston cones have been discussed in detail. In combination with the detailed SiPM simulation G4SiPM discussed in chapter 5, all necessary components for a complete detector simulation of the FAMOUS telescope are available. Figure 7.11 presents images of the Geant4 visualization of the telescope simulation.

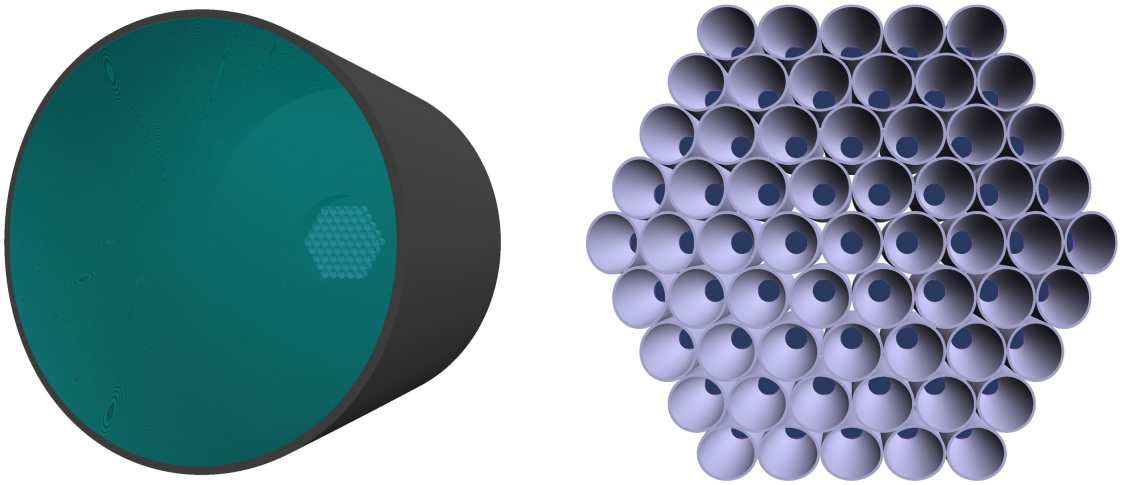

Figure 7.11: Visualizations from the Geant4 simulation of FAMOUS created with the "RayTracer" driver. Left: view of the complete telescope. The tube holds the Fresnel lens, i.e. the translucent element in the front. Behind it, the focal plane is visible. Right: close-up view of the focal plane. The bluish elements at the exits of the single Winston cones are the UG11 filters.

7.1.3.1 Simulation of the lens to focal plane distance dependence

The distance between the lens and the focal plane is critical to the total detection efficiency of the optical system. As discussed in section 7.1.1, the best focus is defined by the distance at which the aberration radius r_{90} is minimal. The behavior of the Fresnel lens in conjunction with the Winston cones, of which the focal plane of FAMOUS is built up, is investigated in the following. For this, the lens to focal plane distance z and the photon wavelength λ have been varied both over a large parameter range

$$z \in \{f - 64\,\text{mm}, f + 64\,\text{mm}\} \quad , \quad \lambda \in \{270, 1020\}\,\text{nm} \tag{7.27}$$

to cover the full photon detection efficiency range of the SiPM and the dispersion of the lens material. The simulations have been carried out for a configuration of the focal plane firstly without UG11 UV band pass filters and secondly with filters (cf. figure 7.12). The results of the simulations without UG11 filter will be used in chapter 9 since these measurements also have been performed without the UG11 filters. The global maximum simulated transmission efficiency obtained in these simulations marks the optimal lens to focal plane distance for FAMOUS. The values obtained without UG11 filter are

$$\epsilon = (18.9 \pm 0.8)\,\% \quad \text{at} \quad \lambda = 454\,\text{nm}, \quad z = 502.3\,\text{mm} \tag{7.28}$$

and with UG11 filter

$$\epsilon = (11.4 \pm 0.6)\,\% \quad \text{at} \quad \lambda = 350\,\text{nm}, \quad z = 485.7\,\text{mm} \quad . \tag{7.29}$$

Hence, the lens to focal plane distance currently applied in the mechanics of FAMOUS is acceptable for the usage without the UG11 filters but should be revised downwards when inserting the filters for the measurement of EASs.

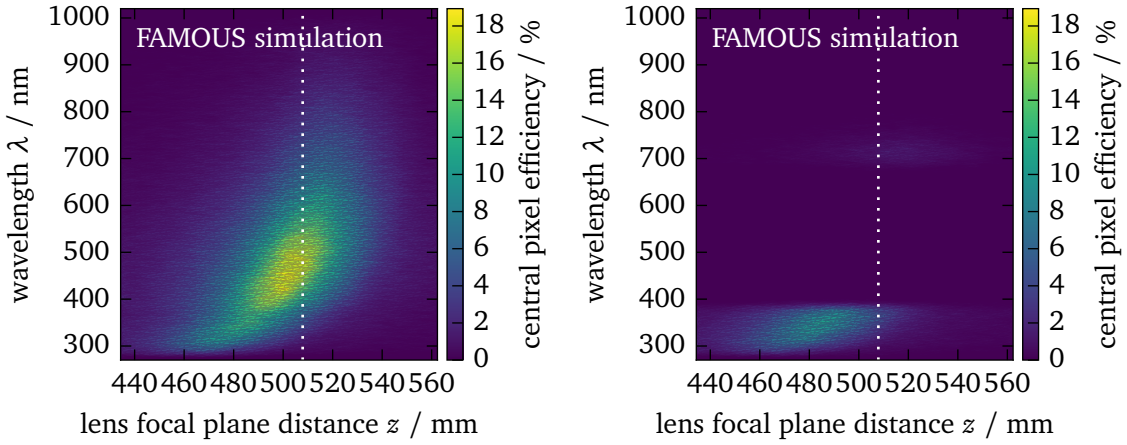

Figure 7.12: Left: simulated detection efficiency of the central pixel of FAMOUS as a function of the lens focal plane distance z and photon wavelength λ. In total, 2^{13} simulations with 3000 rays each without UG11 filter have been performed. The lens to focal plane distance $z = 507.89\,\text{mm}$ of FAMOUS is indicated as white vertical line. Right: simulated detection efficiency of the central pixel of FAMOUS with UG11 filter. Thus, wavelengths $> 400\,\text{nm}$ are suppressed. The points in the two-dimensional parameter space z, λ have been chosen by the Hammersley point picking algorithm which provides a uniformly distributed sampling pattern with large coverage [201]. More details can be found in appendix 4.

7.2 Telescope simulation parameterization

Detailed ray-tracing simulations are very consuming regarding computational resources and computation time. Especially for the simulation of a large set of EASs, likely the same calculations are made over and over again. Therefore, a parameterization of the telescope response can be derived using the Geant4 telescope simulation. The telescope response is given by the detection probability $\epsilon_j(\lambda, \theta, \phi)$ of an incoming photon of wavelength λ and momentum direction θ, ϕ for SiPM j. Here, θ is the polar angle with respect to the optical axis and ϕ is the azimuth angle on the entrance aperture of the telescope. The exact hit position on the aperture of the telescope is insignificant since the large distance between the EAS and the telescope justifies the application of 10-times law. It can be shown that if the distance between a light source and a detector is greater than 10 times the largest dimension of the source, the error made by assuming the source is a point source is less than 1 % [203]. Thus, the shower can be approximated as a point source and the incident position of the shower photons on the entrance aperture of the telescope are purely random. In this case, the EAS is approximated by a set of equidistant point sources along the shower axis. More details can be found in the next section.

As presented above in figure 7.12, the detectable wavelength regime from 270 nm to 400 nm is narrow. Therefore, the dispersion in this regime is negligible and the wavelength dependence of the detection can be simulated separately for perpendicular incidence on the telescope. This permits the decomposition

$$\epsilon_j(\lambda, \theta, \phi) = \frac{\epsilon_0(\lambda, 0, 0)}{\epsilon_0(\lambda_{\text{ref}}, 0, 0)} \epsilon_j(\lambda_{\text{ref}}, \theta, \phi) \tag{7.30}$$

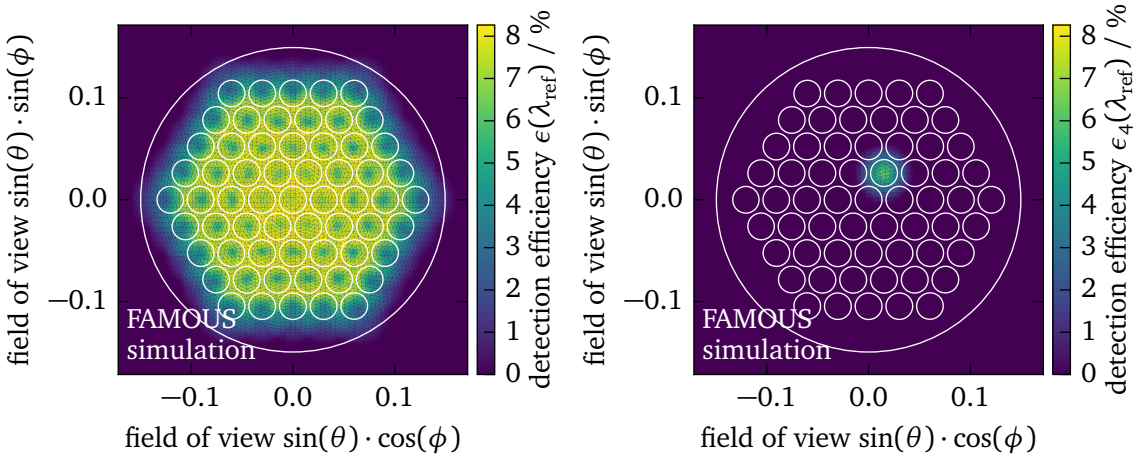

Figure 7.13: Left: simulated detection efficiency of all SiPMs in FAMOUS as a function of the viewing direction θ, ϕ for a reference wavelength of $\lambda_{\text{ref}} = 360\,\text{nm}$. Here, θ is the polar angle with respect to the optical axis and ϕ is the azimuth angle in the plane of the Fresnel lens. The white circles denote the Winston cone entrance apertures of the pixels of FAMOUS. The field of view of the telescope has been divided into bins of equal area by means of the program package HEALpix [202]. More details on HEALPix can be found in appendix 2. The large white circle denotes the field of view border of FAMOUS derived from the simulated data. Right: simulated detection efficiency for a single pixel (pixel 4). Since the point spread function of the Fresnel lens has a diameter of several millimeters, light from near the pixel field of view borders is distributed over several pixels.

with respect to the efficiency of the central pixel $j = 0$ at a reference wavelength $\lambda_{\text{ref}} = 360\,\text{nm}$ which dramatically reduces the computation time. For this wavelength, the detection efficiency of the central pixel is maximal for the applied lens to focal plane distance $z = 507.89\,\text{nm}$ and with UV filters (cf. figure 7.12).

Then, the sky in front of the telescope is divided into solid angle bins of equal area by means of the HEALPix software [202]. The HEALPix software provides algorithms to divide a spherical surface into bins of equal area and is widely used in astroparticle physics. For a description of the HEALPix code please refer to appendix 2. For each HEALPix bin θ_i, ϕ_i in total 10 000 photons with a wavelength of λ_{ref} are uniformly distributed over the entrance aperture of the telescope and traced through the optics. Furthermore, the direction of the photons is randomly distributed over the whole area of the corresponding HEALPix bin. For a good resolution the number of sides of the HEALPix map has been chosen to $n_{\text{side}} = 256$ which corresponds to an angular bin size of $\approx 0.05\,(^\circ)^2$. A maximum zenith angle of $\theta_{\text{max}} = 10^\circ$ is sufficient, to completely cover the field of view of FAMOUS. In total, 5940 HEALPix bins have been simulated. The fraction of detected photons $\epsilon_j(\lambda_{\text{ref}}, \theta_i, \phi_i)$ is recorded separately for each HEALPix bin i and SiPM j.

The detection efficiency $\epsilon(\lambda_{\text{ref}}, \theta_i, \phi_i)$ summed up for all SiPMs j is presented in figure 7.13, left. Here, the maximum recorded efficiency is $\epsilon_j(\lambda_{\text{ref}}, \theta, \phi)|_{\text{max}} = (8.68 \pm 0.29)\,\%$. Furthermore, the field of view of the telescope can be determined by the extent of the HEALPix bins with $\epsilon(\lambda_{\text{ref}}, \theta_i, \phi_i) > 1\,\%$. Thus, the field of view of FAMOUS in its current hardware configuration is $17.2^\circ \times 15.4^\circ$. The enlargement of the field of view in comparison to the design value of

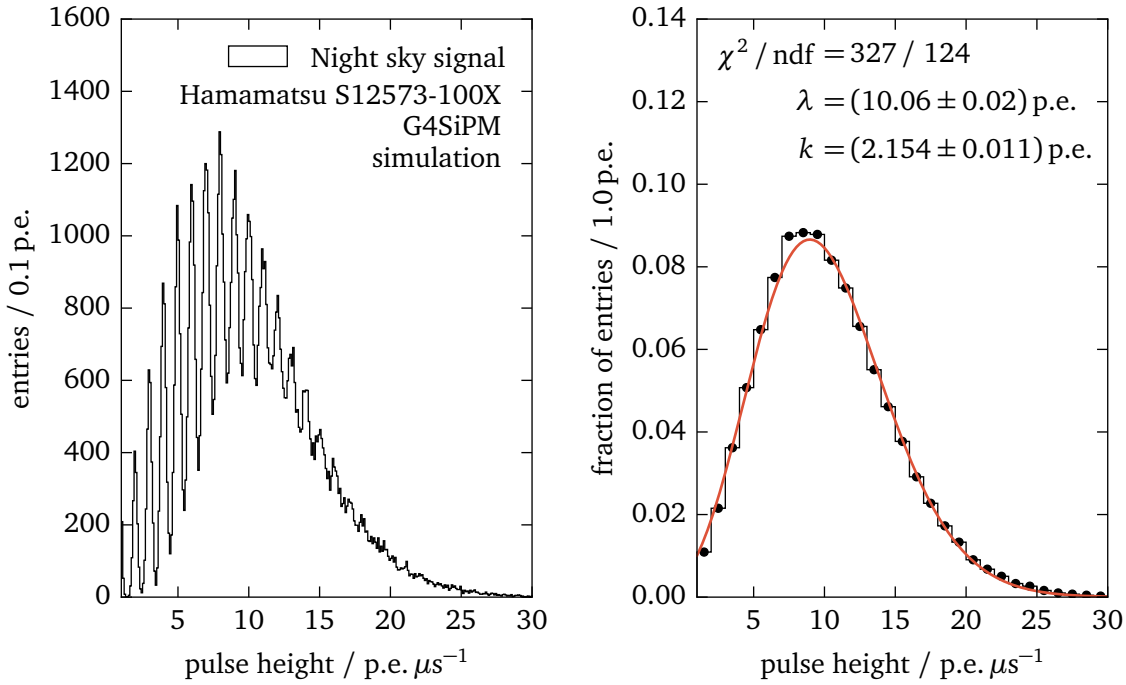

Figure 7.14: Left: simulated pulse height histogram of a SiPM of FAMOUS, Hamamatsu S12573-100X at $v_{ov} = 1.4\,V$ over-voltage, obtained with G4SiPM. The SiPM has been illuminated with photons of $\lambda = 360\,nm$ wavelength at a rate of $f_{nsb,px} = (1.47 \pm 0.26) \cdot 10^7\,s^{-1}$ for the duration of 1 s. The cell triggers have been grouped in time bins of 1 µs width which corresponds to a conservative estimate of the duration of an extensive air shower signal in one pixel. The mean number of thermal noise triggers in a time bin is 2.89. Right: fit of a Poisson distribution to the simulated data to obtain a probability distribution from which the number of photons originating from the night sky background in one pixel can be generated.

$13.5° \times 12.7°$ is caused by the wall thickness of the Winston cones (cf. section 6.2). Figure 7.13, right, presents the detection efficiency $\epsilon_j(\lambda_{ref}, \theta_i, \phi_i)$ for a single SiPM of FAMOUS.

7.2.1 Simulation of the night sky background

Regarding photons originating from the night sky brightness, which is considered as the background in FAMOUS, an absolute diffuse flux of

$$F_{nsb} = (87 \pm 15) \cdot 10^9\,m^{-2}\,sr^{-1}\,s^{-1} \tag{7.31}$$

has been measured in Aachen during dark, moonless nights with a Newton telescope equipped with a Winston cone, an UG11 filter and an SiPM [52]. This value is already corrected for the mean transmission efficiency of the optical system, i.e. the telescope, the Winston cone and the UG11 filter, and is corrected for the mean photon detection efficiency of the used SiPM. The SiPM was a Hamamatsu S10362-33-100C with a sensitive area of $3\,mm^2 \times 3\,mm^2$ and 900 cells which can be considered as a predecessor of the SiPM model mounted in FAMOUS. Since this measurement has been performed with the UG11 filter, the transmitted wavelength spectrum is

very narrow. The wavelength dependence of the Fresnel lens in this regime is negligible. Thus, although the wavelength dependence of this measured value is unknown, it can be applied directly here. With the aperture area A of the Fresnel lens and the solid angle Ω of the field of view of the telescope

$$A = \pi\,(d/2)^2 = 0.198\,\mathrm{m}^2 \tag{7.32}$$

$$\Omega = 2\pi\,(1-\cos\,(\theta_{\mathrm{max}}/2)) = 0.0706\,\mathrm{sr} \tag{7.33}$$

the number of night sky photons per second impinging on FAMOUS derives to

$$f_{\mathrm{nsb}} = (1.21 \pm 0.21)\cdot 10^9\,\mathrm{s}^{-1} \quad . \tag{7.34}$$

Folding this value with the telescope parameterization yields a rate of

$$f_{\mathrm{nsb,px}} = (1.47 \pm 0.26)\cdot 10^7\,\mathrm{s}^{-1} \tag{7.35}$$

for the central pixel. This rate can be used to simulate the number of telescope triggers generated by the night sky background. For this, a G4SiPM simulation with one SiPM of FAMOUS has been performed to illuminate the SiPM with the night sky background rate $f_{\mathrm{nsb,px}}$ at $\lambda = 360\,\mathrm{nm}$ for the duration of 1 s. The detailed trigger simulation of G4SiPM including thermal and correlated noise yields SiPM cell triggers with the number of photon equivalents and time. These triggers have been grouped in time to obtain the number of photon equivalents in 1 µs wide time bins. The chosen time bin width is a conservative estimate for the duration of the shower signal in one pixel of FAMOUS.

The resulting pulse height diagram is presented in figure 7.14. A fit of a scaled Poisson distribution to the simulated data has been performed

$$p_{\mathrm{nsb}}(x) = a\,\frac{(\lambda/k)^{x/k}}{\Gamma\,(x/k+1)}\,e^{-\lambda/k} \tag{7.36}$$

with the number of photon equivalents x, Poisson mean λ, a scale parameter k and the Gamma function which is the generalization of the factorial function to real numbers. The fit yields

$$\lambda = (10.06 \pm 0.02)\,\mathrm{p.e.} \tag{7.37}$$

$$k = (2.15 \pm 0.01)\,\mathrm{p.e.} \quad . \tag{7.38}$$

The probability distribution p_{nsb} of the night sky background can be used to dice a number of detected night sky photons for the SiPMs in FAMOUS when predicting the signal of EASs as discussed in the next section.

7.2.2 Prediction of signals of extensive air showers

The determination of the telescope parameterization $\epsilon_j(\lambda,\theta,\phi)$ permits a quasi instantaneous prediction of the number of photons detected for a simulated shower. An example for this is presented in figure 7.15 for a proton shower with $E = 10^{18.5}\,\mathrm{eV}$ in 5 km distance. The fluorescence light simulation yields the wavelength λ_i, the arrival time t_i and the arrival direction θ_i, ϕ_i of a photon bunch i containing n_i photons. As discussed below, the tracking of the fluorescence light through the atmosphere is carried out for bunches of photons to safe computing time. Thus, the number of detected photons of photon bunch i by pixel j is given by

$$w_{i,j} = n_i\,\epsilon_j(\lambda_i,\theta_i,\phi_i) \quad . \tag{7.39}$$

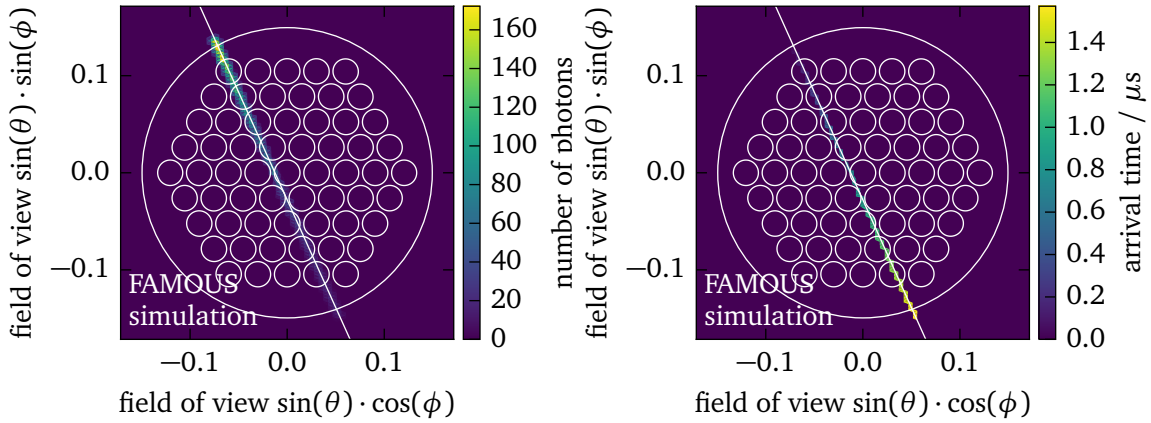

Figure 7.15: Left: simulated arrival directions of fluorescence photons in the field of view of FAMOUS emitted by a proton shower with $E = 10^{18.5}$ eV and 50° zenith angle in 5 km distance. The white circles denote the Winston cone entrance apertures of the pixels of FAMOUS. More details on the shower simulations can be found below in section 7.3. Right: simulated arrival time of fluorescence photons weighted with the telescope response $\epsilon_j(\lambda, \theta, \phi)$ (cf. equation (7.30) and figure 7.13). Here, no night sky background is shown.

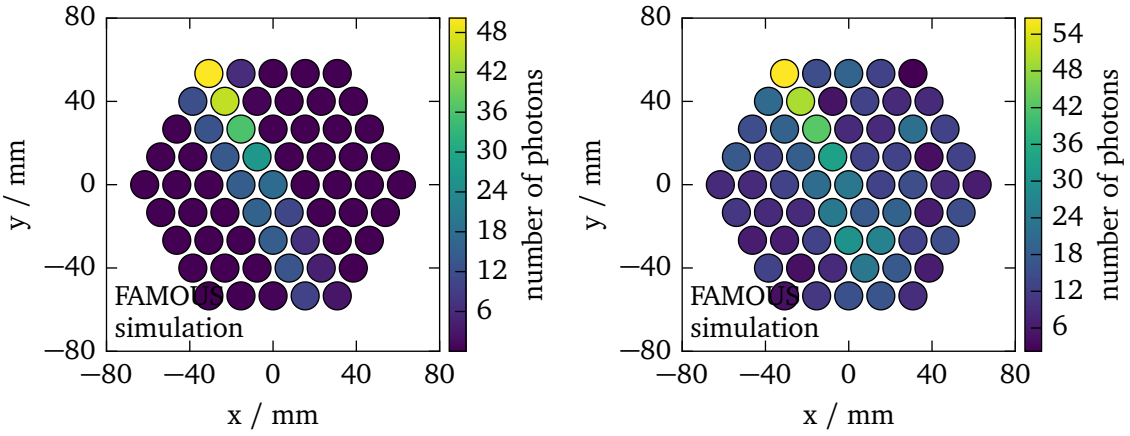

Figure 7.16: Left: simulated number of detected fluorescence photons in FAMOUS emitted by a proton shower with $E = 10^{18.5}$ eV and 50° zenith angle in 5 km distance. Each circle represents one pixel of FAMOUS. This result has been achieved by folding the telescope response parameterization with the arrival direction and wavelength of the shower photons (cf. figure 7.15). Right: simulated number of detected fluorescence photons including night sky background. The night sky background has been picked from the probability distribution in equation (7.36). More details on the shower simulations can be found in section 7.3.

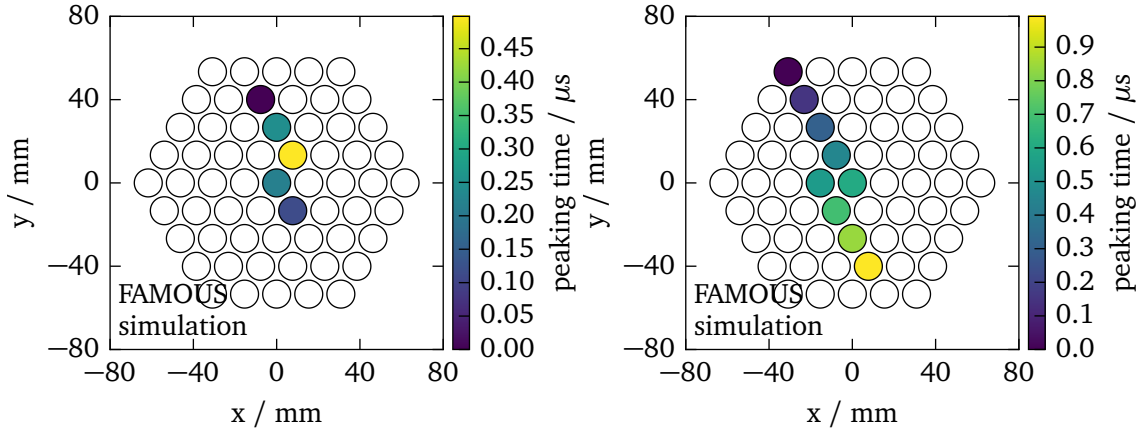

Figure 7.17: Left: simulated peaking time of triggered pixels due to the night sky brightness accidentally on a straight line. This event would be discarded since the triggering times are not geometrically ordered and a fit of the shower detector plane fails (cf. equation (7.42) below). Right: simulated peak arrival time of the shower photons by a proton shower with $E = 10^{18.5}\,\mathrm{eV}$ and 50° zenith angle in 5 km distance. The peaking time is the result of the average arrival time of the photon bunches in one pixel weighted with the number of photons in the bunch. White pixels have not been triggered. More details on the shower simulations can be found in section 7.3.

For n_b photon bunches in total, the total number of photons detected by pixel j is given by

$$n_j = n_{\mathrm{nsb}} + \sum_{i=0}^{n_b} w_{i,j} = n_{\mathrm{nsb}} + \sum_{i=0}^{n_b} n_i\, \epsilon_j(\lambda_i, \theta_i, \phi_i) \tag{7.40}$$

with the number of photons from the night sky background n_{nsb} picked from the probability distribution p_{nsb}. This simple model also allows to derive the peaking time of the pixel signal by computing the weighted average of the arrival times t_i

$$t_j = \frac{\sum_{i=0}^{n_b} w_{i,j}\, t_i}{\sum_{i=0}^{n_b} w_{i,j}} \quad . \tag{7.41}$$

The result of these calculations is presented in figures 7.16 and 7.17.

In summary, the telescope response parameterization $\epsilon_j(\lambda, \theta, \phi)$ permits a fast and simple prediction of the number of detected photons and peaking time of the pixels of FAMOUS. Neglecting the time needed to simulate the telescope parameterization ϵ_j, which can take several hours, the time needed to derive the results for one shower is below 1 s which equates to a speed improvement by a factor 100. This telescope response parameterization will be applied to a large set of EASs in the next section and aid in the derivation of the measured fluxes of stars in chapter 9.

Parameter		
Primary particle energy $\log_{10}(E/\mathrm{eV})$	$\in [15, 18)$	$\in [18, 19.5)$
Spectral index γ	-1.1	-2.2
Zenith angle ϑ	$\in [0, 80)°$	
Azimuth angle ϕ	$\in [0, 360)°$	
Hadronic interaction model	EPOS-LHC	
Particles	proton, iron	
Number of simulations per particle	10 000	10 000

Table 7.2: Parameters used for the simulation of extensive air showers with CONEX v4r37 [40, 41, 42]. The zenith angle is picked from an isotropic flux on a flat surface with $\mathrm{d}N/\mathrm{d}\cos\vartheta \sim \cos\vartheta$. The energy bins and spectral indexes have been chosen similarly as described in [204] and match the energy distribution of the preliminary data measured by the fluorescence detector of the Pierre Auger Observatory without any corrections.

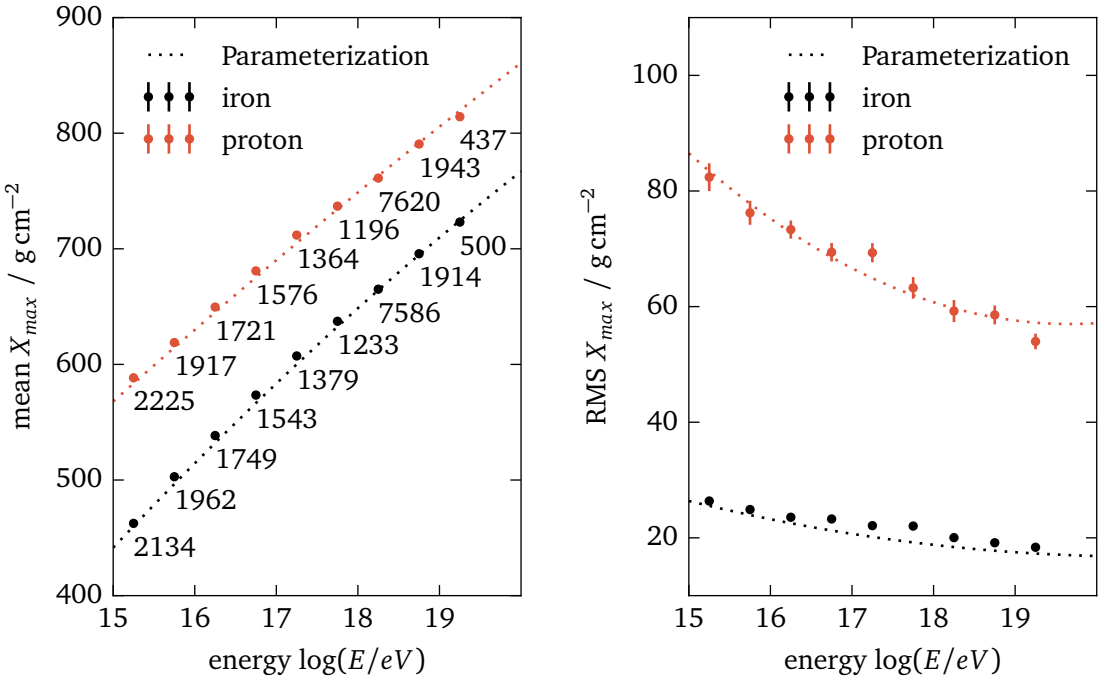

Figure 7.18: Mean and root mean square of the slant depth of the shower maximum of the simulations. The simulated data have been obtained using the CONEX simulation package with EPOS-LHC as hadronic interaction model [40, 41, 42]. The lines represent the moments obtained by a parameterization for proton and iron nuclei [63]. The numbers denote the number of showers contained in each bin. The simulation parameters are enlisted in table 7.2.

7.3 Extensive air shower simulation

The simulation package CONEX is a hybrid Monte Carlo code which can be used for fast simulations of EASs [40, 41, 42]. Its development is related to the CORSIKA Monte Carlo program which simulates the development of EASs in three dimensions. Here, this level of detail is not needed since typically air showers and fluorescence telescopes are far away from each other. Due to the 10-times law, the regions of fluorescence light creation can be approximated as point sources. The CONEX code simulates only the high energy hadronic interactions of the primary cosmic ray particle up to a certain energy threshold. Then, cascade equations are used to predict the number of charged particles, number of muons and their energy deposit in the atmosphere along the shower axis. The shower simulation parameters and results are written to a ROOT file [205]. Several hadronic interaction models are available of which here only the EPOS-LHC model is used [43].

The energies of the protons and iron nuclei are picked from an exponential distribution with a spectral index of $\gamma = -1.1$ and $\gamma = -2.2$ below and above 10^{18} eV, respectively. The zenith angle ϑ is picked from an isotropic flux on a flat surface with $\mathrm{d}N/\mathrm{d}\cos\vartheta \sim \cos\vartheta$ between 0° and 80°. The azimuth angle ϕ is kept unbound. These parameters match the parameters chosen by the Pierre Auger Collaboration in a recent publication for the determination of the atmospheric depth of the shower maximum [204]. A complete list of the parameters used for the simulation can be found in table 7.2. In total 10 000 showers have been simulated for each energy bin and particle type. The mean and root mean square of the X_{max} from these simulations are presented in figure 7.18. It should be noted that each simulated shower can roughly be used 10 times as input for the further simulation chain since its exact position in the field of view of the telescope is random. Thus, a total number of 400 000 EASs has been simulated.

7.3.1 Fluorescence light simulation

The fluorescence light can be calculated from the energy deposit of the EAS along the shower axis. For this task the Auger Offline software framework of the Pierre Auger Collaboration has been used [188]. The simulation chain is controlled by the means of so-called steering cards which are XML text files for the configuration of the modules of the simulation chain. As starting point, the standard set of steering cards for the simulation of the fluorescence detector of the Pierre Auger Observatory has been used. Originally at the end of this simulation chain, modules for the ray-tracing of the fluorescence light through the telescopes of the Pierre Auger Observatory and the simulation of the electronics are placed. Those modules are replaced by a customary module which exports the information on the wavelength, position, arrival time and arrival direction of the photons hitting the aperture of the telescope to a file. The telescope model of the Offline framework has been modified to resemble the smaller aperture size and the smaller field of view of the telescope FAMOUS which reduces the computation time substantially. A short overview over the used modules is given in the following.

7.3.1.1 EventGeneratorOG

The core positions of the EASs, i.e. the impact position of the shower on the ground, are randomized in front of the FAMOUS telescope [206]. To allow showers to have the core position outside the field of view, the opening angle of the field of view cone of the telescope is with

$\delta\phi = 20°$ slightly larger than the value of 18.3° derived above. The maximum allowed telescope to shower distance is $r_{\max} = 10\,\mathrm{km}$.

7.3.1.2 ShowerLightSimulatorKG

The longitudinal profile of the energy deposit of an EAS simulated by CONEX is given in bins of equal atmospheric depth. These bins are reused by the Offline framework. For each atmospheric depth bin, the number of fluorescence photons is calculated using the fluorescence yield [206]. The energy of the photon is chosen randomly from measured fluorescence light spectra [50] (cf. figure 3.1 in section 3.1).

7.3.1.3 LightAtDiaphragmSimulatorKG

For near showers, the telescope might resolve the intrinsic width of the EAS since the 10-times law is not satisfied anymore. Instead of requiring full three-dimensional CORSIKA simulations at this point, a lateral shower profile parameterization is used to smear the point of origin of the photons [206].

7.3.1.4 ShowerPhotonGeneratorKG

To save computing time, photons of one atmospheric depth bin are grouped in up to $n_b = 100$ bunches [206]. The number of photons per bunch is the total number of fluorescence photons divided by the number of bunches n_b. These bunches are traced through the atmosphere respecting the intrinsic absorption length of the atmosphere as well as Rayleigh and Mie scattering which eventually reduce the number of photons contained in a bunch.

7.3.1.5 FdLightInfoWriter

The last module of the simulation chain has been reached. This customary module has been developed to export the wavelength, position, arrival time and arrival position of the photons on the aperture of the telescope to a ROOT file which can be further processed by the Geant4 ray-tracing simulation of FAMOUS. Due to the settings applied in the steering cards, the photon sample is already truncated to the aperture and the field of view of the telescope FAMOUS. This module has already been introduced in [95, 159].

7.3.2 Trigger simulation

The 400 000 simulated EASs with energies between 10^{15} eV and $10^{19.5}$ eV have been processed using the FAMOUS telescope and night sky background parameterization. Thus, for each of the 400 000 EASs, information on the number of photons n_j and peak arrival time t_j is available. To identify showers which potentially trigger the telescope FAMOUS, a triggering scheme is implemented analogous to the trigger of the fluorescence telescopes of the Pierre Auger Observatory [6].

7.3.2.1 First level trigger

The first level trigger applies a threshold $n_{1\mathrm{st}}$ to the mean number of photon equivalents detected by the SiPMs in a time window of $1\,\mu\mathrm{s}$ which corresponds to a conservative estimate

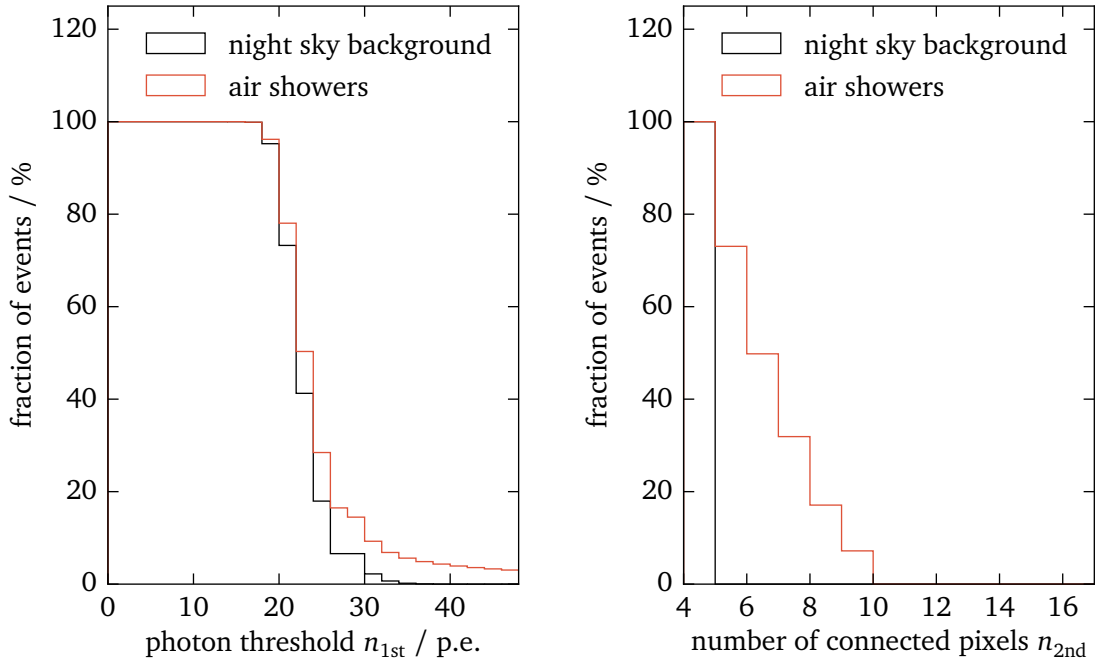

Figure 7.19: Left: simulated efficiency of the first level trigger as a function of the photon threshold value n_{1st} for the library of 400 000 simulated EAS (cf. table 7.2). If the number of photon equivalents of a pixel surpasses the threshold, the pixel is considered as triggered. Right: simulated efficiency of the second level trigger as a function of the path length threshold value n_{2nd} for the simulated EAS library. Pixel with level one triggers are connected to gapless paths. If the path length exceeds the threshold value n_{2nd}, the event is considered as successfully triggered.

of the transition time of air showers in a pixel. The pixels exceeding the threshold are identified as triggered. Due to statistical fluctuations of the night sky background and the thermal noise of the SiPM, accidental triggers occur at a high rate. The purpose of this trigger level is to reduce the trigger rate to a level which can be processed by the data acquisition. Therefore, a trigger threshold of $n_{1st} > 20$ is chosen. The number of coincident accidental triggers due to the night sky background and of signal triggers due to air showers is presented in figure 7.19, left. The percentage of triggers due to the night sky background decreases as soon as the threshold exceeds the maximum of the night sky background probability distribution p_{nsb} (cf. figure 7.14).

7.3.2.2 Second level trigger

The second level trigger connects adjacent pixels, which passed the first level trigger, to straight, gapless paths (cf. figure 7.17). Since EASs appear as a long string of triggered pixels in the camera of fluorescence telescopes, the paths length $n_{2nd} \geq 5$ yields a strong trigger criterion. The percentage of triggers as a function of the paths length n_{2nd} is presented in figure 7.19, right. As a consequence of this strong criterion, the number of accidental triggers from the

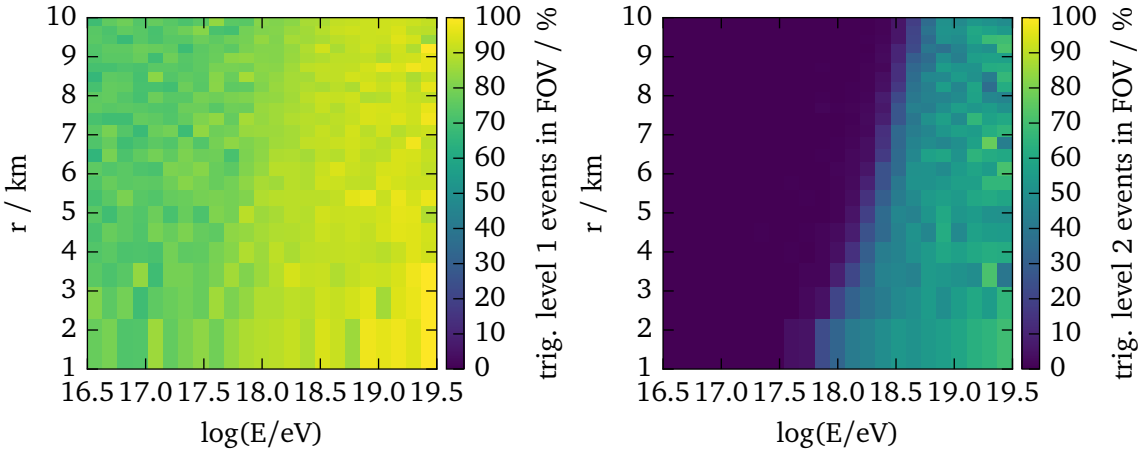

Figure 7.20: Left: simulated efficiency of detection of EAS events including night sky background and SiPM noise as a function of the shower to telescope distance r and primary particle energy E for the first level trigger. The bin size in r is proportional to $\sqrt{r}$ to account for the increased area on the ground covered by the field of view solid angle. Due to the background (cf. equation (7.36)), many events are accidentally triggered resulting in a trigger rate of $\approx 730\,\mathrm{kHz}$. Right: simulated efficiency of detection of EAS events for the second level trigger. The third and fourth trigger level further slightly reduce the overall detection efficiency. Since the binning is logarithmic, the number of events decreases with increasing energy since the energy distribution of the simulated data follows a broken power-law (cf. table 7.2). Therefore, bins with a higher efficiency than the computed mean efficiencies in table 7.3 can occur.

night sky background is low. A value of $(1.591 \pm 0.013)\,\mathrm{Hz}$ has been derived for a $10\,000\,\mathrm{s}$ long sample of night sky background.

7.3.2.3 Third level trigger

The third level trigger orders all pixels with a second level trigger in geometrically descending order. For down going showers, the geometrical order equals the chronological order of the pixel peaking times. Thus, the time difference between a triggered pixel and the geometrically subsequent triggered pixel is greater than zero. In contrast, accidental events from the night sky background possibly not satisfy this criterion. While EAS events are selected with nearly 100 % efficiency in the simulated sample, the night sky background rate can be suppressed by a factor of approximately 40 to $(0.042 \pm 0.002)\,\mathrm{Hz}$.

7.3.2.4 Fourth level trigger

The fourth level trigger performs a χ^2 fit of the shower detector plane to the peaking time of the triggered pixels. The peaking time t_i of pixel i is given by

$$t_i(\chi_i) = t_0 + \frac{1}{c} R_p \tan\left(\frac{\chi_0 - \chi_i}{2}\right) \tag{7.42}$$

$E \in [10^{15}\,\text{eV}, 10^{18}\,\text{eV})$			
Trigger	Showers	Efficiency	Total efficiency
	200 000	-	—
Field of view	124 887	$(62.44 \pm 0.18)\,\%$	100.0 %
1st level	92 649	$(74.19 \pm 0.32)\,\%$	$(74.43 \pm 0.32)\,\%$
2nd level	95	$(0.102 \pm 0.011)\,\%$	$(0.076 \pm 0.008)\,\%$
3rd level	93	$\left(98^{+1}_{-3}\right)\,\%$	$(0.075 \pm 0.008)\,\%$
4th level	73	$\left(79^{+4}_{-5}\right)\,\%$	$(0.059 \pm 0.007)\,\%$
EAS trigger rate			$(0.020 \pm 0.002)\,\text{Hz}$
$E \in [10^{18}\,\text{eV}, 10^{19.5}\,\text{eV})$			
Trigger	Showers	Efficiency	Total efficiency
	200 000	-	—
Field of view	125 430	$(62.71 \pm 0.18)\,\%$	100.0 %
1st level	109 657	$(87.43 \pm 0.36)\,\%$	$(87.43 \pm 0.36)\,\%$
2nd level	20 252	$(18.47 \pm 0.14)\,\%$	$(16.15 \pm 0.12)\,\%$
3rd level	20 013	$(98.82 \pm 0.99)\,\%$	$(15.96 \pm 0.12)\,\%$
4th level	14 038	$(70.14 \pm 0.33)\,\%$	$(11.19 \pm 0.10)\,\%$
EAS trigger rate			$(5.08 \pm 0.04) \cdot 10^{-6}\,\text{Hz}$
Night sky background			
Trigger			Trigger rate
1st level			$(732 \pm 1) \cdot 10^{3}\,\text{Hz}$
2nd level			$(1.591 \pm 0.013)\,\text{Hz}$
3rd level			$(0.042 \pm 0.002)\,\text{Hz}$
4th level			$< 0.0001\,\text{Hz}$

Table 7.3: Selection efficiency of the trigger levels for EASs for the whole field of view of FAMOUS up to a shower core to telescope distance of 10 km after application of the field of view cut. The EAS trigger rate has been determined from an integration of the cosmic ray energy spectrum (cf. figure 2.1 in section 2.1). Night sky background triggers could be suppressed by the fourth trigger level in the 10^4 s long sample.

with the viewing angle χ_i of pixel i with respect to ground, the shower distance R_p perpendicular to the shower axis, the speed of light c and the angle of the shower axis with respect to ground in the shower detector plane χ_0. See also figures 3.7 and 3.8 in section 3.3.3. A high χ^2 per degrees of freedom of $\chi^2/\text{ndof} = 25$ is allowed to permit the triggering of as many EASs as possible. In contrast, the χ^2 threshold is sufficient to completely suppress the night sky background in the 10^4 s long sample. This results in a night sky background rate limit of < 0.0001 Hz which is well below the expected EAS trigger rate.

7.3.2.5 Field of view cut

For the analysis of the efficiency of the trigger it is crucial to identify EASs which pass the field of view of the telescope since this condition is not satisfied for all combinations of core position, azimuth and zenith angle. Thus, a geometrical intersection between the shower axis and the solid angle cone of the circular field of view of FAMOUS is required which can be easily calculated from the viewing direction of the telescope and the position and direction of the shower axes.

7.3.2.6 Results

After applying the field of view cut, the percentage of triggered EASs by the first and the second level trigger $n_{1\text{st}} > 20$ and $n_{2\text{nd}} \geq 5$ can be derived. The result is presented in figure 7.20. As expected, the percentage of the first level trigger is very high regardless the shower distance and energy due to the statistical nature of the night sky background which creates an accidental trigger rate of $\approx 730\,\text{kHz}$. Subsequently, the second level trigger is required to suppress those events and select air showers with high efficiency. Out of 10^{10} night sky background samples, which corresponds to a total time of $10^{10} \cdot 1\,\mu\text{s} = 10^4\,\text{s}$, only few night sky background only events passed resulting in a rate of $(1.591 \pm 0.013)\,\text{Hz}$. However, the rate can be further suppressed by the third level trigger by roughly a factor of 40 to $(0.042 \pm 0.002)\,\text{Hz}$. The efficiency of the EAS selection can be improved by implementing a fourth level trigger using a shower detector plane fit as described in section 3.3.3. This trigger suppresses the night sky background to a rate of $< 0.0001\,\text{Hz}$ which yields a purity of $> 99.5\,\%$. Hence, this trigger is not easily implemented in electronics and thus has to be performed in the later analysis of the recorded data.

In summary, a promising result could be obtained from the EAS simulations. Potentially several showers per hour can be recorded by the SiPM telescope prototype FAMOUS. Nevertheless, also requirements to the yet to be built readout electronics of FAMOUS can be found. First, the first level trigger threshold must be determined in real-time to accommodate for changes in the night sky brightness and stars passing through the field of view of FAMOUS. Furthermore, the trigger rate suppression must be large enough to make the processing of second level triggers in the electronics feasible without sacrificing too many air showers. Since the second and third level triggers exploit only geometrical and chronological criteria, they can be implemented in an FPGA (field programmable array) of the readout electronics. In the end, a final total trigger rate of $\approx 0.06\,\text{Hz}$ can be easily written to conventional hard disks for later further analysis by a fourth trigger level to completely filter out all night sky background events.

CHAPTER 8

The slow control of FAMOUS

The number of different hardware components and a non-trivial data and control flow require a slow control for the FAMOUS telescope. As the name suggests, the purpose of the slow control is to supervise the operation of the hardware by means of slowly changing parameters with a maximal refresh rate in the millisecond range. Additionally, the data have to be presented in real-time to the experimenter in a way that allows the fast recognition of hardware states which impair the quality of the measurement or even lead to failure or damage of the complete system.

The slow control of FAMOUS is installed on a barebone computer with a Linux operating system (Debian 8.0 [207, 208]). The computational requirements of the slow control are low, so a computer with low power consuming components can be used which is important to maintain the portability of the telescope. At the same time, enough computational resources are left to perform the data acquisition once the readout electronics of the FAMOUS telescope has been completed (cf. section 6.4). As for the peripheral connectors, the computer needs to have at least one Ethernet port for remote control capabilities as well as USB ports for additional hardware. Here, an additional Ethernet port (via USB adapter) is used to create a private network to which hardware components with Ethernet capabilities are connected. In this manner, these components are not exposed to the same network the slow control computer is connected to which could impose security issues.

8.1 Requirements

The most important requirement of the slow control is stability since it has to be operational at any time. It has to power up before the beginning of the data taking and power down last. Furthermore, the integrity of the data stored by the slow control and the data acquisition has to be ensured.

Secondly, the user interface must be comprehensible and allow a fast adaption by new users. Furthermore, it should be remotely accessible. The most extreme case is IceAct, which is situated at the South Pole and successfully operated form Europe (cf. section 6.7.3) [187].

Lastly, the slow control must be easily extensible for the adoption of new hardware com-

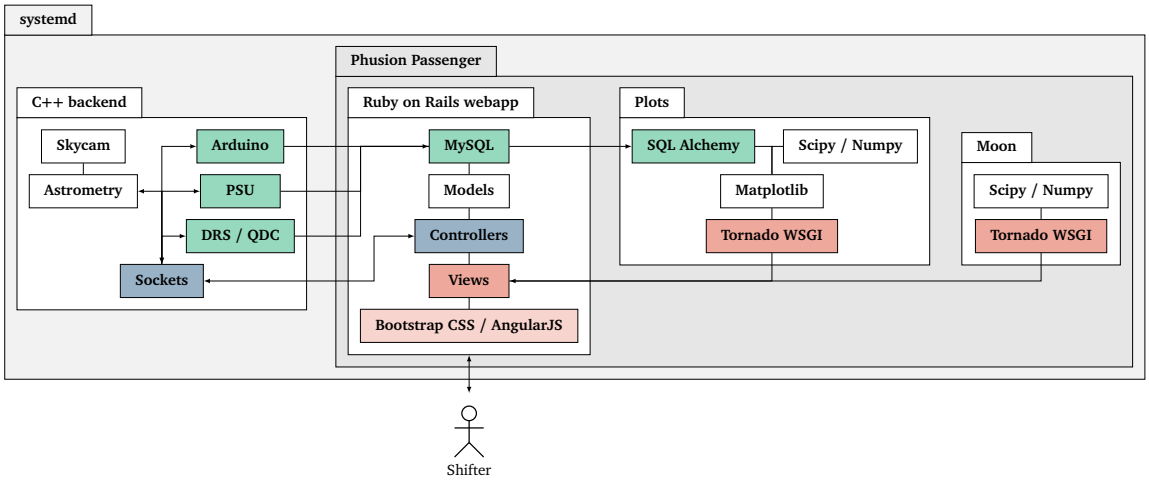

Figure 8.1: The stack of the slow control of the FAMOUS telescope. All processes are controlled by means of "systemd" services whereas all services with web functionality are spawned by a Phusion Passenger application server. The Phusion Passenger application server includes load balancing features to ensure responsiveness in case of multiple users. The central data storage is the MySQL database of the Ruby-on-Rails web application. The controllers of the web application can send commands to the sockets of the C++ backend which controls the often exclusive, synchronous access to the hardware. In the end, the user can access all information via the rendered web frontend in his web browser remotely via the network.

ponents. By using modern code development techniques and languages, the source code of the slow control can maintain a small footprint and does not require complicated constructs to establish the operation. The concepts used are discussed in the next section.

8.2 Software

One of the mantras of modern software development is convention over configuration which allows for radical simplifications of the programming. For example, variable names in a model definition and the corresponding database layout are equal and automatically pluralized; the programmer only has to specify deviations from the convention. This mantra has been implemented in the development of the slow control. The slow control consists of two main parts: the web frontend and the backend controlling the hardware components. Additionally, there are two web services for the generation of plots and for the calculation of the altitude of the sun and the moon above ground by using the current GPS position and time. The former queries data from the database and produces publication ready plots on the fly which are embedded in the web frontend. The backbone of the whole slow control is a MySQL database. A schematic overview of the software components of the slow control and the used libraries can be found in figure 8.1.

8.2.1 The Unix init system systemd

Systemd is an initialization system of Unix operating systems. It is the first process started after booting the kernel [209]. From there, it bootstraps and supervises all system processes. Particularly, systemd allows the definition of dependencies between processes. Thus, the web frontend is started after the MySQL database server which in turn is started after the networking components. If a system process fails, it is automatically restarted and optionally its dependent services. Should the system process fail repeatedly due to a configuration or hardware error, the process is terminated. This behavior can be finely configured and ensures the stability of the slow control computer.

8.2.2 Phusion Passenger middleware

The Phusion Passenger is used as middleware and application server [210, 211]. It is the preferred deployment setup of Ruby-on-Rails applications [212] on which the web frontend of the slow control is based on. Furthermore, Passenger also supports other programming languages such as Python [213], which is used for the plots and moon web services, by means of implementing the WSGI interface, i.e. an interface specification for web applications [214]. Various settings, specifically the network port over which the application is made available, can be configured with configuration files. Since this configuration is persisted in the project repository, the other web services can rely on this information for e.g. interprocess communication. Lastly, the Phusion Passenger features load balancing which means new instances of the managed applications are created to handle incoming requests in parallel. After a specific time, the number of instances is reduced to save system resources. Thus, the load balancing guarantees the responsiveness of the slow control.

8.2.3 Ruby-on-Rails web frontend

Ruby-on-Rails is a full stack web application framework. Full stack means, that it comes with all components required to operate a web server. It implements the so-called model-view-controller concept (MVC).

The start page of the web frontend, i.e. the dashboard, condenses all information and displays the most important quantities and offers actions where and when applicable. An example of the dashboard is given in the screenshots in figure 8.2.

8.2.3.1 Model-view-controller concept

The model is a description of data structures. Regardless of the selected database backend, Rails encapsulates all database specific calls in a common application programming interface (API). The convention over configuration concept is realized here by choosing the table and column names correspondingly to the variable names in the model. The model is also the place to built-in minor calculation functionality e.g. the calculation of the over-voltage from the bias voltage, the breakdown voltage, the ambient temperature and the progression coefficient (cf. equation (4.25) in section 4.3).

The controller is the glue between the model and the rendered web site. It selects the applicable data from the model, handles creation, updating and deletion of model instances and passes the results to the view. The view is an HTML document with special placeholder markups which are filled with the data provided by the controller.

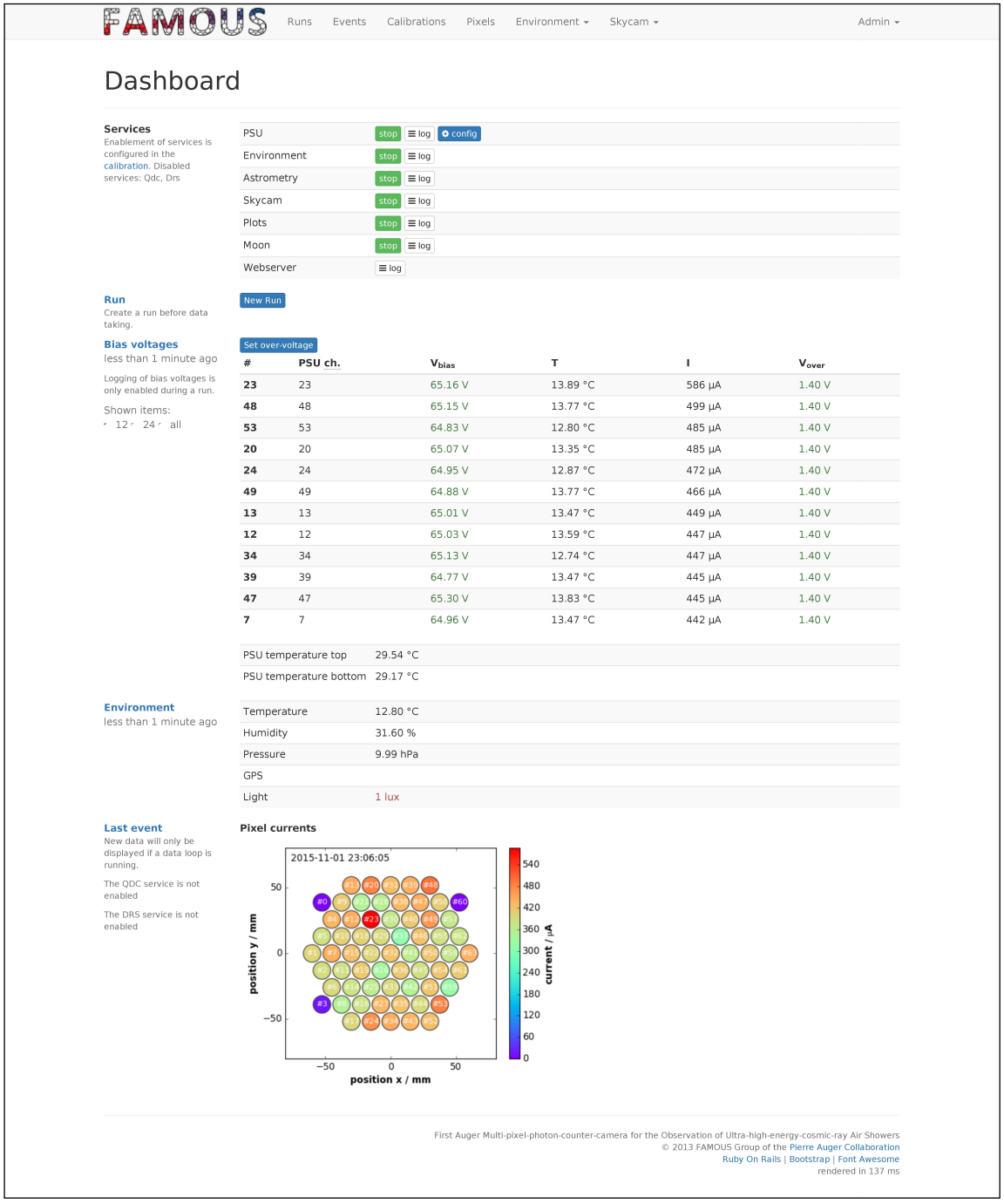

Figure 8.2: Screenshot of the dashboard page of the slow control. Here, all necessary information on the current measurement run and on the hardware components are displayed and dynamically updated without the necessity of a page reload. For clarity, only the 12 pixels with the highest currents are displayed. Due to the responsiveness of the stylesheets, the layout automatically adjusts to the screen size. The displayed data was taken during a measurement of star trails (cf. chapter 9).

8.2.3.2 Stylesheets

The framework Bootstrap is an HTML, CSS and Javascript framework for the development of responsive websites [215]. It offers predefined stylesheets for HTML elements resulting in clear user interfaces. Responsiveness implies that the user interface is automatically adapted to the screen size of the device on which the web frontend is opened. Therefore, the interface is perfectly usable on mobile devices.

8.2.3.3 Client side Javascript

On the client side in the browser, the Javascript framework AngularJS [216] is used for asynchronous updates of content after the page has loaded. Thus, changing quantities displayed in the web frontend are updated without user intervention. At the same time, the amount of data and therefore the network bandwidth usage is reduced dramatically since only small pieces of information have to be transferred. Due to this approach, the telescope could be operated remotely at the South Pole via a low bandwidth, high latency satellite connection [187].

8.2.3.4 Security

A basic HTTP authentication [217] has been implemented requiring the experimenter to provide a username and password before changing settings or the state of the data taking.

8.2.4 Database

The MySQL database is a widely used relational SQL database for fast and scalable storage [218]. Since the database tables and column names are automatically the same as defined in the Ruby-on-Rails models by convention, the database layout is very intuitive. Furthermore, the database is managed by so-called migrations which execute changes of the Rails models. Unless a model property is to be deleted, the migrations are executed without harming the existing data and can even be rolled back if necessary. Hence, the database can evolve with the requirements and the hardware of the experiment.

8.2.5 Plots web service

The plots web service is written in Python [213] and implements WSGI as interface to Phusion passenger. The plots are generated by means of the widely used Matplotlib library [219] from the data persisted in the database whereby the database schema of the Rails application is replicated with Sqlalchemy [220]. Thus, database access is kept in a similar way. The images are generated as pixel graphics in the PNG data format and conducted as stream to the browser of the user. Since all the libraries are kept in the memory of the PC between requests, the time consumption for the creation of one plot is very low ($< 100\,\mathrm{ms}$). This is a $10\times$ speed improvement compared to if the same would be executed as a script with persistence to the disk. Furthermore, the data periods can be selected easily in the web frontend.

8.2.6 Moon web service

The moon web service calculates the altitudes of the Sun and the Moon as well as other properties based on the current position, date and time of the day. The implementation follows [221,

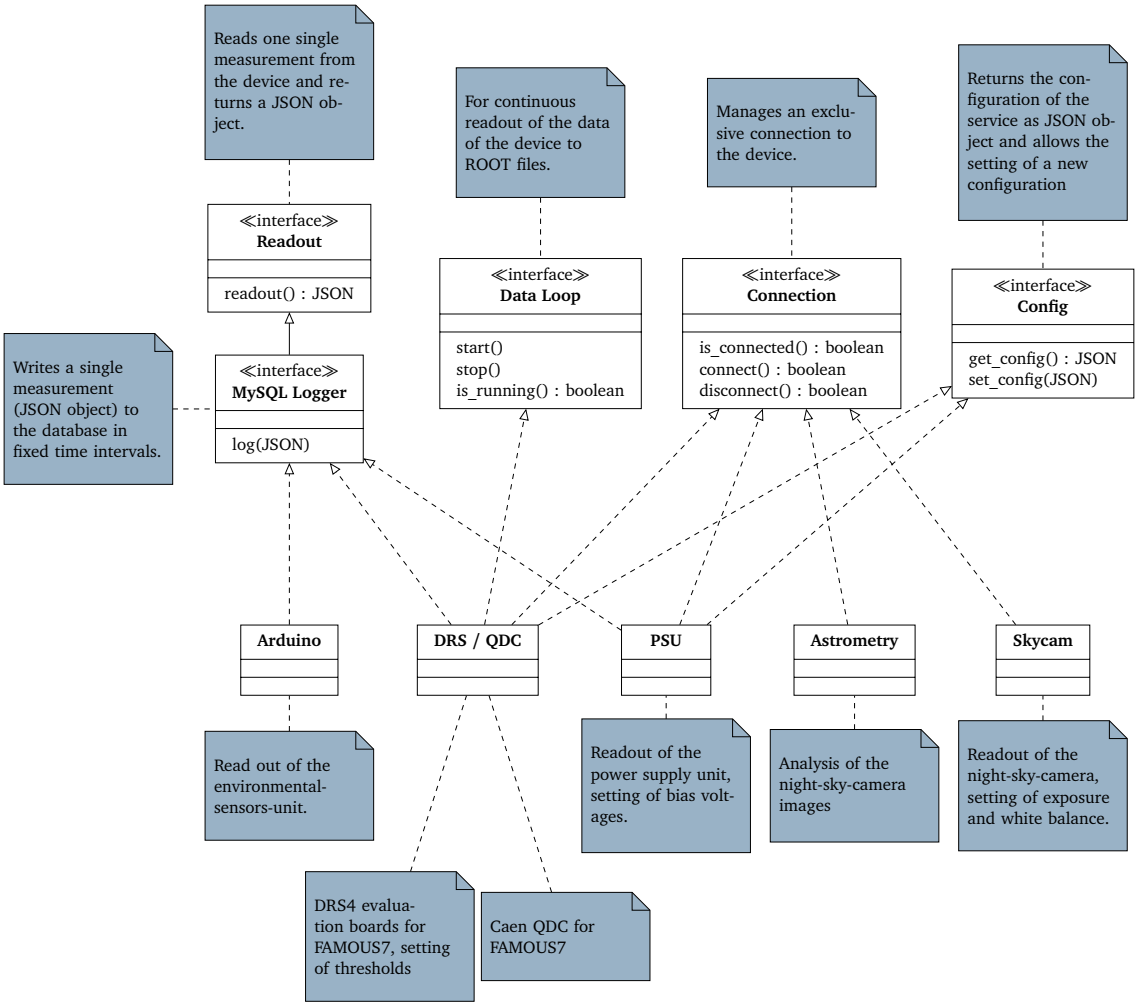

Figure 8.3: Class diagram of the backend C++ services of the slow control of FAMOUS and their purpose. The interfaces act as finite state machines to provide a common API to the hardware components.

222, 223]. From the altitude of the Sun, the type of twilight is calculated: civil twilight corresponds to a sun altitude of 0° to 6° below the horizon, nautical to 12° and astronomical to 18°. Furthermore, the time of the onset of the twilight states and the phase of the moon are predicted. Both contributes to the understanding of the current night sky brightness. The current observation position and observation time can be set via a request parameter. The obtained result is formatted in the text format JSON (JavaScript Object Notation) [224] which can be directly used in Javascript.

8.2.7 Backend

The hardware control backend of the slow control is programmed in C++ [225]. Each hardware component is controlled by its own process running as a systemd service. The standard output log messages, which can yield important information, are automatically accumulated by

systemd. They are made accessible through the web interface for inspection. A class diagram of the implemented backend services and their purpose can be found in figure 8.3.

8.2.7.1 Interprocess communication

Due to the modularization of the slow control, which is mandatory to avoid a single point of failure, the services have to be able to communicate with each other. The interprocess communication is achieved by means of sockets which are either Unix Domain Sockets or TCP sockets (Transmission Control Protocol) [226]. The latter is also accessible via the network. A socket is a communication endpoint represented by a filesystem object or a port and can be used for bidirectional communication by means of a standardized API. Here, the communication is encoded in the human readable JSON format. Albeit JSON is encoded in plain text and not binary, which increases the memory footprint, it is an ideal choice since it is perfectly supported in many programming languages. It is supported by Ruby, Python and Javascript, thus no conversion between data formats is necessary which makes this approach also very robust. On a modern PC, roughly $\mathbb{O}(10^5)$ individual JSON packets per second can be transmitted, received and processed which is the limit of what network connections can achieve with latencies of $\mathbb{O}(0.1\,\mathrm{ms})$ at best.

The following listing presents a JSON packet which has been send by the environmental sensors unit (cf. section 6.6):

```
{
    "temperature":22.91,
    "pressure":98637.0,
    "humidity":28.64,
    "light":{
        "integration_time":100,
        "broadband":13.0,
        "luminosity":1.0,
        "infrared":6.0,
        "gain":16},
    "gps":{
        "checksum":1289,
        "chars":264556,
        "longitude":6.0496,
        "num_satellites":8,
        "sentences":259,
        "latitude":50.7825,
        "height":219.1}
}
```

The packet presented above has been formatted for improved readability. The packets exchanged via the sockets are compressed thus no redundant white spaces are used. A line break marks the termination of each packet.

The memory footprint of the JSON format could be improved by switching to the compatible BSON format, which a binary pendant [227]. Nevertheless, this would require a compatibility layer for the browser appliances written in Javascript. Furthermore, BSON is not acknowledged as standard to the same extend as JSON.

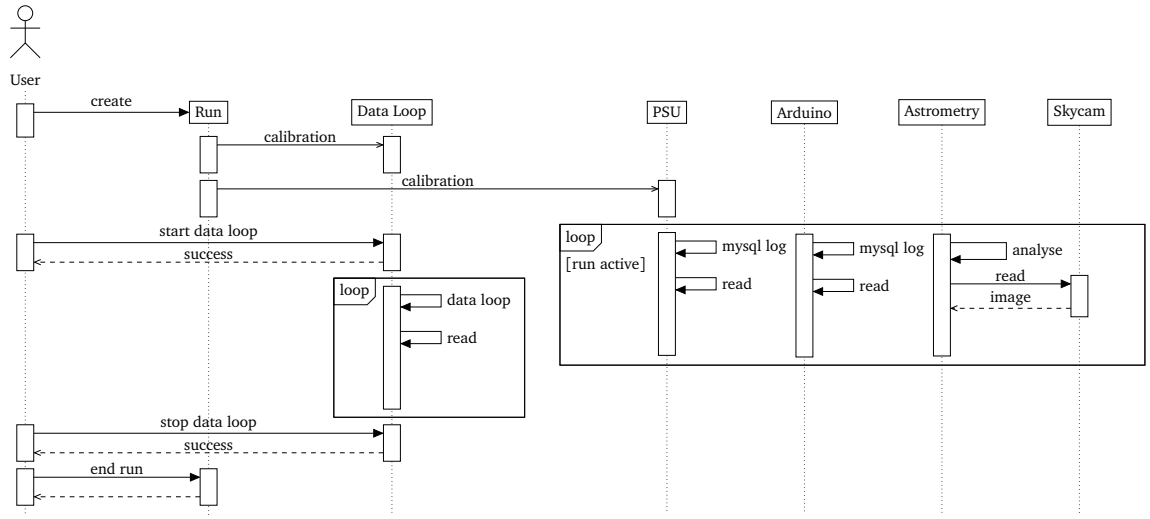

Figure 8.4: Sequence diagram of the execution of measurements with the slow control. When a new run object is created, the selected calibration is injected into the services as configuration and the services begin to log data to the database (PSU and Arduino). The data loop services (QDC and DRS) wait for user input to begin the data loop. Usually, the experimenter would adjust the viewing direction of the telescope or adjust the bias voltage of the SiPMs for the current environmental conditions or the measurement task before starting the loops.

8.2.7.2 Finite state machines

Each backend service implements one or more finite state machines (FSM), i.e. a computational model with a finite number of well defined states of which only one is applicable at a time. This concept can be extended to a behavioral pattern by the introduction of commands. Each state and command is made available via a socket.

Figure 8.3 lists the state machines of the backend services.

The data loop FSM has been implemented for the readout electronics of FAMOUS7. Once a data loop is started, the device is read out continuously and the results are persisted to the disk to binary files in the ROOT format [205]. To improve readout speed, e.g. for the DRS4 evaluation boards, the recorded data are kept in the memory and flushed in large packages to the hard disk to be independent from the disk write latency of $\mathbb{O}(10\,\mathrm{ms})$.

8.2.8 Measurement sequence

In general, periods of data taking are affiliated to so-called runs in the web frontend. Up to this point, all control services remain in a suspended mode. First, a run is created, stating the names of the experimenters as well as some comments on the execution and weather conditions. This approach is inspired by the slow control of the fluorescence detector of the Pierre Auger observatory [228]. Furthermore, the experimenter can choose from a list of calibrations. Calibrations store mechanical and physical calibration constants of the telescope. For example for the power supply unit (cf. section 6.3), the channels are associated to the pixels and the breakdown voltages of the SiPMs. Furthermore, the calibration constants for the calculation of voltages and currents from the corresponding ADC counts are persisted. This enables the

experimenter to easily switch between hardware configurations to account e.g. for a changed SiPM breakdown voltage.

After the creation of the run, the environmental sensors unit, the night sky camera and the power supply are read out continuously. The ambient conditions are logged minutely, the bias voltages, temperatures and currents of the SiPMs every five seconds, which corresponds to the maximum readout speed of the PSU for 64 channels.

For FAMOUS7, the experimenter can start data taking loops. Snapshots of the taken data are persisted to the MySQL database in 1 s intervals and are accessible via the web frontend. The complete data is persisted to an external harddrive and organized in a chronological folder structure.

After the completion of a run, all data taking loops and services are put on suspend again. A schema of this sequence is presented in figure 8.4.

8.3 Night sky camera

Since autonomous operation is required, the exposure of the night sky camera must be controlled automatically by the readout software. For this specific camera model, the gain of the red, green and blue pixels must be adjusted separately from each other. Thus, a white balance algorithm has to be implemented to achieve well balanced photos without under or overexposed color channels potentially increasing noise.

8.3.1 Automatic white balance

The white balance can be understood as the subjective perception of gray or white surfaces. The human brain automatically mixes the colors red, green and blue in a way that grayish surfaces always appear gray regardless the color temperature of the ambient light. The color temperature is the temperature of a black body [229]. Light from candles has a low color temperature of 1000 K to 2000 K resulting in orange hues, light from fluorescent lamps 5000 K to 5500 K resulting in bluish hues [230]. When shooting photographs, the mechanism of the brain has to be emulated to obtain a well exposed photograph without color cast. Let r_i, g_i, b_i be the color values red, green and blue of a pixel i in the photograph. The color values have been obtained after the application of the Bayer filter demosaicking technique [231] and are integer values scaled from 0 to 255. A good white balance is achieved for $r_i = g_i = b_i$ for gray surfaces. Furthermore it can be found that a well balanced photo is a mixture of equal color fractions [232]. Therefore, the mean color values of all pixels N

$$\mu_r = \frac{1}{N}\sum_i^N r_i \quad , \quad \mu_g = \frac{1}{N}\sum_i^N g_i \quad , \quad \mu_b = \frac{1}{N}\sum_i^N b_i \tag{8.1}$$

have to be equal. By keeping the gain g_g of the green pixels fixed to a certain value which ensures image recording with acceptable amplification noise, the adjusted gains of the red and blue pixels g'_r and g'_b can be derived to

$$g'_r = \frac{\mu_r}{\mu_g}\, g_r \tag{8.2}$$

$$g'_b = \frac{\mu_r}{\mu_g}\, g_b \quad . \tag{8.3}$$

Parameter	Vega	Deneb
Capture time (CET)	2015-11-01 21:06h	2015-11-01 22:12h
Right ascension α	$18^{\mathrm{h}}52^{\mathrm{m}}31.446^{\mathrm{s}}$	$20^{\mathrm{h}}33^{\mathrm{m}}41.069^{\mathrm{s}}$
Declination δ	$+36°13'11.998''$	$+45°5'0.743''$
Field of view	$32.1° \times 24.1°$	$31.5° \times 24.0°$
Pixel size	$92''$	$91''$
Background σ	0.48	0.54
Number of detected stars	119	147
Computation time	$\approx$1 s	$\approx$0.2 s
Altitude ϑ	42.3°	52.8°
Azimuth ϕ	278.6°	283.9°

Table 8.1: Results of the image analysis with the Astrometry.net software package (cf. figures 8.5 and 8.6). Using the reconstructed right ascension and declination of the image center with the GPS position and the timestamp of the photograph, the horizontal coordinates altitude ϑ and azimuth ϕ can be reconstructed. These coordinates define the local viewing direction of the telescope. The alignment uncertainty of the optical axis of the night sky camera to the optical axis of the telescope is approximately 1°.

8.3.2 Automatic exposure

The exposure time can now be chosen independently from the gain. Since both the color values r_i, g_i, b_i obtained from the photograph and the exposure time t are scaled linearly with respect to the amount of recorded light, the mean over all colors

$$\mu_{\mathrm{rgb}} = \frac{1}{3}\left(\mu_r + \mu_g + \mu_b\right) \tag{8.4}$$

can be compared to a favored value which for daytime photography is $\mu_{\mathrm{target}} = 254/2 = 127$. However, the night sky yields very dark images with the stars as small white spots, therefore, a smaller value of $\mu_{\mathrm{target}} = 30$ has been found applicable. The new exposure time t' is given by

$$t' = \frac{\mu_{\mathrm{rgb}}}{\mu_{\mathrm{target}}}\, t \quad . \tag{8.5}$$

These values are applied in an iteratively manner every 10 recorded frames. For this, the camera is operated in the live view mode to enable a fast adaption of the white balance and exposure to changes of the night sky conditions such as twilight or clouds continuously changing the hue and the brightness of the images.

8.3.3 Detection of visible stars

During data taking with FAMOUS, photographs of the night sky are autonomously saved every minute to the harddisk for later processing. The pictures are analyzed with the Astrometry.net software package [233], i.e. a software for fast geometric hashing for automated astrometry

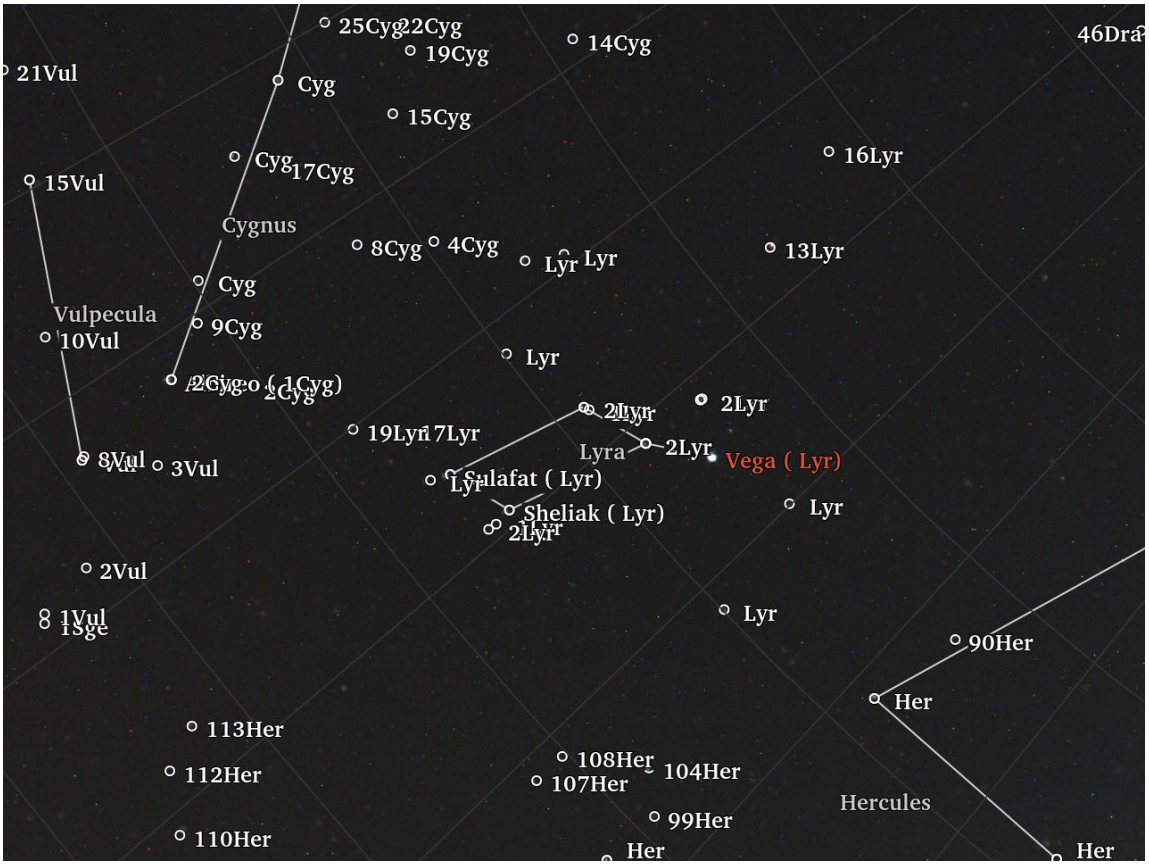

Figure 8.5: Photograph of Vega taken with the night sky camera in Aachen and analyzed with the Astrometry.net software package from the 1st of November 2015, 21:06h CET. Detailed results of the analysis are presented in table 8.1.

setups. The software has been developed with an emphasis on fast and reliable image analysis. For this, catalogs of the celestial objects based on the 2MASS catalog [234] of the night sky have been created. For each catalog, the sky is divided into patches of equal area, HEALPix bins (cf. appendix 2), and the 10 brightest stars are selected for each bin. The catalogs differ in angular size of the HEALPix bins and therefore in the number of contained stars. Starting with the brightest stars, the stars of the patches are grouped into so-called skymarks, i.e. asterisms of four stars, so that each patch contains one skymark with the center of gravity inside the patch and connections to stars in the neighboring patches. As a results, some stars are associated to multiple skymarks whereby other stars to no skymark at all. The catalogs selected for this analysis contain up to 1 452 000 stars and 2 323 200 skymarks with an angular size of $30'$ and larger.

When analyzing the image, the background is removed by subtracting a median smoothed version of the image [233]. The background is used to determine the pixel variance σ^2, and finally, star candidates are identified if the pixel value is $>8\sigma$. The star candidates in turn are connected to possible skymarks which are tested against the skymark catalogs. One matching skymark is sufficient for a successful analysis. Overall, the software achieves a detection rate of over 99.9 % with no false positives. This analysis yields the viewing direction, angular size of the image, the visible stars and other parameters. The right ascension and declination coor-

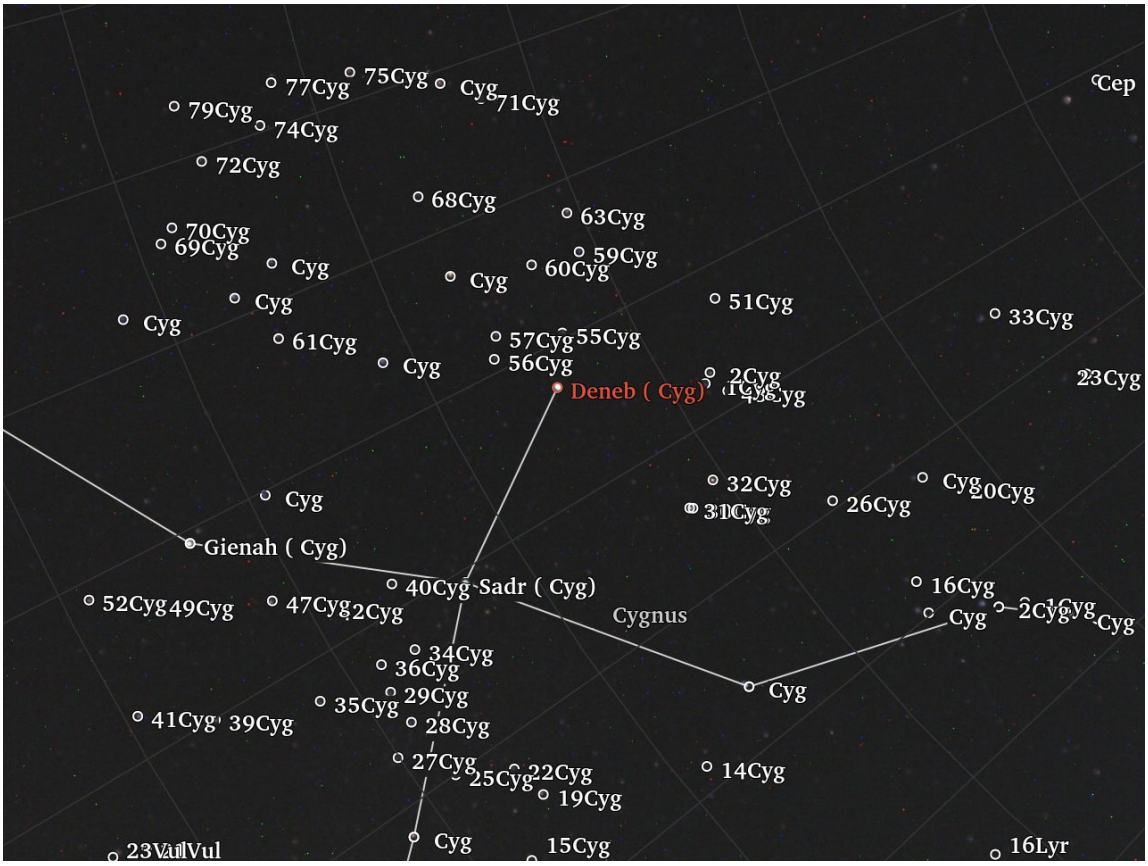

Figure 8.6: Photograph of Deneb taken with the night sky camera in Aachen and analyzed with the Astrometry.net software package from the 1st of November 2015, 22:12h CET. Detailed results of the analysis are presented in table 8.1.

dinates of the viewing direction can be translated to the local viewing direction in horizontal coordinates by using the GPS position of the environmental sensor unit of FAMOUS. Furthermore, the original image can be annotated with marks of the found stars and their name. Two example analyses of photographs with Vega and Deneb and the results can be found in figures 8.5 and 8.6 and table 8.1.

In combination with the correction of the image distortion described in section 6.5, the accuracy of the reconstructed viewing direction is very good and can be used to calibrate the pointing of the telescope by measuring star trails. By comparison of the stars found and the stars with comparable brightness which should have been visible in the field of view of the image, the cloudiness of the night sky can be determined yielding another important environmental parameter for the later data analysis.

CHAPTER 9

Measurement of star trails with FAMOUS

An important measurement to be performed with earth bound telescopes is the measurement of star trails. Many bright stars can be observed during the night. Due to their apparent movement with respect to the observation position on Earth, the trails of stars can be tracked by the telescope at rest, which means no follow up mechanism is needed. Furthermore, the luminosities of stars are well known and measured by many experiments in many distinct wavelength bands. On the other hand, the transmission properties of the atmosphere of the Earth are very variable which thus might present a challenge when comparing the expected light flux with the light flux measured in the device. Nevertheless, such a measurement improves the understanding of the telescope optics and analysis of the recorded data.

As discussed in section 6.3, the 64 channel power supply of FAMOUS is equipped with a current monitor. This current monitor is read out continuously to measure the increase in the current flow through the SiPMs while the star travels through the field of view of the telescope. Several star trails have been observed with the FAMOUS telescope. The stars Vega and Deneb are two of the brightest stars on the night sky and thus are ideal candidates for this measurement. Table 9.1 lists the performed observations.

The first ingredient to the calculation of the expected light flux in the telescope is the stellar spectrum in dependence on the wavelength. Secondly, the distance of the star to the Earth and thirdly, the absorption in the atmosphere of the Earth have to be taken into account. Lastly, the measured light flux is limited by the aperture area of the telescope and the transmission efficiency of the optical system as a function of the wavelength. An akin analysis for a Newton

Star	observation date	start	end
Vega	November 1st, 2015	20:40h	21:40h
Deneb	November 1st, 2015	21:40h	23:00h

Table 9.1: Observation times of the measured star trails recorded with the FAMOUS telescope. The stars have been selected due to their brightness and ease of observation regarding the altitude above the horizon of the measurement time.

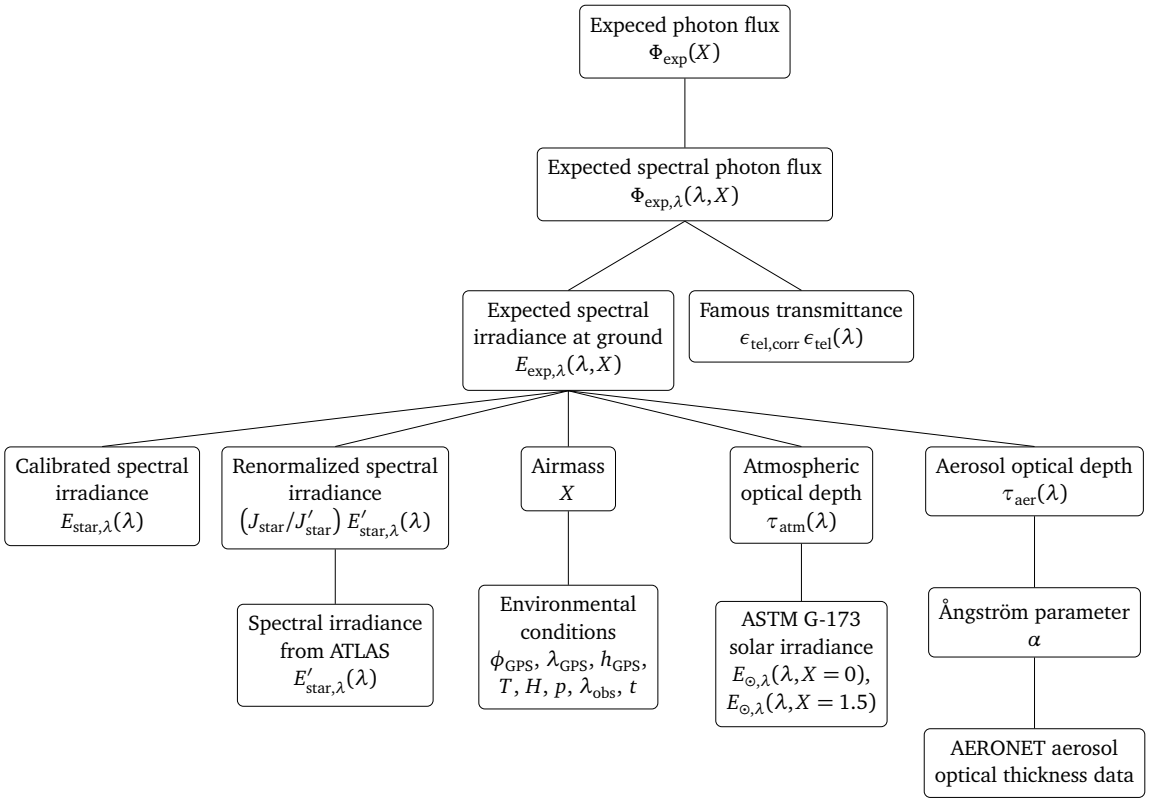

Figure 9.1: Schema of the analysis leading to the calculation of the observed photon flux due to stars in the telescope FAMOUS.

telescope and one pixel of FAMOUS has been performed in [52]. The following sections will discuss each of these analysis steps in detail. Figure 9.1 already provides an overview.

9.1 Stellar source spectra

The stellar source spectrum is the spectral irradiance $E_{\mathrm{star},\lambda}(\lambda)$ of the star emitted by the star as a function of the photon wavelength λ as measured at Earth above the atmosphere. It is usually given in units of $\mathrm{erg\,s^{-1}\,cm^{-2}\,\AA^{-1}}$ with $1\,\mathrm{erg} = 1 \cdot 10^{-7}\,\mathrm{J}$.

For some stars, the source spectra are well known since they are used for calibration purposes, as for example, for the Hubble Space Telescope [241]. Thus, a calibrated spectrum of Vega could be used in this analysis. It should be noted, that in case of Vega, there exist many different luminosity measurements in the literature due to the fact that Vega might be a variable star [253].

However, for other stars, the spectrum has to be calculated. The software package ATLAS can be used to simulate a spectrum given the surface temperature T_{eff}, the surface gravity $\log(g)$ and the metallicity $\log(m)$ of the star [249, 251]. Since the simulations are time consuming, catalogs are available which can be used as lookup table for the given stellar parameters [244,

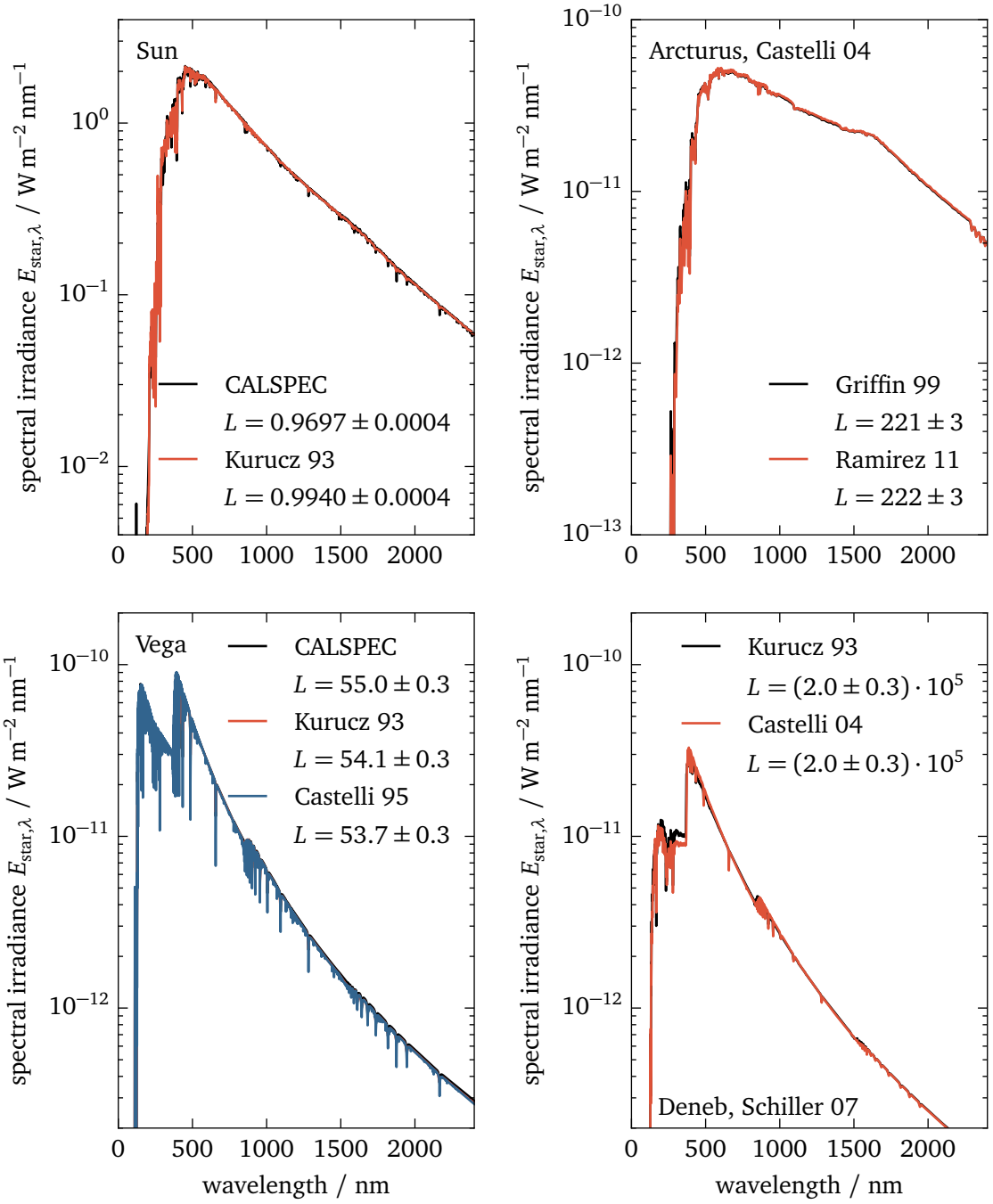

Figure 9.2: The stellar source spectra given as spectral irradiance $E_{\mathrm{star},\lambda}$ as a function of the photon wavelength. The spectra for the Sun and Vega have been obtained from the CALSPEC catalog [241, 242], the spectra for Arcturus and Deneb from the ATLAS parameterization catalog (Kurucz 93 and Castelli 04) [243, 244, 245]. The Arcturus spectrum has been renormalized using the measurements presented in [246, 247, 248]. The spectra have been obtained with the software package PySynphot [249, 250, 251, 252]. All luminosities L are given in multiples of the luminosity of the sun $L_\odot = (3.8460 \pm 0.0014) \cdot 10^{26}$ W.

	Vega [235]	Deneb [236, 237, 238, 239, 240]
Right ascension α	$18^{\mathrm{h}}36^{\mathrm{m}}56.3^{\mathrm{s}}$	$20^{\mathrm{h}}41^{\mathrm{m}}25.9^{\mathrm{s}}$
Declination δ	$+38°47'1.2802''$	$+45°16'49''$
Apparent magnitude m	0.026	1.25
Luminosity $L/L_\odot$	40.12 ± 0.45	$(196 \pm 32) \cdot 10^3$*
Surface temperature T_{eff}/K	9602 ± 180	8525 ± 75*
Metallicity $\log(m)$	-0.5	-0.25 ± 0.05*
Surface gravity $\log(g)$	4.1 ± 0.1	1.10 ± 0.05
Distance d/ly	25.04 ± 0.07	$(2.62 \pm 0.22) \cdot 10^3$
Parallax ρ/mas	130.23 ± 0.36	1.25 ± 0.10* (derived)

Table 9.2: List of the properties of the stars. For Vega, the CALSPEC catalog [241, 242] contains a calibrated stellar source spectrum. The quantities of Deneb marked with an asterisk have been used in this work. The parallax has been derived from the distance in light years.

245]. The obtained spectra have to be renormalized to measurements. For this, the integral of the spectral irradiance yields the radiosity J'_{star} of the model

$$J'_{\mathrm{star}} = \int E'_{\mathrm{star},\lambda}(\lambda)\,\delta\lambda\,\mathrm{d}\lambda \tag{9.1}$$

with the width of the corresponding wavelength bin $\delta\lambda$. The prime corresponds to quantities which have been obtained from the stellar atmospheric model. The expected radiosity can be calculated from the luminosity L and the distance R of the star with

$$J_{\mathrm{star}} = \frac{L}{4\pi R^2} \tag{9.2}$$

whereby the distance R can be calculated from the parallax ρ

$$R = \frac{1\,\mathrm{au}}{\tan\rho} \tag{9.3}$$

given the astronomical unit $1\,\mathrm{au} = (149\,597\,870\,700 \pm 3)\,\mathrm{m}$. Finally, the spectral irradiance values are multiplied by the quotient of the integrated and the calculated radiosity

$$E_{\mathrm{star},\lambda}(\lambda) = \frac{J_{\mathrm{star}}}{J'_{\mathrm{star}}} E'_{\mathrm{star},\lambda}(\lambda) = \frac{L}{4\pi R^2 J'_{\mathrm{star}}} E'_{\mathrm{star},\lambda}(\lambda) \quad . \tag{9.4}$$

The large distance between Earth and Deneb diminishes the very high luminosity and yields a fainter radiosity. Due to the large distance of Deneb, the quoted uncertainty on the parallax of several star catalogs is rather large. Therefore, the same distance as applied in the analysis of the luminosity measurement in [238] has been used to obtain a correct estimation of the light flux at Earth. Table 9.2 summarizes the properties which have been used in this analysis. The source spectra for several celestial objects are presented in figure 9.2.

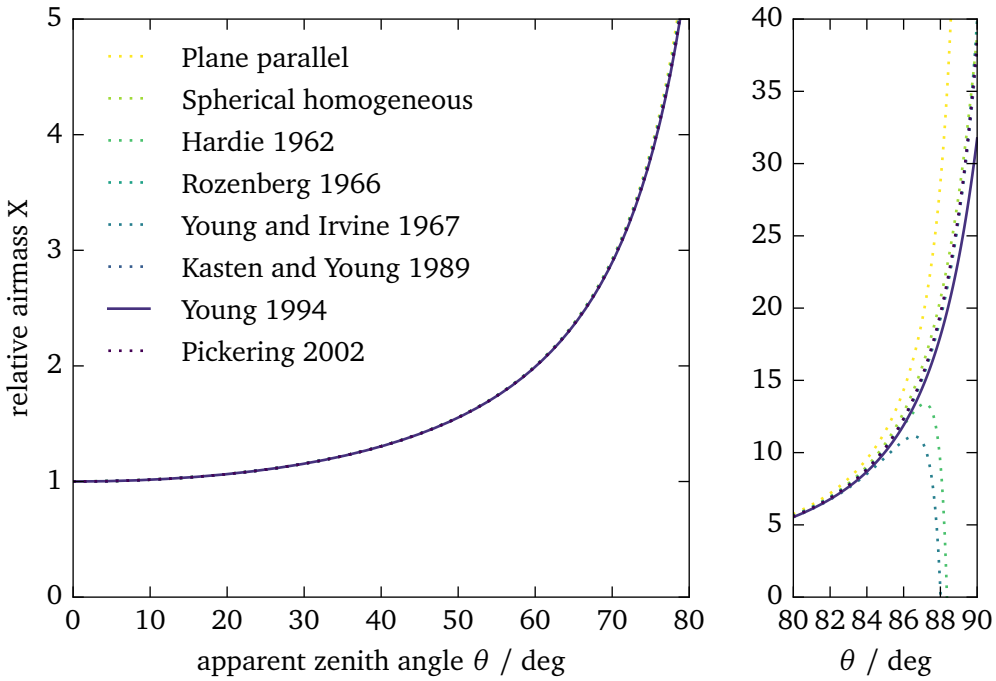

Figure 9.3: The airmass as a function of the zenith angle θ plotted for different approximations [254, 255, 256, 257, 258]. A zenith angle of $\theta = 0°$ corresponds to a perpendicular incidence with respect to the ground, $\theta = 90°$ to the horizon. The right plot presents a zoom into the high zenith angle regime in which the models make very different and in some cases unphysical predictions. For this analysis, the approximation by Young [257] has been selected due to the claimed good overall precision.

	Uncertainty	Uncertainty on airmass X
GPS latitude ϕ	$1 \cdot 10^{-4}\,°$	$1 \cdot 10^{-5}$
GPS longitude λ	$4 \cdot 10^{-5}\,°$	$1 \cdot 10^{-5}$
Observation height h	9 m	$3 \cdot 10^{-10}$
Ambient temperature T	1 °C	$1 \cdot 10^{-4}$
Humidity H	4 %	$3 \cdot 10^{-6}$
Pressure p	0.2 hPa	$6 \cdot 10^{-6}$
Observation wavelength λ_{obs}	10 nm	$4 \cdot 10^{-5}$
Observation time t	2.4 s	0.05
Total uncertainty on X		0.06 %

Table 9.3: Uncertainties on the observation position, time and environmental conditions used to calculate the apparent altitude of the star from a star catalog and subsequently the airmass X.

9.2 Airmass

The light of the stars has to travel through the atmosphere of the Earth to reach the telescope. A common measure for the length of the light path respecting the variable density of the layers of the atmosphere is the dimensionless airmass X. A value of $X = 1$ corresponds to a perpendicular light incidence with respect to ground. The value increases for increasing inclination θ. Several approximations for the airmass $X(\theta)$ exist in the literature [255, 256, 257, 258]. All formulae agree up to a certain zenith angle $\theta \approx 80°$ but yield very different and even unphysical results for the highest inclinations. Therefore, the approximation by Young [257] has been used which yields reasonable values in this regime

$$X(\theta) = \frac{1.002432 \cos^2\theta + 0.148386 \cos\theta + 0.0096467}{\cos^3\theta + 0.149864 \cos^2\theta + 0.0102963 \cos\theta + 0.000303978} \tag{9.5}$$

with a claimed maximum error of $\sigma_X = 0.0037$. Figure 9.3 presents the airmass predictions made by different models.

In the scope of this thesis, the position of the stars is given in horizontal coordinates with the azimuth ϕ and the angular altitude above ground $\vartheta = 90° - \theta$. Due to the refraction of the atmosphere, the apparent observed altitude of the star can be larger than the true altitude. This can be taken into account by including the measured ambient temperature, humidity and pressure when calculating the horizontal coordinates of the stars and is implemented in the software package Astropy [259] used to carry out the calculation of the airmass as a function of the observation time and position. Furthermore, the calculations have been made for a mean observation wavelength of $\lambda = 454\,\text{nm}$ at which the transmission efficiency of the telescope is highest (cf. section 7.1.3.1). The uncertainties on the parameters used for the calculation of the airmass and the resulting uncertainties on the airmass are listed in table 9.3. In summary, the relative uncertainty on the airmass is 0.06 % and therefore negligible.

Finally, the airmass can then be used to model the absorption of the atmosphere by using Beer's law to calculate the transmittance

$$T(X) = \exp^{-\tau X} \tag{9.6}$$

with the atmospheric thickness τ which again is a dimensionless quantity. The next two sections will discuss the atmospheric thickness τ_{atm} due to the intrinsic transmittance of the atmosphere and the thickness τ_{aer} due to aerosols.

9.3 Transmittance of the atmosphere of the Earth

The dry atmosphere of the Earth consists of 78.08 % nitrogen, 20.95 % oxygen, 0.93 % argon, 0.04 % carbon dioxide, and traces of hydrogen, helium, and other noble gases [261]. Therefore several wavelengths will be subject to absorption rendering the atmosphere opaque at certain wavelengths. Frequently, the American Society for Testing and Materials (ASTM) releases reference solar spectra at $X = 0$ and $X = 1.5$ which are mainly used by the solar power industry [260]. The evaluation of the solar spectrum at ground level $X = 1.5$ also incorporates aerosols for a US standard atmosphere [262, 263, 264]. Water vapor is considered as aerosol (cf. next section). Those effects are taken into account by introducing the atmospheric

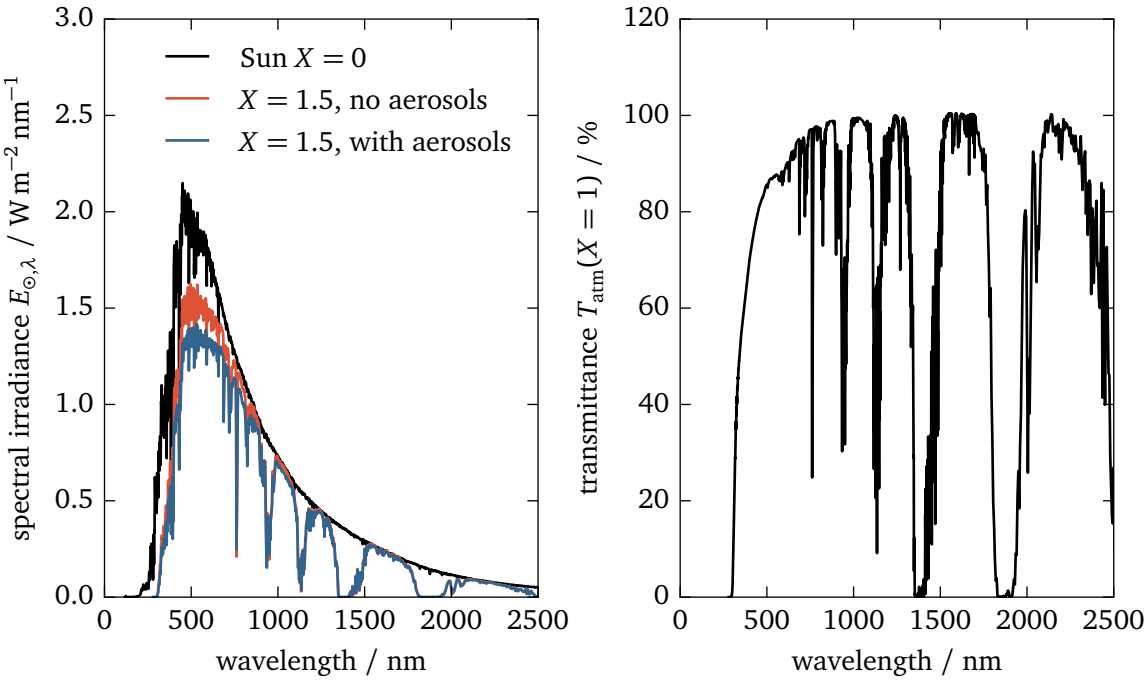

Figure 9.4: Measured solar spectrum above the atmosphere $X = 0$ and at ground level $X = 1.5$ [260]. The right plot shows the calculated transmittance from these data at $X = 1$ without the influence of the aerosols.

thickness τ_{aer} (cf. equation (9.6)) which is a function of the wavelength. A common parameterization of $\tau_{\mathrm{aer}}(\lambda)$ also applied for the US standard atmosphere is the so-called Ångström formula [66, 265]

$$\tau_{\mathrm{aer}}(\lambda) = \tau_{\mathrm{aer},0}\left(\frac{\lambda}{\lambda_0}\right)^{-\alpha} \tag{9.7}$$

with $\tau_{\mathrm{aer},0} = 0.084$, $\lambda_0 = 500\,\mathrm{nm}$ and $\alpha = 1.19$ [262]. The spectral irradiance of the sun at ground level $E'_{\odot,\lambda}(\lambda, X = 1.5)$ can be re-weighted using the Ångström formula (cf. equation (9.7)) and Beer's law (cf. equation (9.6)) to cancel out the reduction due to aerosols

$$E_{\odot,\lambda}(\lambda, X = 1.5) = \frac{1}{\exp^{-\tau_{\mathrm{aer}}(\lambda)\,1.5}} E'_{\odot,\lambda}(\lambda, X = 1.5) \quad . \tag{9.8}$$

Given the measured spectral irradiance $E_{\odot,\lambda}(\lambda, X = 0)$ on top of the atmosphere, the atmospheric thickness of the atmosphere of the Earth without aerosol derives to

$$\tau_{\mathrm{atm}}(\lambda) = -\frac{1}{1.5}\log\left(\frac{E_{\odot,\lambda}(\lambda, X = 1.5)}{E_{\odot,\lambda}(\lambda, X = 0)}\right) \quad . \tag{9.9}$$

The measured spectra of the sun and the calculated transmittance

$$T_{\mathrm{atm}}(X, \lambda) = e^{-\tau_{\mathrm{atm}}(\lambda)X} \tag{9.10}$$

are presented in figure 9.4.

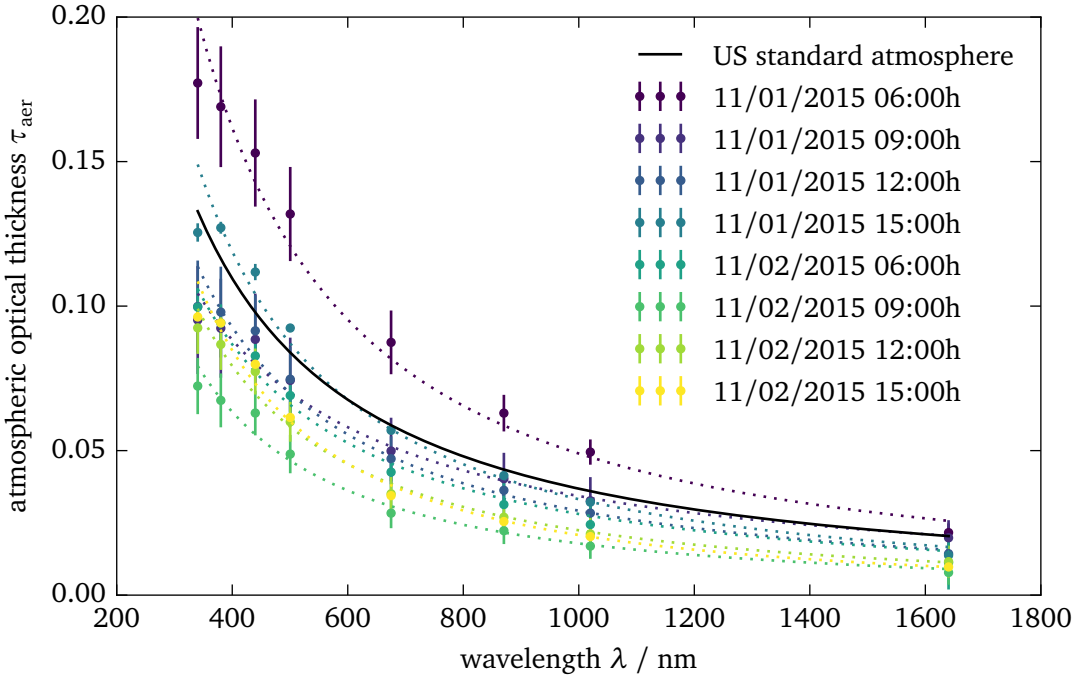

Figure 9.5: Atmospherical optical thickness for different wavelengths as measured by JOYCE before and after the star trail observations. The dotted lines denote fits of the Ångström formulas to the thicknesses. The straight line is the atmospherical thickness of the US standard atmosphere model.

9.4 Absorption due to aerosols

Aerosols are fine particles in the air and of artificial or natural origin and cause additional light scattering and absorption in the atmosphere of the Earth [266]. An example for aerosols of natural origin is water vapor or fog. Aerosols of artificial origin may be haze, dust and smoke or other air pollutants. Both contributions are highly variable and have to be handled with great care [264]. The NASA aerosol robotic network (AERONET) is a large network of roughly 1000 measurement sites which continuously monitor the aerosol content of the atmosphere by means of e.g. sun photometers during daylight with the sun as reference light source [267, 268, 269, 270]. To measure the aerosol content during nighttime, the moon or stars can be used as reference light sources which is more challenging since e.g. the moon has 10^{-5} to 10^{-6} the irradiance of the sun [271, 272]. Apart from seasonal changes, no statistically significant differences has been found between the aerosol content during daytime and nighttime in a longterm study in the city of Granada, Spain [272]. The closest site to the RWTH Aachen university campus is located in Jülich, JOYCE, in a distance of roughly 25 km airline [273, 274].

The data of all stations are analyzed centrally by AERONET. Three different quality levels are available for the most recent version of the analysis algorithms (version 3): level 1.0 corresponds to unscreened data without calibrations applied, level 1.5 data is cloud screened and has the majority of the calibrations applied and level 2.0 has all calibrations applied and has been revised manually [274]. For the analysis in this thesis, data of the level 1.5 will be used

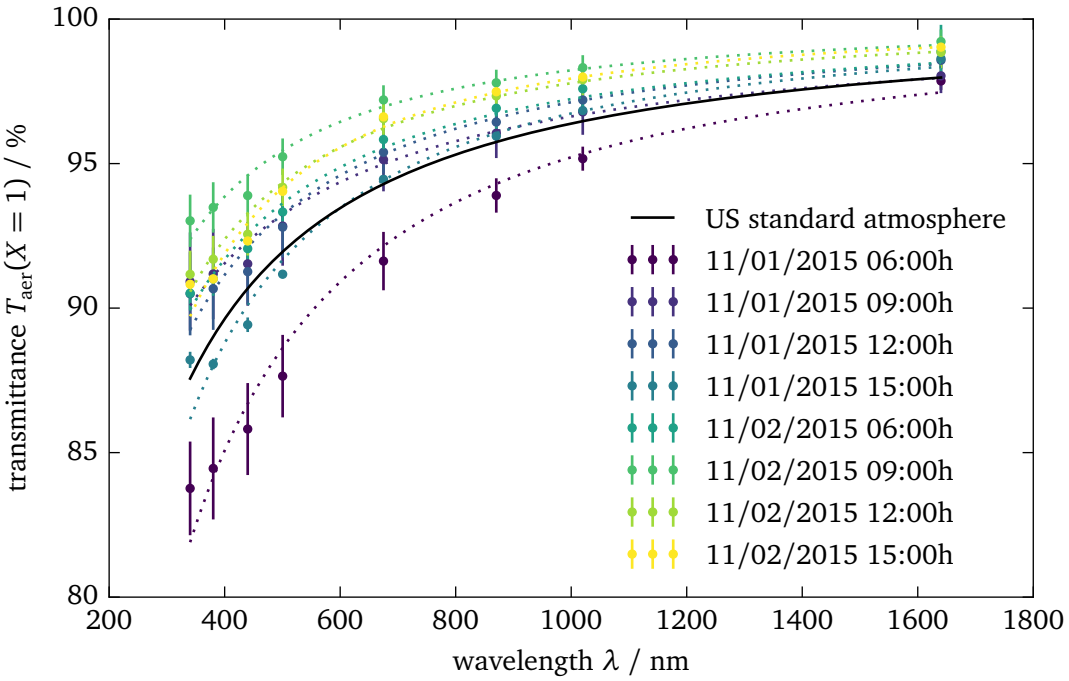

Figure 9.6: Atmospherical transmittance due to aerosols for different wavelengths as measured by JOYCE before and after the star trail observations. Analogously to figure 9.5, the dotted lines denote fit results and the straight line the US standard atmosphere model.

to exclude the presence of clouds which would lead to extremely high atmospheric thicknesses (level 2.0 not yet available). Nevertheless, the data of the JOYCE station already has all detector calibrations applied at the data level 1.5 [275].

The station measures the atmospheric thickness (and reconstructs the Ångström parameter) due to aerosols every 15 min at distinct wavelengths of $\lambda = 340.2\,\text{nm}$, 380.2 nm, 439.9 nm, 500.4 nm, 675.0 nm, 870.3 nm, 1020.0 nm and 1640.2 nm. Water vapor mainly influences the optical thickness for wavelengths $\lambda > 600\,\text{nm}$ and is therefore classified as coarse aerosol particles [268]. The measured atmospheric thicknesses are then averaged in three hour wide windows 18 hours before and after the star trail observation. The sample variance of the averaged samples is taken as uncertainty on these quantities. A χ^2-fit of the Ångström formula

$$\tau_{\text{aer}}(\lambda) = \tau_{\text{aer},0}\left(\frac{\lambda}{\lambda_0}\right)^{-\alpha} \tag{9.11}$$

to the mean atmospheric thicknesses yields the Ångström parameters $\tau_{\text{aer},0}$ and α. The reference wavelength λ_0 has been fixed to $\lambda_0 = 340.2\,\text{nm}$ which corresponds to the first available wavelength in the data. The fit results of the Ångström parameters are compatible with the Ångström parameters provided by AERONET itself whereby the AERONET analysis distinguishes between fine and coarse particles which exceeds the scope of this thesis [263, 276, 277]. The results are presented in figures 9.5 and 9.6. Since no data are available during nighttime, the mean value of all fits is used for the calculation of the expected photon flux. It should be noted that the time gap between the last measurement on the day of the observations

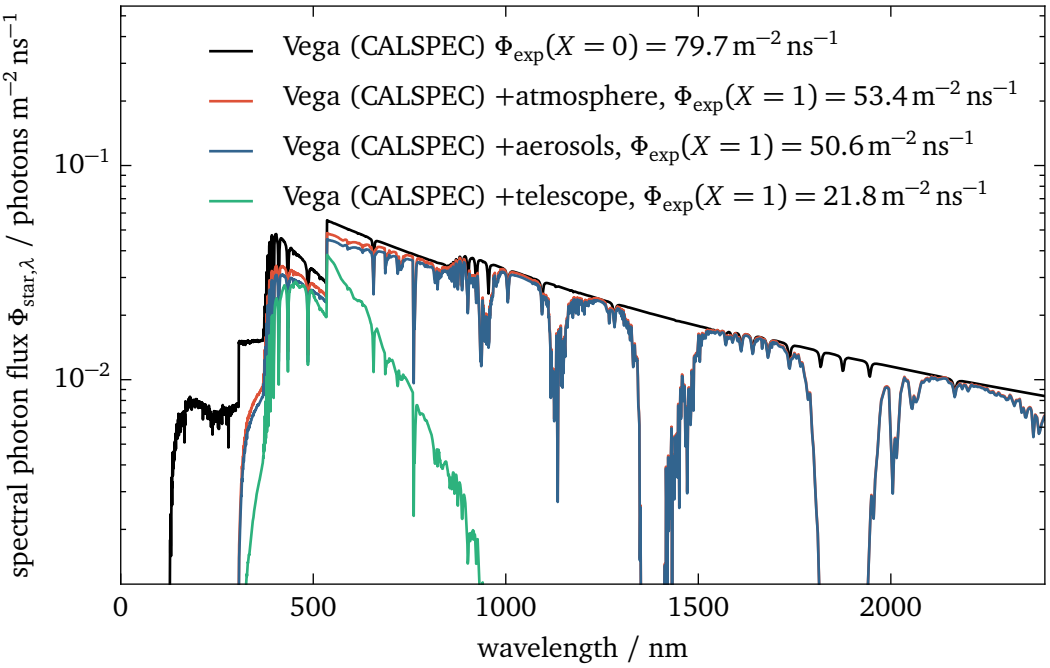

Figure 9.7: The spectral photon flux $\Phi_{exp,\lambda}(\lambda, X)$ for the observation of Vega above the atmosphere at $X = 0$, with the atmosphere, the aerosols and the transmission efficiency of the telescope with its maximum scaled to 1 for this plot. The atmosphere has a notable effect on the photon flux reaching the ground. The reduction by the telescope is important since it is only sensitive in the wavelength regime from $\lambda = 300\,nm$ to $900\,nm$. The stellar spectrum has been taken from CALSPEC [241].

and the first measurement on the next day is approximately 16.5 h (15:07h to 07:32h). Thus, this is the largest systematical uncertainty in this analysis. The relative, statistical uncertainty on the mean atmospheric thickness τ_{aer} due to aerosols is 10 % (cf. table 9.4).

9.5 Expected photon flux

For the observation of the star trails, the environmental parameters have to be taken into account as well as the position and observation height (above sea level). All these quantities are automatically taken into account by the Astropy software package when calculating the apparent observed altitude of the star [259]. The spectral irradiance of the star $E_{star,\lambda}(\lambda)$ is then weighted by the transmittance of the atmosphere (cf. equation (9.10)) and the transmittance due to aerosols (cf. equation (9.11)) to derive the observable spectral irradiance of the star at ground level

$$E_{exp,\lambda}(\lambda, X) = \exp^{-X\,\tau_{atm}(\lambda)}\,\exp^{-X\,\tau_{aer}(\lambda)}\,E_{star,\lambda}(\lambda) \quad . \tag{9.12}$$

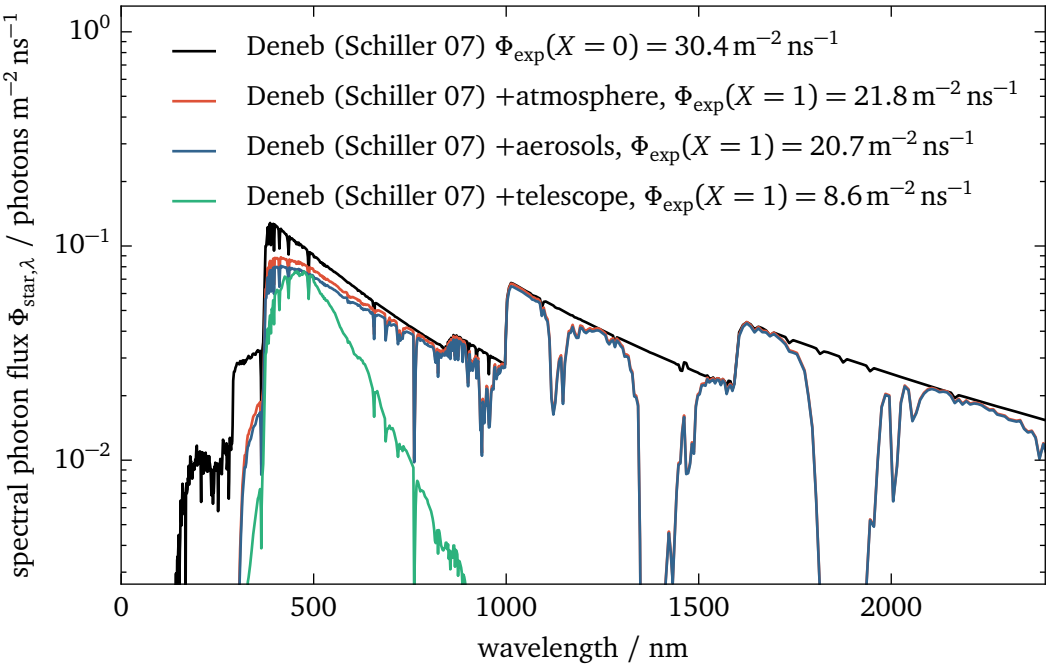

Figure 9.8: The spectral photon flux $\Phi_{exp,\lambda}(\lambda, X)$ for the observation of Deneb above the atmosphere at $X = 0$, with the atmosphere, the aerosols and the transmission efficiency of the telescope with its maximum scaled to 1 for this plot. See also figure 9.7. The stellar spectrum has been taken from ATLAS [245] for the stellar parameters given in [238] (cf. table 9.2).

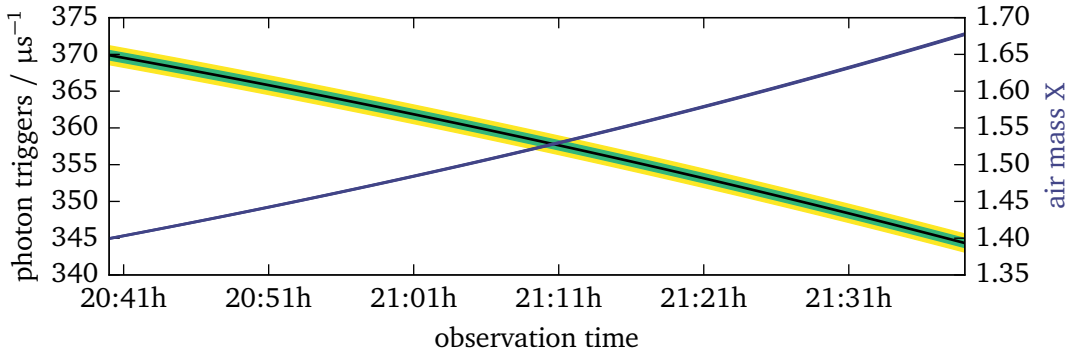

Figure 9.9: The integrated photon flux $\Phi_{exp}(X)$ (black line and colored areas) for the observation of Vega for the environmental conditions given during the observation time as a function of airmass (blue line). The colored regions denote the 1σ and 2σ confidence intervals of the expected photon flux. See also figure 9.7.

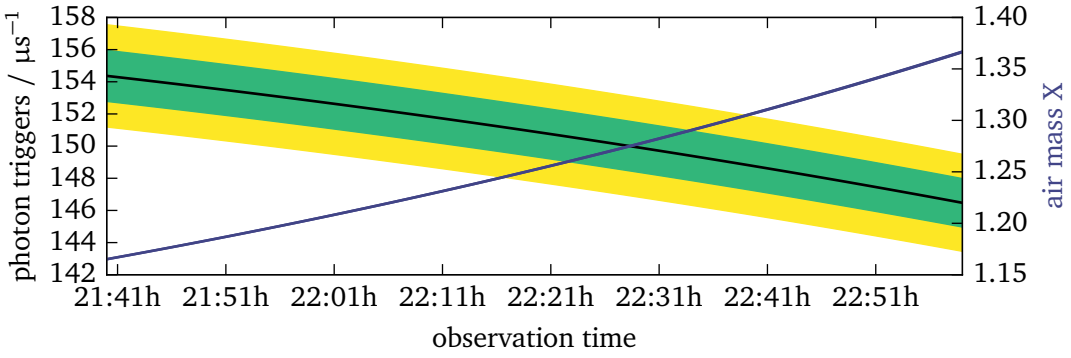

Figure 9.10: The integrated photon flux $\Phi_{\text{exp}}(X)$ (black line and colored areas) for the observation of Deneb for the environmental conditions given during the observation time as a function of airmass (blue line). The colored regions denote the 1σ and 2σ confidence intervals of the expected photon flux. See also figure 9.8.

	Relative uncertainty	
	Vega	Deneb
Temperature T_{eff}	-	1 %
Surface gravity $\log(g)$	-	5 %
Metallicity $\log(m)$	-	20 %
Stellar spectrum $E_{\text{star},\lambda}(\lambda)$	0.5 %	12 %
Parallax ρ	0.06 %	8 %
Atmospheric thickness τ_{atm}	10 %	
Aerosol thickness τ_{aer}	10 %	
Ångström parameter α	12 %	
Transmission efficiency ϵ_{tel}	0.4 %	
Transmission efficiency correction $\epsilon_{\text{tel,corr}}$	0.4 %	
Total uncertainty on $\Phi_{\text{exp}}(X)$	0.2 %	1.0 %

Table 9.4: Uncertainties on the stellar, atmospheric and other parameters which yield the uncertainty on the expected photon flux $\Phi_{\text{exp}}(X)$. See also table 9.3 for the uncertainties on the airmass. It should be noted that the uncertainties on the atmospherical thicknesses have a minor impact on the total uncertainty due to the nature of the exponential function yielding a rather small total uncertainty on $\Phi_{\text{exp}}(X)$ (cf. equation (9.19)).

Star	Vega	Deneb
Observation date	November 1st, 2015	
Start	20:40 h	21:40 h
X	1.3995 ± 0.0011	1.1651 ± 0.0005
$\Phi_{\text{exp}}(X)$	$(369.9 \pm 0.6)\,\mu\text{s}^{-1}$	$(154.4 \pm 1.6)\,\mu\text{s}^{-1}$
Flux ratio	2.40 ± 0.03	
End	21:40 h	23:00 h
X	1.6775 ± 0.0017	1.3666 ± 0.0010
$\Phi_{\text{exp}}(X)$	$(344.3 \pm 0.6)\,\mu\text{s}^{-1}$	$(146.5 \pm 1.5)\,\mu\text{s}^{-1}$
Flux ratio	2.35 ± 0.03	

Table 9.5: The mean expected photon fluxes Φ_{exp} for Vega and Deneb for the beginning and the end of the measurement period. Also given is the ratio of the flux of Vega to the flux of Deneb.

To obtain the number of photons per wavelength bin and unit area, denoted by the photon flux $\Phi_{\text{exp},\lambda}(\lambda, X)$, the spectral irradiance has to be multiplied by the width of the wavelength bin $\delta\lambda$ and divided by the photon energy of the corresponding bin

$$\Phi_{\text{exp},\lambda}(\lambda, X) = E_{\text{exp},\lambda}(\lambda, X)\,\frac{\lambda}{h\,c}\delta\lambda \tag{9.13}$$

with the Planck constant $h = 6.626 \cdot 10^{-34}\,\text{J s}$ and the speed of light c. The expected spectral photon fluxes are presented in figures 9.7 and 9.8. To obtain the photon trigger rate detected by the telescope, the photon flux has to be multiplied by the aperture and the transmission efficiency of the telescope. The aperture, i.e. the light collection area, of the FAMOUS telescope is

$$A_{\text{tel}} = \pi(d/2)^2 = \pi(0.5021\,\text{m}/2)^2 = 0.198\,\text{m}^2 \quad . \tag{9.14}$$

The transmission efficiency of the telescope $\epsilon_{\text{tel}}(\lambda)$ has been determined in a Monte Carlo simulation as described above in section 7.2 (see also figure 7.12, left at $z = 507.89\,\text{mm}$). Here, the telescope has been illuminated with light isotropically emitted from the field of view of the central pixel to obtain a mean detection efficiency independent from the actual position of the star in the field of view of the pixel. The simulated transmission efficiency has a maximum value of

$$\epsilon_{\text{tel}}(\lambda = 475\,\text{nm}) = (13.2 \pm 0.3)\,\% \quad . \tag{9.15}$$

It includes the transmission of the Fresnel lens, the efficiency of the Winston cones and the photon detection efficiency of the SiPMs. However, the simulated Fresnel lens transmission efficiency $T_{\text{lens,sim}}(\lambda)$ is larger than the measured value $T_{\text{lens,meas}}(\lambda)$ [150]. Therefore, the efficiency of the telescope $\epsilon_{\text{tel}}(\lambda)$ is multiplied by a factor of

$$\epsilon_{\text{tel,corr}} = \frac{T_{\text{lens,meas}}(\lambda = 550\,\text{nm})}{T_{\text{lens,sim}}(\lambda = 550\,\text{nm})} = \frac{(50.5 \pm 0.2)\,\%}{(75.57 \pm 0.12)\,\%} = (66.83 \pm 0.29)\,\% \tag{9.16}$$

to account for the overestimation by the simulations. The lower measured value is caused by the manufacturing process, a special groove shape, which is a compromise between imaging

quality and transmission efficiency, and by diffraction not covered in the ray-tracing simulation [144]. In addition, the transmittance of the Fresnel lens might also be significantly reduced due to surface dew on the back side of the lens [278]. If the ambient temperature is lower than inside the telescope, the temperature at the boundary (the lens) can fall below the dew point. Since the mechanics make the telescope a closed system, dew removal is impractical outside the laboratory. A detailed time-dependent SiPM simulation is not necessary at this point since the star light is a continuous light source. Thus, the resulting number of detected photons of the telescope is given by

$$\Phi_{\text{exp}}(X) = \int A_{\text{tel}}\, \epsilon_{\text{tel,corr}}\, \epsilon_{\text{tel}}(\lambda)\, \Phi_{\text{exp},\lambda}(\lambda, X)\, \mathrm{d}\lambda \tag{9.17}$$

$$= \int A_{\text{tel}}\, \epsilon_{\text{tel,corr}}\, \epsilon_{\text{tel}}(\lambda)\, E_{\text{exp},\lambda}(\lambda, X)\, \frac{\lambda}{h\,c}\, \mathrm{d}\lambda \tag{9.18}$$

$$= \int A_{\text{tel}}\, \epsilon_{\text{tel,corr}}\, \epsilon_{\text{tel}}(\lambda)\, \exp^{-X\,\tau_{\text{atm}}(\lambda)}\, \exp^{-X\,\tau_{\text{aer}}(\lambda)}\, E_{\text{star},\lambda}(\lambda)\, \frac{\lambda}{h\,c}\, \mathrm{d}\lambda \tag{9.19}$$

using equations (9.12) and (9.13).

The results for the expected photon flux $\Phi_{\text{exp}}(X)$ can be found in figures 9.9 and 9.10. The uncertainties have been handled with great care and propagated through all steps of the calculation. Regarding the stellar models, the quoted uncertainty for the stellar spectrum of Vega is 0.5 % [242]. For Deneb, the stellar parameters T_{eff}, $\log(m)$ and $\log(g)$ have been varied within their uncertainties. The largest difference between the obtained ATLAS models is taken as conservative estimate of the uncertainty on the stellar spectrum. The constituents of the uncertainty on the expected photon flux Φ_{exp} are quoted in table 9.4. In total, the uncertainty on the expected flux Φ_{exp} due to uncertainties in the models and the environmental conditions is rather low. The mean expected photon fluxes for Vega and Deneb for the beginning and the end of the measurement period are listed in table 9.5. Summarizing, the ratio between the two subsequent observations of Vega and Deneb is calculated to 2.40 ± 0.03. Those results are now compared to the SiPM current measurement in the next section.

9.6 Measurement of the current flow through the SiPMs

The increase of the current flow through the SiPMs has been measured by the power supply unit of FAMOUS (cf. section 6.3). In each readout cycle, the microcontroller of the device reads out the temperatures of each SiPM, adjusts the bias voltage accordingly and measures the current. Due to the large number of operations performed during each readout cycle, one complete measurement of the current of all 64 channels can be obtained every $\approx 5\,\text{s}$. Thus, the current is available as a function of observation time. Since the uncertainty of the current measurement is large, a moving average of $w = 12$ consecutive measurements is applied to the data. The window w has been chosen such that variations due to the measurement uncertainty are suppressed but the shape and most importantly the peak height are affected very little. In combination with the slowly transiting star, the reduction of the peak height is below $<$ 1 %. Nevertheless, the final analysis is performed on the original data with the results from the analysis on the smoothed data as start values. The resulting uncertainty on the current measurement is determined by the sample variance of all values within the window w and yields $\approx 12\,\%$ for Vega. Furthermore, frequent spikes of increased current occur in the current

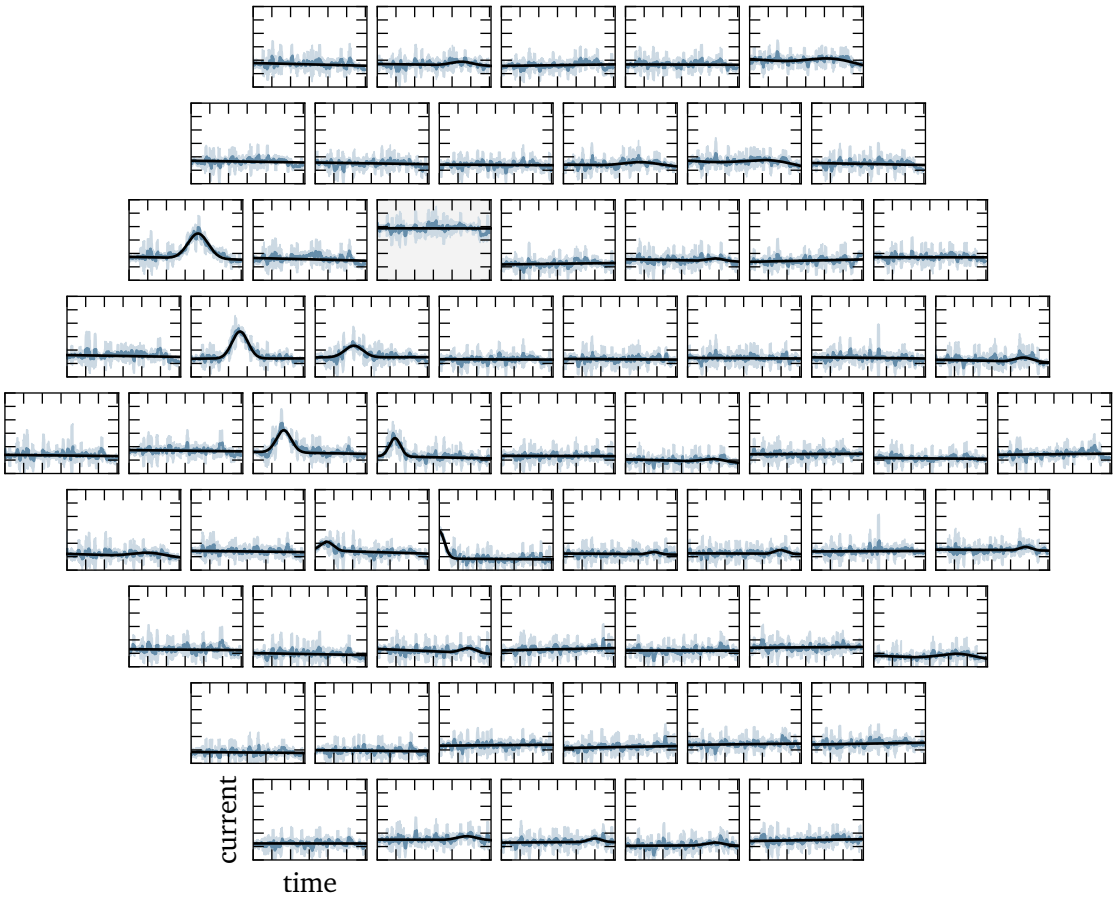

Figure 9.11: Measured currents as a function of time of each channel of the telescope FAMOUS for the observation of Vega. The x-axis is the time from 0 s to 3042 s, the y-axis the current from 200 µA to 800 µA. The data (shaded area) have been smoothed with a moving average. The line denotes a fit to the current increase caused by the star. The arrangement of the plots matches the arrangement of the pixels of the telescope. The not optimal grounding of the diesel generator might have lead to frequent, large spikes which have been sufficiently smoothed by the moving average. One SiPM in the upper left corner of the camera (shaded background) has a higher current compared to the other SiPMs due to a slightly misconfigured bias voltage.

signal, which have been successfully smoothed out by the moving average. This might be due to the not optimal grounding of the diesel generator used to power the telescope. Still, the spikes increase the sample variance. Later on, with the onset of dewing, the spikes do not occur anymore, which also leads to a reduced uncertainty of $\approx 7\,\%$ for the measurement of Deneb (cf. figure 9.12).

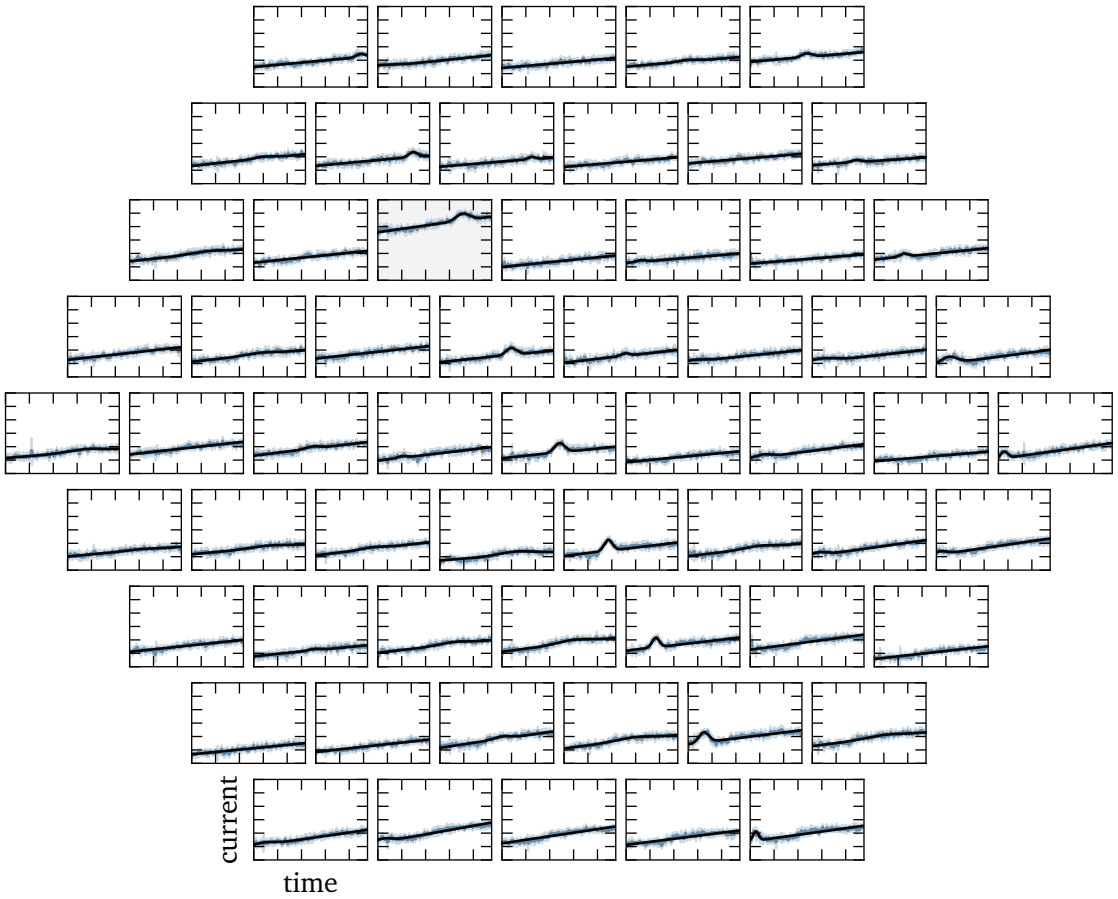

Figure 9.12: Measured currents as a function of time of each channel of the telescope FAMOUS for the observation of Deneb. The x-axis is the time from 0 s to 4766 s, the y-axis the current from 200 µA to 800 µA. The data (shaded area) have been smoothed with a moving average. The line denotes a fit to the current increase caused by the star. The arrangement of the plots matches the arrangement of the pixels of the telescope. Although the current excesses produced by the star are small compared to Vega (cf. figure 9.11), the transit of Deneb is well reconstructed. Additionally, the background increases significantly due to dewing of the lens.

9.6.1 Signal extraction

In the case of the star trails, the signal of the stars is given in the rise and set of the current signal above a more or less constant background. The signal can be modeled as a Gaussian function

$$s(t) = i_{\text{peak}}\, e^{(t-\mu)^2/(2\sigma^2)} \tag{9.20}$$

with the amplitude i_{peak}, i.e. the peak current increase, the position of the maximum μ and the width σ. The background contribution by the dark noise of the SiPMs is constant if the ambient temperature is constant. On the other hand, the night sky might change over time or, in case of the observation of Deneb, the amount of stray light increased due to dewing of the

Star	Vega	Deneb
Observation date	November 1st, 2015	
Time of maximum	20:39:56 h ±30 s	22:10:52 h ±8 s
Airmass X	1.3995 ± 0.0011	1.2312 ± 0.0007
Expected photon flux Φ_{exp}	$(369.9 \pm 0.6)\,\mu\text{s}^{-1}$	$(151.7 \pm 1.6)\,\mu\text{s}^{-1}$
Expected flux ratio	2.44 ± 0.03	
Measured photon flux Φ_{meas}	$(297 \pm 24)\,\mu\text{s}^{-1}$	$(118 \pm 5)\,\mu\text{s}^{-1}$
Measured flux ratio	2.53 ± 0.23	
Measured night sky photon flux	$(490 \pm 8)\,\mu\text{s}^{-1}$	$(458 \pm 8)\,\mu\text{s}^{-1}$

Table 9.6: The peak measured photon fluxes for Vega and Deneb. Compared to the expectation, the measured peak values are lower. Possible explanations are unknown changes in the aerosol content during the 16.5 h with no photometer measurements available, the reduction of the transmission efficiency of the telescope due to dew or systematic offsets in the simulated telescope efficiency. Since the telescope is a closed system, dew removal outside the laboratory is impractical. Also given is the ratio of the flux of Vega to the flux of Deneb which matches the expectation within the uncertainties. The measured photon flux from the diffuse night sky background has been determined by the mean offset of the first degree polynomial i_0 (cf. equation (9.22)) excluding the pixel with the inaccurate bias voltage.

lens. Nevertheless, these processes are slow compared to the movement of the star, thus their contribution is modeled by a first degree polynomial

$$b(t) = i_0 + t\, i_b \tag{9.21}$$

with a constant offset i_0 and slope i_b. The sum of both functions models the current flow $i(t)$

$$i(t) = i_0 + t\, i_b + i_{\text{peak}} \exp^{\frac{(t-\mu)^2}{2\sigma^2}} \tag{9.22}$$

A fit of this function to the measured current $i_{\text{meas}}(t)$ to each channel is performed. As described above, $i_{\text{meas}}(t)$ is smoothed with a moving average with a window width of $w = 12$. To improve the fit result, firstly, $b(t)$ is fitted to $i_{\text{meas}}(t)$, then $s(t)$ to the background subtracted measurement $i_{\text{meas}}(t) - b(t)$. Lastly, with the results of the previous two fits as start values, the final fit of $i(t)$ to the not-smoothed data $i_{\text{meas}}(t)$ is performed. The result of these fits is presented in figures 9.11 and 9.12.

9.6.2 Reconstruction of the photon flux from the SiPM current

As discussed in the previous section, the peak current i_{peak} increase caused by the observed star on the night sky could be reconstructed. Using the known properties of the SiPM, the mean photon trigger rate can be calculated from the current. The mean photon trigger rate can be compared to the calculated expectation since both values incorporate all necessary efficiencies and most importantly the photon detection efficiency of the SiPM.

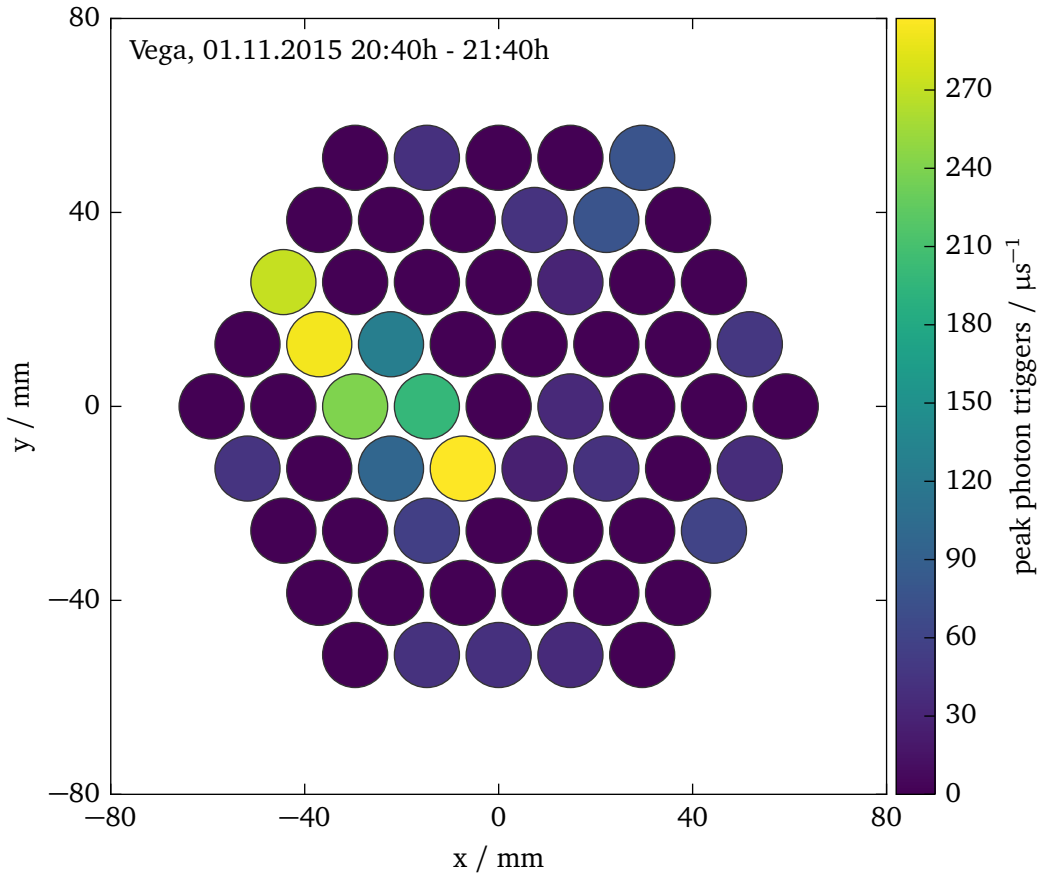

Figure 9.13: Reconstructed photon trigger rate for the observation of the star trail of Vega. Each colored circle signifies a pixel of the telescope FAMOUS. The values have been determined by fits to the measured current. The star has first been seen in the center of the camera with the trail continuing to the upper left corner of the camera (lower right of the telescope).

Given the mean gain of the SiPMs of $g = (2.807 \pm 0.005) \cdot 10^6$, the mean current of n avalanche breakdowns in the SiPM is simply

$$i_{\text{sipm}}(n) = n\, g\, e \tag{9.23}$$

with the elementary charge e. Additionally, the trigger rate of the SiPM is increased by optical crosstalk with a probability of $p_{\text{ct}} = 35\,\%$. Starting from the order zero, i.e. no occurrence of optical crosstalk, the sum including all possible higher orders of optical crosstalk results in a geometric series which can be simplified to

$$\sum_{k=0}^{\infty} p_{\text{ct}}^k = \frac{1}{1-p_{\text{ct}}} \quad . \tag{9.24}$$

Thus, the maximum measured peak current is given by

$$\max\left(i_{\text{peak}}\right) = \frac{1}{1-p_{\text{ct}}}\, g\, e\, \Phi_{\text{meas}} \quad . \tag{9.25}$$

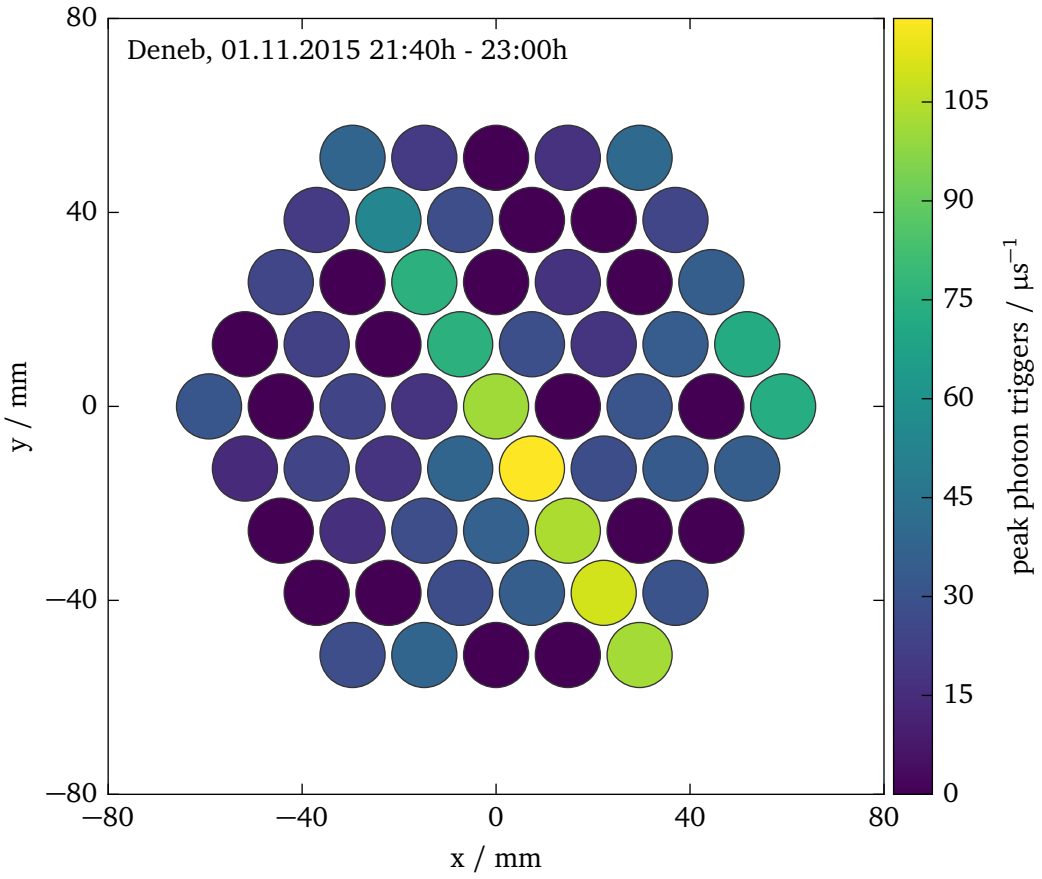

Figure 9.14: Reconstructed photon trigger rate for the observation of the star trail of Deneb (see also figure 9.13). Here, the star trail could be observed in all pixels of the telescope from the lower right to the upper left part of the camera. The signal of the star trail decreases over time due to dewing of the Fresnel lens of the telescope. Thus, the relative difference between pixel on the lower left and the pixel on the upper right, which have a similar detection efficiency, amounts to $(63 \pm 7)\,\%$ whereby the expected flux reduction due to the atmosphere is $(5.0 \pm 1.4)\,\%$.

By inversion, the measured photon flux can be derived from the measured current

$$\Phi_{\text{meas}} = \left(\frac{1}{1 - p_{\text{ct}}} \, g \, e \right)^{-1} \max\left(i_{\text{peak}} \right) \quad . \tag{9.26}$$

It should be noted, this simple approach is only valid for ideal SiPMs since the current flow through the real counterpart saturates due to the limited amount of G-APDs on the device. Here, the light flux is sufficiently small. The reconstructed peak fluxes Φ_{meas} are presented in figures 9.13 and 9.14 in a camera view. The trails, going from the bottom right to the upper left corner, are clearly visible. Small peak currents could be fitted to pixels which seem to contain only night sky background.

The resulting maximum measured photon fluxes are presented in table 9.6. Compared to the expected photon fluxes, the measured peak photon flux is systematically lower for both

stars by approximately 20 %. Possible explanations are unknown changes in the atmospherical thickness during the observations, a reduction of the telescope transmission due to dewing of the optical elements or a remaining systematic offset of the simulated transmission efficiency of the single optical elements. The dewing of the lens which was visible especially at the end of the tracking of Deneb as white fog on the backside of the lens but may have existed less pronounced from the beginning of the tracking of Vega. Thus, the relative difference of the measured photon flux between the beginning of the star trail and the end is (63 ± 7) % whereas a flux reduction of (5.0 ± 1.7) % is expected from the models. Since the start and the end pixel of the trail have the same viewing angle with respect to the optical axis of the telescope, the reduction is not induced by light falloff. The Winston cones are made from aluminum and are thermally connected to the telescope tube which is also made from aluminum. While this reduces the temperature of the SiPMs attached to the cones, condensation might occur inside the tube on the reflective surfaces of the Winston cones and potentially reduce their reflectivity [157]. However, due to the dewing of the lens, this was not examinable. Nevertheless, the ratio of the measured photon fluxes of Vega and Deneb matches the expectation within the uncertainties.

In summary, this is a very important result since it demonstrates that the FAMOUS telescope prototype is understood to a level of detail which allows measurements with feasible results. Should the 20 % systematically lower measured photon flux be caused by an overestimation of the detector simulation and not by environmental conditions, the simulated transmission efficiency of the telescope can be scaled down by this factor to obtain better estimates on the detection efficiency of extensive air showers. Furthermore, the light falloff of the optics of FAMOUS can be obtained by quantifying the flux reduction in pixels far off the optical axis compared to pixels in the center of the camera. Since the results of this analysis also quantified the large negative influence of dew on the detection efficiency of the telescope, the development and construction of a prevention mechanism is necessary before performing further measurements of star trails or of air showers in the near future.

Chapter 10

Conclusion and outlook

The fluorescence light detection of extensive air showers by means of telescopes equipped with photomultiplier tubes is a well established technique and employed at several observatories. For instance, at the Pierre Auger Observatory in total 27 telescopes oversee the air above a 3000 km^2 large ground array of water Cherenkov stations. However, a major shortcoming of photomultiplier tubes is their fragility regarding high light intensities which presents a challenge when measuring during twilight or moonlit nights.

The prototype telescope FAMOUS is the first fluorescence telescope to use silicon photomultipliers (SiPMs). The main optical element of FAMOUS is a thin acrylic Fresnel lens with a diameter and a focal length of 502 mm which is transparent in the ultraviolet. Despite the fragmentation of the lens surface due to the Fresnel lens construction principle, the optical imaging quality has been measured to be sufficient for the use with the focal plane. The image quality has been measured by the radius r_{90} encircling 90 % of the energy in an image of an infinitely distant point source. Given the fluorescence light of extensive air showers complies with a point source moving with the speed of light, the image size is small enough to be fully captured by the light funnels of the focal plane. These so-called Winston cones are circular hollow light concentrators made from polished aluminum with an entrance radius of 6.71 mm and 0.69 mm wall thickness. At the exit of each cone, one Hamamatsu S12573-100X SiPM with an active area of 6 mm × 6 mm and 3600 cells is placed. The SiPM is a special model from the manufacturer with a silicone coating for improved photon detection efficiency for wavelengths $\lambda < 330$ nm which amounts for a substantial fraction of the fluorescence light. The photon detection efficiency of the SiPMs is 35 % at a peak wavelength of $\lambda = 420$ nm. The Hamamatsu S12573-100X benefits from large improvements made with newer SiPM generations regarding the dark noise. Hence, the afterpulsing with a probability of $p_{\mathrm{ap}} < 1\,\%$ is negligible. The overall dark noise rate amounts to $f_{\mathrm{dark}} = 2$ MHz. Nevertheless, the crosstalk probability $p_{\mathrm{ct}} = 35\,\%$ is rather high. To improve the signal to noise ratio, a Schott UG11 ultraviolet band pass filter can be installed between the Winston cones and the SiPMs. The focal plane of FAMOUS has 61 pixels, which each consist of one Winston cone, one UG11 filter plate and one SiPM. Furthermore, three dark SiPMs are installed for noise monitoring. The pixels are arranged in a hexagonal grid around a central pixel to minimize the dead space between the circular Winston

cones. The Winston cones are glued into a metal frame and fixed to the printed circuit board on which the SiPMs are situated in conjunction with one temperature sensor each. The board is connected to a 64 channel power supply unit which continuously reads out the temperature sensors and automatically finely adjusts the bias voltage of each SiPM to account for changes in the ambient temperature. As a result, the gain is stable at the 1 % level.

Since SiPMs are made up from single cells, the dynamic range of these devices is limited. Therefore, a dedicated SiPM simulation has been developed in the scope of this thesis. The G4SiPM simulation framework provides the means to include SiPMs in Geant4 simulations. Geant4 is a simulation framework for the simulation of the interaction of fundamental particles with matter and is widely used in particle physics. Geant4 is also capable of ray-tracing of photons while respecting optical properties. The G4SiPM implementation follows a phenomenological model of SiPMs which is driven by input quantities which either can be looked up in datasheets or measured in the laboratory: the photon detection efficiency, the thermal noise rate, the probabilities of crosstalk and afterpulsing, the time constants of afterpulsing and the recovery time as well as geometrical parameters and refractive indexes of the materials. All parameters can be supplied as a function of the over-voltage. To validate the predictions made by G4SiPM, input quantities obtained by a voltage trace analysis of SiPM signals have been fed into G4SiPM for the simulation of dark noise. The simulated data have been processed with the same analysis to compare the reconstructed parameters to the input. Apart from the afterpulsing time constants, which show a systematic offset due to the analysis method, the parameters match within less than 5 % deviation. Furthermore, a measurement of the dynamic range could be successfully reproduced with G4SiPM. In summary, G4SiPM is capable of correctly simulating all relevant properties of SiPMs and can aid in important design choices or improve the comprehension of the detector.

Based on the G4SiPM package, a dedicated Geant4 ray-tracing simulation for FAMOUS has been developed. The simulation includes a detailed model of the Fresnel lens and the Winston cones. Thus, the simulation correctly reproduces the measured optimal focus distance of the Fresnel lens. As for the aberration radius, the simulation results in smaller values for r_{90} since it does not cover mechanical imperfections and diffraction at the fine structures of the lens. The simulation of FAMOUS has been used to compile a telescope response parameterization. The telescope response parameterization yields the detection efficiency of each pixel including the optics of the Fresnel lens, the transmission efficiency of the Winston cones, the UG11 filters and the photon detection efficiency of the SiPMs as a function of the incidence direction of the photons on the telescope and their wavelength. Therefore, the telescope response parameterization permits a quasi instantaneous calculation of the number of photons detected from extensive air showers and the night sky background. The CONEX simulation tool and the simulation framework Offline of the Pierre Auger Collaboration have been used to simulate the amount of fluorescence light reaching the telescope from longitudinal profiles of the energy deposit of extensive air showers. Consequently, the detection efficiency for extensive air showers could be determined as a function of the shower core distance and the shower energy which results in several detected air showers per hour measurement time. In addition, events originating from night sky brightness could be successfully suppressed.

Finally, the telescope FAMOUS has been successfully commissioned by the development of a dedicated slow control system which supervises the data taking and records environmental parameters. The slow control presents viable information in real-time via a remotely accessible web interface. Thus, a seven pixel prototype of the telescope named IceAct can be operated remotely at the South Pole for the detection of Cherenkov light of extensive air showers. Fur-

thermore, photographs of the night sky can be taken for later analysis for the detection of visible stars which can be used to determine the viewing direction of the telescope. With this information, trails of the two bright stars Vega and Deneb have been recorded. Since the power supply unit of FAMOUS also monitors the current flow through the SiPMs, the current increase due to the transition of the stars could be used to reconstruct the photon flux originating from the stars. This result has been compared to a theoretical expectation achieved by models of the spectral intensity of stars, a measurement of the intrinsic absorption of the atmosphere and the absorption due to aerosols both as a function of the apparent height of the star above the horizon. Since the trails of Vega and Deneb have been measured during the same night, the systematic effects of the atmosphere and the telescope could be canceled by deriving the ratios of photon fluxes of the two stars. The measured and the expected ratios match within their uncertainties which is a great step forward to the successful detection of extensive air showers with FAMOUS.

The dedicated self-triggering data acquisition system of the focal plane of FAMOUS is currently under development. It will be based on the TARGET ASIC originally developed for the telescope cameras of the CTA project but is also applicable for fluorescence light detection. Once the data acquisition is fully operational, first extensive air showers can be detected with FAMOUS which will be a great achievement for the project and a prospect for future experiments due to an expected increase in sensitivity and measurement time. By enabling detailed measurements of the physics of air showers, ultimately the means to answer the pending questions of astroparticle physics regarding the origin and creation mechanisms of ultra high energy cosmic rays could be provided.

References

[1] J. Blümer, R. Engel, and J. R. Hörandel. “Cosmic rays from the knee to the highest energies”. In: *Prog. Part. Nucl. Phys.* 63.2 (2009), pp. 293–338. DOI: 10.1016/j.ppnp.2009.05.002.

[2] H. Bergeson et al. “Measurement of light emission from remote cosmic-ray air showers”. In: *Phys. Rev. Lett.* 39.13 (1977), p. 847. DOI: 10.1103/physrevlett.39.847.

[3] R. Baltrusaitis et al. “The Utah fly’s eye detector”. In: *Nucl. Instrum. Methods Phys. Res., Sect. A* 240.2 (1985), pp. 410–428. DOI: 10.1016/0168-9002(85)90658-8.

[4] T. Abu-Zayyad et al. “The prototype high-resolution Fly’s Eye cosmic ray detector”. In: *Nucl. Instrum. Methods Phys. Res., Sect. A* 450.2 (2000), pp. 253–269. DOI: 10.1016/s0168-9002(00)00307-7.

[5] H. Kawai et al. “Telescope array experiment”. In: *Nucl. Phys. B Proc. Suppl.* 175 (2008), pp. 221–226. DOI: 10.1016/j.nuclphysbps.2007.11.002.

[6] J. Abraham et al. “The fluorescence detector of the Pierre Auger Observatory”. In: *Nucl. Instrum. Methods Phys. Res., Sect. A* 620.2 (2010), pp. 227–251. DOI: 10.1016/j.astropartphys.2009.10.005.

[7] H. Tokuno et al. “New air fluorescence detectors employed in the Telescope Array experiment”. In: *Nucl. Instrum. Methods Phys. Res., Sect. A* 676 (June 2012), pp. 54–65. DOI: 10.1016/j.nima.2012.02.044.

[8] D. Renker and E. Lorenz. “Advances in solid state photon detectors”. In: *J. Inst.* 4.04 (Apr. 2009), P04004. DOI: 10.1088/1748-0221/4/04/p04004.

[9] Hamamatsu Photonics. *Hamamatsu News 2-2013*. Nov. 2013. URL: http://www.hamamatsu-news.com.

[10] P. Eckert et al. “Characterisation studies of silicon photomultipliers”. In: *Nucl. Instrum. Methods Phys. Res., Sect. A* 620.2-3 (Aug. 2010), pp. 217–226. DOI: 10.1016/j.nima.2010.03.169.

[11] S. Agostinelli et al. “GEANT4 — a simulation toolkit”. In: *Nucl. Instrum. Methods Phys. Res., Sect. A* 506.3 (2003), pp. 250–303. DOI: 10.1016/S0168-9002(03)01368-8.

[12] T. Niggemann et al. “G4SiPM: A novel silicon photomultiplier simulation package for Geant4”. In: *Nucl. Instrum. Methods Phys. Res., Sect. A* (2015). ISSN: 0168–9002. DOI: 10.1016/j.nima.2015.01.067.

[13] Orafol Fresnel Optics GmbH. *PositiveLinsen 1*. 2013. URL: http://www.orafol.com/tl_files/EnergyEurope/documents/PDF/Productlist/PositiveLinsen_1.pdf.

[14] Hamamatsu Photonics. *MPPC Array S12573 Series Product Array*. Oct. 2013.

[15] J. Schumacher et al. "Dedicated power supply system for silicon photomultipliers". In: *Proceedings of Science* PoS(ICRC2015)605 (2015). URL: http://pos.sissa.it/archive/conferences/236/605/ICRC2015_605.pdf.

[16] R. A. Millikan and I. Bowen. "High Frequency Rays of Cosmic Origin I. Sounding Balloon Observations at Extreme Altitudes". In: *Phys. Rev.* 27.4 (Apr. 1926), pp. 353–361. DOI: 10.1103/physrev.27.353.

[17] M. Schein and P. S. Gill. "Burst frequency as a function of energy". In: *Rev. Mod. Phys.* 11.3-4 (1939), p. 267. DOI: 10.1103/revmodphys.11.267.

[18] P. Auger et al. "Extensive cosmic-ray showers". In: *Rev. Mod. Phys.* 11.3-4 (1939), p. 288. DOI: 10.1103/revmodphys.11.288.

[19] M. Nagano and A. A. Watson. "Observations and implications of the ultrahigh-energy cosmic rays". In: *Rev. Mod. Phys.* 72.3 (July 2000), pp. 689–732. DOI: 10.1103/revmodphys.72.689.

[20] A. Watson. "Extensive Air Showers and Ultra High Energy Cosmic Rays". In: *Summer School in Mexico* (2002), pp. 1–50.

[21] P. Blasi. "The origin of galactic cosmic rays". In: *The Astronomy and Astrophysics Review* 21.1 (2013), pp. 1–73. DOI: 10.1007/s00159-013-0070-7.

[22] K. Olive et al. "The Review of Particle Physics". In: *Chinese Phys. C* 38.9 (Aug. 2014). Ed. by P. D. Group, p. 090001. DOI: 10.1088/1674-1137/38/9/090001.

[23] K.-H. Kampert. "Ultrahigh-Energy Cosmic Rays: Results and Prospects". In: *Braz. J. Phys.* 43.5-6 (2013), pp. 375–382. DOI: 10.1007/s13538-013-0150-1.

[24] A. Schulz et al. "The measurement of the energy spectrum of cosmic rays above 3× 1017 eV with the Pierre Auger Observatory". In: *Proceedings of the 33rd ICRC, Rio de Janeiro* (2013).

[25] J. R. Hörandel. "Models of the knee in the energy spectrum of cosmic rays". In: *Astropart. Phys.* 21.3 (2004), pp. 241–265. DOI: 10.1016/j.astropartphys.2004.01.004.

[26] R. Cowsik and L. Wilson. "The nested leaky-box model for Galactic cosmic rays". In: *Proceedings of the 14th ICRC, Munich*. Vol. 2. 1975, p. 659.

[27] M. Aartsen et al. "Observation of high-energy astrophysical neutrinos in three years of IceCube data". In: *Phys. Rev. Lett.* 113.10 (2014), p. 101101. DOI: 10.1103/physrevlett.113.101101.

[28] K. V. Ptitsyna and S. V. Troitsky. "Physical conditions in potential accelerators of ultra-high-energy cosmic rays: updated Hillas plot and radiation-loss constraints". In: *Phys. Usp.* 53.7 (2010), p. 691. DOI: 10.3367/ufne.0180.201007c.0723.

[29] J. Aublin et al. "Arrival directions of the highest-energy cosmic rays detected with the Pierre Auger Observatory". In: *Proceedings of Science* PoS(ICRC2015)310 (2015). URL: http://pos.sissa.it/archive/conferences/236/310/ICRC2015_310.pdf.

[30] J. Tueller et al. “Swift BAT survey of AGNs”. In: *The Astrophysical Journal* 681.1 (2008), p. 113. DOI: 10.1086/588458.

[31] E. Fermi. “On the origin of the cosmic radiation”. In: *Phys. Rev.* 75.8 (1949), p. 1169. DOI: 10.1063/1.3066509.

[32] A. Aab et al. “Searches for anisotropies in the arrival directions of the highest energy cosmic rays detected by the Pierre Auger Observatory”. In: *The Astrophysical Journal* 804.1 (Apr. 2015), p. 15. DOI: 10.1088/0004-637X/804/1/15.

[33] T. Abu-Zayyad et al. “Correlations of the arrival directions of ultra-high energy cosmic rays with extragalactic objects as observed by the telescope array experiment”. In: *The Astrophysical Journal* 777.2 (2013), p. 88. DOI: 10.1088/0004-637X/777/2/88.

[34] I. Al Samarai et al. “Indications of anisotropy at large angular scales in the arrival directions of cosmic rays detected at the Pierre Auger Observatory”. In: *Proceedings of Science* PoS(ICRC2015)372 (2015). URL: http://pos.sissa.it/archive/conferences/236/372/ICRC2015_372.pdf.

[35] K.-H. Kampert and P. Tinyakov. “Cosmic rays from the ankle to the cutoff”. In: *C. R. Phys.* 15.4 (2014), pp. 318–328. DOI: 10.1016/j.crhy.2014.04.006.

[36] R. Engel et al. “Upgrade of the Pierre Auger Observatory (AugerPrime)”. In: *Proceedings of Science* PoS(ICRC2015)686 (2015). URL: http://pos.sissa.it/archive/conferences/236/686/ICRC2015_686.pdf.

[37] A. Aab et al. “The Pierre Auger Observatory Upgrade-Preliminary Design Report”. In: *arXiv preprint* (2016). arXiv: 1604.03637.

[38] W. Heitler. *The quantum theory of radiation*. Courier Corporation, 1954.

[39] J. Matthews. “A Heitler model of extensive air showers”. In: *Astropart. Phys.* 22.5 (2005), pp. 387–397. DOI: 10.1016/j.astropartphys.2004.09.003.

[40] T. Bergmann et al. “One-dimensional hybrid approach to extensive air shower simulation”. In: *Astropart. Phys.* 26 (2007), pp. 420–432. DOI: 10.1016/j.astropartphys.2006.08.005.

[41] T. Pierog et al. “First Results of Fast One-dimensional Hybrid Simulation of EAS Using CONEX”. In: *Nucl. Phys. B Proc. Suppl.* 151.1 (Jan. 2006), pp. 159–162. DOI: 10.1016/j.nuclphysbps.2005.07.029.

[42] G. Bossard et al. “Cosmic ray air shower characteristics in the framework of the parton-based Gribov-Regge model NEXUS”. In: *Phys. Rev. D* 63.5 (Feb. 2001), p. 054030. DOI: 10.1103/physrevd.63.054030.

[43] T. Pierog et al. “EPOS LHC: Test of collective hadronization with data measured at the CERN Large Hadron Collider”. In: *Phys. Rev. C* 92.3 (Sept. 2015), p. 034906. DOI: 10.1103/physrevc.92.034906.

[44] T. K. Gaisser and A. M. Hillas. “Reliability of the method of constant intensity cuts for reconstructing the average development of vertical showers”. In: *Proceedings of the 15th ICRC, Plovdiv*. Vol. 8. 1977, pp. 353–357.

[45] M. Ave et al. “Measurement of the pressure dependence of air fluorescence emission induced by electrons”. In: *Astropart. Phys.* 28.1 (2007), pp. 41–57. DOI: 10.1016/j.astropartphys.2007.04.006.

[46] J. Rosado, F. Blanco, and F. Arqueros. “On the absolute value of the air-fluorescence yield”. In: *Astropart. Phys.* 55 (2014), pp. 51–62. DOI: 10.1016/j.astropartphys.2014.02.003.

[47] M. Risse. “Properties of extensive air showers”. In: *arXiv preprint* (2004). arXiv: astro-ph/0402300.

[48] M. Risse and D. Heck. “Energy release in air showers”. In: *Astropart. Phys.* 20.6 (Mar. 2004), pp. 661–667. DOI: 10.1016/j.astropartphys.2003.10.006.

[49] M. Ave et al. “Energy dependence of air fluorescence yield measured by AIRFLY”. In: *Nucl. Instrum. Methods Phys. Res., Sect. A* 597.1 (2008), pp. 46–49. DOI: 10.1016/j.nima.2008.08.051.

[50] F. Arqueros, J. R. Hörandel, and B. Keilhauer. “Air fluorescence relevant for cosmic-ray detection - Summary of the 5th fluorescence workshop, El Escorial 2007”. In: *Nucl. Instrum. Methods Phys. Res., Sect. A* 597.1 (2008), pp. 1–22. DOI: 10.1016/j.nima.2008.08.056.

[51] C. Benn and S. Ellison. “Brightness of the night sky over La Palma”. In: *New Astron. Rev.* 42.6 (1998), pp. 503–507. DOI: 10.1016/s1387-6473(98)00062-1.

[52] M. Stephan. “Measurement of the Light Flux of Stars and the Night-Sky with Silicon Photomultipliers”. PhD Thesis. RWTH Aachen University, 2014.

[53] K. Krisciunas and B. E. Schaefer. “A model of the brightness of moonlight”. In: *Publ. Astron. Soc. Pac.* 103.667 (Sept. 1991), p. 1033. DOI: 10.1086/132921.

[54] I. Allekotte et al. “The surface detector system of the Pierre Auger Observatory”. In: *Nucl. Instrum. Methods Phys. Res., Sect. A* 586.3 (2008), pp. 409–420. DOI: 10.1016/j.nima.2007.12.016.

[55] T. Huege et al. “Radio detection of cosmic rays in the Pierre Auger Observatory”. In: *Nucl. Instrum. Methods Phys. Res., Sect. A* 617.1-3 (May 2010), pp. 484–487. DOI: 10.1016/j.nima.2009.10.012.

[56] B. Daniel et al. “The AMIGA enhancement of the Pierre Auger Observatory”. In: *Journal of Physics: Conference Series*. Vol. 632. 1. IOP Publishing. 2015, p. 012088. DOI: 10.1088/1742-6596/632/1/012088.

[57] The Pierre Auger Collaboration. “Statistical and systematic uncertainties in the event reconstruction and S (1000) determination by the Pierre Auger surface detector”. In: *Proceedings of the 29th ICRC, Pune* (2005). arXiv: astro-ph/0507029.

[58] C. Bonifazi et al. “The angular resolution of the Pierre Auger Observatory”. In: *Nuclear Physics B-Proceedings Supplements* 190 (2009), pp. 20–25. DOI: 10.1016/j.nuclphysbps.2009.03.063.

[59] P. Assis et al. “A simulation of the fluorescence telescopes of the Pierre Auger Observatory using Geant4”. In: *Proceedings of the 31th ICRC, Łódz*. 2009.

[60] M. L. de Oliveira et al. “Manufacturing the Schmidt corrector lens for the Pierre Auger Observatory”. In: *Nucl. Instrum. Methods Phys. Res., Sect. A* 522.3 (Apr. 2004), pp. 360–370. DOI: 10.1016/j.nima.2003.11.409.

[61] *Photomultiplier tubes product specifications XP3062*. HZC Photonics Technology Co., Ltd. Mar. 2016. URL: http://www.hzcphotonics.com/products/XP3062.pdf.

[62] A. Aab et al. “Depth of maximum of air-shower profiles at the Pierre Auger Observatory. I. Measurements at energies above $10^{17.8}$ eV”. In: *Phys. Rev. D* 90.12 (Dec. 2014). DOI: 10.1103/physrevd.90.122005.

[63] The Pierre Auger Collaboration. “Measurements of X_{max} above 10^{17} eV with the fluorescence detector of the Pierre Auger Observatory”. In: *Proceedings of Science* PoS(ICRC2015)420 (2015). URL: http://pos.sissa.it/archive/conferences/236/420/ICRC2015_420.pdf.

[64] C. Song et al. “Energy estimation of UHE cosmic rays using the atmospheric fluorescence technique”. In: *Astropart. Phys.* 14.1 (2000), pp. 7–13. DOI: 10.1016/s0927-6505(00)00101-8.

[65] D. Bates. “Rayleigh scattering by air”. In: *Planet. Space Sci.* 32.6 (1984), pp. 785–790. DOI: 10.1016/0032-0633(84)90102-8.

[66] A. Ångström. “The parameters of atmospheric turbidity”. In: *Tellus* 16.1 (1964), pp. 64–75. DOI: 10.3402/tellusa.v16i1.8885.

[67] The Pierre Auger Collaboration. “A study of the effect of molecular and aerosol conditions in the atmosphere on air fluorescence measurements at the Pierre Auger Observatory”. In: *Astropart. Phys.* (2010). DOI: 10.1016/j.astropartphys.2009.12.005.

[68] V. Verzi. “The energy scale of the Pierre Auger Observatory”. In: *Proceedings of the 33rd ICRC, Rio de Janeiro* (2013).

[69] H. Gemmeke et al. “Design of the trigger system for the Auger fluorescence detector”. In: *IEEE Trans. Nucl. Sci.* 47.2 (2000), pp. 371–375. DOI: 10.1109/23.846184.

[70] A. Schmidt et al. “Third level trigger for the fluorescence telescopes of the Pierre Auger Observatory”. In: *Nucl. Instrum. Methods Phys. Res., Sect. A* 601.3 (Apr. 2009), pp. 347–353. DOI: 10.1016/j.nima.2009.01.002.

[71] A. Bross and A. Dyshkant. “FNAL-NICADD extruded scintillator”. In: *Nuclear Science Symposium Conference Record, 2004 IEEE*. Vol. 2. IEEE. 2004, pp. 790–793. DOI: 10.1109/nssmic.2004.1462328.

[72] F. Schmidt et al. “Applying Extensive Air Shower Universality to Ground Detector Data”. In: *arXiv preprint* (2007). arXiv: 0706.1990.

[73] A. Yushkov et al. “Precise determination of muon and EM shower contents from shower universality property”. In: *arXiv preprint* (2011). arXiv: 1107.5240.

[74] R. Foord et al. “The Use of Photomultiplier Tubes for Photon Counting”. In: *Appl. Opt.* 8.10 (Oct. 1969), pp. 1975–1989. DOI: 10.1364/ao.8.001975.

[75] B. Dolgoshein et al. “Large area UV SiPMs with extremely low cross-talk”. In: *Nucl. Instrum. Methods Phys. Res., Sect. A* 695 (Dec. 2012), pp. 40–43. DOI: 10.1016/j.nima.2011.12.024.

[76] SensL Technologies Ltd. *J Series (High Performance/TSV) - Datasheet*. May 2016. URL: http://sensl.com/downloads/ds/DS-MicroJseries.pdf.

[77] S. M. Sze and K. K. Ng. *Physics of semiconductor devices*. John wiley & sons, 2006.

[78] H. Photonics. *Physics and operation of an MPPC*. Mar. 2016. URL: http://www.hamamatsu.com/us/en/community/optical_sensors/sipm/physics_of_mppc/index.html.

[79] S. Cova et al. “Avalanche photodiodes and quenching circuits for single-photon detection”. In: *Appl. Opt.* 35.12 (Apr. 1996), p. 1956. DOI: 10.1364/ao.35.001956.

[80] R. H. Haitz. “Model for the electrical behavior of a microplasma”. In: *J. Appl. Phys.* 35.5 (1964), pp. 1370–1376. DOI: 10.1063/1.1713636.

[81] A. Gallivanoni, I. Rech, and M. Ghioni. “Progress in quenching circuits for single photon avalanche diodes”. In: *IEEE Trans. Nucl. Sci.* 57.6 (Dec. 2010), pp. 3815–3826. DOI: 10.1109/tns.2010.2074213.

[82] M. Lauscher. “Characterisation Studies of Silicon Photomultipliers for the Detection of Fluorescence Light from Extensice Air Showers”. Master’s Thesis. RWTH Aachen University, 2012.

[83] Hamamatsu Photonics. 2016. URL: http://www.hamamatsu.com.

[84] SensL Technologies Ltd. 2016. URL: http://www.sensl.com.

[85] D. E. Aspnes and A. A. Studna. “Dielectric functions and optical parameters of Si, Ge, GaP, GaAs, GaSb, InP, InAs, and InSb from 1.5 to 6.0 eV”. In: *Phys. Rev. B* 27 (2 Jan. 1983), pp. 985–1009. DOI: 10.1103/PhysRevB.27.985.

[86] D. Wilson. “Angular Dependence of the Relative Photon Detection Efficiency of Silicon Photomultipliers”. Bachelor’s Thesis. RWTH Aachen University, 2012.

[87] M. Nemallapudi et al. “SiPM angular response and enhanced light extraction”. In: *2013 IEEE Nuclear Science Symposium and Medical Imaging Conference (2013 NSS/MIC)*. IEEE. Oct. 2013, pp. 1–5. DOI: 10.1109/nssmic.2013.6829586.

[88] M. L. Cutler. “Reflection of light from multi-layer films”. Bachelor’s Thesis. Massachusetts Institute of Technology, 1939.

[89] W. G. Oldham, R. Samuelson, and P. Antognetti. “Triggering phenomena in avalanche diodes”. In: *IEEE Trans. Electron Devices* 19.9 (Sept. 1972), pp. 1056–1060. ISSN: 0018-9383. DOI: 10.1109/t-ed.1972.17544.

[90] Hamamatsu Photonics. *MPPC S12571 Series Product*. Oct. 2013.

[91] J. Schumacher. “Characterization Studies of Silicon Photomultipliers: Noise and Relative Photon Detection Efficiency”. Bachelor’s Thesis. RWTH Aachen University, 2011.

[92] A. N. Otte. “Observation of VHE gamma-Rays from the Vicinity of magnetized Neutron Stars and Development of new Photon-Detectors for Future Ground based gamma-Ray Detectors”. PhD Thesis. Technische Universität München, 2007.

[93] R. Mirzoyan, R. Kosyra, and H. G. Moser. “Light emission in Si avalanches”. In: *Nucl. Instrum. Methods Phys. Res., Sect. A* 610.1 (Oct. 2009), pp. 98–100. DOI: 10.1016/j.nima.2009.05.081.

[94] A. L. Lacaita et al. “On the bremsstrahlung origin of hot-carrier-induced photons in silicon devices”. In: *IEEE Trans. Electron Devices* 40.3 (Mar. 1993), pp. 577–582. DOI: 10.1109/16.199363.

[95] T. Niggemann et al. “Status of the Silicon Photomultiplier Telescope FAMOUS for the Fluorescence Detection of UHECRs”. In: *dep* 3 (2013), d2Nγ. arXiv: 1502.00792.

[96] L. Gallego et al. “Modeling crosstalk in silicon photomultipliers”. In: *J. Instrum.* 8.05 (May 2013), P05010. DOI: 10.1088/1748-0221/8/05/p05010.

[97] J. Rosado and S. Hidalgo. “Characterization and modeling of crosstalk and afterpulsing in Hamamatsu silicon photomultipliers”. In: *J. Instrum.* 10.10 (2015), P10031. DOI: 10.1088/1748-0221/10/10/p10031.

[98] P. Buzhan et al. “An advanced study of silicon photomultiplier”. In: *ICFA Instrumentation Bulletin* 21 (2001), p. 28. DOI: 10.1142/9789812776464_0101.

[99] T. Bretz et al. “Dynamic Range Measurement and Calibration of SiPMs”. In: *J. Instrum.* (2016). DOI: 10.1088/1748-0221/11/03/p03009.

[100] H. T. van Dam et al. “A Comprehensive Model of the Response of Silicon Photomultipliers”. In: *IEEE Trans. Nucl. Sci.* 57.4 (Aug. 2010), pp. 2254–2266. DOI: 10.1109/tns.2010.2053048.

[101] S. Seifert et al. “Simulation of Silicon Photomultiplier Signals”. In: *IEEE Trans. Nucl. Sci.* 56.6 (Dec. 2009), pp. 3726–3733. DOI: 10.1109/tns.2009.2030728.

[102] A. Vacheret et al. “Characterization and simulation of the response of Multi-Pixel Photon Counters to low light levels”. In: *Nucl. Instrum. Methods Phys. Res., Sect. A* 656.1 (Nov. 2011), pp. 69–83. DOI: 10.1016/j.nima.2011.07.022.

[103] P. Eckert, R. Stamen, and H.-C. Schultz-Coulon. “Study of the response and photon-counting resolution of silicon photomultipliers using a generic simulation framework”. In: *J. Instrum.* 7.08 (2012), P08011. DOI: 10.1088/1748-0221/7/08/p08011.

[104] L. Dovrat et al. “Simulations of photon detection in silicon photomultiplier number-resolving detectors”. In: *Phys. Scr.* 2012.T147 (2012), p. 014010. DOI: 10.1088/0031-8949/2012/t147/014010.

[105] H. Miyamoto et al. “SiPM development and application for astroparticle physics experiments”. In: *Proceedings of the 31th ICRC, Łódz*. 2009, p. 1320.

[106] R. Mirzoyan and E. Popova. “SiPM for atmospheric Cherenkov telescopes”. In: *Optical Components and Materials X*. Ed. by M. J. F. Digonnet, S. Jiang, and J. C. Dries. SPIE. Mar. 2013, pp. 862106–862106. DOI: 10.1117/12.2002598.

[107] A. Otte et al. “Development of a SiPM Camera for a Schwarzschild-Couder Cherenkov Telescope for the Cherenkov Telescope Array”. In: *arXiv preprint* (2015). arXiv: 1509.02345.

[108] A. Baldini et al. “MEG upgrade proposal”. In: *arXiv preprint* (2013). arXiv: 1301.7225.

[109] Z. Xu and G. Haefeli. “Scintillating fibre tracker front-end electronics for LHCb upgrade”. In: (Nov. 2014), p. 071. DOI: 10.1109/nssmic.2014.7431160.

[110] J. Frangenheim. “Measurements of the drift velocity using a small gas chamber for monitoring of the CMS muon system”. Diploma Thesis. RWTH Aachen University, 2007.

[111] B. Lutz et al. “Upgrade of the CMS hadron outer calorimeter with SiPM sensors”. In: *Journal of Physics: Conference Series*. Vol. 404. 1. IOP Publishing. 2012, p. 012018. DOI: 10.1088/1742-6596/404/1/012018.

[112] The Geant4 Collaboration. *Geant4 User Documentation*. 2016. URL: http://geant4.web.cern.ch/geant4/UserDocumentation/UsersGuides/IntroductionToGeant4/html/index.html.

[113] M. Berglund and M. E. Wieser. “Isotopic compositions of the elements 2009 (IUPAC Technical Report)”. In: *Pure Appl. Chem.* 83.2 (2011), pp. 397–410. DOI: 10.1351/pac-rep-10-06-02.

[114] M. Wang et al. “The Ame2012 atomic mass evaluation”. In: *Chin. Phys. C* 36.12 (2012), p. 1603. DOI: 10.1088/1674-1137/36/12/003.

[115] M. E. Wieser et al. “Atomic weights of the elements 2011 (IUPAC Technical Report)”. In: *Pure Appl. Chem.* 85.5 (2013), pp. 1047–1078. DOI: 10.1351/pac-rep-13-03-02.

[116] F. Scheuch et al. “Electrical characterization and simulation of SiPMs”. In: *Nucl. Instrum. Methods Phys. Res., Sect. A* 787 (July 2015), pp. 340–343. DOI: 10.1016/j.nima.2015.01.066.

[117] J. Pulko et al. “A Monte-Carlo model of a SiPM coupled to a scintillating crystal”. In: *J. Instrum.* 7.02 (Feb. 2012), P02009. DOI: 10.1088/1748-0221/7/02/p02009.

[118] S. S. Majos et al. “Noise and radiation damage in silicon photomultipliers exposed to electromagnetic and hadronic radiation”. In: *Nucl. Instrum. Methods Phys. Res., Sect. A* 602.2 (2009), pp. 506–510. DOI: 10.1016/j.nima.2009.01.176.

[119] Y. Qiang et al. “Radiation hardness tests of SiPMs for the JLab Hall D Barrel calorimeter”. In: *Nucl. Instrum. Methods Phys. Res., Sect. A* 698 (2013), pp. 234–241. DOI: 10.1016/j.nima.2012.10.015.

[120] CAEN S.p.A. *Technical Information Manual Model V1729 4 Channel 12 bit 2 GS/s FADC*. July 2013. URL: http://www.caen.it/csite/CaenProd.jsp?parent=11&idmod=398.

[121] R. Lewke. “Integration of a Fiber Tracker into a Time-of-Flight Spectrometer for Nuclear Cross Section Measurements for Particle Therapy”. Master’s Thesis. RWTH Aachen University, 2012.

[122] K. Beck. *Test-driven development: by example*. Addison-Wesley Professional, 2003.

[123] I. Google. *Google Test*. Mar. 2016. URL: https://github.com/google/googletest.

[124] B. George and L. Williams. “A structured experiment of test-driven development”. In: *Information and Software Technology* 46.5 (2004), pp. 337–342. DOI: 10.1016/j.infsof.2003.09.011.

[125] C. Heidemann et al. “Optical test setup for Silicon Photomultipliers”. In: *Nucl. Instrum. Methods Phys. Res., Sect. A* 787 (2015), pp. 261–264. ISSN: 0168-9002. DOI: 10.1016/j.nima.2014.12.047.

[126] C. Piemonte. “A new silicon photomultiplier structure for blue light detection”. In: *Nucl. Instrum. Methods Phys. Res., Sect. A* 568.1 (Nov. 2006), pp. 224–232. DOI: 10.1016/j.nima.2006.07.018.

[127] M. Bass et al. *Handbook of Optics*. 2nd. Vol. Volume 1, Fundamentals, Techniques and Design. Optical Society of America, 1995.

[128] M. Putignano, A. Intermite, and C. Welsch. “A non-linear algorithm for current signal filtering and peak detection in SiPM”. In: *J. Instrum.* 7.08 (Aug. 2012), P08014. DOI: 10.1088/1748-0221/7/08/p08014.

[129] Hamamatsu Photonics. *Hamamatsu News 1-2016*. Mar. 2016. URL: http://www.hamamatsu-news.com.

[130] A. Biland et al. “Calibration and performance of the photon sensor response of FACT - the first G-APD Cherenkov telescope”. In: *J. Instrum.* 9.10 (2014), P10012. DOI: 10.1088/1748-0221/9/10/p10012.

[131] C. Peters. “Design Studies for an Air Fluorescence Telescope with Silicon Photomultipliers for the Detection of Ultra-high-energy Cosmic Rays”. Master’s Thesis. RWTH Aachen University, 2013.

[132] T. Hebbeker et al. “Muon measurement using scintillator tiles with SiPM readout”. In: *Internal Note of the Pierre Auger Collaboration* GAP2013-057 (2013).

[133] D. Sommer. “Trigger simulation study of the air shower fluorescence telescope FAMOUS”. Bachelor’s Thesis. RWTH Aachen University, Nov. 2014.

[134] E. Dietz-Laursonn. “Detailed Studies of Light Transport in Optical Components of Particle Detectors”. PhD Thesis. RWTH Aachen University, 2016.

[135] E. Dietz-Laursonn. *GODDeSS Source Code Repository*. 2016. URL: https://forge.physik.rwth-aachen.de/projects/goddess.

[136] F. Bisconti. “Private communications”. Nov. 2014.

[137] C. Peters et al. “The muon detector prototype AMD for the determination of the muon content in UHECRs”. In: *Proceedings of Science* PoS(ICRC2015)596 (2015). URL: http://pos.sissa.it/archive/conferences/236/596/ICRC2015_596.pdf.

[138] Saint-Gobain Crystals. *Scintillating Optical Fibers*. Mar. 2016. URL: http://www.crystals.saint-gobain.com/uploadedFiles/SG-Crystals/Documents/SGC%20Fibers%20Brochure.pdf.

[139] S. Blin, P. Barrillon, and C. de La Taille. “MAROC, a generic photomultiplier readout chip”. In: *Nuclear Science Symposium Conference Record (NSS/MIC), 2010 IEEE*. IEEE. 2010, pp. 1690–1693.

[140] K. S. Kölbig and B. Schorr. “A program package for the Landau distribution”. In: *Comput. Phys. Commun.* 31.1 (1984), pp. 97–111.

[141] K. Kölbig and B. Schorr. “Erratum to: A program package for the Landau distribution”. In: *Comput. Phys. Commun.* 178.12 (2008), p. 972.

[142] L. Middendorf. “The Aachen Muon Detector”. PhD Thesis. RWTH Aachen University, To be published.

[143] R. N. Wilson. *Reflecting Telescope Optics II: Manufacture, Testing, Alignment, Modern Techniques*. Springer Science & Business Media, 2013.

[144] Orafol Fresnel Optics GmbH. “Private communications”. May 2011.

[145] R. A. Pagon et al. “Duane’s Foundations of Clinical Ophthalmology”. In: *Duane’s Foundations of Clinical Ophthalmology* (1995). URL: http://80.36.73.149/almacen/medicina/oftalmologia/enciclopedias/duane/index.html.

[146] Schott GmbH. *UV Bandpass UG11*. 2008. URL: http://www.schott.com/advanced_optics/german/download/schott-uv-bandpass-ug11-oct-2015-de.pdf.

[147] O. Miller, J. McLeod, and W. Sherwood. “Thin Sheet Plastic Fresnel Lenses of High Aperture”. In: *J. Opt. Soc. Am.* 41.11 (Nov. 1951), pp. 807–815. DOI: 10.1364/josa.41.000807.

[148] B. Aničin, V. Babović, and D. Davidović. “Fresnel lenses”. In: *Am. J. Phys* 57.4 (1989), pp. 312–316. DOI: 10.1119/1.16071.

[149] T. Niggemann. “New Telescope Design with Silicon Photomultipliers for Fluorescence Light Detection of Extensive Air Showers”. In: *Internal Note of the Pierre Auger Collaboration* GAP2012-017 (2012).

[150] H. M. Eichler. “Characterisation studies on the optics of the prototype fluorescence telescope FAMOUS”. Master’s Thesis. RWTH Aachen University, 2014.

[151] Sony Corporation. *NEX-5*. 2016. URL: http://www.sony.de/support/de/product/nex-5.

[152] LibRaw LCC. *LibRaw raw image decoder*. version 0.17. 2016. URL: http://www.libraw.org/about.

[153] B. S. Reddy and B. N. Chatterji. “An FFT-based technique for translation, rotation, and scale-invariant image registration”. In: *IEEE Transactions on Image Processing* 5.8 (1996), pp. 1266–1271. DOI: 10.1109/83.506761.

[154] A. Averbuch and Y. Keller. “A unified approach to FFT based image registration”. In: *IEEE* (2002). DOI: 10.1109/ICASSP.2002.5745436.

[155] A. D. Rakić et al. “Optical properties of metallic films for vertical-cavity optoelectronic devices”. In: *Appl. Opt.* 37.22 (1998), pp. 5271–5283. DOI: 10.1364/ao.37.005271.

[156] G. Hass and J. Waylonis. “Optical Constants and Reflectance and Transmittance of Evaporated Aluminum in the Visible and Ultraviolet”. In: *J. Opt. Soc. Am.* 51.7 (July 1961), pp. 719–722. DOI: 10.1364/josa.51.000719.

[157] S. Mann. “Measurement of the UV Reflectivity of Aluminium in Different Stages of Oxidation”. Bachelor’s Thesis. RWTH Aachen University, Sept. 2012.

[158] R. Winston et al. *Nonimaging Optics*. Academic Press, 2005.

[159] T. Niggemann et al. “The optics and detector-simulation of the air fluorescence telescope FAMOUS for the detection of cosmic rays”. In: *SPIE Astronomical Telescopes+ Instrumentation*. SPIE. 2012, pp. 844430–844430. DOI: 10.1117/12.925305.

[160] J. Schumacher. “Private communications”. 2016.

[161] L. Tibaldo et al. “TARGET: toward a solution for the readout electronics of the Cherenkov Telescope Array”. In: *arXiv preprint* (2015). arXiv: 1508.06296.

[162] QHYCCD. *A high sensitivity CMOS Guide/Planetary Camera*. 2016. URL: http://www.qhyccd.com/QHY5L-II.html.

[163] Edmund Optics. *8mm MegaPixel Fixed Focal Length Lens*. 2016. URL: http://www.edmundoptics.com/imaging-lenses/fixed-focal-length-lenses/megapixel-fixed-focal-length-lenses/56786/.

[164] D. C. Brown. “Decentering distortion of lenses”. In: *Photometric Engineering* 32.3 (1966), pp. 444–462.

[165] Z. Zhang. “A flexible new technique for camera calibration”. In: *IEEE Transactions on Pattern Analysis and Machine Intelligence* 22.11 (2000), pp. 1330–1334. DOI: 10.1109/34.888718.

[166] J.-Y. Bouguet. *MATLAB calibration tool*. Oct. 2015. URL: http://www.vision.caltech.edu/bouguetj/calib_doc/.

[167] G. Bradski. "The opencv library". In: *Doctor Dobbs Journal* 25.11 (2000), pp. 120–126.

[168] J. Grothoff. "Development of a Data Acquisition System for the Air Shower Fluorescence Telescope FAMOUS". Bachelor's Thesis. RWTH Aachen University, 2013.

[169] WIZnet Co. *W5100 Datasheet*. 1.2.6. 2011. URL: http://www.wiznet.co.kr/product-item/w5100/.

[170] Arduino. *Arduino Ethernet*. 2016. URL: https://www.arduino.cc/en/Main/ArduinoBoardEthernet.

[171] Atmel. *ATmega48A/PA/88A/PA/168A/PA/328/P datasheet*. Nov. 2015. URL: http://www.atmel.com/devices/atmega328.aspx.

[172] Adafruit Industries, LLC. *Bosch BMP085 Breakout Board*. 2016. URL: https://learn.adafruit.com/bmp085/overview.

[173] Bosch Sensortec. *BMP085 Digital pressure sensor data sheet*. July 2008.

[174] SparkFun Electronics. *SparkFun Humidity Sensor Breakout - HIH-4030*. 2016. URL: https://www.sparkfun.com/products/9569.

[175] Honeywell. *HIH-4030/31 Series Humidity Sensors*. 2008.

[176] Adafruit Electronics. *TSL2561 Luminosity Sensor*. 2016. URL: https://learn.adafruit.com/tsl2561/overview.

[177] Texas Advanced Optoelectronic Solutions Inc. *TSL2560 light to digital converter*. Dec. 2005.

[178] SparkFun Electronics. *SparkFun GPS Shield 10710*. 2016. URL: https://www.sparkfun.com/products/10710.

[179] SparkFun Electronics. *GPS Receiver - EM-406A SiRF III (20 Channel)*. 2016. URL: https://www.sparkfun.com/products/retired/465.

[180] GlobalSat Technology Corporation. *Product user manual GPS receiver engine board EM-406A*. 1.4.1.

[181] C. Robusto. "The Cosine-Haversine Formula". In: *The American Mathematical Monthly* 64.1 (1957), pp. 38–40. DOI: 10.2307/2309088.

[182] F. Knuth. "Commissioning Of The Air Shower Fluorescence Telescope Prototype FAMOUS". Bachelor's Thesis. RWTH Aachen University, 2014.

[183] M. Schaufel. "Commissioning of a prototype telescope IceAct to measure the Cherenkov light of CR induced air showers". Bachelor's Thesis. RWTH Aachen University, 2014.

[184] CAEN S.p.A. *Technical Information Manual Model V965/V965A 16/8 channel dual range QDC*. July 2008. URL: http://www.caen.it/csite/CaenProd.jsp?parent=11&idmod=398.

[185] J. Adam et al. "The MEG detector for μ -> e+ γ decay search". In: *The European Physical Journal C* 73.4 (2013), pp. 1–59. DOI: 10.1140/epjc/s10052-013-2365-2.

[186] S. Ritt. *DRS4 Evaluation Board User's Manual*. Paul Scherrer Institute. Jan. 2014. URL: http://www.psi.ch/drs/documentation.

[187] J. Auffenberg et al. “Design study of an air-Cherenkov telescope for harsh environments with efficient air-shower detection at 100 TeV”. In: *Proceedings of Science* PoS(ICRC2015)1155 (2015). URL: http://pos.sissa.it/archive/conferences/236/1155/ICRC2015_1155.pdf.

[188] S. Argiro et al. “The Offline software framework of the Pierre Auger Observatory”. In: *Nucl. Instrum. Methods Phys. Res., Sect. A* 580.3 (2007), pp. 1485–1496. DOI: 10.1109/nssmic.2005.1596422.

[189] M. N. Polyanskiy. *Refractive index database*. Mar. 1, 2016. URL: http://refractiveindex.info.

[190] M. Bass et al. *Handbook of Optics*. 2nd. Vol. Volume 2, Design, fabrication and testing, sources and detectors, radiometry and photometry. Optical Society of America, 2009.

[191] W. J. Smith. *Modern optical engineering*. Tata McGraw-Hill Education, 1966.

[192] Schott GmbH. *Refractive index and dispersion*. 2007. URL: http://www.schott.com/advanced_optics/english/download/schott_tie-29_refractive_index_and_dispersion_eng.pdf.

[193] M. Szczurowski. *23 °C. PMMA synthesized in Marie-Curie University in Lublin, Poland*. 2013. URL: http://refractiveindex.info/download/data/2013/Szczurowski%20-%20n_PMMA_raw.png.

[194] J. J. Stamnes. “Focusing of a perfect wave and the Airy pattern formula”. In: *Opt. Commun.* 37.5 (1981), pp. 311–314. DOI: 10.1016/0030-4018(81)90425-9.

[195] H. Gross, W. Singer, and M. Totzeck. *Handbook of optical systems. Physical image formation 2*. Wiley VCH, GmbH & Co., KGaA, 2005.

[196] J. C. Wyant and K. Creath. “Basic wavefront aberration theory for optical metrology”. In: *Applied Optics and Optical Engineering, Volume XI*. Vol. 11. s 29. 1992, p. 2.

[197] F. Träger. *Springer handbook of lasers and optics*. Springer Science & Business Media, 2012. DOI: 10.1007/978-3-642-19409-2.

[198] D. A. Atchison. “Recent advances in representation of monochromatic aberrations of human eyes”. In: *Clinical and Experimental Optometry* 87.3 (2004), pp. 138–148.

[199] ZEMAX. *OpticStudio*. Mar. 1, 2016. URL: http://www.zemax.com/os/opticstudio.

[200] M. Janecek and W. W. Moses. “Simulating scintillator light collection using measured optical reflectance”. In: *IEEE Trans. Nucl. Sci.* 57.3 (June 2010), pp. 964–970. DOI: 10.1109/tns.2010.2042731.

[201] T.-T. Wong, W.-S. Luk, and P.-A. Heng. “Sampling with Hammersley and Halton points”. In: *Journal of graphics tools* 2.2 (1997), pp. 9–24. DOI: 10.1080/10867651.1997.10487471.

[202] K. M. Gorski et al. “HEALPix: a framework for high-resolution discretization and fast analysis of data distributed on the sphere”. In: *The Astrophysical Journal* 622.2 (2005), p. 759. DOI: 10.1086/427976.

[203] W. Fincham and M. Freeman. *Optics*. Elsevier Science, 2013. ISBN: 9781483103228.

[204] A. Aab et al. “Depth of maximum of air-shower profiles at the Pierre Auger Observatory. II. Composition implications”. In: *Phys. Rev. D* 90.12 (Dec. 2014). DOI: 10.1103/physrevd.90.122006.

[205] R. Brun and F. Rademakers. “ROOT - an object oriented data analysis framework”. In: *Nucl. Instrum. Methods Phys. Res., Sect. A* 389.1 (1997), pp. 81–86. DOI: 10.1016/s0168-9002(97)00048-x.

[206] L. Prado Jr. et al. “Simulation of the fluorescence detector of the Pierre Auger Observatory”. In: *Nucl. Instrum. Methods Phys. Res., Sect. A* 545.3 (June 2005), pp. 632–642. DOI: 10.1016/j.nima.2005.01.346.

[207] M. Shacklette. “Linux Operating System”. In: *Handbook of Computer Networks: LANs, MANs, WANs, the Internet, and Global, Cellular, and Wireless Networks, Volume 2* (1995), pp. 78–90. DOI: 10.1002/9781118256114.ch6.

[208] R. Hertzog and R. Mas. *The Debian Administrator’s Handbook*. 8.3. Software in the Public Interest, Inc. Jan. 2016. URL: https://www.debian.org/doc/manuals/debian-handbook/.

[209] K. Sievers and L. Poettering. *systemd System and Service Manager*. Red Hat Inc. Mar. 2016. URL: https://www.freedesktop.org/wiki/Software/systemd/.

[210] W. Reese. “Nginx: the high-performance web server and reverse proxy”. In: *Linux Journal* 2008.173 (2008), p. 2.

[211] Phusion Holding B.V. *Phusion Passenger*. Mar. 2016. URL: https://www.phusionpassenger.com/.

[212] D. H. Hansson et al. *Ruby on rails*. 4.2. Mar. 2016. URL: http://www.rubyonrails.org.

[213] Python Software Foundation. *Python*. Mar. 2016. URL: http://python.org/.

[214] G. James. “The Web Server Gateway Interface (WSGI)”. In: *The Definitive Guide to Pylons*. Springer Science + Business Media, 2009, pp. 369–388. DOI: 10.1007/978-1-4302-0534-0_16.

[215] Twitter, Inc. *Bootstrap*. Mar. 2016. URL: http://getbootstrap.com/.

[216] Google, Inc. *AngularJS*. Mar. 2016. URL: https://angularjs.org/.

[217] J. Franks et al. *HTTP authentication: Basic and digest access authentication*. 1999. DOI: 10.17487/rfc2617.

[218] Oracle Corporation. *MySQL*. Mar. 2016. URL: www.mysql.com.

[219] J. D. Hunter. “Matplotlib: A 2D graphics environment”. In: *Computing In Science & Engineering* 9.3 (2007), pp. 90–95. DOI: 10.1109/mcse.2007.55.

[220] M. Bayer. *Sqlalchemy - the database toolkit for python*. Mar. 2016. URL: http://www.sqlalchemy.org.

[221] P. Duffett-Smith. *Practical astronomy with your calculator*. Cambridge University Press, 1981.

[222] A. Barmettler. *Sonne/Mond-Formeln in Javascript*. Jan. 2009. URL: http://www.astronomie.info.

[223] P. Duffett-Smith and J. Zwart. *Practical Astronomy with your calculator or spreadsheet*. Cambridge University Press, 2011.

[224] T. E. Bray. *The JavaScript Object Notation (JSON) Data Interchange Format*. RFC 7159. Mar. 2014. URL: http://www.rfc-editor.org/info/rfc7159.

[225] B. Stroustrup. *The C++ programming language*. Pearson Education India, 1986.

[226] C. Kohlhoff. *Boost. Asio*. 2003. URL: http://www.boost.org/doc/libs/release/libs/asio/.

[227] *BSON - Binary JSON*. Mar. 2016. URL: http://bsonspec.org/.

[228] C. Bethge. "Entwicklung und Aufbau eines Slow Control Systems für die Pierre Auger Fluoreszenzdetektoren". Master's Thesis. Universität Karlsruhe, 2003.

[229] D. B. Judd et al. "Spectral Distribution of Typical Daylight as a Function of Correlated Color Temperature". In: *J. Opt. Soc. Am.* 54.8 (Aug. 1964), pp. 1031–1040. DOI: 10.1364/josa.54.001031.

[230] R. Davis and K. S. Gibson. *Filters for the Reproduction of Sunlight and Daylight and the Determination of Color Temperature*. 114. US Govt. print. off., 1931. DOI: 10.6028/nbs.mp.114.

[231] R. W. Schafer and R. M. Mersereau. "Demosaicking: color filter array interpolation". In: *Signal Processing Magazine, IEEE* 22.1 (2005). DOI: 10.1109/msp.2005.1407714.

[232] B. Hemingway and R. McElroy. *White Balance as a part of Bayer Interpolation*. CSE 467, Advanced Digital Design. Aug. 2008. URL: https://courses.cs.washington.edu/courses/cse467/08au/.

[233] D. Lang et al. "Astrometry.net: Blind Astrometric Calibration of Arbitrary Astronomical Images". In: *The Astronomical Journal* 139.5 (2010), p. 1782. DOI: 10.1088/0004-6256/139/5/1782.

[234] M. Skrutskie et al. "The two micron all sky survey (2MASS)". In: *The Astronomical Journal* 131.2 (2006), p. 1163. DOI: 10.1007/978-94-011-5784-1_3.

[235] European Space Agency. *The Hipparcos Catalogue*. Vega. 2016. URL: http://vizier.u-strasbg.fr/viz-bin/VizieR-5?-out.add=.&-source=I/239/hip_main&HIP=91262.

[236] European Space Agency. *The Hipparcos Catalogue*. Deneb. 2016. URL: http://vizier.u-strasbg.fr/viz-bin/VizieR-5?-out.add=.&-source=I/239/hip_main&HIP=102098.

[237] M. A. Perryman et al. "The HIPPARCOS catalogue". In: *Astron. Astrophys.* 323 (1997), pp. L49–L52.

[238] F. Schiller and N. Przybilla. "Quantitative spectroscopy of Deneb". In: *Astronomy & Astrophysics* 479.3 (2008), pp. 849–858. DOI: 10.1051/0004-6361:20078590.

[239] F. Van Leeuwen. "Validation of the new Hipparcos reduction". In: *Astronomy & Astrophysics* 474.2 (2007), pp. 653–664. DOI: 10.1051/0004-6361:20078357.

[240] F. van Leeuwen. "The Hipparcos catalog-Commentary on: Perryman MAC, Lindegren L., Kovalevsky J., et al., 1997, A&A, 323, L49". In: *Astronomy & Astrophysics* 500.1 (2009), pp. 505–506. DOI: 10.1051/0004-6361/200912202.

[241] R. Bohlin. "HST CALSPEC Flux Standards: Sirius (and Vega)". In: *arXiv preprint* (2014). arXiv: 1403.6861.

[242] R. C. Bohlin, K. D. Gordon, and P.-E. Tremblay. "Techniques and review of absolute flux calibration from the ultraviolet to the mid-infrared". In: *Publ. Astron. Soc. Pac.* 126.942 (2014), p. 711. DOI: 10.1086/677655.

[243] C. I. Short and J. B. Lester. “Missing opacity in the atmospheric models of red giants”. In: *The Astrophysical Journal Letters* 436 (Dec. 1994), pp. L165–L168. DOI: 10.1086/187658.

[244] R. Kurucz. “ATLAS9 Stellar Atmosphere Programs and 2 km/s grid”. In: *Smithsonian Astrophysical Observatory* 13 (1993). Ed. by M. Cambridge. Kurucz CD-ROM No. 13.

[245] F. Castelli and R. Kurucz. “New grids of ATLAS9 model atmospheres”. In: *arXiv preprint* (2004). arXiv: astro-ph/0405087.

[246] I. Ramírez and C. A. Prieto. “Fundamental parameters and chemical composition of Arcturus”. In: *The Astrophysical Journal* 743.2 (2011), p. 135. DOI: 10.1088/0004-637x/743/2/135.

[247] R. Griffin and A. Lynas-Gray. “The effective temperature of Arcturus”. In: *The Astronomical Journal* 117.6 (1999), p. 2998. DOI: 10.1086/300878.

[248] D. E. Blackwell et al. “The continuum flux distribution for Arcturus”. In: *Mon. Not. R. Astron. Soc.* 171 (May 1975), pp. 425–439. DOI: 10.1093/mnras/171.2.425.

[249] L. Sbordone et al. “ATLAS and SYNTHE under Linux”. In: *Memorie della Societa Astronomica Italiana Supplementi* 5 (2004), p. 93. arXiv: astro-ph/0406268.

[250] L. Sbordone. “Kurucz’s codes under GNU-Linux”. In: *Memorie della Societa Astronomica Italiana Supplementi* 8 (2005), p. 61. arXiv: astro-ph/0509337.

[251] L. Sbordone, P. Bonifacio, and F. Castelli. “ATLAS 9 and ATLAS 12 under GNU-Linux”. In: *Proc. Int. Astron. Union* 2.S239 (2006), pp. 71–73. DOI: 10.1017/s1743921307000142.

[252] V. G. Laidler et al. “Pysynphot: A Python Re-Implementation of a Legacy App in Astronomy”. In: *SciPy Conference, Pasadena*. 2008, p. 36.

[253] M. Bessell and S. Murphy. “Spectrophotometric libraries, revised photonic passbands, and zero points for ubvri, hipparcos, and tycho photometry”. In: *Publ. Astron. Soc. Pac.* 124.912 (2012), p. 140. DOI: 10.1086/664083.

[254] R. Hardie. “Astronomical techniques”. In: *Stars and Stellar Systems*. Vol. 2. University of Chicago Press, 1962, p. 196.

[255] J. Paton and G. Rozenberg. *Twilight - A Study in Atmospheric Optics*. Vol. 18. 1. IOP Publishing, 1967, p. 24.

[256] F. Kasten and A. T. Young. “Revised optical air mass tables and approximation formula”. In: *Appl. Opt.* 28.22 (1989), pp. 4735–4738. DOI: 10.1364/ao.28.004735.

[257] A. T. Young. “Air mass and refraction”. In: *Appl. Opt.* 33.6/2 (1994). DOI: 10.1364/ao.33.001108.

[258] K. A. Pickering. “The southern limits of the Ancient Star Catalog and the Commentary of Hipparchos”. In: *DIO* 12 (2002), pp. 3–27.

[259] T. P. Robitaille et al. “Astropy: A community Python package for astronomy”. In: *Astronomy & Astrophysics* 558 (2013), A33. DOI: 10.1051/0004-6361/201322068.

[260] National Renewable Energy Laboratory. *Reference Solar Spectral Irradiance: ASTM G-173*. 2016. URL: http://rredc.nrel.gov/solar/spectra/am1.5/astmg173/astmg173.html.

[261] D. R. Williams. “Earth fact sheet”. In: *Structural geology of the Earth′s interior: Proc. Natl. Acad. Sci. NASA (17 Nov 2010)* 76.9 (2004). URL: http://nssdc.gsfc.nasa.gov/planetary/factsheet/earthfact.html.

[262] ASTM International. “Standard Tables for Reference Solar Spectral Irradiances: Direct Normal and Hemispherical on 37° Tilted Surface”. In: *Book of Standards* 14.04 (2012). DOI: 10.1520/G0173-03R12.

[263] O. Dubovik, M. D. King, et al. “A flexible inversion algorithm for retrieval of aerosol optical properties from Sun and sky radiance measurements”. In: *J. Geophys. Res.* 105.D16 (2000), pp. 20673–20696. DOI: 10.1029/2000jd900282.

[264] O. Dubovik et al. “Variability of absorption and optical properties of key aerosol types observed in worldwide locations”. In: *J. Atmos. Sci.* 59.3 (2002), pp. 590–608. DOI: 10.1175/1520-0469(2002)059<0590:voaaop>2.0.co;2.

[265] F. Wagner and A. Silva. “Some considerations about Ångström exponent distributions”. In: *Atmos. Chem. Phys. Discuss.* 7.4 (2007), pp. 12781–12805. DOI: 10.5194/acpd-7-12781-2007.

[266] A. Bucholtz. “Rayleigh-scattering calculations for the terrestrial atmosphere”. In: *Appl. Opt.* 34.15 (1995), pp. 2765–2773. DOI: 10.1364/ao.34.002765.

[267] M. Blumthaler, W. Ambach, and A. Blasbichler. “Measurements of the spectral aerosol optical depth using a sun photometer”. In: *Theor. Appl. Climatol.* 57.1-2 (1997), pp. 95–101. DOI: 10.1007/bf00867980.

[268] B. Holben et al. “AERONET - A federated instrument network and data archive for aerosol characterization”. In: *Remote Sens. Environ.* 66.1 (1998), pp. 1–16. DOI: 10.1016/s0034-4257(98)00031-5.

[269] D. R. Brooks and F. M. Mims. “Development of an inexpensive handheld LED-based Sun photometer for the GLOBE program”. In: *J. Geophys. Res.* 105 (2001), pp. 4733–4740. DOI: 10.1029/2000jd900545.

[270] NASA Goddard Space Flight Center. *Aerosol Robotic Network (AERONET)*. 2016. URL: http://aeronet.gsfc.nasa.gov/.

[271] T. A. Berkoff et al. “Nocturnal aerosol optical depth measurements with a small-aperture automated photometer using the moon as a light source”. In: *J. Atmos. Oceanic Technol.* 28.10 (2011), pp. 1297–1306.

[272] D. Pérez-Ramírez et al. “Columnar aerosol properties from sun-and-star photometry: statistical comparisons and day-to-night dynamic”. In: *Atmos. Chem. Phys.* 12.20 (2012), pp. 9719–9738. DOI: 10.5194/acp-12-9719-2012.

[273] U. Löhnert et al. “JOYCE: Jülich observatory for cloud evolution”. In: *Bull. Amer. Meteor. Soc.* 96.7 (2015), pp. 1157–1174. DOI: 10.1175/bams-d-14-00105.1.

[274] B. Bohn. *FZJ-JOYCE AERONET Data*. 2016. URL: http://aeronet.gsfc.nasa.gov/new_web/photo_db/FZJ-JOYCE.html.

[275] B. Bohn. “Private communications”. 2016.

[276] V. Kirchhoff, A. Silva, and D. Pinheiro. “Wavelength dependence of aerosol optical thickness in the UV-B band”. In: *Geophys. Res. Lett.* 29.12 (2002). DOI: 10.1029/2001gl014141.

[277] N. T. O'Neill et al. "Spectral discrimination of coarse and fine mode optical depth". In: *Journal of Geophysical Research: Atmospheres* 108.D17 (2003). 4559. ISSN: 2156-2202. DOI: 10.1029/2002jd002975.

[278] B. Briscoe and K. Galvin. "The effect of surface fog on the transmittance of light". In: *Sol. Energy* 46.4 (1991), pp. 191–197. DOI: 10.1016/0038-092x(91)90063-3.

[279] A. Rouhani, E. Bernhardsson, E. Freider, et al. *Luigi*. Spotify USA Inc. 2016. URL: http://luigi.readthedocs.org/en/stable/.

[280] C. Rosset et al. *Healpy*. 2016. URL: http://healpy.readthedocs.org/.

[281] A. Levi et al. *Computer and Information Sciences - ISCIS 2006: 21th International Symposium Istanbul*. Lecture Notes in Computer Science. Springer Berlin Heidelberg, 2006. ISBN: 9783540472438. DOI: 10.1007/11902140.

[282] I. Her. "Geometric transformations on the hexagonal grid". In: *IEEE Transactions on Image Processing* 4.9 (1995), pp. 1213–1222. DOI: 10.1109/83.413166.

[283] P. Wang. *Array Grammars, Patterns and Recognizers*. Computer science. World Scientific, 1989. ISBN: 9789810200831.

[284] A. Patel. *Hexagonal Grids*. Red Blob Games. 2016. URL: http://www.redblobgames.com/grids/hexagons/.

[285] T. Niggemann, M. Lauscher, M. Stephan, et al. "The optics and detector-simulation of the air fluorescence telescope FAMOUS for the detection of cosmic rays". In: *SPIE Astronomical Telescopes+ Instrumentation*. SPIE. 2012, pp. 844430–844430. DOI: 10.1117/12.925305.

[286] T. Niggemann et al. "Status of the Silicon Photomultiplier Telescope FAMOUS for the Fluorescence Detection of UHECRs". In: *dep* 3 (2013), d2Nγ. arXiv: 1502.00792.

[287] T. Niggemann et al. "G4SiPM: A novel silicon photomultiplier simulation package for Geant4". In: *Nucl. Instrum. Methods Phys. Res., Sect. A* (2015). ISSN: 0168–9002. DOI: 10.1016/j.nima.2015.01.067.

[288] M. Lauscher et al. "FAMOUS — A Prototype Silicon-Photomultiplier-Telescope for the Fluorescence Detection of Extensive Air Showers". In: *Internal Note of the Pierre Auger Collaboration* (2012).

[289] T. Niggemann. "New Telescope Design with Silicon Photomultipliers for Fluorescence Light Detection of Extensive Air Showers". In: *Internal Note of the Pierre Auger Collaboration* GAP2012-017 (2012).

[290] M. Lauscher, L. Middendorf, T. Niggemann, et al. "Muon measurement using scintillator tiles with SiPM readout". In: *Internal Note of the Pierre Auger Collaboration* GAP2013-057 (2013).

[291] T. Bretz et al. "SiPMs for SSD". In: *Internal Note of the Pierre Auger Collaboration* GAP2015-043 (2015).

Appendices

1 Luigi

Luigi is an open-source Python package for building complex pipelines of batch jobs conceptually similar to GNU Make used for the compilation of C++ programs [279].

The central element when building a work-flow using Luigi is a “task” (cf. source code example below). Besides the instructions for the execution, a task has an output and can have a requirement, i.e. another task. In most cases, the output consists of one or many local files on the hard-disk. During execution of the work-flow, task dependencies are automatically resolved in such a way that the optimal order of execution is found. An example of the web-interface used for supervision of the execution of the pipelines, is given in figure 1. Depending tasks would receive the output of their requirement as input. If a failure happens in a certain task, the pipeline is stopped. Since the outputs of intermediate tasks have been persisted to their out-

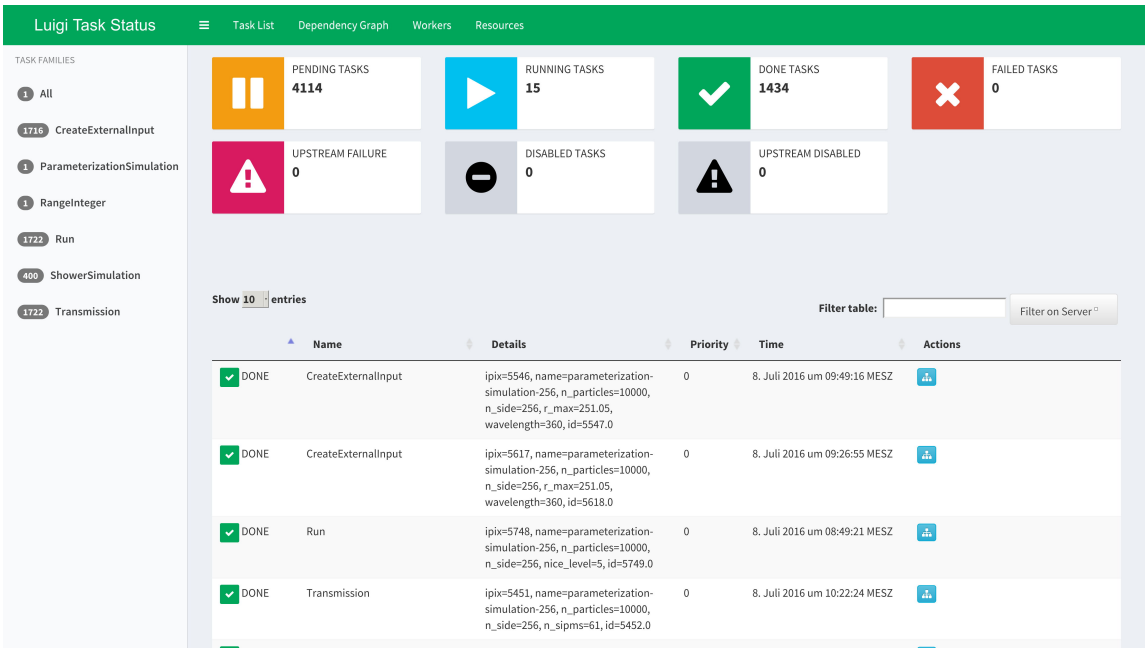

Figure 1: Web frontend of the visualizer for job monitoring. Since the frontend is served as a website, it can also be accessed on remote machines via network.

puts, the pipeline can be continued from this point on when the failure is fixed. The following code example demonstrates the aforementioned functionality:

```
import luigi

# An external task has no execution code and only references input files
# needed for the execution of this pipeline.
class SomeInputTask(luigi.ExternalTask):
        # The output of this task.
    def output(self):
        return luigi.LocalTarget("path/to/input.txt")

# Definition of a task.
class MyTask(luigi.Task):
    # Parameters of this task.
    # Tasks with same parameter values automatically share the
    # same instance.
    param = luigi.Parameter(default=42)

    # What the other task depends on.
    # The output of the dependent task will be available as input for
    # this task.
    def requires(self):
        return SomeInputTask()

    # Execution code of this task.
    def run(self):
        # Open the output file in write mode.
        with self.output().open("w") as o:
            # Write something into it.
            print >>o, "hello world", self.input().open("r").read()

    # The output of this task.
    # The directories and the file will be automatically created.
    def output(self):
        return luigi.LocalTarget("path/to/output-%d.txt" % self.param)

if __name__ == '__main__':
    # Run luigi framework.
    # The parameters of the tasks are automatically available as command
    # line parameters.
    luigi.run()
```

Thus, Luigi is a very powerful tool for the planning of complex simulation jobs. Simulations can be divided into separate tasks and executed in parallel. The analysis of the simulation data can also be executed, if split into separate tasks, in parallel. The analysis can be either directly programmed in Python and thus make use of the powerful linear algebra libraries or in another programming language of choice. If the analysis changed, only the output of the analysis would be deleted. If something in the simulation code changed significantly, all outputs would be deleted and the whole pipeline reprocessed.

2 HEALPix

HEALPix (Hierarchical Equal Area isoLatitude Pixelization of a sphere) is a software package that implements a pixelization algorithm of a sphere [202]. The algorithm produces pixels of

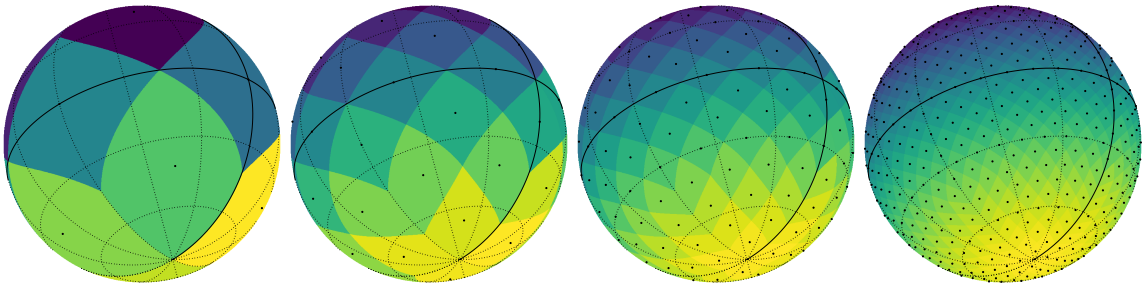

Figure 2: Four examples of a HEALPix pixelization. From left to right: 12 equal sized pixels, 48 pixels, 192 pixels and 768 pixels. The latter corresponds to a angular width of $\approx 7.3°$. The color-code in the orthographic maps denotes the pixel id (dark to bright).

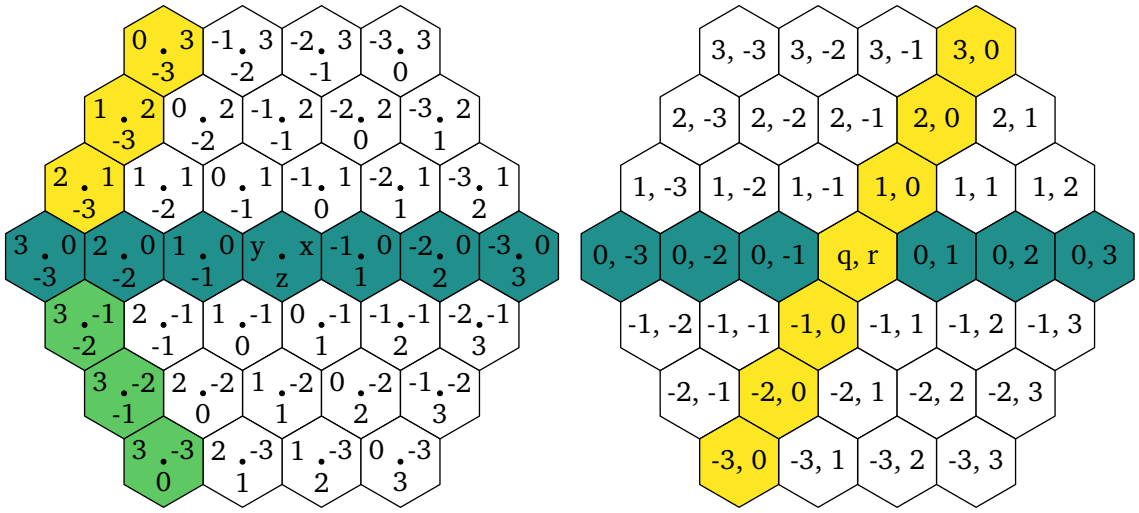

Figure 3: Left: hexagonal grid with cube coordinates. Right: the same hexagonal grid but with axial coordinates.

equal surface area. Furthermore, the pixel centers are arranged on rings of constant latitude. The number of rings depends on the resolution of the HEALPix pixelization. Figure 2 presents the pixelization result of HEALPix for four distinct number of pixels. The functionality of the HEALPix package has been made available in Python by the module Healpy [280].

3 Hexagonal grids

Hexagonal grids are very useful for the handling of hexagonally arranged objects and calculations, e.g. the distance between two hexagons [281, 282, 283]. There are two complementary coordinate systems which have been used in the scope of this thesis: axial and cube coordinates. These coordinates ignore the size of the hexagons. Cube coordinates consist, analogously to Cartesian coordinates, of a x-, y- and z- axis given

$$x + y + z = 0 \quad . \tag{1}$$

The angle between the three axes is 60°. Given equation (1), the y-axis can be expressed by the other two which yields the axial coordinates r, q. Thus, the coordinates transformations are

$$q = x \tag{2}$$
$$r = z \tag{3}$$

and

$$x = q \tag{4}$$
$$z = r \tag{5}$$
$$y = -x - z \quad . \tag{6}$$

The distance d between two hexagons (x_1, y_1, z_1) and (x_2, y_2, z_3) in cube coordinates is

$$d = \frac{1}{2}\left(|x_1 - x_2| + |y_1 - y_2| + |z_1 - z_2|\right) \tag{7}$$

whereby $d = 1$ denotes direct neighbors. Finally, for plotting, the hexagon coordinates can be transformed to Cartesian coordinates given a certain size s

$$x = \sqrt{3}s\left(q + \frac{1}{2}r\right) \tag{8}$$
$$y = \frac{3}{2}s\,r \tag{9}$$

and the back transformation

$$q = \frac{1}{3s}\left(\sqrt{3}\,x - y\right) \tag{10}$$
$$r = \frac{2}{3s}y \quad . \tag{11}$$

Since the back transformation does not yield integer numbers, the coordinates have to be rounded

$$\begin{cases} -\lfloor y \rceil - \lfloor z \rceil, \lfloor y \rceil, \lfloor z \rceil & \text{if } |\lfloor x \rceil - x| > |\lfloor y \rceil - y| \wedge |\lfloor x \rceil - x| > |\lfloor z \rceil - z| \\ \lfloor x \rceil, -\lfloor x \rceil - \lfloor z \rceil, \lfloor z \rceil & \text{else } |\lfloor y \rceil - y| > |\lfloor z \rceil - z| \\ \lfloor x \rceil, \lfloor y \rceil, -\lfloor x \rceil - \lfloor y \rceil & \text{else} \end{cases} \tag{12}$$

whereas the notation $\lfloor x \rceil$ refers to rounding of x to the nearest integer. A comprehensive guide to hexagonal grids including source code examples can be found in [284].

4 Hammersley point picking

When sampling a parameter space, the traditional approach is to pick random numbers from a uniform distribution. Especially for two-dimensional or higher dimensional parameter spaces, this approach is to be disfavored since a very large number of random numbers has to be generated to achieve a good coverage of the whole parameter space, especially if the results are to be binned for further analysis.

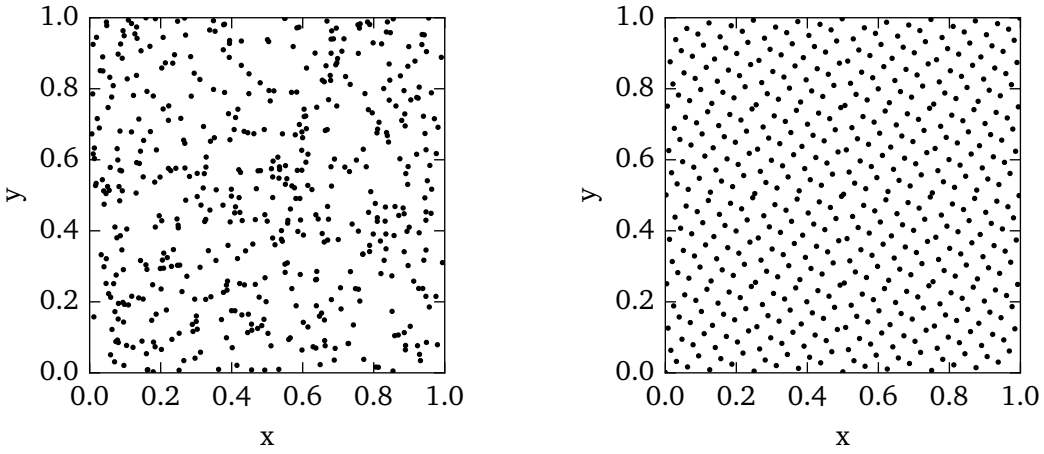

Figure 4: Left: random two-dimensional positions with the coordinates picked from uniform distributions for $n = 512$ points. Right: random positions achieved by the Hammersley algorithm. As expected, the Hammersley point set achieves a good coverage of the parameter space, whereas the random point picking approach suffers from clusters and voids.

For this, the Hammersley algorithm provides a deterministic formula which provides uniformly distributed sets of numbers either on an unit plane or an unit sphere [201]. This approach is widely used in computer graphics for the creation of pixel images of three-dimensional models. Given a set of $n > 1$ points

$$\mathbb{P}_n = \{p_1, \ldots, p_i, \ldots, p_n\} \tag{13}$$

on a unit square $|p_i| \in [0, 1)$, the Cartesian coordinates of the point p_i are given by

$$p_i = \begin{pmatrix} i/n \\ \phi(i) \end{pmatrix} = \begin{pmatrix} x \\ y \end{pmatrix} \tag{14}$$

with the so-called Van der Corput sequence $\phi(i)$. Given the binary representation of i with the individual integer digits $a_0, a_1, \ldots, a_r$

$$i = a_0 + a_1\, 2 + a_2\, 2^2 + \cdots + a_r\, 2^r \tag{15}$$

the Van der Corput sequence mirrors the binary representation of i at the decimal point

$$\phi(i) = \frac{a_0}{2} + \frac{a_1}{2^2} + \cdots + \frac{a_r}{2^{r+1}} \quad . \tag{16}$$

The result for $n = 1000$ points is presented in figure 4.

Declaration of pre-released partial results

The following publications contain pre-released partial results of this work and are cited with shortened author lists. The text of these publications has been written by the author of this thesis and was revised and copy-edited by the co-authors of the publications:

- T. Niggemann, M. Lauscher, M. Stephan, et al. "The optics and detector-simulation of the air fluorescence telescope FAMOUS for the detection of cosmic rays". In: *SPIE Astronomical Telescopes+ Instrumentation*. SPIE. 2012, pp. 844430–844430. DOI: 10.1117/12.925305
- T. Niggemann, P. Assis, P. Brogueira, A. Bueno, H. M. Eicher, M. Ferreira, T. Hebbeker, M. Lauscher, L. Mendes, L. Middendorf, et al. "Status of the Silicon Photomultiplier Telescope FAMOUS for the Fluorescence Detection of UHECRs". In: *dep* 3 (2013), d2Nγ. arXiv: 1502.00792
- T. Niggemann et al. "G4SiPM: A novel silicon photomultiplier simulation package for Geant4". In: *Nucl. Instrum. Methods Phys. Res., Sect. A* (2015). ISSN: 0168–9002. DOI: 10.1016/j.nima.2015.01.067

Additionally, partial results of this work have been pre-released in internal notes of the Pierre Auger Collaboration. Major parts of the text of these publications have been written by the author of this theses:

- M. Lauscher, C. Meurer, T. Niggemann, J. Schumacher, M. Stephan, et al. "FAMOUS — A Prototype Silicon-Photomultiplier-Telescope for the Fluorescence Detection of Extensive Air Showers". In: *Internal Note of the Pierre Auger Collaboration* (2012)
- T. Niggemann. "New Telescope Design with Silicon Photomultipliers for Fluorescence Light Detection of Extensive Air Showers". In: *Internal Note of the Pierre Auger Collaboration* GAP2012-017 (2012)
- M. Lauscher, L. Middendorf, T. Niggemann, et al. "Muon measurement using scintillator tiles with SiPM readout". In: *Internal Note of the Pierre Auger Collaboration* GAP2013-057 (2013)
- T. Bretz, J. Kemp, M. Lauscher, R. Meißner, L. Middendorf, T. Niggemann, C. Peters, J. Schumacher, et al. "SiPMs for SSD". in: *Internal Note of the Pierre Auger Collaboration* GAP2015-043 (2015)

Acknowledgments - Danksagungen

Mit großer Freude möchte ich mich bei den unzähligen Kollegen, Freunden, meiner Familie und vor allem bei meiner Freundin Ximena Ayala Galindo bedanken. Ihr habt mir diese Arbeit überhaupt erst ermöglicht und mich tatkräftig unterstützt. Ximena hat mir vor allem in der Schlussphase jederzeit zur Seite gestanden und mich wenn nötig ermutigt.

Von all denen, mit denen ich arbeiten durfte, bin ich besonders Prof. Thomas Hebbeker zu Dank verpflichtet für die einzigartige Chance an diesem interessanten Projekt in einer großen, internationalen Kollaboration arbeiten und dabei meine eigenen Forschungsinteressen verfolgen zu können. Sein Wissen und langjährige Erfahrung waren von unschätzbarem Wert für mich und für meine Arbeit. Besonders dankbar bin ich außerdem für die vielen Besuche des Pierre Auger Observatoriums in Argentinien und die Teilnahme an internationalen Konferenzen in und außerhalb von Europa. Mein aufrichtiger Dank geht ebenfalls an PD Dr. Oliver Pooth für die Begutachtung meiner Arbeit.

Für die kollegiale und freundliche Arbeitsatmosphäre, die zahlreichen interessanten Meetings und fruchtbaren Diskussionen möchte ich allen Mitgliedern des Instituts und insbesondere der Arbeitsgruppe danken. Namentlich seinen an dieser Stelle Thomas Bretz, Markus Lauscher, Lukas Middendorf, Christine Peters, Matthias Plum, Florian Scheuch, und Johannes Schumacher genannt, sowie viele Kollegen, die ihre Arbeit am Institut mittlerweile abgeschlossen haben, wie zum Beispiel Hans Michael Eichler, Julian Grothoff, Franziska Knuth, Sebastian Mann und Maurice Stephan. Johannes Schumacher möchte ich gerne für die Unterstützung bei den Feldmessungen und die Entwicklung und den Bau der Stromversorgung des Teleskops zusammen mit Daniel Louis der Elektronikwerkstatt des III. Physikalischen Instituts A unter Leitung von Franz-Peter Zantis danken. Der Mechanikwerkstatt des III. Physikalischen Instituts A unter Leitung von Barthel Philipps und all seinen Mitarbeitern sei insbesondere für die Konstruktion und den Bau der Mechanik des Teleskops gedankt.

Ebenfalls danke ich den Mitarbeitern der IceAct Arbeitsgruppe des III. Physikalischen Instituts B, darunter Jan Auffenberg, Leif Rädel, Merlin Schaufel und Sebastian Schoenen, die es ermöglicht haben einen Prototypen des Teleskops am Südpol zu installieren und erfolgreich zu betreiben. Ich danke Birger Bohn und seinen Mitarbeitern für die wertvollen Daten der FZJ-JOYCE Station des NASA Aerosol Robotic Network, welche ich in meiner Analyse verwenden durfte. Des Weiteren bedanke ich mich bei Sergio Navas Concha der Universität Granada und bei Markus Lauscher für die Bereitstellung der SiPM Dynamikbereichsmessungen. Zu guter Letzt möchte ich ganz herzlich den kritischen Korrekturlesern meines Manuskriptes Prof. Thomas Hebbeker, Christine Peters, Florian Scheuch und Johannes Schumacher danken.

Diese Arbeit wurde vom Bundesministerium für Wissenschaft und Forschung (BMBF), dem Astroparticle Eranet (ASPERA) und der Helmholtz-Gemeinschaft Deutscher Forschungszentren e.V. finanziert und unterstützt.